Dynamics and stability of flow through abdominal aortic aneurysms

Shyam Sunder Gopalakrishnan

THÈSE DE L'UNIVERSITÉ DE LYON

délivrée par

L'UNIVERSITÉ CLAUDE-BERNARD LYON 1

ÉCOLE DOCTORALE MEGA

Laboratoire de mécanique des fluides et d'acoustique (LMFA)

par **Shyam Sunder GOPALAKRISHNAN**

Dynamics and Stability of Flow through Abdominal Aortic Aneurysms

soutenue publiquement le 19 février 2014 devant le jury composé de

Rapporteurs :   Valérie DEPLANO
                         Peter SCHMID

Examinateurs :   Patrick FEUGIER
                         Michel LANCE
                         Anne-Virginie SALSAC

Encadrants :   Arie BIESHEUVEL
                         Benoît PIER

UNIVERSITÉ DE LYON

Abstract

The main objective of this thesis is to characterise the flow fields observed in an abdominal aortic aneurysm (AAA) under different physiological conditions during its progressive enlargement. An axisymmetric AAA, modeled as an inflation of gaussian shape on a vessel of circular cross-section, is considered in the present study. This means that the results are more significant for the early stages of growth of an AAA. The model AAA is characterized by a maximum height H and width W, made dimensionless by the upstream vessel diameter. To begin with, the flow characteristics in AAAs are investigated using steady flows. The global linear stability of the base flows is analysed by determining the eigenfrequencies and eigenfunctions of small-amplitude perturbations. In order to understand the instability mechanisms, the energy transfer between the base flow and the perturbations is computed. The flow in relatively shallow aneurysms (of relatively large width) become unstable by the lift-up mechanism and have a perturbation flow which is characterized by stationary, growing modes. More localized aneurysms (with relatively small width) become unstable at larger Reynolds numbers, presumably by an elliptic instability mechanism; in this case the perturbation flow is characterized by oscillatory modes. For the case of pulsatile flows, two types of physiological flowrate waveforms are considered in our study, corresponding to rest and exercise conditions. The flows are observed to remain attached to the walls during the systolic phase, with flow separation generally observed during the deceleration after the peak systole. During this phase, the vorticity is found to roll-up into a vortex at the proximal end. This vortex enlarges with time and impinges at the downstream end of the AAA, resulting in large spatial gradients of wall shear stress (WSS) along the wall, which are not found in the healthy case. The flow conditions are observed to vary significantly with Womersley (Wo) and Reynolds (Re) numbers, with the flow remaining attached to the walls for longer times, as the Womersley number Wo increases. The principal effect of increasing Re is that the primary vortex formed after peak systole is stronger. Clinically relevant flow characteristics of aneurysmal flow, i.e. detachement of flow and impingement on the distal end, the presence of low oscillatory WSS within the AAA, are observed even for very shallow aneurysms. For deep aneurysms, multiple vortices are observed throughout the cycle within the AAA cavity. Stability analysis of pulsatile base flows reveals that the maximum values of the perturbations are observed near the distal end of the AAA. However, they are not entirely confined to the AAA cavity and extend downstream, implying that once an AAA is formed, the disturbed flow conditions spread even to the undeformed arterial walls downstream of the AAA. Finally, by considering two equivalent AAA shapes modeled by a sinusoidal and a gaussian function, the sensitivity of these results with respect to the details of the geometry has been established.

Résumé

Le principal objectif de cette thèse est de caractériser l'écoulement dans un anévrisme abdominal aortique (AAA) sous différentes conditions physiologiques et à différents stades de son développement. Cette étude est consacrée aux AAA axisymétriques, modélisés comme une dilatation de profil gaussien et de section circulaire. Ainsi, les résultats s'appliquent surtout aux étapes précoces du développement d'un AAA. Le modèle d'AAA est caractérisé par une hauteur maximale H et une largeur W, l'unité de mesure étant le diamètre d'entrée de l'artère. Pour commencer, la dynamique est étudiée pour les écoulements stationnaires. La stabilité globale de ces écoulements de base est analysée en calculant les valeurs propres et les fonctions propres pour des perturbations de faible amplitude. Pour comprendre les mécanismes d'instabilité, le transfer d'énergie entre l'écoulement de base et les perturbations est calculé. L'écoulement pour des AAA peu profonds (ou de grande longueur) se déstabilise par un mécanisme de 'lift-up' et les perturbations amplifiées sont stationnaires. Des anévrismes plus localisés (ou plus profonds) deviennent instables pour des nombres de Reynolds plus élevés, sans doute par instabilité elliptique ; dans cette situation, les perturbations sont des modes oscillants. Dans le cas des écoulements pulsés, deux types de profil de débit physiologique ont été considérés dans cette étude, correspondant à une situation de repos ou d'exercice physique. Ces écoulements restent collés aux parois pendant la phase de systole et un écoulement décollé est généralement observé pendant la décélération après le maximum de systole. Dans cette phase, un vortex se forme à l'extrémité aval. Ce vortex s'agrandit au cours du temps et impacte l'extrémité aval de l'AAA, ce qui conduit à de forts gradients de contrainte pariétale, qui ne sont pas observés dans les cas sains. Il a été observé que les conditions d'écoulement varient significativement avec les nombre de Womersley (Wo) et de Reynolds (Re); l'écoulement reste attaché aux parois plus longtemps pour des nombres de Womersley croissants. Le principal effet d'une augmentation de Re est un renforcement du vortex primaire qui se forme après le maximum de systole. Les décollements de l'écoulement, l'impact de vortex au bord aval de l'AAA ou encore de faibles contraintes pariétales oscillantes (des caractéristiques importantes dans les cas d'anévrismes pathologiques) sont observés même pour des anévrismes de faible profondeur. Pour des anévrismes plus développés, des vortex multiples sont observés tout au long du cycle dans la cavité de l'AAA. Une analyse de stabilité de ces écoulements de base pulsés a montré que le maximum des perturbations se développe vers l'extérmité aval des AAA. Cependant, les perturbations ne sont pas complètement confinées dans la cavité de l'AAA et se développent aussi au-delà en aval. On en déduit qu'une fois qu'un AAA s'est développé, les perturbations affectent aussi les artères saines en aval de l'AAA. Enfin, en considérant deux profils équivalents d'AAA, de formes sinusoïdale et gaussienne, la sensibilité des résultats aux détails de la géométrie a pu être établie.

Acknowledgements

I would like to extend my deepest gratitude to my advisors Benoît Pier and Arie Biesheuvel for their guidance and motivation which I received during my PhD. Meticuluous research, attention to detail, interpretation of results in a sound manner, having a clear idea of the various project aims, are some of the traits that I learnt (to some extent) from Benoît. Arie on the other hand has been very instrumental in getting me to think from an application point of view, as in how my results obtained using fluid mechanics would shed light in understanding the pathology of aneurysms and so on. I thank both of them for introducing me to the fascinating field of bio-fluid dynamics and for all the help and support, which I hope, will continue in the future too.

An interesting feedback on my work was provided by the rapporteurs, Peter Schmid and Valérie Deplano, and I thank them for taking their time off for my defence. In the same vein, I would like to thank Patrick Feugier and Anne-Virginie Salsac for being a part of the jury. Also, a special mention goes out to Michel Lance, the director of our lab for his cooperation during my stay in the lab.

During my thesis, I used to be involved in teaching activities at the university, which has been a great experience, and in this regard I would like to say a special thank you to Severine Millet, Faouzi Laadhari, Ivana Vinkovic and Delphine Doppler.

My life at LMFA would not have been interesting if not for my wonderful friends around me. Firstly, my office mates, Clement, Jorge, Alex and Colin, with whom I used to go out in the evenings, and play babyfoot, have provided me with a wonderful retreat from work. My friends from Club Microfiche, Loic, Wouter, Philippe, Michael, Faouzi, Shimpei and others have made my stay all the more pleasant. In particular Loic, with whom I used to go out to play football along with the others from lab, notably, Sebastien, Benoît, Pierre and Xavier have been really great. I would also like to thank my friends outside the lab, Laure, Cyril, Gigite (JB2), Pedro, Niko, Aurélien, Guillaume and many others for having made my stay in Lyon the most enriching time of my life.

Thanks are also due to my supervisors and friends from Ladhyx where I did my Masters, Patrick Huerre in particular, who introduced me to Benoît. Also, to my friends from IISc, Jyothirmoy Dey, Alakesh Mandal, Manu and Bharath who were instrumental in me getting to France for my graduate studies.

I wouldn't have been here without the unwavering support from my family. Being so far away from home has been difficult both for me and for my parents and my brother, Jayaram. But I have always been able to count on their encouragement, and I am counting on it for my future endeavors as well.

And finally, the French Ministry for providing me with a scholarship for pursuing my education here in France.

Thanks and praises,
Shyam

Contents

Introduction

This introduction begins with a description of an abdominal aortic aneurysm (AAA) along with the various biological aspects involved in the pathogenesis of an AAA. Then a broad overview of the role that fluid mechanics has played in understanding the nature of blood flow is presented, with an emphasis on literature related to cardiovascular diseases. This includes discussion of geometries other than aneurysms, including stenoses. The final section describes the aims of the present thesis.

1.1 Abdominal Aortic Aneurysms

1.1.1 General introduction

Aneurysms are localized permanent arterial dilatations due to disease or other complex processes that result in the weakening of the arterial walls (Lasheras, 2007). The word aneurysm is from the Greek word *aneurusma* (*ana* throughout and *eurus* wide) and the use of this word in medicine dates back to Guy de Chauliac (1373)(Duclaux *et al.*, 2010). Although this complex vascular disease forms in many blood vessels, it mainly appears in arteries, primarily in the abdominal and thoracic portions of the aorta and in the intracranial arteries surrounding the Circle of Willis. Aneurysms are often classified according to their shape and location in the human body into two main groups: fusiform and saccular aneurysms. Among these, fusiform aneurysms are characterised by a bulge about the vessel centerline, whereas saccular aneurysms have a berry-like shape. The marked differences in their shape and in their location in the human body suggest that their pathogenesis is likely to be different.

Fusiform aneurysms are most commonly found in the abdominal portion of the aorta, below the renal arteries and upstream of its bifurcation into the iliac arteries; these are known as Abdominal Aortic Aneurysms (AAAs) (figure1.1(a)). A localized aortic dilatation is clinically considered an aneurysm when its maximal diameter is greater than 1.5 times the healthy diameter (Johnston *et al.*, 1991). It is important to note that generally only the maximum diameter is used as a criterion for risk of rupture associated with an AAA. The length (width) of an AAA, which is indicative of the size, is not taken into account. As about one fifth of large abdominal aneurysms are not limited to just the aorta, but have extended to one or both of the common iliac arteries (Armon *et al.*, 1998), it is believed that the width of an abdominal aneurysm could also be an important parameter (figure 1.1(b)). However, a common iliac artery aneurysm is seldom seen in the absence of an AAA (Huang *et al.*, 2008).
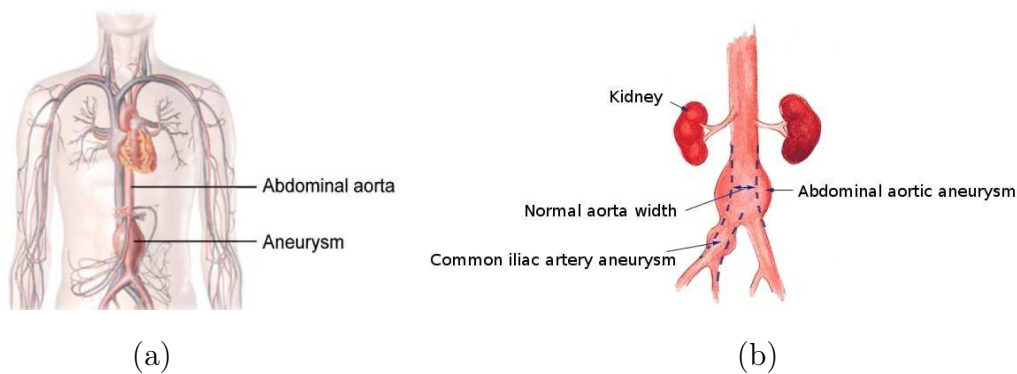
Figure 1.1: (a) An abdominal aortic aneurysm (Lasheras, 2007). (b) An abdominal aortic aneurysm extending to the common iliac artery (www.drstandley.com).

1.1.2   Wall composition and associated changes with the progression of an AAA

An arterial vessel wall is a complex structure, having a specific function for each body location. All the vessel walls are composed of three layers (or tunicae): the tunica intima, the tunica media (or muscular), and the tunica external (adventitia) (Fung, 1993, Holzapfel, 2002) (figure 1.2). The thickness and composition of each layer depends on its proximity to the heart and on the specific function of the organ or tissue supplied by the vessel. Arteries are generally thicker with varying degree of elasticity depending on function. The innermost layer, intima, is composed of a single layer of endothelial cells that rests on a thick basal membrane and a subendothelial layer whose thickness varies with topography, age and disease. The endothelial cells are in direct contact with the blood. The media is the thickest layer with different structures at different locations along the circulatory system. It is composed of smooth muscle cells, a network of elastin and collagen fibrils and elastic laminae which separate the media into a number of fiber-reinforced layers. The primary constituents of the adventitia are thick bundles of collagen fibrils arranged in helical structures. The adventitia, which is the outermost layer, is surrounded by loose connective tissue.

The main cellular components of an arterial wall are smooth muscle cells and endothelial cells. The high content of smooth muscle cells in the media is mainly responsible for the viscoelastic behaviour of an arterial wall. The endothelial cells play an important role in many physiological functions, like controlling the wall permeability and hemostasis. They are semipermeable and allow for regulated transport of fluids and solutes into and out of the blood, while at the same time acting as a barrier for the passage of large molecules. A common function of the endothelium is to maintain blood in a fluid state, and to promote limited clot formation when there is a breech in the integrity of the vascular wall.

Once an AAA is formed, the structural composition of the arterial wall undergoes considerable changes. As the mechanical properties of the aortic wall depend largely on its composition, an alteration in composition should cause changes in mechanical properties. In this context, the elastin and collagen content are found to play a pivotal role in controlling the elasticity of the walls. The elastin content decreases by about 91% in
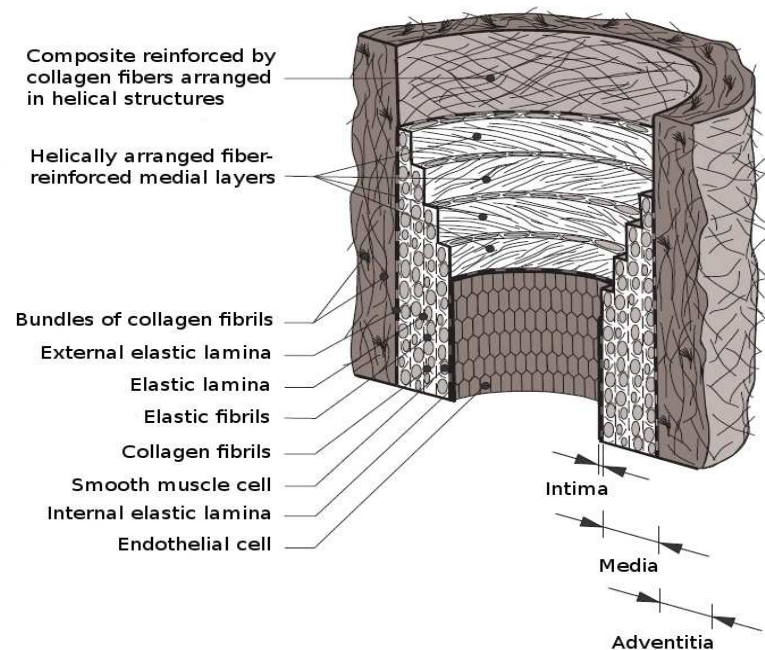
Figure 1.2: Diagrammatic model of the major components of a healthy elastic artery composed of three layers: intima, media and adventitia (Holzapfel, 2002).

terms of volume fraction when compared with a nonaneurysmal aorta (He & Roach, 1994). The degradation of elastin has been associated with an increase in elastase activity which accelerates the breakdown process of elastin, resulting in a low content of elastin in AAAs. The collagen content has been observed to increase with the formation of an AAA by about 77% (He & Roach, 1994). The vessel wall becomes stiffer and less distensible as the ratio of elastin to collagen decreases with the progresssion of an AAA. Such an increase in stiffness in the vessel wall alters the pulse wave propagation through the abdominal aorta, leading to changes in hemodynamics.

1.1.3 Pathogenesis

There are many risk factors associated with cardiovascular diseases, like age, genetic factors, high blood pressure, high cholesterol, obesity, diabetes, cigarette smoking, high alcohol consumption, etc (Choke *et al.*, 2005, Lasheras, 2007). Smoking is the risk factor most strongly associated with abdominal aortic aneurysms, followed by age, hypertension, hyperlipidemia, and atherosclerosis (Lederle *et al.*, 1997). Sex and genetics also influence aneurysm formation. Men are 10 times more likely than women to have an abdominal aortic aneurysm of 4 cm or greater (Lederle *et al.*, 2001) but women are more at risk. The prevalence of abdominal aortic aneurysms is $\approx 5\%$ among men ≤ 65 years of age screened by ultrasound (Group, 2002). Those with a family history of abdominal aortic aneurysm have an increased risk of 30% (Frydman *et al.*, 2003), and their aneurysms tend to occur at a younger age and carry a greater risk of rupture than do sporadic aneurysms.

The strength of the aortic wall lies in the elastin and collagen of its extracellular

matrix. Consequently, degradation of these structural proteins weakens the aortic wall and allows aneurysms to develop. Atherosclerosis has been associated with the pathogenesis of abdominal aortic aneurysms as they are usually observed in the presence of an AAA. The infrarenal abdominal aorta is most affected by the atherosclerotic process and is similarly the most common site of abdominal aneurysm formation. Atherosclerosis is the process in which fatty materials are deposited on the arterial walls resulting in plaque formation. The propensity for plaque formation at bifurcations, branchings, and curvatures has led to conjectures that local mechanical factors such as wall shear stress (WSS) and mural tensile stress potentiate atherogenesis. Recent studies of the human vessels at high risk, and of corresponding models, have provided quantitative evidence that plaques tend to occur where flow velocity and shear stress are reduced and flow departs from a laminar, unidirectional pattern. Such flow characteristics tend to increase the residence time of circulating particles in susceptible regions while particles are cleared rapidly from regions of relatively high wall shear stress and laminar unidirectional flow (Glagov *et al.*, 1988). The flow patterns and WSS distributions associated with plaque localization are most prominent during systole. However, current research suggests that genetic, environmental, hemodynamic, and immunologic factors all contribute to the development of aneurysms (Isselbacher, 2005).

In this context, the endothelial cells which line the arterial vessel wall with direct exposure to blood flow, are understood to play a key role in the wall physiology and thereby influence the pattern of the stresses acting on the wall as they are affected by the disturbed flow patterns (Chiu & Chien, 2011, Jilkova *et al.*, 2013). Studies have identified that endothelial cells are susceptible to damage under excessive levels of WSS (Fry, 1968, Chiu & Chien, 2011). Among the various physiological functions that the endothelial cells perform, one of them is the control of wall permeability (Aird, 2007). Regions of low wall permeability are favored locations for atherosclerotic plaque deposits (Aird, 2007, Pedley, 1979) as the discontinuity in the vessel wall enables the passage of low density lipoproteins and cholesterol deposits, which in turn result in the formation of lesions, thereby altering the wall physiology. The endothelial cells are more receptive to changes in the WSS values than the flow rate, and the wall permeability is found to be affected by the WSS variations along the vessel wall (Shaaban & Duerinckx, 2000). Atherosclerotic deposits are found in some localized sites of the abdominal aorta. The comparison of the sites of the disease with the local hemodynamic conditions reveals that the regions of low WSS are strongly correlated with atherosclerotic intimal thickening (Ku, 1997).

There has also been evidence of inflammatory infiltrates within the wall or aortic aneurysms resulting in the degradation of the extracellular part of the tissues (Isselbacher, 2005). Such inflammatory sites can result in the production of enzymes that may participate in the abdominal aortic aneurysm formation. These can degrade the elastin and collagen, eventually degrading the aortic wall.

In addition, the endoluminal thrombus lining the lumen of an AAA is also believed to play an important role in the enlargement of an AAA (Thubrikar *et al.*, 2003). The presence of thrombus reduces the effective lumen area and consequently the pressure load on the aneurysm wall may be reduced and reduces the wall stress by its ability to sustain tensile loads. It has also been postulated that the thrombus may form fibrous connections thereby preventing the aneurysm from further dilation. Such a reinforcing effect by the thrombus has a marked reduction in the expansion rate of an AAA (Thubrikar *et al.*, 2003). Thus for two aneurysms of identical size, the one with a mural thrombus has a

lower wall stress and is less likely to rupture than the one without the mural thrombus. But, if the thrombus undergoes lysis, or breaks down, then the aneurysmal wall would have to bear the stress previously borne by the thrombus, and hence resulting in a sudden dilation of the aneurysm. Also, thrombus could act as a barrier to the normal oxygen diffusion from the lumen to inner layers of the aortic wall, in which case the intima and media may be deprived of oxygen supply, thereby weakening the arterial vessel wall (Vorp et al., 2001).

Age is an important risk factor, and the incidence of abdominal aortic aneurysm rises rapidly after the age of 55 years in men and 70 in women. This has led to the hypothesis that the changes in the structure of the arterial vessel wall with the normal aging process, results in different hemodynamics, which in turn initiates a feedback loop that modifies the structure of the vessel wall. Though the associated biochemical mechanisms contributing to the vascular diseases act systematically throughout the entire vascular system, it is however observed that most cardiovascular diseases preferentially develop at specific locations in the circulatory system. This striking 'disease's localization' hints at specific hemodynamic conditions (mechanical stimuli) as one of the leading causes. The influence of pulse pressure on cardiovascular prognosis has been well-established (Nichols & O'Rourke, 1998, Amar et al., 2001). Since pulse pressure is partly determined by artery stiffness, the elasticity of arterial walls is considered to be a relevant tool to assess cardiovascular risk. The number of elastic laminae in the medial layer is found to be smaller in the abdominal aorta than in the thoracic aorta, and therefore the latter has a higher elastic modulus. This may account for much higher incidence of aneurysms in the abdominal aorta than in the thoracic segment. For instance, an AAA is located in the abdominal aorta, upstream of the iliac arteries, where the amplitude of the pressure pulse is considerably modified as a result of the reflection of the wave in the bifurcation. Such an increase in amplitude may initiate and accelerate the formation of the aneurysms in the elderly population. As the ratio between the cross-sectional area of the bifurcated arteries (iliacs) and the parent vessel (abdominal aorta) decreases, the amplitude of the reflected wave in the abdominal aorta increases. The cross-sectional area of the iliac arteries decreases with ageing, atherosclerosis and hypertension. The progressive changes in the wave speed of the transmitted wave caused by ageing, together with the increase in the ratio of cross-sectional areas may then result in an increase in peak systolic pressure in the abdominal aorta causing an increase in the wall stresses. As a result, the wall tissue loses integrity, initiating a positive feedback loop leading to further increase in the arterial diameter.

1.1.4   Diagnosis and treatment

Aneurysms are usually detected incidentally on routine physical examination or on imaging studies ordered for other indications. Steady and gnawing pain in the lower back is the typical complaint. Actual rupture is associated with an abrupt onset of back pain along with abdominal pain and tenderness. Most of the patients appear critically ill. Detection of aneurysms on physical examination is usually made as a palpable, pulsatile abdominal mass. Though aneurysms can be detected on physical examination, its sensitivity is limited, as even large aneurysms may be difficult or impossible to detect in overweight or obese individuals (Lederle & Simel, 1999). Also, a precise estimation of the size of an aneurysm on physical examination is impossible and sizes are normally overestimated, as sometimes, even normal aortas may feel enlarged.
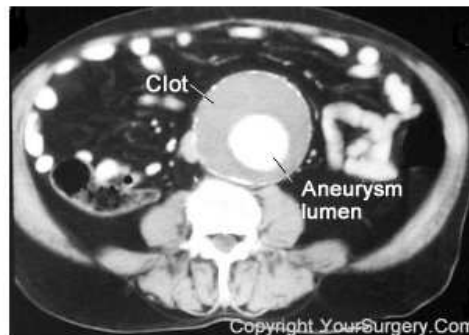
Figure 1.3: CT scan through an AAA revealing the presence of mural thrombus and size of the lumen (YourSurgery.com).

Therefore several diagnostic imaging modalities are now available for detecting and serially monitoring abdominal aortic aneurysms. Among these are abdominal ultrasonography, computed tomography (CT) scanning, magnetic resonance (MR) angiography. Abdominal ultrasonography is perhaps the most practical way to screen for aneurysms. Its major advantages are that it is relatively inexpensive and noninvasive and does not require the use of a contrast agent. Compared with ultrasonography, CT scanning has the advantage that it can better define the shape and extent of the aneurysm, as well as the local anatomic relationships of the visceral and renal vessels. It is also superior to ultrasonography in imaging suprarenal aortic aneurysms. Disadvantages include its cost and its use of ionizing radiation and intravenous contrast media. Nevertheless, although CT is less practical than ultrasonography as a screening tool, its high accuracy in sizing aneurysms makes it an excellent modality for serially monitoring changes in aneurysm size. MR angiography is used as an alternative for patients who are contraindicated (e.g. allergy). The image quality provided by CT scanning and MR angiography makes them a superior tool in detecting abdominal aortic aneurysms. Figure 1.3 shows an image obtained by CT scan that reveals the presence of the endoluminal thrombus and providing an estimate of the size of an AAA.

Once an aneurysm is detected, the next major hurdle is its evaluation, i.e, to make predictions on its growth rate, risk of rupture, when to provide surgical treatment etc. Presently, surgery is recommended for patients with a maximum diameter $\geq$ 5.5 cm (Isselbacher, 2005, Conway et al., 2001). The risk of rupture depends on the size of the aneurysm: with aneurysms < 4 cm, 4 to 4.9 cm, and 5 to 5.9 cm, the annual risk of rupture was 0.3%, 1.5% and 6.5%, respectively (Brown et al., 1996). Although abdominal aneurysms are less prevalent among women than men, when present they rupture 3 times more frequently and at a smaller aortic diameters (mean of 5 versus 6 cm) (Isselbacher, 2005). Rupture is also more common among current smokers and those with hypertension (Brown et al., 1996). A rapid rate of expansion predicts aneurysm rupture. Although the mean rate of abdominal aortic aneurysm expansion is thought to approximate 0.4 cm/y, the rates of expansion within a population are extremely variable. The prediction of expansion rate based on the maximum diameter could be misleading. It is to be noted that the aneurysm growth rate is not accurately predicted by means of size at initial presentation (Conway et al., 2001).
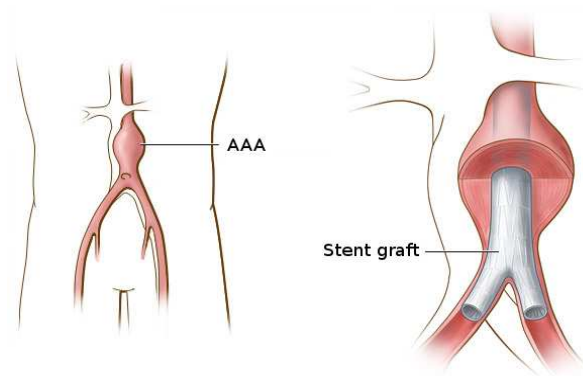
Figure 1.4: An expanding endovascular stent-graft employed for the treatment of an AAA (virchicago.com).

Also the growth rate is not usually observed to be uniform in time. However, a promising new technique is based on the analyses of the wall stress. A 3-dimensional reconstruction of the aortic aneurysm is performed with the use of CT angiography, and wall stress is then determined by finite-element analysis and blood pressure (see Fillinger *et al.* (2003) for more details). It is observed that the sensitivity and specificity of peak wall stress were superior to maximum aortic diameter for predicting risk of aortic rupture (Fillinger *et al.*, 2003). Although this technique still needs to be refined and better studied, it holds promise to become an important tool in determining the timing of aortic repair.

As mentioned previously, surgery is recommended for patients with the maximum aneurysm diameter exceeding 5.5 cm(Isselbacher, 2005, Conway *et al.*, 2001). However, these results were based on a study carried out on men. As the risk of rupture is found to be higher in women when compared to men, this observation is not generalizable to women (Thompson, 2003). Hence, it is recommended that women undergo selective surgery at a smaller aortic diameter of 4.5 to 5 cm. Prior to surgery, medical management is essential to control the growth of the aneurysm. This implies reducing the cholesterol levels, which contribute to plaque formation, reducing hypertension (e.g discontinuing smoking), periodic surveillance of the aneurysm through CT scanning. After these steps, if an aneurysm is deemed to be unsafe, then surgical intervention is recommended. The more common method for the treatment of aneurysms is by carrying out an open surgery. In this process, the surgeon inserts a graft into the area where the aneurysm is detected. This ensures that the blood flowing through the aorta does not affect the expanded part of the aneurysm thereby not exerting pressure on the walls of the aneurysm. A less-invasive alternative to open surgery for repair of abdominal aortic aneurysms is the use of percutaneously implanted, expanding endovascular stent-grafts (White & Stavropoulos, 2009). An illustration of this technique is shown in figure 1.4. Once deployed, the stent-graft serves to bridge the region of the aneurysm, thereby excluding it from the circulation while allowing aortic blood flow to continue distally through the prosthetic stent-graft lumen. One of the major technical difficulty associated with the stent-graft technique is the presence of endoleaks, which is the flow into the aneurysm sac because of the failure to completely exclude the aneurysm from the aortic circulation, leaving the patient susceptible to aneurysm expansion or rupture.

1.2 Role of Fluid Mechanics

In this section we discuss the role that fluid mechanics has played in understanding cardiovascular flows. We begin by describing the work carried out on modeling blood flow, followed by a discussion of flows in related geometries relevant to our present work and finally providing a literature survey on work carried out on abdominal aortic aneurysms.

1.2.1 Modeling blood flow

Blood acts as a medium by which nutrients and wastes are transported within the human body, and consists of a complex mixture of cells, proteins, lipoproteins and ions (Ku, 1997). One of the major constituents of blood are the red blood cells, comprising about 40% of blood by volume. The red blood cells affect the viscosity of blood significantly, making it about four times more viscous than water. Though blood does have variable viscosity, in most arteries it behaves in a Newtonian fashion, and the viscosity can be taken as a constant, 4 centipoise. As the diameter of the abdominal aorta is typically around 2 cm, it is deemed safe to assume the blood to be Newtonian in our study (Pedley, 1979, Berger & Jou, 2000).

The description of the blood flow in the cardiovascular system is complicated by its nature. Nichols & O'Rourke (1998) provide a detailed review of the earlier body of work on quantifying the blood flow in arteries. Sexl (1930) developed an analytical solution to the momentum equation for a Newtonian fluid flow subjected to an oscillatory pressure gradient. A similar technique was later used by Szymanski (1932) to develop an analytical solution to the momentum equation for a flow subjected to a step change in pressure gradient, where the gradient jumps from zero to a constant value. However, the experimental work of McDonald (McDonald, 1955) had identified localised flow reversals in rabbit and dog arteries. The presence of a phase lag between the pulsatile pressure gradient and the flow velocity, led the researchers to theorise that the observed flow reversals resulted from the elastic nature of the artery walls. In an effort to explain these observations, the intial foundation to explain the flow in mammalian blood vessels was made by Womersley (1955). Womersley was one of the first to analyse the phase relationship between the pressure gradient and the resulting velocity field. For a purely oscillatory flow, the characteristic time is proportional to the reciprocal of the frequency of the flow whereas if the flow is pulsatile, there are two time scales (imposed by the mean flow velocity and by the frequency of the flow). The frequency used is the dominant frequency in blood flow arising from the heart beat. The two dimensionless parameters that are generally used to quantify the flow of blood in arteries, are the Womersley number Wo, and the Reynolds number Re, that are given by

$$Wo = \frac{D}{2}\sqrt{\frac{\omega}{\nu}}, \tag{1.1}$$

$$Re = \frac{\overline{U}D}{\nu}, \tag{1.2}$$

where D is the internal diameter of the cylindrical vessel, ω is the pulsation of the unsteady flow, ν is the kinematic viscosity of blood and $\overline{U}$ is the average of fluid velocity. The Womersley number is the ratio of the unsteady inertial forces to the viscous forces and helps in characterising the unsteady nature of flows in blood vessels. An oscillating flow

component leads to a boundary layer of thickness $\delta = \sqrt{\frac{\nu}{\omega}}$. Thus the Womersley number corresponds to the ratio of the vessel radius to the oscillating boundary layer as $Wo = \frac{D}{2\delta}$. A typical value of Wo in the aorta is between 10 and 15, and 1, for the smaller arteries. The typical Reynolds number range of blood flow in the body varies from 1 in small arterioles to approximately 4000 in the largest artery, the aorta (Ku, 1997). Whereas the peak Reynolds numbers in the abdominal aorta can vary from 600 at rest and up to 6000 under exercise conditions (Ku, 1997). Thus the flow spans a range in which viscous forces are dominant on one end and inertial forces are more important on the other.

1.2.2   Analytical solution to pulsatile flow

A formal analysis to compute the velocity and flow rate within a blood vessel is presented here, based on the work of Womersley (1955). Suppose that the pressure-gradient waveform can be expressed as the Fourier series

$$\frac{\partial p}{\partial z} = \sum_{n=-\infty}^{\infty} G_n \mathrm{e}^{in\omega t}, \tag{1.3}$$

where z is the axial coordinate. The axial momentum equation for parallel flow in a tube reduces to

$$\frac{\partial U_z}{\partial t} = -\frac{1}{\rho}\frac{\partial p}{\partial z} + \nu\left(\frac{\partial^2 U_z}{\partial r^2} + \frac{1}{r}\frac{\partial U_z}{\partial r}\right), \tag{1.4}$$

with r being the radial coordinate and ρ the density of the fluid. The boundary conditions on the axial velocity $U_z(r,t)$ follow from the no-slip condition and axial symmetry

$$U_z(D/2, t) = 0, \qquad \frac{\partial U_z}{\partial r}(0, t) = 0. \tag{1.5}$$

The problem is linear and therefore its solution can be written as

$$U_z(r,t) = \sum_{n=-\infty}^{\infty} U_{z,n}(r)\mathrm{e}^{in\omega t}, \tag{1.6}$$

yielding a separate problem for each n. Introducing equations (1.3) and (1.6) into equation (1.4) gives

$$\frac{d^2 U_{z,n}}{dr^2} + \frac{1}{r}\frac{dU_{z,n}}{dr} - \frac{in\omega}{\nu}U_{z,n} = -\frac{G_n}{\nu\rho}, \tag{1.7}$$

to be solved for

$$U_{z,n}(D/2) = 0, \qquad \frac{dU_{z,n}}{dr}(0) = 0. \tag{1.8}$$

For $n \neq 0$, introduction of

$$Wo_n = D/2(n\omega/\nu)^{1/2}, \qquad s_n = \mathrm{i}^{3/2}\, Wo_n 2r/D, \tag{1.9}$$

into the homogeneous part of equation (1.7) yields

$$\frac{d^2 U_{z,n}}{ds_n^2} + \frac{1}{s_n}\frac{dU_{z,n}}{ds_n} + U_{z,n} = 0, \tag{1.10}$$

which is the Bessel equation of order 0. By the symmetry condition the homogeneous solution is the Bessel function of the first kind of order 0, $J_0(s_n)$. Together with the particular solution of equation (1.7),

$$U_{z,n} = -\frac{G_n}{\rho\omega},$$ (1.11)

the general solution becomes

$$U_{z,n}(s_n) = A_n J_0(s_n) - \frac{G_n}{\rho\omega},$$ (1.12)

where the constants A_n follow from the boundary condition $U_{z,n} = 0$ on the vessel wall ($s_n = \mathrm{i}^{3/2}\,Wo_n$). We get the solution as

$$U_{z,n}(r) = \frac{G_n D^2}{4\mathrm{i}\nu\rho\,Wo_n^2}\left[1 - \frac{J_0(\mathrm{i}^{3/2}\,Wo_n 2r/D)}{J_0(\mathrm{i}^{3/2}\,Wo_n)}\right].$$ (1.13)

Adding the steady Poiseuille flow component, $U_0(r) = \frac{\bar{U}}{2}(1 - (2r/D)^2)$, to the unsteady flow, we get the net axial velocity in a tube as

$$U_z(r,t) = \frac{Re G_0 D^2}{16}\left(1 - \left(\frac{2r}{D}\right)^2\right) + \frac{Re D^2}{4\mathrm{i}}\sum_{n=-\infty}^{\infty}\frac{G_n}{Wo_n^2}\left[1 - \frac{J_0(\mathrm{i}^{3/2}\,Wo_n 2r/D)}{J_0(\mathrm{i}^{3/2}\,Wo_n)}\right]\mathrm{e}^{\mathrm{i}n\omega t}.$$ (1.14)

The Fourier coefficients G_n of the pressure are thus related to the Fourier coefficients Q_n of the flow rate as

$$G_0 = \frac{128}{\pi D^4 Re}Q_0, \qquad G_n = \frac{16\mathrm{i}\,Wo_n^2}{\pi D^4 Re(1 - F(Wo_n))}Q_n,$$ (1.15)

where

$$F(Wo_n) = \frac{2}{\mathrm{i}^{3/2}\,Wo_n}\frac{J_1(\mathrm{i}^{3/2}\,Wo_n)}{J_0(\mathrm{i}^{3/2}\,Wo_n)}.$$ (1.16)

The shape of flow profiles obtained using the Womersley solution have a strong dependence on the Womersley number Wo. Figure 1.5 shows the velocity profiles at different phases in a single cycle of a sinusoidally varying pressure gradient for three values of Wo. When the Womersley number is less than 1, viscous forces dominate and a quasi-steady behaviour is observed, and the velocity profiles approach the Poiseuille profile shape slowly modulated in time. Also, the velocity profiles are in phase with the pressure gradient, with almost zero velocity when the pressure gradient is zero. With an increase in Womersley number, a phase lag appears between the velocity profiles and the pressure gradient, with non-zero values of velocity even when the pressure gradient is zero. One can also observe that the velocity profiles tend to become flatter, resembling a top-hat velocity profile in the bulk with thin boundary layers near the walls. In this way, flows with different Womersley numbers exhibit very different near-wall behaviour. We now present the various flow rate waveforms that are used in the present work, along with the various flow parameters.

1.2.3 Physiological waveforms

The flow rate waveform significantly differs under rest and exercise conditions. One of the objectives of the present study is to investigate the flow dynamics prevailing in a model
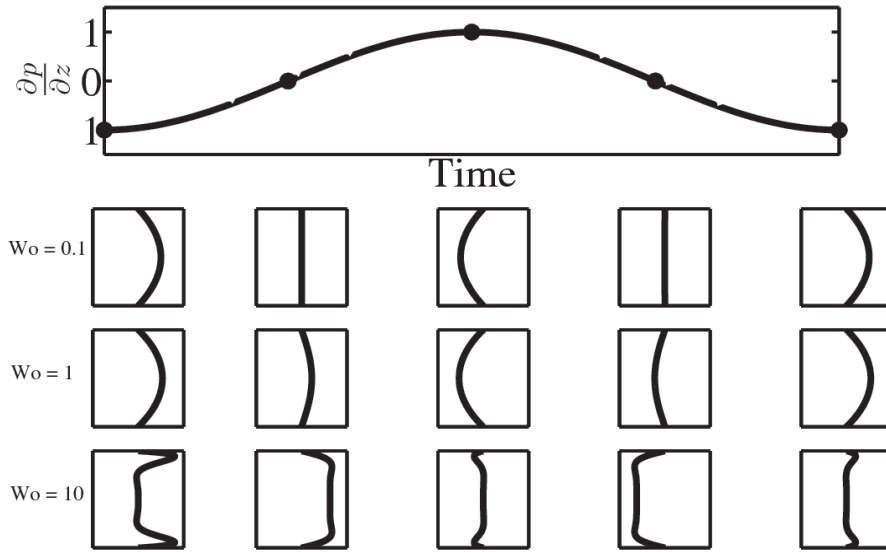
Figure 1.5: Velocity profiles obtained at different phases in a single cycle of a sinusoidally varying pressure gradient for three values of the Womersley number.

abdominal aortic aneurysm (AAA) for different physiological waveforms, including rest and exercise conditions. A number of studies have been carried out recently aiming to elucidate these differences and to understand how doing exercises is helpful in reality. The studies carried out by Salsac *et al.* (2006) and Sheard (2009), used an inlet flow rate waveform obtained from a healthy male subject at rest. However, with the onset and progression of the pathology, the flow rate waveforms could also be significantly modulated, due to the changes in geometry associated with it. Therefore, we will use the data presented in the recent article by Suh *et al.* (2011) where the flow rate waveforms were measured in patients with AAAs, both at rest and at exercise conditions.

The flow rate waveform is also highly dependent on the location of the aorta where it is measured. Figure 1.6 shows a scan of an abdominal aorta with an aneurysm, along with its various branches. Suh *et al.* (2011) carried out analysis using waveforms measured at two different locations of an aorta: supraceliac (upstream of the celiac artery) and infrarenal. Approximately 70% of the blood that enters the abdominal aorta under resting conditions is extracted by the celiac, superior mesenteric, and renal arteries. Most of the remaining 30% flows down the infrarenal segment through the bifurcation into the legs. Under lower limb exercise conditions, the total abdominal aorta flow increases and, in addition, the amount of blood extracted by the celiac, superior mesenteric, and renal arteries decreases, which further increases the infrarenal blood flow (Taylor *et al.*, 1999). Hence in our analysis, we have used the flow rate waveforms measured at the infrarenal location, just upstream of the AAA as the input in our analysis (see figure 1.6), taken from Suh *et al.* (2011). An interesting feature that one can observe from figure 1.6 is that the shape of an AAA is quite complex and also varies from person to person. The AAA geometries considered in the present study are discussed in detail in the following chapter (see section 2.4.2).
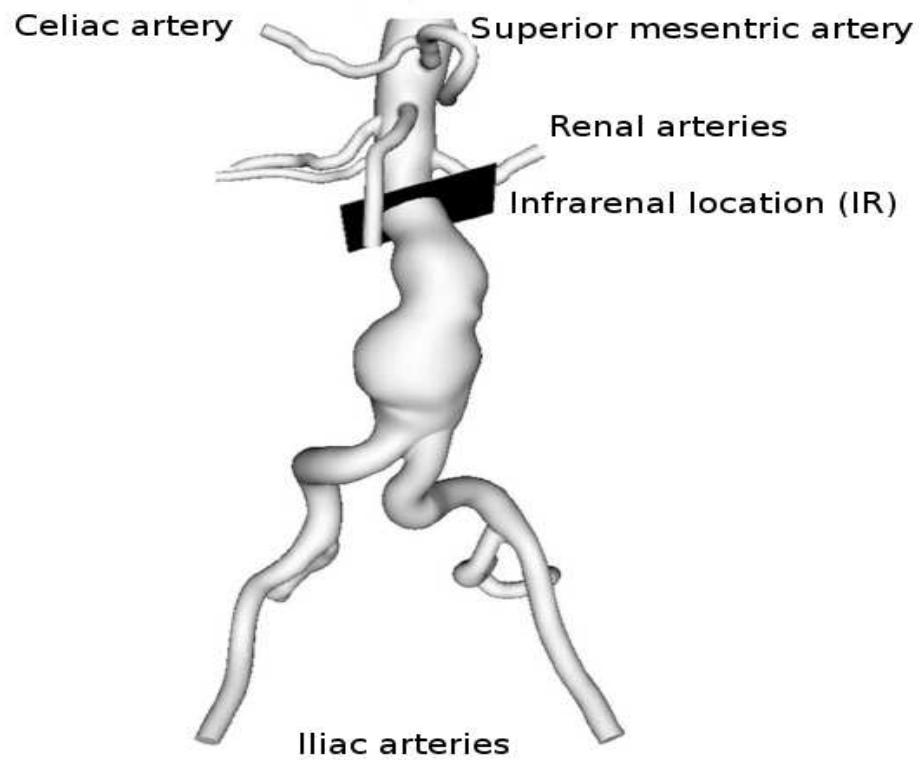
Figure 1.6: A scan of the abdominal aorta with branches showing the location (IR) where the waveforms are measured for analysis (from Suh *et al.* (2011)).
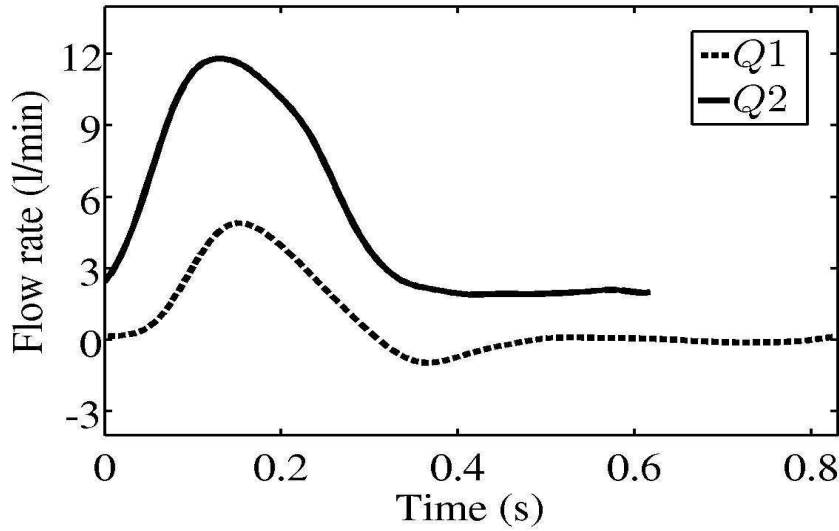
Figure 1.7: The waveforms corresponding to rest ($Q1$) and exercise ($Q2$) conditions measured at infrarenal location obtained from Suh *et al.* (2011).

In the study carried out by Suh *et al.* (2011), the waveforms were measured using the data obtained from nine male and one female subjects, with a mean age of 71.2 ± 7.9 years with small AAAs (maximum diameter < 5cm). The data corresponding to the rest condition were obtained with the subjects seated, while for exercise, they were instructed to elevate their heart rate to 30–40% greater than their resting rate. This was achieved by carrying out lower limb exercises while being seated.

The waveforms corresponding to rest and exercise conditions presented in Suh *et al.* (2011) are shown in figure 1.7. In their study, blood is assumed to be a Newtonian fluid with a density of 1.06g/cm^3 and a dynamic viscosity μ, of 0.04 Poise (0.004 Pa s). As the measurements were made in 10 different AAA subjects, a precise value of the diameter of the aorta at the location of measurement is not provided by them. However, to convert the dimensional volumetric flow rates to non-dimensional values, one needs a value of the diameter of the abdominal aorta, which depends on the location of its measurement, and also depends on the person under consideration. We have assumed a value of 1.7 cm in our analysis. This value corresponds to a typical inlet diameter of an AAA. The corresponding values of various physiological quantities for rest and exercise conditions are summarized in table 1.1. The non-dimensionalisation using inlet diameter D, and average velocity $\bar{U}$, for lengths and velocities respectively, yields the corresponding values for Re and Wo. Figure 1.8 shows the non-dimensional flow rate waveforms considered in the present study. It is to be noted that the waveforms shown in figure 1.8 are such that the mean flow rate is normalized to one. The Fourier coefficients of the flow rate (Q_n) corresponding to different waveforms are provided in table 1.2. Ten Fourier coefficients were used for approximating the inletwaveforms.

In order to check the sensitivity of the waveform that is used to flow parameters, we have

Waveform	D(cm)	$\overline{Q}$(l/min)	Heart rate(min^{-1})	μ(Pa s)	Re	Wo
Rest($Q1$)	1.7	0.8	72	0.004	264	12
Exercise($Q2$)	1.7	5.1	95	0.004	1700	13.8

Table 1.1: Physiologically relevant values.
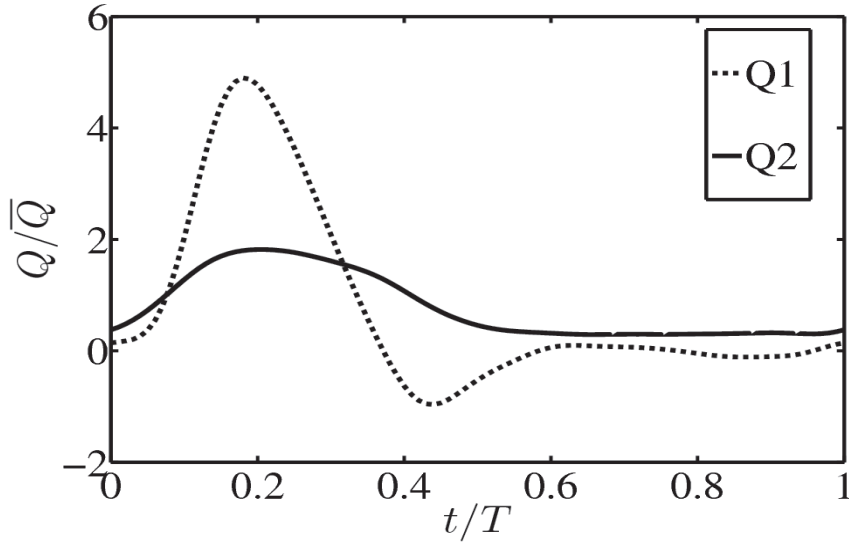
Figure 1.8: Non-dimensional plot of the different waveforms considered in the present study. The waveform corresponding to the rest condition ($Q1$) is shown using dotted lines and the one corresponding to exercise ($Q2$) is shown using continuous lines.

Q_0	1.0	1.0	1.0
Q_1	$0.4461 - i0.9481$	$0.0203 - i0.4735$	$1.5848 - i0.7364$
Q_2	$-0.7231 - i0.5638$	$-0.1923 - i0.0389$	$-1.6606 - i2.1846$
Q_3	$-0.3046 + i0.3181$	$-0.0392 + i0.0068$	$-0.7096 + i0.7976$
Q_4	$0.0042 + i0.1447$	$-0.0405 + i0.0103$	$-0.1835 + i0.4286$
Q_5	$0.0469 + i0.1112$	$-0.0054 + i0.0170$	$-0.0354 + i0.1776$
Q_6	$0.0780 + i0.0169$	$-0.0026 + i0.0008$	$-0.0028 + i0.0823$
Q_7	$0.0256 - i0.0184$	$-0.0009 + i0.0023$	$0.0047 + i0.0416$
Q_8	$0.0192 - i0.0104$	$0.0013 + i0.0003$	$0.0061 + i0.0224$
Q_9	$-0.0021 - i0.0119$	$-0.0002 - i0.0022$	$0.0059 + i0.0124$
	(a)	(b)	(c)

Table 1.2: The Fourier coefficients Q_n considered in the present study corresponding to the waveforms $Q1$ (rest), $Q2$(exercise) and $Q3$ shown in figures 1.8,1.9 are given in (a), (b) and (c) respectively.
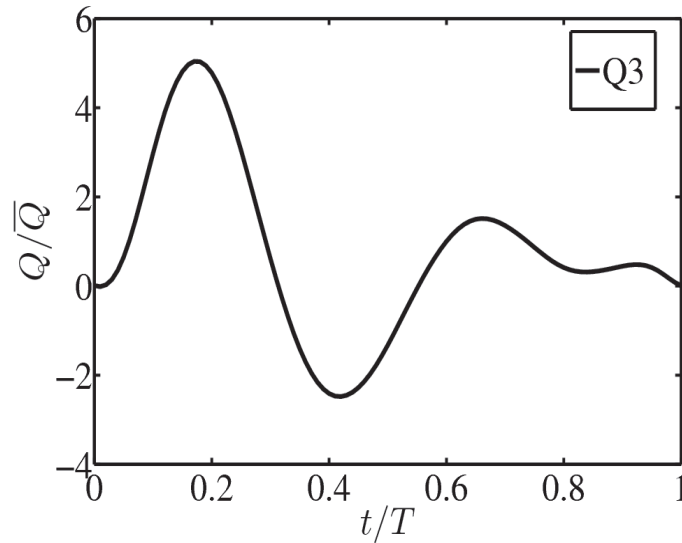
Figure 1.9: The waveform considered in the study by Salsac *et al.* (2006), Sheard (2009).

carried out simulations using the rest waveform $Q1$ albeit with different values of Re and Wo. A different choice of the inlet diameter, for instance 2 cm (instead of 1.7 cm, see table 1.1), would result in $Re = 250$ and $Wo = 15$, for the same choice of the waveform. Hence, we have carried out calculations using the waveform $Q1$ for a range of Re between 200 and 500, and using three different Womersley numbers (10, 12, 15) to analyse the sensitivity of our results to the choice of parameters. These are discussed in more detail in the chapter on pulsatile base flow characteristics (chapter 4).

Salsac *et al.* (2006), Sheard (2009) carried out calculations using the waveform shown in figure 1.9 which was obtained using the data presented in Maier *et al.* (1989). The Reynolds number and Womersley number used in their analyses were 330 and 10.7 respectively. One has to keep in mind that the flow rate waveform was measured in the abdominal aorta of a healthy volunteer at rest, which is shown in figure 1.9 and is termed as $Q3$. As the waveform and the flow parameters are altered due to the presence of an AAA, the flow characteristics could be different too. We can see that the waveform $Q3$ has a larger reversed flow when compared to $Q1$. This illustrates that the waveforms considered in various studies in the literature are not at all universal and the discrepancies between results obtained using different waveforms may be worth investigating.

1.2.4 Further studies of flow in circular pipes

Before moving on to the discussion on flows through AAAs and other related geometries, it is pertinent to have an idea on the various works carried out in literature on flows through circular pipes following the work of Womersley, without any aneurysm. This would provide us with some background on flows through a healthy abdominal aorta, in the absence of an aneurysm.

Flows in the arterial branches are found to undergo transition to turbulence which was first observed by Nerem *et al.* (1972). This has stimulated the interest of the researchers to study the stability of oscillatory and pulsatile flows in pipes (Yang & Yih, 1977, Grosch & Salwen, 1968, Stettler & Hussain, 1986, Tozzi & von Kerczek, 1986). An excellent review on the stability analyis of time-periodic flows is provided by Davis (1976). One of the first works on understanding the stability of an oscillatory flow in a pipe was carried out by Yang & Yih (1977). The analyses carried out for axisymmetric disturbances revealed that the flows were stable for all Reynolds numbers and all frequencies of the primary flow, and all wavenumbers of the axisymmetric disturbance. They also concluded that time-periodic component stabilizes the flow, which had been observed earlier for the case of time-dependent plane Poiseuille flow (Grosch & Salwen, 1968). These were also observed experimentally by Stettler & Hussain (1986), who observed the transition to turbulence based on the amplitude of the oscillation and made comparisons with theoretical work on the transition Reynolds number. Tozzi & von Kerczek (1986) carried out a stability analysis of an oscillatory pipe flow. They too observed that the time-periodic flow is more stable than its steady counterpart and the flow transition to a turbulent regime is suppressed. However, the addition of a mean flow component, to the oscillatory part is seen to have drastic influence on the characteristics of the eigenmodes (Thomas *et al.*, 2011). For a purely oscillatory flow, the eigenmodes were relatively stationary with respect to the base flow which is not observed with the addition of a mean flow component. These observations may have an implication on the differences observed in experimental and numerical simulations.

A more extensive work on the stability analysis of oscillatory pipe flows was carried out by Fedele *et al.* (2005). They carried out the linear stability analysis of pulsatile pipe flow to axisymmetric perturbations. They also observed the pulsatile pipe flow to be slightly more stable than the steady flow. The flow structures corresponding to maximum energy growth were found to be toroidal vortex tubes. These structures are stretched along the streamwise direction by the shear stresses of the mean flow. A transient growth analysis performed by them revealed that as the Womersley number is decreased, the flow perturbation is characterized by successively smaller maximum energy growth than its steady counterpart. This is in coherence with the observation made by Tozzi & von Kerczek (1986) where the turbulent spots were suppressed in pulsatile pipe flow transition for low frequency regimes. However, as their study was limited to axisymmetric disturbances, there could be non-axisymmetric disturbances resulting in a greater energy growth. An investigation into the stability analysis of an oscillatory pipe flow to non-axisymmetric disturbances was carried out recently by Nebauer & Blackburn (2009). They concluded that the periodic pipe flows are linearly stable. However, an error was made in their analyses, as they carried out the stability analysis considering each Fourier component of the base flow separately. To our knowledge, a systematic study of the stability of oscillatory pipe flows to non-axisymmetric disturbances is not to be found in the literature, let alone for physiologically relevant pulsatile flows.

We now turn our attention to the role that fluid mechanics has played in understanding an arterial disease related to our present work: stenotic flows.

1.2.5 Flows in stenotic geometries

Recently, there has been an increase in interest in the fluid mechanics community in understanding flow through arterial branches. This has been motivated by observations that atherosclerotic lesions occurred in arteries and arterioles in regions of high curvature or where there are bifurcations. In particular, the association of arterial disease with flow-related mechanisms has motivated the study of steady and pulsatile flow within both model and anatomically derived arterial model stenoses (Berger & Jou, 2000). A review of the experimental work performed on idealised stenoses is provided in Berger & Jou (2000), Griffith (2007).

1.2.5.1 Steady flows

With the advances in computational facilities, several numerical investigations have been undertaken for simulating the flow characteristics in both axisymmetric and non-axisymmetric stenoses. Sherwin & Blackburn (2005) carried out a stability analysis of a steady flow through an idealised model of stenosis where the blockage was modeled as a sinusoidal function. In that study, a 75% area reduction stenosis of length $2D$ was used. They found that the steady flow was unstable at a Reynolds number 722 (based on the mean velocity and the inlet pipe diameter) to $m = 1$ azimuthal Fourier mode. The leading perturbation consists of a jet emanating from the stenosis accompanied by a loss of symmetry of the jet. As an extension of this work, Blackburn & Sherwin (2007) carried out a study to investigate the role of convective instability by periodically forcing the steady flow at the inlet. They observed that the shear layer rolled up into vortices and deduced that the flow is susceptible to convective instabilities.

To further verify the role of convective instability in steady stenotic flows, Griffith *et al.* (2008) carried out a stability analysis, both numerically and experimentally, of a steady flow through an axisymmetric stenosis. However, here the stenoses were modeled as a semi-circular perturbation of the circular pipe rather than by a sinusoidal function, resulting in a severer disruption of the flow leading to higher velocities. They observed that with an increase in the blockage ratio, the flows become unstable at lower Reynolds numbers. For lower values of blockage ratio, the $m = 1$ Fourier mode is the leading unstable mode, while higher mode numbers become unstable with increasing blockage ratios. Also, at a high stenosis degree, the perturbation consists of a deflection or deviation of the jet from the tube centreline, while for lower stenosis degrees, it consists of a pinching or flattening centred on the centreline. The role of convective instability was verified using experimetal observations, which revealed large convective growth of shear layer modes, leading to strong turbulence within a short distance downstream of the stenosis. Similar to Sherwin & Blackburn (2005), they investigated the response of their flow to a small amplitude forcing and found out that the strongest response was observed when the forcing period was higher than the period of oscillation of the shear layer.

In another study by Varghese *et al.* (2007*a*), a direct numerical simulation was performed on an idealised stenotic geometry (same as the one used in Sherwin & Blackburn (2005)) to address the question of flow transition in arterial branches. Though earlier experiments carried out at a Reynolds number of 1000 revealed evidence of flow transition, they observed their flow to remain laminar even downstream of the stenosis. However, when a 5% eccentricity was introduced to their stenotic model, they observed flow transition and localized turbulence downstream of the stenosis at a Reynolds

number of 1000. This was manifested in large temporal and spatial variations in instantaneous wall shear stress levels, rising by more than a factor of ten within the turbulent region.

The role of eccentricity was investigated numerically in a very recent work by Griffith *et al.* (2013). The motivation behind their work stemmed from the observation made by Vétel *et al.* (2008), where the leading critical mode of a flow through an axisymmetric stenosis was recovered experimentally which was similar to the one observed numerically by Sherwin & Blackburn (2005), albeit at a much lower Reynolds number ($\approx$ 250). As small non-axisymmetric imperfections or perturbations present in the experimental setup could account for an early breaking of the symmetry, a numerical simulation of an eccentric stenosis would help in explaining the differences between numerical and experimental simulations. They observed that the flow characteristics were highly sensitive to eccentricity, in coherence with the non-axisymmetric states observed experimentally.

1.2.5.2   Pulsatile flows

A pulsatile flow consists of a mean flow to which an oscillating component is added. Though a physiologically relevant pulsatile flow needs about ten Fourier modes for an accurate representation, much of the work on stenotic flows used a single Fourier harmonic oscillation for an ease in analysis of various parametric conditions. We present here only the recent advances made in this field. For a review on earlier works, the interested reader is referred to Berger & Jou (2000), Griffith (2007). The study carried out by Sherwin & Blackburn (2005) was one of the first to explain the stability characteristics observed in a pulsatile stenotic flow. They considered two waveforms, consisting of one and two Fourier harmonics respectively, with different peak to mean ratio of flow rates. For all the pulsatile cases considered, instability occurred through a period-doubling bifurcation, and the nature of the instability was identified as alternating tilting of vortex rings generated during sequential pulsatile cyclic ejections from the stenotic constriction. The role of convective instability was investigated using an analysis of the response of the flow to inlet forcing, revealing shear-layer oscillations. Varghese *et al.* (2007*b*) performed a direct numerical simulation of an axisymmetric stenotic flow, and similar to the case of steady flows, the observed flow field was laminar. Similarly, the introduction of an eccentricity resulted in occurrence of localized transition to turbulence downstream of the stenosis. The WSS values observed downstream of the stenosis were found to rise 75 times to the values observed upstream at peak flow conditions, implying the significance of such work in understanding the progression of diseases such as atherosclerosis.

A numerical and experimental analysis of a pulsatile flow through an axisymmetric stenosis was carried out by Griffith *et al.* (2009). They used a single harmonic Fourier mode in their inlet waveform, and varied the amplitude of the oscillation, the stenosis degree (constriction of the pipe) and the time-period systematically. At lower stenosis degrees, they observed that the flow was unstable to period-doubling vortex tilting modes with an azimuthal Fourier mode $m = 1$. However, keeping the amplitude of the flow waveform the same, when the stenosis degree was increased, the higher azimuthal Fourier modes were found to be more unstable. Using an experimental analysis, they showed that convective instability seemed to be the major cause of instability, along with the observation of vortices in the shear layer bearing the hallmark of a Kelvin–Helmholtz type of instability.

One of the first works carried out on understanding the WSS distributions down-

stream for a stenosis using a sinusoidal and a physiological flow rate waveform was by Deplano & Siouffi (1999). The temporal evolution of WSS distributions was analysed both experimentally and numerically. A key result of their study was that the presence of a stenosis results in low and oscillatory WSS values during the cycle and high peak values at the throat. Recently, Mao *et al.* (2011) carried out a transient growth analysis of a flow through a sinusoidal stenosis, using a physiologically relevant pulsatile waveform. This was motivated by the fact that significant transient growth of energy has been observed in these geometries, even when the flows were globally stable (Blackburn *et al.*, 2008). The unstable modes arising due to a period-doubling instability were found difficult to be excited, due to the large separation of fronts (Blackburn *et al.*, 2008, Mao *et al.*, 2011). Under certain conditions, a combination of the vortex tilting instability and a transient shear layer instability, corresponding to a Kelvin–Helmholtz instability in the shear layer, can result in significant transient energy growths.

The investigations of Sherwin & Blackburn (2005), Griffith *et al.* (2009) have been used to validate our Floquet stability solver and are discussed in more detail in the chapter on methodology (chapter 2).

1.2.6 Flows in abdominal aortic aneurysms

In the pathogenesis of an abdominal aortic aneurysm (AAA), the hemodynamics within an AAA is found to play an imporant role in the progression of an AAA. As the flows observed in AAAs are complex, it is important to analyse these using simplified models and hypotheses that would enable us to reach conclusions that encapsulate the underlying physics. The goal of fluid dynamicists is to enhance our understanding of flows in abdominal aortic aneurysms by means of mathematical modeling or by computation or by experiment. A review on the various objectives of scientists in understanding blood flow in arteries can be found in Lighthill (1972), Pedley (2003). The motivation behind researchers in fluid mechanics in understanding this complex phenomenon are mainly twofold:

(a) Firstly, it is understood that the stresses acting on the vessel walls have a profound influence in the pathology of an AAA, as discussed earlier. However, even with the advances made in the field of medicine, due to the complexity of measuring the flow inside an aneurysm, there has been no successful attempt at measuring the wall shear stresses *in vivo* inside an AAA. The current radiological imaging techniques described earlier (MRI, ultrasound, etc.) do not have a high enough spatial resolution to provide a reliable measurement of the velocity fields. Hence, by making use of both simplified, and patient-specific models, studies have focused on obtaining accurate flow fields by which a reliable prediction of the stresses can be made.

(b) Secondly, for lack of any other reliable method, the maximum aneurysm diameter is the current standard by which the risk associated with an AAA is estimated. As the wall composition of an AAA changes with the progression of the disease, it is clear that the aneurysmal rupture is due to the failure of the wall's structure to support the stresses resulting from the pulsatile internal blood flow. Hence, calculating the risk of rupture requires the calculation of the tensile stresses on the aneurysm wall and knowledge of the corresponding stress failures. This in turn could be affected by the flow fields in AAAs. However, the relatively complex shape of the elastic walls of an AAA poses some difficulties, due to the current inability of the various medical imaging techniques

to provide precise information on not only the thickness of the wall, but also on the composition and structure of the wall at various locations, which in turn determines the mechanical properties.

1.2.6.1 Steady flows

As a first step, many studies involving steady flows through an AAA were conducted (Schrader *et al.*, 1992, Budwig *et al.*, 1993, Peattie *et al.*, 1994, 1996, Asbury *et al.*, 1995, Bluestein *et al.*, 1996, Vorp *et al.*, 1998). Though the steady flows may not be directly relevant to the understanding of hemodynamics within an AAA, as the flow in the aorta is pulsatile, it does provide us with information on the flow characteristics, without having the complexity brought in by the unsteadiness of the flow. Budwig *et al.* (1993) studied the flow patterns in four simplified AAA models subject to steady flows. They carried out both experimental and numerical work to provide a good picture of the flow patterns observable in aneurysms. They found that the WSS magnitude within the aneurysm zone is about ten times less, than in the entrance tube. They also studied the transition to turbulence in these models and observed that the presence of turbulent slugs within the flow greatly altered the WSS values within the aneurysm. This was further investigated by Peattie *et al.* (1994), who carried out experimental work on four different aneurysmal geometries, subjected to steady flows, and investigated the critical Reynolds number for the flow to become turbulent. The transition was first observed at the distal end, which subsequently infiltrated the entire bulge region. The critical Reynolds numbers were around 2000, which decreased with increase in dilatation ratio. Asbury *et al.* (1995) carried out a similar experimental investigation of steady flows within an AAA in which they varied the bulge height systematically with a fixed bulge length. They estimated the critical Reynolds numbers at which the flow becomes turbulent, and their observations agreed with Peattie *et al.* (1994). Larger models were found to become unstable at a lower Reynolds number than smaller models. An interesting study aimed at correlating the effect of eccentricity on wall shear stress distributions in AAAs was carried out by Vorp *et al.* (1998). The flow conditions corresponding to peak systolic flow rate were imposed in an AAA and the effect of asymmetry on three-dimensional stress distribution on the wall of AAAs was quantified. Their study indicated that the critical diameter criterion often used to guide decisions for elective AAA repair could be misleading as the stress distributions depend on the shape of the AAAs, which are generally much more complex in reality.

A study on correlation between fluid dynamics and blood platelet deposition was carried out by Bluestein *et al.* (1996) for steady flows. The presence of coexisting high and low wall shear stresses within the bulge region was found to promote thrombus formation. Also platelet deposition was aggravated within the regions of low WSS, within the bulge region, as they were found to be trapped within the recirculating zone. Yu (2000) carried out an experimental study of a steady flow within an AAA, where the AAA was modeled as a semi-circular dilatation of a straight circular pipe. Such a model involving geometric singularities is not ideal, as flow separation is highly influenced by the presence of sharp edges. Similarly, Finol & Amon (2002) performed a numerical study of a steady flow through a double aneurysm, made out of two consecutive expansions which is not relevant to our present work, as the geometries are very different. Sheard & Blackburn (2010) carried out a global and transient stability of a steady flow through a model AAA. They found that the flow is unstable to quasi-periodic global modes of azimuthal mode numbers 4 and 5, at a Reynolds number of 3900 (based on area-averaged velocity and inlet pipe diameter).

However, there are no studies in the literature where the various geometrical parameters defining an AAA were varied systematically and the resulting changes in flow stabilities recorded.

Another interesting point of view for this problem is that the limiting case of Poiseuille flow in a pipe is linearly stable (Drazin & Reid, 1981). An investigation on the minimum corrugation needed from a straight circular pipe for the flow to become unstable has received much attention within the fluid dynamics community. This is augmented by the fact that transient growth of disturbances have been observed, resulting in significant energy growth over short time intervals, even though the eigenmodes are in the stable regime (Schmid & Henningson, 2001). Cho *et al.* (1988) carried out the linear stability analysis of a flow through sinusoidal wavy-walled channels. They found that when the wall variation is smaller than a critical value, the flow becomes unstable to three-dimensional stationary disturbances and for higher values of wall corrugation, the flow becomes unstable to two-dimensional oscillatory disturbances. Floryan (2003) studied the linear stability of Poiseuille flow in a converging-diverging channel. In contrast to flows in a cylindrical geometry, plane Poiseuille flow is unstable to two-dimensional disturbances. The study of Cotrell *et al.* (2008) was mainly concerned with the instabilities in the low corrugation amplitude limit. They found that a minimum critical amplitude for the corrugation was required for the flow to develop a vortex in the bulge region which is almost identical to the value below which the flow remains stable. Consequently, the instability is directly related to the formation of a vortex in the bulge region and the cause of instability is likely to be vortex separation. Also, according to their results, axisymmetric disturbances were the least stable at low and finite corrugation amplitudes. More recently, Loh & Blackburn (2011) performed a stability analysis of a steady flow through an axially corrugated pipe. They imposed an axial periodicity on both the base and perturbation flows, with the same axial wavelength as the corrugation. Contrary to the study of Cotrell *et al.* (2008), they concluded that at low-to-moderate corrugation amplitudes, the flow is unstable to non-axisymmetric disturbances with azimuthal mode numbers $m = 3$ or 4. The underlying mechanism was attributed to centrifugal instability although no specific computations were carried out to clarify this result. This has been another motivation for our present work, where we investigate the minimum inflation of the vessel wall that is needed for a steady flow to become unstable (chapter 3).

1.2.6.2 Pulsatile flows

As the nature of flow characteristics are drastically different under pulsatile conditions, lot of studies in literature on flows in AAAs have used a time-dependent waveform. The reviews by Lasheras (2007), Humphrey & Taylor (2008) provide an extensive database of the various works carried out in literature. The first study to use a physiologically relevant waveform to study the influence of the dilatation of an AAA was Fukushima *et al.* (1989). They studied experimentally the flow through three different sized aneurysms in the range of mean Reynolds numbers $289 \leq \overline{Re} \leq 748$ and Womersley numbers $4.07 \leq Wo \leq 10.6$. It was shown that the flow remained attached to the walls during the acceleration phase of the cycle (systole), with detachment being observed at the onset of the deceleration (beginning of diastole), resulting in a large primary vortex, followed by a weaker secondary vortex, and a recirculation zone with low velocities. However, they did not make measurements of the WSS, which was made only by using a numerical simulation of an idealized laminar flow inside the AAA. It was seen that the peak WSS occurred at the downstream end

(distal area) and the aneurysm wall was characterized by low WSS. Taylor & Yamaguchi (1994) carried out simulations in a model three-dimensional AAA using both steady and pulsatile flow rate waveforms. They observed that the regions of maximum pressure moved within the aneurysm for a pulsatile flow, with local areas of maximum pressure observed at the distal end straining the arterial walls. Also, shear stress values were highest at the proximal and distal aneurysm points, in contrast to the steady flow case. In another experimental study by Peattie *et al.* (2004), pulsatile flow conditions corresponding to a rest state were simulated in rigid, axisymmetric models. They observed similar flow features as presented in Fukushima *et al.* (1989), and in addition, they measured the WSS for different sized aneurysms by varying the dilatation ratio. Apart from observing that the maximum stress occurred at the distal end during the peak systole for different sized aneurysms, they noted that disturbed flow conditions were present during a greater percentage of each cardiac cycle with increase in dilatation ratio.

An excellent experimental study to quantify the variation of WSS systematically during the progressive enlargement of an AAA was made recently by Salsac *et al.* (2004, 2006). They carried out an experimental investigation using rigid symmetric AAA models and systematically investigated the spatial and temporal distribution of the WSS with the growth of the AAA. They concluded that for all the aneurysm models characterized by a dilatation ratio greater than 1.5, the mean WSS consistently dropped from the healthy aorta value of 0.40 Nm^{-2} to values very close to zero, when averaged over the whole aneurysm length. However, a minor limitation of their study was that the WSS distributions at the arterial wall was underestimated, particularly at the point of impact of the primary vortex, because of the very small size of the Stokes layer and of the resolution of their measurements, which was pointed out by them. In another recent work, Duclaux *et al.* (2010) addressed the questions of the localization and growth of an AAA using a simplified physical experiment, and proposed a scaling argument that relates to the aneurysm location. They also concluded that aneurysms develop only above a critical flow rate.

The influence of wall compliance on hemodynamics in model AAAs was investigated by Gaillard *et al.* (2007). They observed that the evolution of the vortices formed after the systolic phase to be different when the AAA wall is compliant as opposed to a rigid wall. Various other studies have aimed at developing models to capture the stress acting on the vessel walls, to understand the mechanical behaviour of the aneurysm wall. Raghavan & Vorp (2000) developed a finite strain material model for an AAA based on experimental data to make predictions for WSS to describe the mechanical behaviour of the aneurysm wall. They also extended this to three-dimensionally reconstructed patient-specific AAAs to estimate the WSS (Raghavan *et al.*, 2000). These were mainly aimed at predicting the risk of rupture, by making use of WSS to estimate the wall strength. A review of the related work is provided in Vorp *et al.* (2001).

It has been observed that the aneurysms tend to be symmetric at the early stages of the disease, but they may become non-symmetric when they reach larger sizes (Salsac, 2005). Also, as the AAA shapes observed *in vivo* are complex in nature, some studies have concentrated on comparing the flow features observed in a symmetrical AAA with an asymmetrical one (Taylor & Yamaguchi, 1994, Salsac, 2005, Deplano *et al.*, 2007, Vorp, 2007). The geometric asymmetry affects flow separation and prevents the formation of a closed vortex ring as observed in symmetric AAAs. The vortex shed from the proximal

end during flow deceleration is of a higher strength when compared to that formed in a symmetric AAA, and is likely to generate a stronger transition to turbulence in the diastole. However, most of the typical flow features observed in symmetric AAAs persist in non-symmetric models, with significant deviations only observed for large values of asymmetry. Due to these observations, and for simplicity, we have used a symmetric model of AAA in our study, with the primary focus being on characterising the flow fields during the early stages of growth of an AAA.

With the recent advances made in computing techniques, a few groups have performed numerical simulations in AAAs to provide accurate measurements of the flow fields. Sheard (2009) recently carried out a numerical study of a pulsatile flow through an idealized AAA, where the dilatation was modeled using a sinusoidal function. The geometry used in the study was one of the typical geometries considered in the study by Salsac *et al.* (2006). Using well-resolved numerical simulations, they were able to capture the vorticity and flow fields accurately. Sheard (2009) reported that the highest wall shear-stress within an AAA is 2.4 times greater than the highest wall shear-stress recorded in a healthy vessel. They also carried out a stability analysis of the pulsatile baseflow and concluded that the most unstable mode corresponded to an azimuthal mode number of $m = 3$. The critical modes were localized at the distal end of the bulge (Sheard & Blackburn, 2010, Sheard & Ryan, 2008), though no information on the growth rates were provided by them. To investigate whether a difference in the modelling of the AAA wall could lead to changes in flow characteristics, we have carried out studies using the model used by Sheard (2009) and have compared the flow characteristics with an equivalent AAA modeled using a gaussian function. More details on this is provided in chapter 2.

One of the first groups to tackle the fluid-structure interaction problem of a flow through an aneurysm was Martino *et al.* (2001). By taking into account the vessel morphology, blood flow and wall thickness, they were able to estimate the effect of thrombus layer on wall stresses. Patient-specific modeling of flows through aneurysms have also attracted a lot of interest in the recent years, making use of numerical simulations to analyse the complex flow patterns observed *in vivo* systems. The geometry is obtained using image-based reconstructed models, with the aid of magnetic resonance angiography (MRA). Some of the recent studies are (Stamatopoulos *et al.*, 2011, Sheidaei *et al.*, 2011, Arzani & Shadden, 2012) to name a few. Stamatopoulos *et al.* (2011) carried out an experimental work using realistic geometries, wherein they observed high stresses appearing at the inlet and outlet of the aneurysms, along with a swirling motion at peak systole. The expansion rate of a realistic AAA was computed numerically by Sheidaei *et al.* (2011) along with analysing the changes of the aneurysm wall. Arzani & Shadden (2012) used six different models of realistic AAA geometries and observed that similar aneurysm shapes could still have very different flow topologies. The effect of the aortao-iliac bifurcation downstream of an AAA was looked into by Deplano *et al.* (2013). The flow rates observed in AAAs are influenced by the iliac bifurcation, thereby modifying the flow characteristics and the stresses acting on the walls. In our present work, we use an idealized geometry to model an aneurysm, as we believe that more general information on flow characteristics could be extracted with such a study.

Another interesting aspect which has received much attention concerning research on AAAs, is the effect of varying physiological conditions on the flow topology. As the flow rate waveforms, the Reynolds numbers and the Womersley numbers are very different

under rest and exercise conditions, the hemodynamics could be very different too. Some of the notable works are those by Taylor *et al.* (1999), Egelhoff *et al.* (1999), Deplano *et al.* (2007), Les *et al.* (2010), Suh *et al.* (2011). The study carried out by Taylor *et al.* (1999) to investigate the effect of exercise on flow conditions in the abdominal aorta showed that moderate levels of exercise eliminated flow reversal and hence regions of low WSS, which prevail during resting conditions, which are conducive for arterial health. Egelhoff *et al.* (1999) studied pulsatile flows, for both rest and exercise conditions, in two AAA model shapes and four sizes, emulating early AAA development through moderately large growth, using experiments. Their results showed that the flow remained attached over the entire cardiac cycle in small AAAs at resting conditions, with vortex formation in moderate size AAAs. However, under exercise conditions, turbulence was observed for moderate size AAAs, which could be important for thrombogenesis. Recently, using MR exercise imaging and image-based computational fluid dynamics, the effect of increase in exercise intensity on flow conditions was quantified by Suh *et al.* (2011), using data obtained from ten AAA subjects. As the level of exercise intensity increased, the mean WSS increased and the oscillatory WSS decreased. Using this, they suggested that mild exercise conditions could be helpful in removing oscillatory and stagnant hemodynamic conditions in AAAs, thereby removing the disturbed flow conditions. In our present work, we use the flow rate waveforms obtained by Suh *et al.* (2011) from AAA subjects under rest and exercise conditions, which was discussed earlier (see section 1.2.3), to investigate the effect of physiological conditions on flow characteristics.

Many of the above mentioned studies, notably Raghavan *et al.* (2000), Stamatopoulos *et al.* (2011), Les *et al.* (2010), Suh *et al.* (2011), Sheidaei *et al.* (2011), Vorp (2007) have used patient-specific models of AAA to investigate the distribution of wall shear stresses (WSS) along the arterial wall. All of these studies have provided a good qualitative description of the flow in an AAA, and the most relevant features like the concentration of WSS at the distal end, low oscillatory WSS within the AAA cavity and the presence of disturbed flow conditions, were captured. These studies are highly relevant as they help us to get a clear picture of the true complexity present *in vivo* AAAs. However, a major drawback is that it is often difficult to derive general conclusions using this approach due to the sheer complexity of geometries used in these studies. Hence in the present work, we have used a model AAA geometry, as the various geometrical parameters, namely the bulge height H and bulge width W, of the AAA, can be varied systematically, and a precise description of the flow characteristics under varying physiological flow conditions may be obtained.

1.3 Summary

1.3.1 Objectives

The above studies, for both steady and pulsatile flows, using experimental and numerical tools, provide a good qualitative description of the flow in an AAA. However, nowhere in the literature can be found a fundamental study that examines the stability of flows in AAAs, even in the simplest case of an axisymmetric flow. The purpose of a linear stability analysis of axisymmetric basic flows through AAAs (whether steady or pulsatile) is to identify the flow conditions that lead to the temporal amplification of three-dimensional perturbations. Comparison of critical flow parameters for onset of instability with those prevailing in physiological conditions would help us in understanding the flow behaviour

in more complex configurations.

The objectives of the present work are the following. An investigation of the base flow characteristics for the case of steady flows for different sized AAAs is provided, enabling us to analyse the flow characteristics in such a geometrical configuration without the additional complexity of pulsatility. The stability of steady flows through model AAAs and an investigation of the minimum deviation needed from a circular pipe for the instability to develop is then carried out. A qualitative description of the various instability mechanisms inherent in AAAs is provided. For the case of pulsatile flows, no comprehensive study on the flow fields in an AAA under varying physiological flow conditions and during the enlargement of an AAA has been reported, and more importantly, no fundamental study that examines the stability of the flows, even in the simplest case of an axisymmetric flow through a smooth AAA is to be found in the literature. The aim of this study is therefore to provide precise description of the base flow characteristics, like wall shear stress distributions, under varying flow conditions and geometrical parameters. This is followed by an investigation on the stability characteristics of these pulsatile base flows. The effect of the shape of AAA wall is also presented by considering two equivalent AAAs modeled using a sinusoidal and a gaussian function.

1.3.2 Outline

The thesis is structured in the following manner. Chapter 2 provides a description of the various numerical tools used in our analysis along with the various validation tests of our numerical method. The stability of steady flows in AAAs are discussed in chapter 3 and a qualitative description of the instability mechanisms inherent in these geometries is also provided. The pulsatile flow characterisitics in an AAA using a physiological flow rate waveform corresponding to rest and exercise conditions is presented in chapter 4. The effect of various geometrical parameters on flow characteristics is also investigated. Chapter 5 provides the results obtained from a linear stability analysis of these pulsatile base flows. Finally some conclusions and general perspectives are provided in chapter 6.

Methodology

The aim of the present thesis is to investigate the dynamics of steady and pulsatile flows through different geometries using numerical simulations. The first part of this chapter discusses the techniques used for obtaining the base flow fields, followed by details of the methods used for stability analyses. The geometries and the boundary conditions are discussed subsequently. The chapter concludes with the validation of our methods with data published in literature. As similar methods have been used in the recent past, some parts of this chapter are inspired from the theses by Marquet (2007), Derham (2011).

2.1 Numerical Method

The flow dynamics is assumed to be goverened by the incompressible Navier–Stokes equations, written in non-dimensional form as

$$\partial_t \mathbf{u} + (\mathbf{u}.\nabla)\mathbf{u} = -\nabla p + \frac{1}{Re}\Delta\mathbf{u}, \tag{2.1a}$$

$$\nabla.\mathbf{u} = 0, \tag{2.1b}$$

where $\mathbf{u}$ is the non-dimensional velocity field, p is the non-dimensional pressure field and the Reynolds number is defined as $Re = \bar{U}D/\nu$, with ν the kinematic viscosity of the fluid, D the inlet diameter and $\bar{U}$ the average velocity through the inlet. Throughout our study, a cylindrical coordinate system has been used, where z, r, θ denote axial, radial and azimuthal coordinates respectively.

2.1.1 Temporal discretization

A general outline of the numerical methods used to solve the time-integration of the Navier–Stokes equations are presented here. The same procedure applies to the different problems of interest: two-dimensional axisymmetric equations for the base flow (steady and pulsatile), and three-dimensional Navier–Stokes equations linearized around these base flows. These particular problems are discussed in further detail in the subsequent sections of this chapter.

The Navier–Stokes equations given by (2.1) can be rewritten as

$$\partial_t \mathbf{u} + \mathcal{N}(\mathbf{u}) + \mathcal{L}(\mathbf{u}, p) = 0, \tag{2.2a}$$

$$\nabla.\mathbf{u} = 0, \tag{2.2b}$$

where $\mathcal{N}(\mathbf{u})$ denotes the convective terms and $\mathcal{L}(\mathbf{u}, p) = \nabla p - \frac{1}{Re}\Delta\mathbf{u}$. If we denote the base

flow velocity fields as $\mathbf{U}$ and the perturbation as $\mathbf{u}$, the convective terms from the Navier–Stokes equations for the base flow would be given by the nonlinear expression $(\mathbf{U}.\nabla)\mathbf{U}$, while for the linearized Navier–Stokes equations we have the linear term $(\mathbf{U}.\nabla)\mathbf{u}+(\mathbf{u}.\nabla)\mathbf{U}$. Equation (2.2) is discretized in time and we look for the solution $(\mathbf{u}^{n+1}, p^{n+1})$ at time t^{n+1} as function of the previous solutions $(\mathbf{u}^n, p^n), (\mathbf{u}^{n-1}, p^{n-1})$, etc. The time-step is denoted by $\Delta t = t^{n+1} - t^n$ and is chosen as a fixed value. The time-derivative term is approximated at order 1 by

$$\frac{\partial \mathbf{u}}{\partial t} = \frac{\mathbf{u}^{n+1} - \mathbf{u}^n}{\Delta t}. \tag{2.3}$$

The $\mathcal{L}$ term is treated implicitly and evaluated at time $t = t^{n+1}$, while the $\mathcal{N}(\mathbf{u})$ term is evaluated using the flow fields obtained at previous time steps. At first-order, the discretized Navier–Stokes equations for the base flow can then be written as

$$\frac{\mathbf{U}^{n+1}}{\Delta t} + \nabla p^{n+1} - \frac{1}{Re}\Delta \mathbf{U}^{n+1} = \frac{\mathbf{U}^n}{\Delta t} - (\mathbf{U}^n.\nabla)\mathbf{U}^n, \tag{2.4a}$$

$$\nabla.\mathbf{U}^{n+1} = 0, \tag{2.4b}$$

and for the linearized Navier–Stokes equations, we would have

$$\frac{\mathbf{u}^{n+1}}{\Delta t} + \nabla p^{n+1} - \frac{1}{Re}\Delta \mathbf{u}^{n+1} = \frac{\mathbf{u}^n}{\Delta t} - (\mathbf{U}^n.\nabla)\mathbf{u}^n - (\mathbf{u}^n.\nabla)\mathbf{U}^n, \tag{2.5a}$$

$$\nabla.\mathbf{u}^{n+1} = 0. \tag{2.5b}$$

For the case of second-order, the time derivative is approximated as

$$\frac{\partial \mathbf{u}}{\partial t} = \frac{3\mathbf{u}^{n+1} - 4\mathbf{u}^n + \mathbf{u}^{n-1}}{2\Delta t}. \tag{2.6}$$

The convective terms from the Navier–Stokes equations for the base flow are approximated by $2(\mathbf{U}^n.\nabla)\mathbf{U}^n - (\mathbf{U}^{n-1}.\nabla)\mathbf{U}^{n-1}$. Using these expressions, the equations for the base flow become

$$\frac{3\mathbf{U}^{n+1}}{2\Delta t} + \nabla p^{n+1} - \frac{1}{Re}\Delta \mathbf{U}^{n+1} = \frac{2\mathbf{U}^n}{\Delta t} - \frac{\mathbf{U}^{n-1}}{2\Delta t} \tag{2.7a}$$
$$-2(\mathbf{U}^n.\nabla)\mathbf{U}^n + (\mathbf{U}^{n-1}.\nabla)\mathbf{U}^{n-1},$$

$$\nabla.\mathbf{U}^{n+1} = 0, \tag{2.7b}$$

and for the linearized Navier–Stokes equations, we would have

$$\frac{3\mathbf{u}^{n+1}}{2\Delta t} + \nabla p^{n+1} - \frac{1}{Re}\Delta \mathbf{u}^{n+1} \tag{2.8a}$$
$$+(\mathbf{U}^{n+1}.\nabla)\mathbf{u}^{n+1} - (\mathbf{u}^{n+1}.\nabla)\mathbf{U}^{n+1} = \frac{2\mathbf{u}^n}{\Delta t} - \frac{\mathbf{u}^{n-1}}{2\Delta t},$$

$$\nabla.\mathbf{U}^{n+1} = 0. \tag{2.8b}$$

	γ_0	γ_1	γ_2	β_1	β_2
BDF$_1$	1	-1		1	
BDF$_2$	3/2	-2	1/2	2	-1

Table 2.1: Coefficients of the BDF$_g$ methods where g is the order of the scheme Derham (2011).
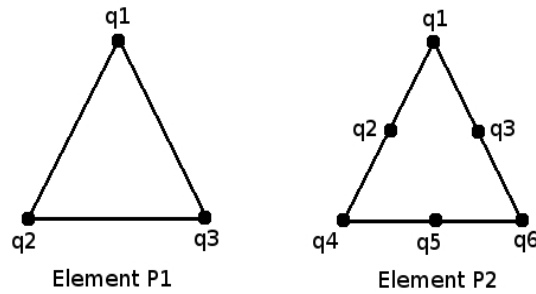

Figure 2.1: Schematic of the elements $P1$ and $P2$ along with their nodes.

The above equations can be written in a concise form as

$$\frac{\gamma_0}{\Delta t}\mathbf{u}^{n+1} + \mathcal{L}(\mathbf{u}^{n+1}, p^{n+1}) = -\sum_{j=1}^{g}\left[\frac{\gamma_j}{\Delta t}\mathbf{u}^{n+1-j} + \beta_j\mathcal{N}(\mathbf{u}^{n+1-j})\right], \qquad (2.9a)$$

$$\nabla.\mathbf{u}^{n+1} = 0, \qquad (2.9b)$$

where the coefficients γ and β are given in table 2.1.

2.1.2 Spatial discretization

A finite-element method has been employed in our present work for spatial discretization of the governing equations. This involves two steps: (i) formulating the weak form of the governing equations (ii) spatially discretizing the resulting set of equations. The spatial discretization has been performed by using the free software *FreeFem++* developed by Frédéric Hecht, Olivier Pironneau, Antoine Le Hyaric and Kohji Ohtsuka (http://www.freefem.org (Hyaric *et al.*, 2011)). An excellent introduction to the finite-element method is presented in the book by Reddy (2006).

The first step involved in the spatial discretization is the definition of a mesh. If we denote the computational domain as Ω, and its border by Γ, the finite element mesh is generated using *FreeFem++*, which generates an automatic triangulation of the domain Ω. The number of triangles is used to quantify the refinement of the mesh, which is adjusted by fixing the number of vertices of the triangle on each edge of the domain. For a given mesh, the flow field components, the velocity and pressure, are then discretized on a finite-dimensional

approximation of the state-space. The appropriate state-space (so that the variational approximations are not ill-posed) is $P2$–$P1$, namely the velocity fields are projected onto-six node quadratic triangular elements with quadratic interpolation ($P2$ − elements) whereas the pressure field is discretized using three-node triangular elements ($P1$ − elements). An illustration of these elements is shown in figure 2.1. The basis functions $\psi_i(x, y)$ of the state-space $P1$ are polynomial functions of order 1 on each triangle defined as

$$
\begin{aligned}
\psi_i(x, y) &= a_i^k + b_i^k x + c_i^k y \qquad \text{for} \qquad (x, y) \in T_k, & \text{(2.10a)} \\
\psi_i(q_i) &= 1 \qquad \text{and} \qquad \psi_i(q_j) = 0, \qquad \text{if} \qquad i \neq j. & \text{(2.10b)}
\end{aligned}
$$

Similarly, the basis functions $\phi_i(x, y)$ of the state-space $P2$ are polynomial functions of order 2 on each triangle such that

$$
\begin{aligned}
\phi_i(x, y) &= a_i^k + b_i^k x + c_i^k y + d_i^k x^2 + e_i^k xy + f_i^k y^2 \quad \text{for } (x, y) \in T_k, & \text{(2.11a)} \\
\phi_i(q_i) &= 1 \qquad \text{and} \qquad \phi_i(q_j) = 0, \qquad \text{if} \qquad i \neq j. & \text{(2.11b)}
\end{aligned}
$$

As a result, the pressure is represented by 3 degrees of freedom on each triangle while a component of the velocity has 6 degrees of freedom.

We now consider the weak formulation of the Navier–Stokes equations, corresponding to equation (2.9). For this, we consider the continuous state-spaces $\mathcal{X} = \mathsf{H}_1(\Omega)$ ($\mathsf{H}_1(\Omega)$ is the Sobolev space) and $\mathcal{M} = \mathsf{L}_2(\Omega)$ ($\mathsf{L}_2(\Omega)$ is the linear space of 2nd order integrable functions on Ω) in the physical domain. The velocity $\mathbf{u}$ and pressure fields p belong to $\mathcal{X}^2$ and $\mathcal{M}$ respectively (since we consider two components of the velocity field). Equations (2.9) are multiplied by test functions $\mathbf{v} \in \mathcal{X}^2$ and $q \in \mathcal{M}$ which gives after integration and application of Green's formula

$$
\frac{\gamma_0}{\Delta t} \int_\Omega \mathbf{v}.\mathbf{u}^{n+1} \mathrm{d}\Omega - \int_\Omega (\nabla.\mathbf{v}) p^{n+1} \mathrm{d}\Omega
$$

$$
+ \frac{1}{Re} \int_\Omega \nabla\mathbf{v}.\nabla\mathbf{u}^{n+1} \mathrm{d}\Omega + \int_\Gamma \mathbf{v}.(p\mathbf{n}) \mathrm{d}\Gamma - \frac{1}{Re} \int_\Gamma \mathbf{v}.(\nabla\mathbf{u}^{n+1}.\mathbf{n}) \mathrm{d}\Gamma =
$$

$$
- \frac{\gamma_j}{\Delta t} \int_\Omega \sum_{j=1}^g \mathbf{v}.\mathbf{u}^{n+1-j} \mathrm{d}\Omega - \beta_j \int_\Omega \sum_{j=1}^g \mathbf{v}.\Big[(\mathbf{u}^{n+1-j}.\nabla) \mathbf{u}^{n+1-j} \Big] \mathrm{d}\Omega, \qquad \text{(2.12a)}
$$

$$
\int_\Omega q(\nabla.\mathbf{u}^{n+1}) \mathrm{d}\Omega = 0, \qquad \forall \mathbf{v} \in \mathcal{X}^2 \quad \text{and} \quad \forall q \in \mathcal{M}, \qquad \text{(2.12b)}
$$

where $\mathbf{n}$ is the outward normal unitary vector of the boundary. The boundary conditions on the wall and at the inlet are Dirichlet conditions so that the components of the velocity field are fixed. At the outlet a standard no-stress condition (Marquet *et al.*, 2009) is used, given by

$$
p\mathbf{n} - \frac{1}{Re}(\nabla\mathbf{u}).\mathbf{n} = 0, \qquad \text{(2.13)}
$$

where $\mathbf{n}$ is the outward unit normal vector and $\mathbf{u}$ is the velocity field. This allows us to cancel the boundary integrals in equation (2.12). The above equations can be written in a

more concise form as

$$\frac{\gamma_0}{\Delta t}a(\mathbf{v},\mathbf{u}^{n+1}) + \frac{1}{Re}d(\mathbf{v},\mathbf{u}^{n+1}) + b(\mathbf{v},p^{n+1}) = a(\mathbf{v},\mathbf{f}) \ \forall \mathbf{v} \in \mathcal{X}^2, \quad (2.14a)$$

$$b(\mathbf{u}^{n+1},q) = 0 \qquad \forall q \in \mathcal{M}, \quad (2.14b)$$

where we have denoted the explicit convective terms by $\mathbf{f}$ and introduced the following operators

$$a(\mathbf{v},\mathbf{u}) = \int_\Omega \mathbf{v}.\mathbf{u}\mathrm{d}\Omega, \quad d(\mathbf{v},\mathbf{u}) = \int_\Omega \nabla\mathbf{v}.\nabla\mathbf{u}\mathrm{d}\Omega, \quad b(\mathbf{v},p) = -\int_\Omega (\nabla.\mathbf{v})p\mathrm{d}\Omega. \quad (2.15)$$

We now reform the above equations in the discrete state-spaces denoted by $\mathcal{X}_h$ and $\mathcal{M}_h$ for the velocity and pressure fields respectively. Denoting the discretized forms of the previous variables as $\mathbf{u}_h \in \mathcal{X}_h^2$, $p_h \in \mathcal{M}_h$ and $\mathbf{f}_h \in \mathcal{X}_h$ and introducing them into the equation (2.14), we get

$$\frac{\gamma_0}{\Delta t}a(\mathbf{v}_h,\mathbf{u}_h^{n+1}) + \frac{1}{Re}d(\mathbf{v}_h,\mathbf{u}_h^{n+1}) + b(\mathbf{v}_h,p_h^{n+1}) = a(\mathbf{v}_h,\mathbf{f}_h) \ \forall \mathbf{v}_h \in \mathcal{X}_h^2, \quad (2.16a)$$

$$b(\mathbf{u}_h^{n+1},q_h) = 0 \quad \forall q_h \in \mathcal{M}_h. \quad (2.16b)$$

The above numerical tools are used for the computation of our base flows and to perform the stability analysis, which are discussed in subsequent sections.

2.2 Base flows

The base flows in our present study are assumed to be axisymmetric along with no velocity component in the azimuthal direction. The Navier–Stokes equations in cylindrical coordinates then become

$$\frac{\partial U_r}{\partial t} + \left(U_r\frac{\partial U_r}{\partial r} + U_z\frac{\partial U_r}{\partial z}\right) = -\frac{\partial P}{\partial r} + \frac{1}{Re}\left[\frac{1}{r}\frac{\partial}{\partial r}\left(r\frac{\partial U_r}{\partial r}\right) + \frac{\partial^2 U_r}{\partial z^2} - \frac{U_r}{r^2}\right], \quad (2.17a)$$

$$\frac{\partial U_z}{\partial t} + \left(U_r\frac{\partial U_z}{\partial r} + U_z\frac{\partial U_z}{\partial z}\right) = -\frac{\partial P}{\partial z} + \frac{1}{Re}\left[\frac{1}{r}\frac{\partial}{\partial r}\left(r\frac{\partial U_z}{\partial r}\right) + \frac{\partial^2 U_z}{\partial z^2}\right], \quad (2.17b)$$

$$\frac{\partial U_r}{\partial r} + \frac{U_r}{r} + \frac{\partial U_z}{\partial z} = 0, \quad (2.17c)$$

where $U_r(r,z)$ and $U_z(r,z)$ denote radial and axial components of the velocities respectively, and $P(r,z)$ stands for the pressure field. For the case of pulsatile flows, the above equations are time-marched till a time-periodic base flow is obtained using appropriate boundary conditions that are discussed later in this section. However, for the case of steady flow fields, the base flow was computed as in (Marquet *et al.*, 2009) wherein a time-dependent simulation of the two-dimensional Navier–Stokes equations is first used to obtain an approximate solution of the steady flow at low Reynolds number, where it is stable to two-dimensional perturbations. A Newton iteration method is then applied to solve the stationary Navier–Stokes equations, starting the procedure with the approximate steady solution as a guess which is discussed below.

2.2.1 Steady flows: Newton method

The base flow fields at a small value of Reynolds number are computed first by time-marching the Navier–Stokes equations for a sufficiently long time. Flow fields at a slightly higher Reynolds number are obtained using a Newton method where the solution obtained at a smaller Reynolds number being used as an initial guess for the iteration. The same procedure is also applied for computing the base flow fields at a slightly different geometrical setting wherein the bulge height is varied at small increments. Also at times, this procedure has been used to compute the base flow fields obtained by interpolation from other mesh grids, particularly in the eigenvalue analysis, where the flow fields obtained on a highly refined grid are interpolated on to a coarser grid. The Newton method used for the computation of the base flow field is discussed below.

Starting from an initial guess Φ_0, this method involves iterations of the guess value $\Phi_0 + \delta\Phi_0$ until the $L^2(\Omega)$- norm of the numerical residual $R(\Phi_0)$ in the flow field becomes smaller than 10^{-12}. The steady state solution of the Navier–Stokes equations can be written as

$$R(\Phi_0) = 0. \tag{2.18}$$

The starting point of this method is to consider the numerical residual $R(\Phi_0)$ of an initial guess flow field of which the residual shall be driven to zero by imposing a $\delta\Phi_0$ such that

$$R(\Phi_0 + \delta\Phi_0) = 0. \tag{2.19}$$

After a first-order expansion, one obtains

$$R(\Phi_0) + R'(\Phi_0)\delta\Phi_0 = 0, \tag{2.20}$$

where $R'(\Phi_0) \equiv \nabla R(\Phi_0)$ states the Jacobian considering the $O(1)$ terms, which has the same form as the linearized Navier–Stokes equations, which we will see in the subsequent section. The residual $R(\Phi_0)$ accounts for the higher-order terms. An improvement in the flow field solution can be obtained as

$$\delta\Phi_0 = -R'(\Phi_0)^{-1}R(\Phi_0), \tag{2.21a}$$
$$\Phi_{0,+} = \Phi_0 + \delta\Phi_0. \tag{2.21b}$$

This process is carried out until the residual error norm of an iterate basic flow solution $\Phi_{0,+}$ falls below the chosen threshold. Then, the flow field $\Phi_{0,+}$ has converged to the final base flow Φ_0.

The steady Navier–Stokes equations governing the base flow $(\mathbf{U}, P)$ are given by

$$(\mathbf{U}.\nabla)\mathbf{U} = -\nabla P + \frac{1}{Re}\nabla^2\mathbf{U}, \tag{2.22a}$$
$$\nabla.\mathbf{U} = 0, \tag{2.22b}$$

with associated boundary conditions. Let the initial guess for the Newton method be

($\mathbf{U}_0, P_0$). As this is an approximate solution, they do not satisfy the equations (2.22), which can be written as

$$\text{NS}(\mathbf{U}_0, P_0) \neq 0, \tag{2.23}$$

where the Navier–Stokes operator is defined by

$$\text{NS}(\mathbf{U}_0, P_0) = \begin{pmatrix} (\mathbf{U}_0.\nabla)\mathbf{U}_0 + \nabla P_0 - \frac{1}{Re}\nabla^2 \mathbf{U}_0 \\ \nabla.\mathbf{U}_0 \end{pmatrix}. \tag{2.24}$$

Now we look for the correction ($\delta\mathbf{U}, \delta P$) such that the flow state ($\mathbf{U}_0 + \delta\mathbf{U}, P_0 + \delta P$) is a solution of equation (2.22) resulting in $\text{NS}(\delta\mathbf{U}, \delta P) = 0$. The linearized Navier–Stokes equations about the approximate solution can be written as

$$\text{LNS}_{(\mathbf{U}_0, P_0)}(\delta\mathbf{U}, \delta P) = -\text{NS}(\mathbf{U}_0, P_0), \tag{2.25}$$

where $\text{LNS}_{(\mathbf{U}_0, P_0)}$ denotes the Navier–Stokes equations linearized about the state ($\mathbf{U}_0, P_0$) such that

$$\text{NS}(\mathbf{U}_0, P_0) \neq 0, \tag{2.26}$$

where the Navier–Stokes operator is defined by

$$\text{LNS}_{(\mathbf{U}_0, P_0)} = \begin{pmatrix} (\mathbf{U}_0.\nabla)\delta\mathbf{U} + (\delta\mathbf{U}.\nabla)\mathbf{U}_0 + \nabla(\delta P) - \frac{1}{Re}\nabla^2(\delta\mathbf{U}) \\ \nabla.\delta\mathbf{U}_0 \end{pmatrix}. \tag{2.27}$$

As explained earlier, we compute ($\delta\mathbf{U}, \delta P$) iteratively till $\text{NS}(\mathbf{U}_0, P_0) = 0$, reducing ($\mathbf{U}_0, P_0$) to the base flow solution.

2.2.2 Boundary conditions

We now discuss the boundary conditions that are employed for steady and pulsatile flow field calculations.

2.2.2.1 Steady flows

For the case of steady flows, no-slip conditions were employed on the walls. At the inlet, an equilibrium Hagen–Poiseuille profile is prescribed, the axial velocity being given by

$$U_z(r) = 2\bar{U}\left(1 - \frac{4r^2}{D^2}\right), \tag{2.28}$$

where $\bar{U}$ is the average velocity, defined as $\bar{U} = 4Q/\pi D^2$ (Q being the flow rate in the tube). At the outlet, a standard no-stress condition is employed (Marquet *et al.*, 2009), given by

$$P - \frac{1}{Re}\frac{\partial U_z}{\partial z} = 0, \qquad \frac{\partial U_r}{\partial z} = 0. \tag{2.29}$$

On the axis, standard symmetry conditions are employed.

2.2.2.2   Pulsatile flows

The only difference for the case of pulsatile flows from steady flows is that a time-dependent velocity profile is imposed at the inlet, with other boundary conditions being the same. As discussed in detail in the previous chapter (see section 1.2.1), an analytical Womersley solution is applied at the inlet. The time-dependent Dirichlet boundary condition for the axial velocity component is completely determined by the frequency ω and the Fourier components Q_n of the imposed flow rate

$$Q(t) = \sum_{n=-\infty}^{\infty} Q_n \mathrm{e}^{in\omega t}. \tag{2.30}$$

More details on the derivation of these velocity profiles along with the coefficients Q_n of various flow rate waveforms are provided in the previous chapter 1.

2.3   Stability analysis

To analyse the stability of a base flow field, a small perturbation is added and its evolution is monitored in time after linearization of the Navier–Stokes equations. Consider the base flow field which is axisymmetric and time-dependent, $\mathbf{U}(r,z,t) = (U_r(r,z,t), 0, U_z(r,z,t), P(r,z,t))$. To this basic flow, a linear disturbance vector is added, $\mathbf{u}'(r,\theta,z,t) = (u_r'(r,\theta,z,t), u_\theta'(r,\theta,z,t), u_z'(r,\theta,z,t), p'(r,\theta,z,t))$. The resulting velocity field $\mathbf{U}(r,z,t) + \mathbf{u}'(r,\theta,z,t)$ is substituted into the Navier–Stokes equations. Linearization around the base flow field then yields the linearized Navier–Stokes equations as

$$\frac{\partial u_r'}{\partial t} + U_r \frac{\partial u_r'}{\partial r} + U_z \frac{\partial u_r'}{\partial z} + u_r' \frac{\partial U_r}{\partial r} + u_z' \frac{\partial U_r}{\partial z} = \tag{2.31a}$$
$$-\frac{\partial p'}{\partial r} + \frac{1}{Re}\Big(\frac{\partial^2 u_r'}{\partial r^2} + \frac{1}{r}\frac{\partial u_r'}{\partial r} + \frac{1}{r^2}\frac{\partial^2 u_r'}{\partial \theta^2} + \frac{\partial^2 u_r'}{\partial z^2} - \frac{u_r'}{r^2} - \frac{2}{r^2}\frac{\partial u_\theta'}{\partial \theta}\Big),$$

$$\frac{\partial u_\theta'}{\partial t} + U_r \frac{\partial u_\theta'}{\partial r} + U_z \frac{\partial u_\theta'}{\partial z} + \frac{U_r u_\theta'}{r} = \tag{2.31b}$$
$$-\frac{1}{r}\frac{\partial p'}{\partial \theta} + \frac{1}{Re}\Big(\frac{\partial^2 u_\theta'}{\partial r^2} + \frac{1}{r}\frac{\partial u_\theta'}{\partial r} + \frac{1}{r^2}\frac{\partial^2 u_\theta'}{\partial \theta^2} + \frac{\partial^2 u_\theta'}{\partial z^2} - \frac{u_\theta'}{r^2} + \frac{2}{r^2}\frac{\partial u_r'}{\partial \theta}\Big),$$

$$\frac{\partial u_z'}{\partial t} + U_r \frac{\partial u_z'}{\partial r} + U_z \frac{\partial u_z'}{\partial z} + u_r' \frac{\partial U_z}{\partial r} + u_z' \frac{\partial U_z}{\partial z} = \tag{2.31c}$$
$$-\frac{\partial p'}{\partial z} + \frac{1}{Re}\Big(\frac{\partial^2 u_z'}{\partial r^2} + \frac{1}{r}\frac{\partial u_z'}{\partial r} + \frac{1}{r^2}\frac{\partial^2 u_z'}{\partial \theta^2} + \frac{\partial^2 u_z'}{\partial z^2}\Big),$$

$$\frac{u_r'}{r} + \frac{\partial u_r'}{\partial r} + \frac{1}{r}\frac{\partial u_\theta'}{\partial \theta} + \frac{\partial u_z'}{\partial z} = 0. \tag{2.31d}$$

The perturbations are chosen as normal modes in the azimuthal direction with unspecified time-dependence (general case) as

$$\begin{pmatrix} u_r'(r,\theta,z,t) \\ u_\theta'(r,\theta,z,t) \\ u_z'(r,\theta,z,t) \\ p'(r,\theta,z,t) \end{pmatrix} = \begin{pmatrix} \hat{u}_r(r,z,t) \\ \hat{u}_\theta(r,z,t) \\ \hat{u}_z(r,z,t) \\ \hat{p}(r,z,t) \end{pmatrix} \exp \mathrm{i}(m\theta) + \text{c.c.} \tag{2.32}$$

The equations governing the evolution of perturbations $(\hat{u}_r(r,z,t), \hat{u}_\theta(r,z,t), \hat{u}_z(r,z,t), \hat{p}(r,z,t))$ do not assume any axis of symmetry and are in

general, complex variables. But without loss of generality, one may assume that there is a plane of symmetry for the perturbations by considering $(\hat{u}_r(r,z,t), \hat{u}_z(r,z,t), \hat{p}(r,z,t))$ to be purely real, and $\hat{u}_\theta(r,z,t)$ to be purely imaginary. Rewriting the equations in terms of these purely real variables reduces the computational cost. For this, the equation for $\hat{u}_\theta(r,z,t)$ is multiplied by i and $\hat{u}_\theta(r,z,t)$ is replaced by $i\hat{u}_\theta(r,z,t)$. Using these assumptions, yields

$$\frac{\partial \hat{u}_r}{\partial t} + U_r \frac{\partial \hat{u}_r}{\partial r} + U_z \frac{\partial \hat{u}_r}{\partial z} + \hat{u}_r \frac{\partial U_r}{\partial r} + \hat{u}_z \frac{\partial U_r}{\partial z} = \tag{2.33a}$$
$$-\frac{\partial \hat{p}}{\partial r} + \mathrm{Re}^{-1}\left(\frac{\partial^2 \hat{u}_r}{\partial r^2} + \frac{1}{r}\frac{\partial \hat{u}_r}{\partial r} - \frac{\mathrm{m}^2 \hat{u}_r}{r^2} + \frac{\partial^2 \hat{u}_r}{\partial z^2} - \frac{\hat{u}_r}{r^2} - \frac{2\mathrm{m}\hat{u}_\theta}{r^2}\right),$$

$$\frac{\partial \hat{u}_\theta}{\partial t} + U_r \frac{\partial \hat{u}_\theta}{\partial r} + U_z \frac{\partial \hat{u}_\theta}{\partial z} + \frac{U_r \hat{u}_\theta}{r} = \tag{2.33b}$$
$$+\frac{\mathrm{m}\hat{p}}{r} + \mathrm{Re}^{-1}\left(\frac{\partial^2 \hat{u}_\theta}{\partial r^2} + \frac{1}{r}\frac{\partial \hat{u}_\theta}{\partial r} - \frac{\mathrm{m}^2 \hat{u}_\theta}{r^2} + \frac{\partial^2 \hat{u}_\theta}{\partial z^2} - \frac{\hat{u}_\theta}{r^2} - \frac{2\mathrm{m}\hat{u}_r}{r^2}\right),$$

$$\frac{\partial \hat{u}_z}{\partial t} + U_r \frac{\partial \hat{u}_z}{\partial r} + U_z \frac{\partial \hat{u}_z}{\partial z} + \hat{u}_r \frac{\partial U_z}{\partial r} + \hat{u}_z \frac{\partial U_z}{\partial z} = \tag{2.33c}$$
$$-\frac{\partial \hat{p}}{\partial z} + \mathrm{Re}^{-1}\left(\frac{\partial^2 \hat{u}_z}{\partial r^2} + \frac{1}{r}\frac{\partial \hat{u}_z}{\partial r} - \frac{\mathrm{m}^2 \hat{u}_z}{r^2} + \frac{\partial^2 \hat{u}_z}{\partial z^2}\right),$$

$$\frac{\hat{u}_r}{r} + \frac{\partial \hat{u}_r}{\partial r} + \frac{\mathrm{m}\hat{u}_\theta}{r} + \frac{\partial \hat{u}_z}{\partial z} = 0. \tag{2.33d}$$

The methods used when the base flow field is either steady or time-periodic are now detailed separately.

2.3.1 Steady flows

For a steady axisymmetric base flow, the perturbations may be considered in normal mode form with exponential time-dependence as

$$\begin{pmatrix} u_r'(r,\theta,z,t) \\ u_\theta'(r,\theta,z,t) \\ u_z'(r,\theta,z,t) \\ p'(r,\theta,z,t) \end{pmatrix} = \begin{pmatrix} \hat{u}_r(r,z) \\ \hat{u}_\theta(r,z) \\ \hat{u}_z(r,z) \\ \hat{p}(r,z) \end{pmatrix} \exp \mathrm{i}(m\theta - \omega t), \tag{2.34}$$

where m is an integer azimuthal mode number and $\omega \equiv \omega_r + \mathrm{i}\omega_i$ a complex frequency. With positive growth rate, $\omega_i > 0$, the perturbation grows exponentially in time. Substitution of expression (2.34) into the linearized Navier–Stokes equations (2.33) yields, in classical fashion, a generalized eigenvalue problem of the form

$$-\mathrm{i}\omega \mathbf{B}.\hat{\mathbf{u}} = \mathbf{A}.\hat{\mathbf{u}}, \tag{2.35}$$

where $\hat{\mathbf{u}} = (\hat{u}_r, \hat{u}_\theta, \hat{u}_z, \hat{p})$ and $\mathbf{A}$ and $\mathbf{B}$ are the associated matrices which are defined as:

$$\mathbf{A} = \begin{pmatrix} \mathsf{D} - \mathsf{C} - \partial_r U_r - \frac{1}{Re} 1/r^2 & -\frac{1}{Re} 2m/r^2 & -\partial_z U_r & -\partial_r \\ -\frac{1}{Re} 2m/r^2 & \mathsf{D} - \mathsf{C} - U_r/r - \frac{1}{Re} 1/r^2 & 0 & m/r \\ -\partial_r U_z & 0 & \mathsf{D} - \mathsf{C} - \partial_z U_z & -\partial_z \\ 1/r + \partial_r & m/r & \partial_z & 0 \end{pmatrix}, \quad (2.36a)$$

$$\mathbf{B} = \begin{pmatrix} 1 & 0 & 0 & 0 \\ 0 & 1 & 0 & 0 \\ 0 & 0 & 1 & 0 \\ 0 & 0 & 0 & 0 \end{pmatrix}, \quad (2.36b)$$

where $\mathsf{D} = \frac{1}{Re}(\partial_{rr} + 1/r\partial_r - m^2/r^2 + \partial_{zz})$ accounts for the viscous diffusion of the perturbation and $\mathsf{C} = U_r\partial_r + U_z\partial_z$ for its advection by the base flow.

To compute the eigenvalues with the largest imaginary part of the eigenvalue problem given by expression (2.35), which determine the stability, a shift-and-invert strategy is used as in Marquet *et al.* (2009), Ehrenstein & Gallaire (2005). The resulting generalized eigenvalue problems are then solved using the *Implicitly Restarted Arnoldi method* of the library. This method is discussed in more detail in Sorensen (1992), Nayar & Ortega (1993).

2.3.2 Pulsatile flows

As discussed earlier, the perturbations are chosen as normal modes (equation (2.32)), using which we obtain the linearized Navier–Stokes equations given by equation (2.33). To analyse the stability of time-periodic base flows, the linearized Navier–Stokes equations (2.33) are time-marched for a suitable number of pulse cycles and the perturbation fields are monitored till they converge. Once the perturbations have converged, the evolution of the perturbation velocity fields at a specific point in the computational domain is investigated to determine the Floquet multiplier. According to Floquet theory, the velocity and pressure perturbations grow or decay exponentially from period to period. Thus, the perturbation fields are expected to satisfy the relationship

$$\hat{u}(r, z, t + T) = \exp(\sigma T)\hat{u}(r, z, t). \quad (2.37)$$

The coefficient $\mu = \exp(\sigma T)$ is often called the Floquet multiplier, where T is the time period of the pulsatile base flow and $\sigma = \lambda + i\omega$ is the complex growth rate. Here, the absolute value of the Floquet multiplier $|\mu|$ is computed as

$$|\mu| = E_k(t + T)/E_k(t), \quad (2.38)$$

where $E_k(t)$ is defined as,

$$E_k(t) = \sqrt{\int_\Omega [u_r'(t)^2 + u_\theta'(t)^2 + u_z'(t)^2]d\Omega}. \quad (2.39)$$

A Floquet multiplier $|\mu| > 1$ indicates an unstable flow, while $|\mu| < 1$ indicates a stable

one. A Floquet multiplier $|\mu| = 1$ represents neutral stability. Also, depending on the value of the Floquet multiplier μ, several mode classifications are possible. A real bifurcation ($\mu = 1$) has the same period as the base flow. A subharmonic bifurcation is indicated by a negative Floquet multiplier ($\mu = -1$), where the perturbation is period-doubling, operating at a period twice that of the base flow. A subharmonic bifurcation can be detected by investigation of the perturbation field, as the sign of a period-doubling bifurcation will alternate from one base flow period to the next. A third-type, complex-conjugate bifurcations, consist of standing- or travelling-wave solutions. A complex Floquet multiplier can be identified using the evolution of the absolute value of Floquet multiplier, $|\mu|$. An oscillation around a mean value indicates a complex Floquet multiplier (Robichaux *et al.*, 1999, Sheard *et al.*, 2005).

2.3.3 Energy-transfer analysis

To address the question of why the flow amplifies a particular type of perturbation, we search for the regions within the flow domain where the kinetic energy is transferred from the basic flow to the perturbation. This provides information regarding the instability mechanisms involved in the evolution of disturbances (Lanzerstorfer & Kuhlmann, 2012*a*,*b*). A brief description of this analysis is provided here, which follows from Lanzerstorfer & Kuhlmann (2012*a*,*b*). The kinetic energy per unit mass of the perturbation flow is defined as $E_{kin} = \int_\Omega \mathbf{u}'^2 dV/2$, where the integration is carried out over the computational domain denoted as Ω. Scalar multiplication of the linear perturbation equations (2.31) by $\mathbf{u}'$ from the left-hand side and integrating over the volume yields the Reynolds–Orr equation, which can be solved for the rate of change of the kinetic energy dE_{kin}/dt (see e.g. Joseph, 1976) to obtain

$$\frac{dE_{kin}}{dt} = -D + \sum_{i=1}^{4} \int_\Omega E_{p,i} d\Omega - \frac{1}{2}\int_{\Gamma_o} E_{p,5} dS. \tag{2.40}$$

The term D represents the average dissipation given by

$$D = \frac{1}{Re}\int_\Omega \mathbf{u}'.\nabla^2\mathbf{u}' d\Omega, \tag{2.41}$$

and $E_{p,i}$ are given in equation (2.44) below. The surface integral

$$-\frac{1}{2}\int_{\Gamma_o} E_{p,5} dS = -\frac{1}{2}\int_{\Gamma_o} \mathbf{u}'^2 \mathbf{U} dS, \tag{2.42}$$

represents the rate of change of the kinetic energy of the perturbations which is advected out of the domain by the basic flow. In addition, no perturbation energy is convected into the domain, either through the inlet or through the solid walls on which $\mathbf{u}' = 0$.

For an analysis of the energy transfer rates it is useful to decompose the perturbation velocity $\mathbf{u}'$ into components parallel ($\mathbf{u}'_\parallel$) and perpendicular ($\mathbf{u}'_\perp$) to the basic flow $\mathbf{U}$,

$$\mathbf{u}'_\parallel = \frac{(\mathbf{u}' . \mathbf{U})\mathbf{U}}{\mathbf{U} . \mathbf{U}}, \qquad \mathbf{u}'_\perp = \mathbf{u}' - \mathbf{u}'_\parallel, \tag{2.43}$$

such that the local energy transfer terms are given by

$$\sum_{i=1}^{4} E_{p,i} = -[\mathbf{u}'_\perp . (\mathbf{u}'_\perp . \nabla\mathbf{U}) + \mathbf{u}'_\parallel . (\mathbf{u}'_\perp . \nabla\mathbf{U}) + \mathbf{u}'_\perp . (\mathbf{u}'_\parallel . \nabla\mathbf{U}) + \mathbf{u}'_\parallel . (\mathbf{u}'_\parallel . \nabla\mathbf{U})], \tag{2.44}$$
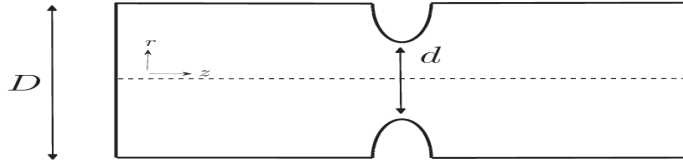
Figure 2.2: Schematic of the geometry considered in Griffith *et al.* (2008), Griffith (2007), Griffith *et al.* (2009) (*Model A*).

where i numbers all terms on the right-hand side consecutively. The local energy production rates given by the terms $E_{p,i}$ represent the coupling of the base flow $\mathbf{U}$ to the perturbation $\mathbf{u}'$ and each term represents a certain energy transport process. The use of the coordinates, locally aligned with the flow direction $\mathbf{U}/U$, is suitable, because no other distinguished direction exists locally. As an example, $E_{p,2}$ is the local rate of change of perturbation energy density per unit mass by the convective transport due to a cross-stream perturbation flow $(\mathbf{u}'_\perp \,.\, \nabla)$ of basic-state momentum ($\mathbf{U}$). Hence, if $\mathbf{u}'_\perp \,.\, \nabla \mathbf{U}$ has a component parallel to and in the direction of $\mathbf{u}'_\parallel$, kinetic energy is locally transferred from the basic state to the perturbation flow. If $E_{p,2} < 0$, the perturbation locally loses energy to the basic flow.

2.4 Flow geometries

The different geometries that are investigated during this project are described in this section.

2.4.1 Stenotic flows

Flows through stenotic geometries were used in the present work to validate our numerical solver. For this, we consider two geometries used in the literature: (a) stenosis modeled as a semi-circular blockage (b) stenosis modeled using a sinusoidal function. Griffith *et al.* (2008), Griffith (2007), Griffith *et al.* (2009) modeled the stenosis as an axisymmetric blockage in the form of a semi-circle, whereas Sherwin & Blackburn (2005) used a sinusoidal function. We use the term *Model A* and *Model B* correspondingly for these geometries.

Model A consists of a long, straight tube with an axisymmetric blockage described by a single parameter, the stenosis degree, defined as

$$b = 1 - \left(\frac{d}{D}\right)^2,\tag{2.45}$$

where D is the diameter of the tube and d is the diameter at the centre of the stenosis. This is shown in figure 2.2.

The radius of the blockage, dependent on d,

$$r_b = \frac{D-d}{2} = \frac{D}{2}(1 - \sqrt{1-b}).\tag{2.46}$$
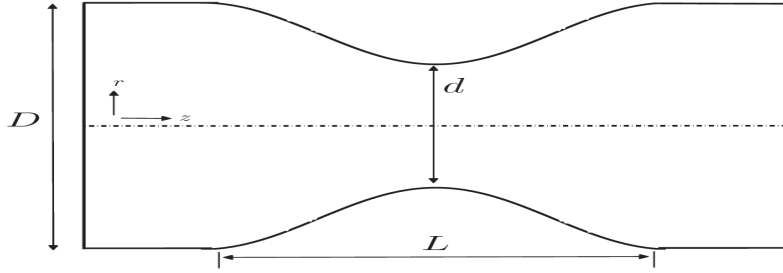
Figure 2.3: Schematic of the geometry considered in Sherwin & Blackburn (2005) (*Model B*).

The advantage of using this model is that the effect of the geometry can be analysed by varying a single parameter, but at the same time, the use of a semi-circular constriction introduces geometric singularities.

In the study carried out by Sherwin & Blackburn (2005), the stenosis is described using a sinusoidal variation. The schematic of this geometry is shown in figure 2.3 which is termed as *Model B* in our study. The radial variation $r(z)$ is of the following form

$$r(z) = \frac{d}{2} + \frac{1}{2}(D - d)\sin^2(\pi z/L) \qquad (-0.5 \leq (z/L) \leq 0.5). \qquad (2.47)$$

An axisymmetric geometry with a 50% reduction in radius leads to a 75% reduction in area. The stenosis length defined by L is fixed at a value of $L = 2D$.

The main difference between the two stenotic geometries, *Model A* and *Model B*, is that the former has a much shorter contraction and sharp corners, whereas the latter has a longer, smoother contraction. This is expected to have a direct effect on the nature of the separating shear layer which forms downstream of the stenosis. The inlet conditions used in the analysis of flows through these geometries are the Hagen–Poiseuille flow profile for steady flows and a Womersley solution for the case of pulsatile flows. However, only a single Fourier component was used to define the flow rate waveform for the case of pulsatile flows, given by

$$Q(t) = 1 + A\sin(2\pi t/T), \qquad (2.48)$$

where the sectionally averaged velocity oscillates sinusoidally around the temporally averaged flow velocity with a period T and an amplitude A.

2.4.2 Aneurysmal flows

An axisymmetric fusiform aneurysmal geometry is considered in the present study and is shown in figure 2.4. The geometry is characterised by the inlet diameter D the bulge height H (height of the bulge above the inlet diameter) and the width of the bulge W. The shape of the wall is designed using a gaussian function as

$$r(z) = \left[\frac{D}{2} + H\exp\left(-\frac{z^2}{2W^2}\right)\right], \qquad (2.49)$$
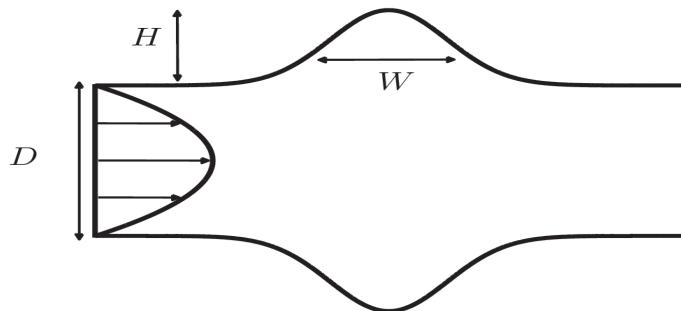
Figure 2.4: A typical geometry considered in the present study.

where z and r denote axial and radial directions with the origin taken at the bulge center. The dilatation ratio D_R, which is the ratio of the maximum diameter to the inlet diameter, is here given by $D_R = 1 + 2H/D$. Subsequently, distances are non-dimensionalized with the inlet diameter D. To cover different sized aneurysms and to analyse the changes in the hemodynamic forces at different stages of development, the following parameter ranges are considered in the present investigation: $0.25 \leq W/D \leq 2$ and $0.1 \leq H/D \leq 1$ (corresponding to $1.2 \leq D_R \leq 3$).

Sheard (2009) used a sinusoidal function to model an aneurysm (which was the same as *Model 3* in Salsac *et al.* (2006)), where the shape of the wall is given by

$$r(z) = \begin{cases} D/2, & \text{if } |z/L| > 1/2, \\ \frac{D_R+1}{4} + \frac{D_R-1}{4}\cos(\frac{2\pi z}{L}), & \text{if } |z/L| \leq 1/2, \end{cases} \qquad (2.50)$$

where L is the length of the aneurysm and D_R is the dilatation ratio (ratio of the maximum diameter to the inlet diameter). The use of a gaussian function to model the walls ensures that the shape of the walls is continuously differentiable to all orders. This is a desirable feature, particularly in the context of hydrodynamic stability, to avoid any singularities due to the geometry.

To investigate whether such a difference in the modeling of the wall could lead to changes in flow characteristics, a study using the model used by Sheard (2009) is carried out and the flow characteristics are compared with a gaussian equivalent (the parameter W appearing in equation (2.49) is chosen such that the areas of both the geometries, in an axisymmetric plane, are the same). This is shown in figure 2.5 where the geometry used in the study by Sheard (2009) (which was the same as *Model 3* in Salsac *et al.* (2006)) is shown using dotted lines. The dilatation ratio D_R and the length ratio L_R, are 1.9 and 2.9 respectively. The equivalent gaussian geometry is shown using continuous lines. One can see that both shapes are hardly distinguishable but that the dilatation modeled using a gaussian function relaxes to a straight pipe slightly more smoothly. We will see that despite very close similarity of these shapes, the flow dynamics may display significant differences.
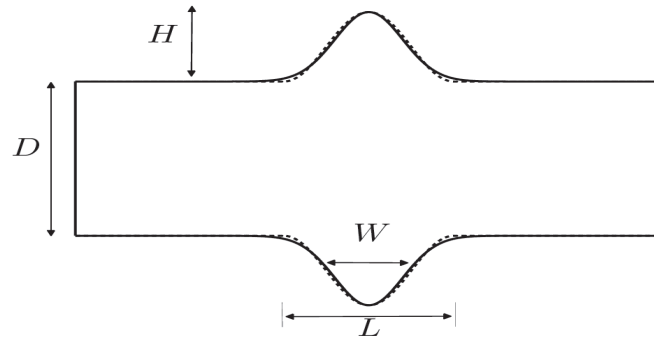
Figure 2.5: The geometry considered in the study by Sheard (2009) is shown using dotted lines, where the dilatation was modeled as a sinusoidal function. The gaussian equivalent geometry is shown using continuous lines. Parameter settings: $H = 0.45$, $L = 2.9$, $W = 0.5785$.

2.5   Code validation

In this section, the various validation tests carried out as part of the present study are presented. As mentioned earlier, flows through stenotic geometries were used to validate our numerical codes, both for steady and pulsatile flows. This is followed by further tests performed on aneurysmal geometries, as part of the present work, where the effect of temporal and spatial resolution on base flows and stability calculations are analysed.

2.5.1   Stenotic flows

2.5.1.1   Steady flows

The results presented in this section are carried out with *Model A* using the boundary conditions mentioned for steady flows earlier. For this problem formulation Griffith *et al.* (2008) have shown that the critical Reynolds number for instability is $Re_c = 2350$. The base flow characteristics at a Reynolds number 2000 is shown in figure 2.6. The spatial distribution of the axial velocity contours along with representative streamlines are shown in figure 2.6(a) and the azimuthal vorticity component is shown in figure 2.6(b). As described in Griffith *et al.* (2008), the flow can be characterized as a confined jet emanating from the constriction, which expands downstream of the stenosis. The recirculation zone is apparent, seen from the separating streamline. As the Reynolds number is increased, the length of the recirculation zone downstream of the stenosis increases. As a result, long outlet lengths are required for carrying out calculations on stenotic flows to remove any effect of the outlet.

We now turn our attention towards stability calculations. Though the outlet length needs to be varied significantly with varying stenosis degree, we keep the outlet length fixed at a value of $30D$ as sufficiently precise results were obtained using them. This is summarized in table 2.2 where L_0 denotes the length of the vessel outlet in units of vessel diameter. The growth rate of the leading eigenvalue obtained by our calculations is denoted by ω_{1i}, whereas the value found in Griffith *et al.* (2008) is denoted as $\omega_{1i,g}$.
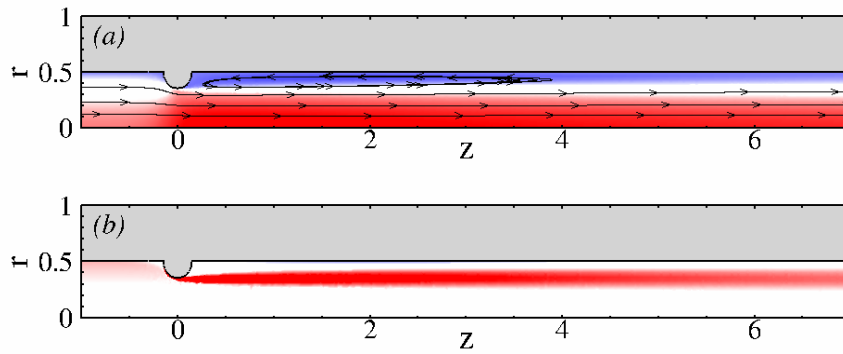
Figure 2.6: Base flow characteristics. (a) Axial velocity contours along with representative streamlines. (b) Azimuthal vorticity component. Parameter settings: $b = 0.50$, $Re = 2000$, *Model A*.

L_o	b	Re	m	ω_{1i}	$\omega_{1i,g}$
30	0.50	2000	2	-0.014780	-0.014783
30	0.50	2350	2	2.5731e-04	0.00000
30	0.75	770	1	-1.4151e-04	0.00000

Table 2.2: Results of the stability calculations for a steady flow through a stenosis. $\omega_{1i,g}$ refers to the value presented in Griffith *et al.* (2008).
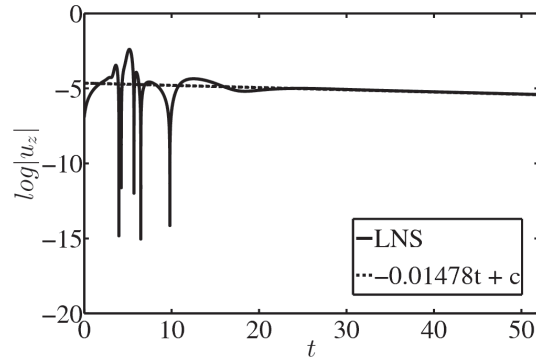
Figure 2.7: Time trace of the axial velocity component at a point downstream of the stenosis. Parameter settings: $b = 0.50$, $Re = 2000$, *Model A*.
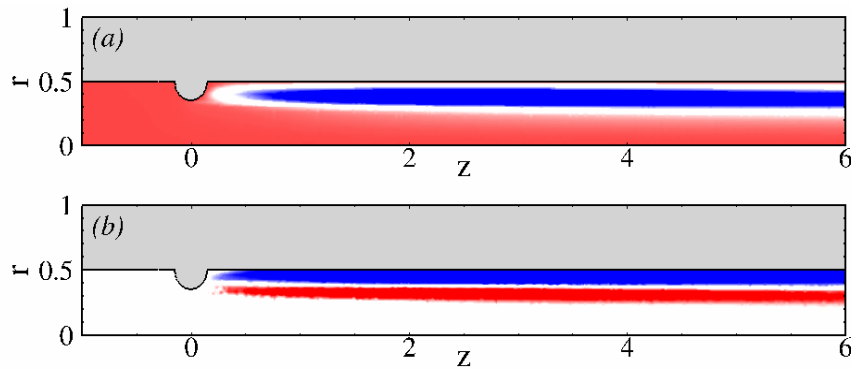
Figure 2.8: Leading global mode characteristics. (a) Axial velocity contours. (b) Azimuthal vorticity component. Parameter settings: $b = 0.50$, $Re = 2000$, $m = 2$, *Model A*.

The time trace of the perturbation at a point in the domain gives us information regarding the stability of the flow, similar to the kinetic energy norm defined in the previous section. This is demonstrated in figure 2.7. The growth (in this case decay) of the perturbation, ω_{1i}, is given by the slope.

Figure 2.8 depicts the structure of the leading unstable mode corresponding to $b = 0.50$, $Re = 2000$, $m = 2$ visualized by axial velocity and azimuthal vorticity components. The perturbation flow structures are in good agreement with those presented in Griffith *et al.* (2008).

2.5.1.2 Pulsatile flows

<u>*Model A*</u>

We start by presenting the results of our validation tests obtained using *Model A*. The geometry and the inlet boundary conditions are described in the preceding sections. Figure 2.9 shows the azimuthal vorticity contours of the pulsatile flow fields for a stenosis degree
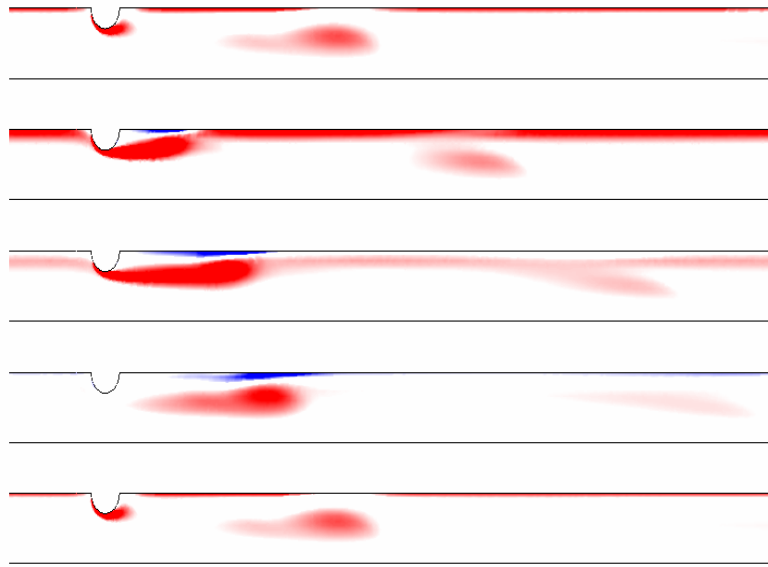
Figure 2.9: Contours of the azimuthal vorticity of the flow through different stages of the pulse, starting with $t = 0.0T$ with increments of $0.25T$ in each subsequent frame from top to bottom. Parameter settings: $b = 0.50$, $A = 0.75$, $T = 2.5$, $Re = 300$.

$b = 0.5$. The strong flow acceleration through the stenosis causes a flow separation to occur, with a separating shear layer emanating from the blockage walls. The shear layer rolls up, forming a vortex ring which propagates downstream and leaves a trail of positive vorticity in its wake.

One can further observe that the extent to which the vortex emanating from the blocakge walls convects downstream of the stenosis, depends strongly on the stenosis degree (see figure 2.9). This indicates that the pulsatile flow through a stenosis is more dependent on the outlet length. Also, for large stenosis degrees, a higher spatial resolution is required to get accurate flow fields, as large velocities are involved. As the main purpose of our work was to validate our stability solver for aneurysms, special efforts are not taken to obtain very highly resolved flow fields in stenotic geometries.

Table 2.3 shows the values of the Floquet multipliers obtained by our calculations $(|\mu|)$ in comparison with the values presented in Griffith (2007)$(|\mu|_g)$. To be noted is that, for the preliminary calculations, we have fixed the outlet length to $30D$ and subsequently chosen the same values as used in the calculations by Griffith (2007). The Floquet multiplier converges to the value cited by Griffith (2007) with increasing outlet length. But the meshes used in the present study are not refined to a high degree, as would be required for these constriction ratios. For the flow through aneurysms, the outlet length and mesh refinement play a weaker role compared to the flow through a stenosis. So, further tests are not carried out as a satisfactory agreement was obtained for small stenosis degrees, with the differences being less than 1%. Discrepancies in the results may be due to relatively coarser meshes used in our simulations.

L_o	b	A	m	$|\mu|$	$|\mu|_g$
30	0.50	1.25	1	1.0648	–
40	0.50	1.25	1	1.1741	1.1708
30	0.60	1.00	1	1.3495	–
50	0.60	1.00	1	1.3757	1.3761

Table 2.3: Results of the stability calculations for a steady flow through a stenosis. $|\mu|_g$ refers to the value obtained in Griffith (2007).
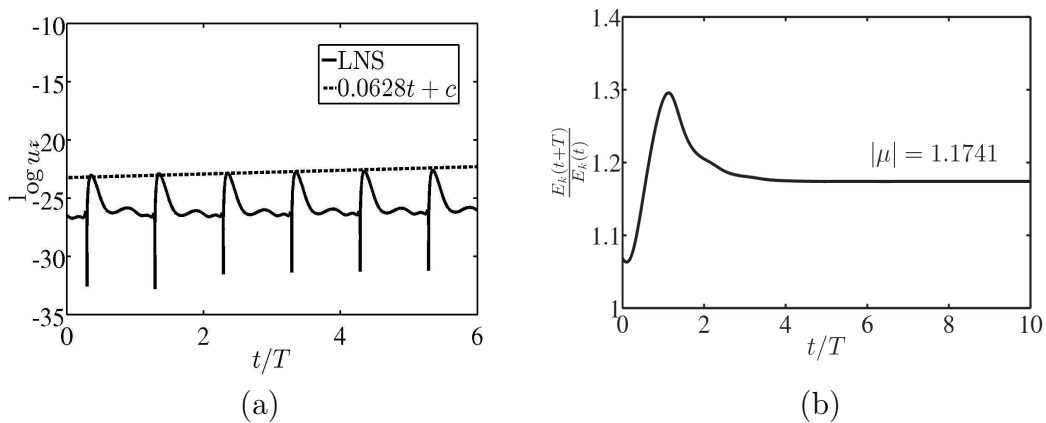

(a)   (b)

Figure 2.10: (a) Time trace of the axial velocity component at a point downstream of the stenosis. (b) Floquet multiplier $|\mu|$ converging to a value of $\exp \sigma T$. Parameter settings: $b = 0.50$, $A = 1.25$, $T = 2.5$, $Re = 300$, $m = 1$.

It is reported in Griffith *et al.* (2009) that, for the cases considered in table 2.3, the critical modes were found to be of period-doubling nature. Such subharmonic modes can be detected by the investigation of the perturbation field; the sign of a period-doubling bifurcation will alternate from one base flow period to the next. Figure 2.10 shows the time trace of the axial velocity component at a point in the domain, downstream of the stenosis, and also the absolute value of the Floquet multiplier calculated using the ratio of amplitudes of the kinetic energy between successive time periods. Figure 2.12 shows the axial component of the base flow field and of the leading global mode at $t = 0.0T$.

Model B

The geometry and the inlet boundary conditions are described in detail in the preceding sections. Figure 2.14 shows the azimuthal component of the vorticity of the basic pulsatile flow at different stages of the pulse cycle. Once again, we can observe that a vorticity ring is generated at the stenosis, due to the strong axial spatial gradient in velocity. The vortex ring is found to propagate down the pipe for very long distances. The principal difference between *Model A* and *Model B* is that in the former the length of the stenosis is shorter

(a)   (b)
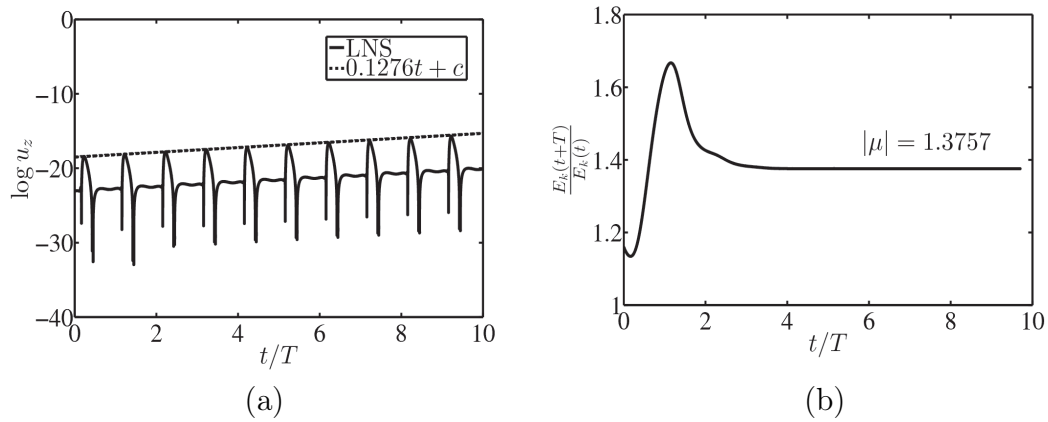
Figure 2.11: (a) Time trace of the axial velocity component at a point downstream of the stenosis. (b) Floquet multiplier $|\mu|$ converging to a value of $\exp \sigma T$. Parameter settings: $b = 0.60$, $A = 1.0$, $T = 2.5$, $Re = 300$, $m = 1$.
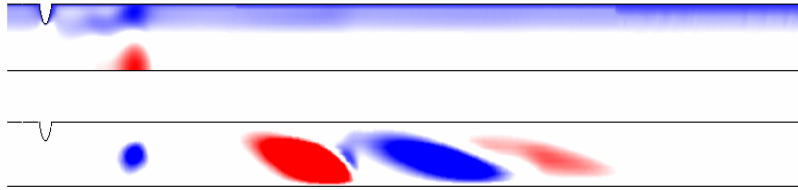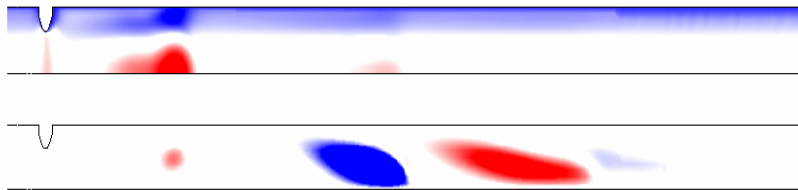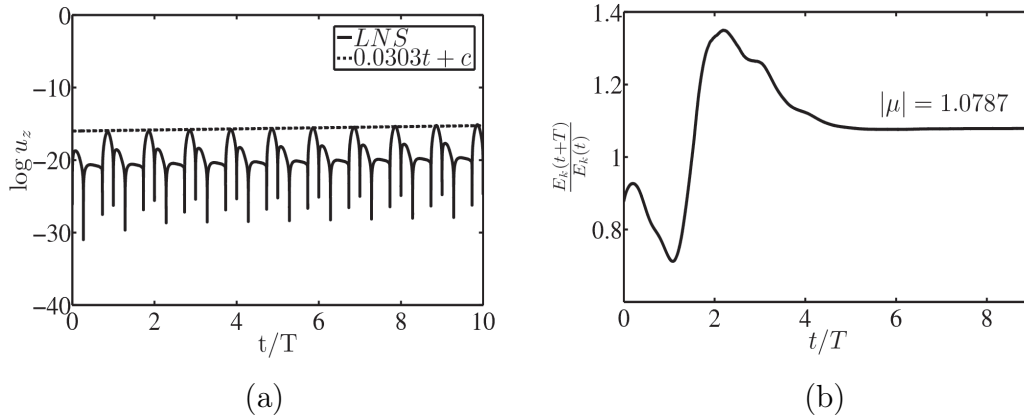

Figure 2.12: Axial velocity contours of the base flow (top) and axial velocity component of the leading critical mode (down). Parameter settings: $b = 0.50$, $A = 1.25$, $T = 2.5$, $Re = 300$, $m = 1$.
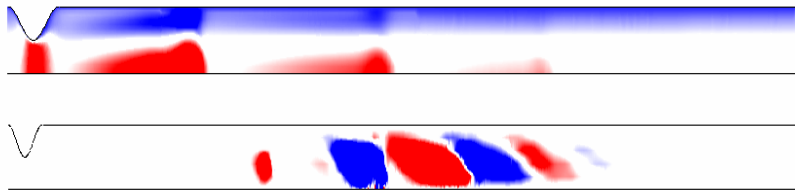

Figure 2.13: Axial velocity contours of the base flow (top) and axial velocity component of the leading critical mode (down). Parameter settings: $b = 0.60$, $A = 1.0$, $T = 2.5$, $Re = 300$, $m = 1$.
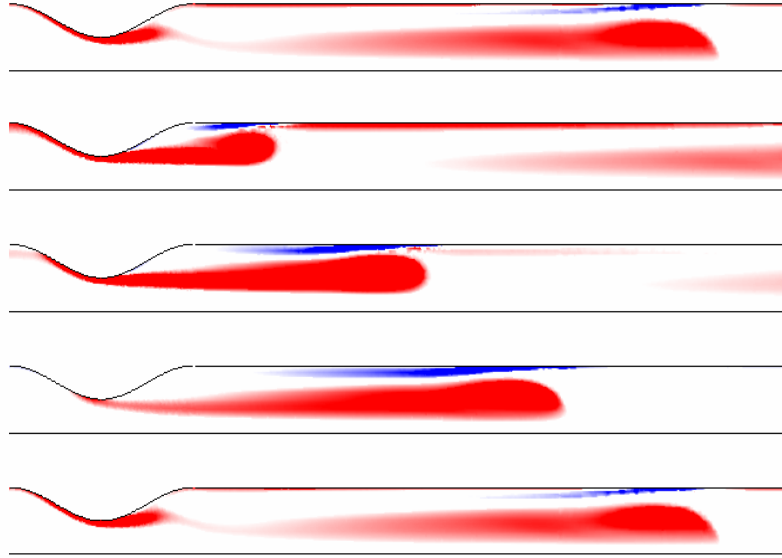
Figure 2.14: Contours of the azimuthal vorticity of the flow through different stages of the pulse, starting with $t = 0.0T$ with increments of $0.25T$ in each subsequent frame (top to bottom). Parameter settings: $A = 0.75$, $T = 2.5$, $Re = 400$.

L_o	A	m	$|\mu|$	$|\mu|_s$
30	0.75	1	1.1312	–
45	0.75	1	1.0787	1.073

Table 2.4: Results of the stability calculations for a pulsatile flow through a stenosis. $|\mu|_s$ refers to the value obtained in Sherwin & Blackburn (2005).

resulting in a severer disruption of the flow, whereas in the latter, the geometry is much smoother, resulting in the propagation of the vortex ring for longer distances.

Table 2.4 shows the Floquet multipliers computed using our calculations ($|\mu|$) and those that are presented in Sherwin & Blackburn (2005) ($|\mu|_s$). They have used an outlet length, L_o, of $45D$. We can see that with the increase in value of the outlet length, our Floquet multiplier converges to the value found in Sherwin & Blackburn (2005) showing that significant outlet lengths are necessary for stenotic flows. This is more evident from figure 2.16 where the axial component of the perturbation has not decayed at the outlet.

2.5.2 Aneurysmal flows

We now turn our attention to the flow through model abdominal aortic aneurysms (AAAs). The geometries and the boundary conditions are already described in detail in the preceding sections. Here, we present the tests that were carried out to check for spatial and temporal convergence, for both steady and pulsatile flows through AAAs.

(a)   (b)

Figure 2.15: (a) Time trace of the axial velocity component at a point downstream of the stenosis. (b) Floquet multiplier $|\mu|$ converging to a value of $\exp \sigma T$. Parameter settings: $A = 0.75$, $T = 2.5$, $Re = 400$, $m = 1$.

Figure 2.16: Axial velocity contours of the base flow (top) and axial velocity component of the leading critical mode (down). Parameter settings: $A = 0.75$, $T = 2.5$, $Re = 400$, $m = 1$.

Mesh	Ω	N_2	N_1
M_b	$(-10, 10)$	183061	46516
M_{b1}	$(-10, 10)$	152449	38788
M_{b2}	$(-10, 10)$	66398	17050
M_{b3}	$(-10, 10)$	17058	4490
M_{bs}	$(-5, 5)$	136049	34613
M_{bl}	$(-20, 20)$	229558	58515

Table 2.5: Meshes used to validate the computation of the base flow for $H = 0.5$, $W = 0.5$.

2.5.2.1 Steady flows

In this section we outline our convergence tests for both the base flow and stability calculations to establish that the numerical results we present are well resolved. There are two central issues in checking convergence of the base flow calculations: the external dimensions of the domain considered in our study and the degree of internal refinement. The check for the external dimensions of the domain is of pivotal importance to make sure that the results are not affected by the outlet conditions as a slight modification of the base flow could have an impact on the eigenvalue computations. This is done by carrying out the calculations on different domains with different sizes. In this section we present the validation tests carried out on three different sized domains though we have performed a large number of tests to establish our results. Carrying out the study for the internal refinement is a bit more challenging as our study involves large values of Reynolds numbers.

The size of the computational domain is characterized by Ω, which gives the axial extension measured in vessel diameters with respect to the origin. The number of nodes associated with the P2 and P1 elements of a mesh are denoted N_2 and N_1, respectively. The subscript b indicates that the mesh is associated with the computation of a base flow, the subscripts s and l indicate that the computational domain is smaller or larger than the 'standard domain' $(-10, 10)$.

We use the wall shear stress (WSS) distributions to check the convergence of the base flow fields and as a sensitive measure of the overall grid resolution. The WSS distribution follows from an evaluation of the expression

$$\text{WSS} = 2 \left(\frac{\partial U_r}{\partial r} - \frac{\partial U_z}{\partial z} \right) \frac{R'(z)}{1 + R'(z)^2} - \left(\frac{\partial U_r}{\partial z} + \frac{\partial U_z}{\partial r} \right) \left[\frac{1 - R'(z)^2}{1 + R'(z)^2} \right] \tag{2.51}$$

at the vessel wall $r = R(z)$, and $R'(z)$ stands for the first derivative. A negative value of the wall shear stress corresponds to reversed flow. Though this quantity is measured only along the walls, the distribution of WSS is significantly affected by the changes in the flow fields in the core part of the flow through momentum transport.

Figure 2.17 presents the results of the computation of the wall shear stress distribution in a vessel inflation using the meshes listed in table 2.5. This distribution is normalized by the value of the wall shear stress exerted by the associated Hagen–Poiseuille
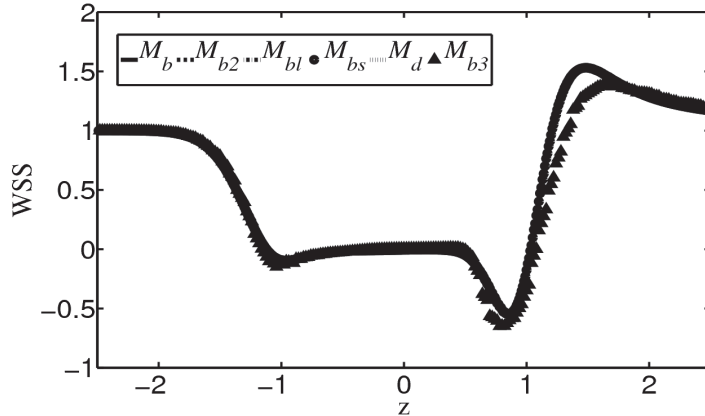
Figure 2.17: The distribution of WSS along the upper wall computed using different meshes mentioned in table 2.5. Parameter settings: $H = 0.5$, $Re = 2500$, $W = 0.5$.

Mesh	Ω	N_2	N_1	ω_{1i}	ω_{1r}
M_{s1}	$(-10, 10)$	124566	31742	-0.0301923	0.0310782
M_{s2}	$(-10, 10)$	66398	17050	-0.0301750	0.0311178
M_{s3}	$(-10, 10)$	17058	4490	-0.0293571	0.0304471
M_{s0}	$(-10, 10)$	152449	38788	-0.0302183	0.0310903
M_{bs}	$(-5, 5)$	136049	34613	-0.0302199	0.0310871

Table 2.6: Size of the computational domain, as characterized by Ω, and number of nodes N_1 and N_2, used in convergence tests of the stability analysis; ω_{1i} and ω_{1r} are the computed imaginary and real parts of the eigenfrequency of the wavenumber $m = 1$. Parameter settings: $H = 0.5$, $W = 0.5$, $Re = 2500$.

flow. The Reynolds number is 2500. It is observed that where the vessel is inflated, corresponding roughly to the range $-1 < z < 1$, the wall shear stress is reduced significantly; in fact, it becomes vanishingly small. Near the downstream end of the inflation, however, a sudden change occurs from a negative relative value of -0.5 to a positive relative value of 1.5. With the exception of the computations done with the rather coarse mesh M_{b3}, all other computations match perfectly to the computations carried out on the fine mesh M_{bl}.

We now turn our attention to the validation of our stability calculations. The tests carried out using $W = 0.5$ are presented. Table 2.6 shows some of the different meshes used for validating our stability calculations.

The results of tests carried out for the values $W = 0.5$, $H = 0.5$ and $Re = 2500$ are presented. The meshes used in this case are specified in table 2.6, which also presents the computed values of the real and imaginary parts of ω_1, the eigenfrequency with the largest imaginary part associated with wavenumber $m = 1$. With the exception of the coarse mesh M_{s3}, all meshes yield values for the eigenfrequencies which agree up to the fourth digit.

Mesh	Ω	N_2	N_1	ω_{1i}	ω_{1r}
M_{s1}	(-10, 10)	124566	31742	0.000333584	0.0409547
M_{s2}	(-10, 10)	66398	17050	0.000358289	0.0412757
M_{s3}	(-10, 10)	17058	4490	-0.001396340	0.0127780
M_{sl}	(-20, 20)	178112	31742	0.000355735	0.0411971

Table 2.7: Results of the convergence test on the stability calculations. Parameter settings: $W = 0.5$, $H = 0.5$, $Re = 5000$, $m = 4$.

Mesh	Ω	N_2	N_1	ω_{1i}	ω_{1r}
M_{s1}	(-10, 10)	122346	31187	0.00119180	0.0138370
M_{s2}	(-10, 10)	66310	17028	0.00110433	0.0138551

Table 2.8: Results of the convergence test on the stability calculations. Parameter settings: $W = 0.5$, $H = 0.8$, $Re = 5000$, $m = 3$.

This finding permits us to use mesh M_{s2} for the stability computations.

Table 2.7 shows the convergence results of our stability calculations for $H = 0.5$ at a higher Re for $m = 4$. We can see that the values corresponding to the coarse mesh M_{s3} differ considerably from the rest. But a good agreement can be seen between the values corresponding to M_{s1} and M_{s2}, though mesh M_{s2} is considerably coarser than mesh M_{s1} but sufficiently fine to obtain highly resolved flow fields. Also calculations were carried out with a bigger domain corresponding to mesh M_{sl} and the eigenvalues obtained are in good agreement with the values obtained using smaller domains as only the fifth digit varies. This again stengthens our argument to use the mesh denoted by M_{s2} to be used for our stability computations. Some further tests are shown in table 2.8 cementing the argument to use mesh M_{s2} for our stability calculations.

For different values of bulge widths, W, different sized domains were used for carrying out the computations. Table 2.9 shows the domain sizes for different widths that were used to carry out all the computations presented in this study.

W	Ω	N_2	N_1
0.25	(-10, 10)	64626	16607
0.50	(-10, 10)	66398	17050
1.00	(-10, 10)	68570	17593
2.00	(-15, 15)	57082	14721

Table 2.9: The meshes used for the base flow calculations for $H = 0.5$.

2.5.2.2 Pulsatile flows

We have already validated our stability solver using flows through stenotic geometries (see 2.5.1.2). We now turn our attention to pulsatile flows through AAAs. It is to be reminded that flows through AAAs offer different challenges to the ones posed by flows through stenotic geometries. In the former, as we have seen for the case of steady flows, the base flow vorticity and perturbations are localized within the bulge, whereas in the latter, vortex ring structures generated at the constriction of the stenoes propagate far downstream. Hence, the dependence on outlet lengths and on spatial resolutions are very different for the two flows.

Base flow fields

Before we move on to pulsatile flows through AAA geometries, we carried out some pre-liminary checks using a pulsatile through a circular pipe flow, without any dilatation, as it presents us with an opportunity to compare our results with analytical solutions. The computations were carried out on domains that are $20D$ units in length. At the inlet, the analytical Womersley solution is imposed using a single Fourier component and the flow is integrated in time for about 10 cycles. The error E_{pipe} is calculated as an integral over the domain given by

$$E_{pipe}(r, z, t) = \sqrt{\int_{\Omega} \left((U_{z,exact} - U_{z,DNS})^2 + U_{r,DNS}^2 \right)}, \qquad (2.52)$$

where $U_{z,exact}$ refers to the exact analytical solution obtained from the equation (1.13), $U_{z,DNS}$ and $U_{r,DNS}$ stand for the axial and radial velocity profiles obtained from our DNS solver. A second-order temporal scheme is employed to time-mach our DNS solver. The variation of error with the time step size is shown in figure 2.18. The mesh density p denotes the number of vertices per unit length. Figure 2.18(a) shows the order of magnitude of the error for various values of dt that saturates with the decrease in dt and becomes independent of dt. The second-order accuracy of the temporal scheme is demonstrated in figure 2.18(b). A time-step size of $dt \leq 0.0005$ gives us flow fields having an error of the order of 10^{-9} which was then fixed for subsequent calculations.

Having established that our base flow solver works for the case of pulsatile flows through circular pipes, using realistic flow rate waveforms at the inlet, we now discuss the tests conducted in the presence of an AAA. The base flows for the case of pulsatile flows through AAAs were time marched for a sufficient number of cycles so that the mean flow had time to convect through the entire computational domain. For the parameter conditions explored in the present study, the flow is integrated in time for 10 cycles to attain periodicity. Time traces of the velocities at various points within the domain (corresponding to $z/d = -1, 0, 1, 5, 15$ and $r/d = 0.25$) were then checked at a specific phase in the cycle to confirm that the flows have converged to a time-periodic state. An inlet length of $10D$ units and an outlet length of $20D$ units is considered to carry out the simulations. At the start of the calculation, at $t = 0$, the analytical solution of Womersley given by equation (1.2.2) is applied within the domain corresponding to a circular pipe. A zero velocity field is imposed within the bulge region. The waveform corresponding to the rest state, $Q1$ at $Re = 264$ and $Wo = 12$ was chosen. The different domains considered in the study are shown in table 2.10.
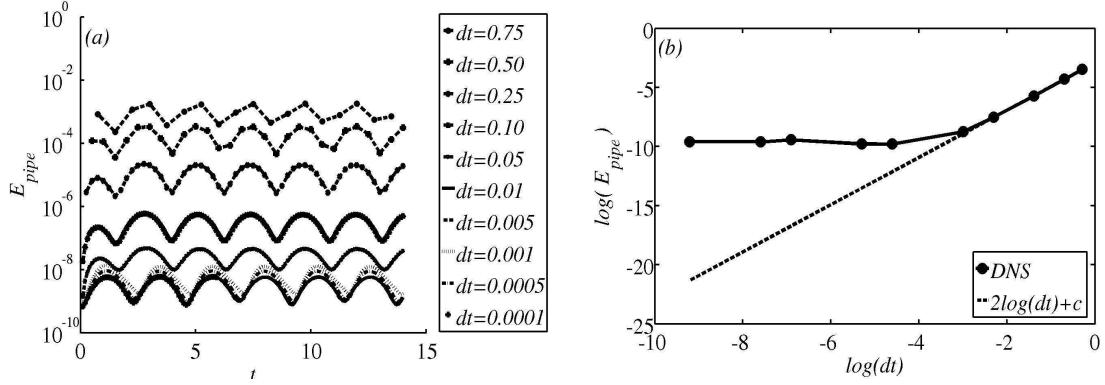
Figure 2.18: (a) Plot of error E_{pipe} for different time-steps dt. Parameter settings: $p = 30$. (b) Plot of log(dt) vs log(E) showing a second-order relation. Parameter settings: $p = 30$.

Mesh	Ω	N_2	N_1	N
M_{b1}	(-10, 20)	7152	1941	16245
M_{b2}	(-10, 20)	16752	4417	37921
M_{b3}	(-10, 20)	26858	7020	60736
M_{b4}	(-10, 20)	38902	10081	87885
M_{b5}	(-10, 20)	43254	11195	97703
M_{b6}	(-10, 20)	60652	15621	136925
M_{b7}	(-10, 20)	105582	27006	238170
M_{b8}	(-10, 20)	32006	8332	72344
M_{b9}	(-10, 20)	32006	8332	72344
M_{b10}	(-10, 20)	32006	8332	72344

Table 2.10: The meshes used for pulsatile base flow calculations at $H = 0.5$, $W = 0.5$.
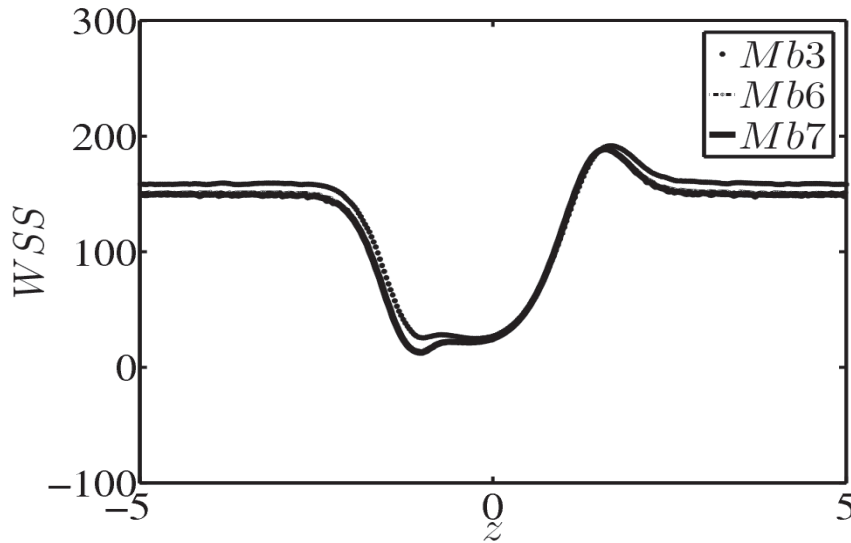
Figure 2.19: The WSS at $t = 0.2T$ computed using 3 representative meshes. Mesh $Mb3$ represents a coarse mesh, whereas $Mb6$ and $Mb7$ represent relatively finer meshes. The convergence of the WSS with increasing mesh refinement can be observed. Parameter settings: $H = 0.5$, $W = 0.5$, $Re = 264$, $Wo = 12$.

The WSS distributions were used to check for spatial resolution of the base flow fields. Figure 2.19 shows the spatial distribution of WSS obtained using three different meshes. Mesh $Mb3$ corresponds to a coarse mesh, whereas $Mb6$ and $Mb7$ represent finer meshes. For the coarse mesh, the WSS distribution differs significantly from those obtained using finer meshes. We have used mesh $Mb6$ for carrying out further tests on our stability solver, which will be discussed subsequently

Stability analysis

We have already seen that our stability solver was able to reproduce the results presented in the literature for the case of flows through stenoses. Some of the tests carried out using a pulsatile waveform for the case of flow through an AAA are presented. Most of the tests were carried out using the rest waveform, $Q1$ (see section 1.2.3), using the geometrical configuration corresponding to a typical AAA ($W = 0.5$, $H = 0.5$). We begin by checking for the spatial resolution of meshes needed for convergence of Floquet multipliers. Tables 2.11 show the values of $|\mu|$ obtained using different meshes at various parameter conditions. As seen earlier for the case of base flows, mesh corresponding to $Mb6$ provides us with a good approximation of the Floquet multiplier.

Using mesh $Mb6$, we check for the temporal resolution needed for the convergence of the Floquet multiplier. Table 2.12 shows the convergence of the Floquet multiplier with time step Δt. For most of our calculations, we have used a time step that corresponds to $T/10000$ to obtain accurate reuslts.

Mesh	$|\mu|$
M_{b3}	0.923
M_{b6}	1.199
M_{b7}	1.195

(a)

Mesh	$|\mu|$
M_{b3}	1.452
M_{b6}	1.184
M_{b7}	1.190

(b)

Mesh	$|\mu|$
M_{b3}	2.225
M_{b6}	1.677
M_{b7}	1.683

(c)

Table 2.11: The convergence of the Floquet multiplier. (a) Parameter settings: $Q1$, $Re = 264$, $Wo = 12$, $W = 0.5$, $H = 0.5$, $m = 1$, (b) $Q1$, $Re = 300$, $Wo = 15$, $W = 0.5$, $H = 0.5$, $m = 3$, (c) $Q1$, $Re = 300$, $Wo = 10$, $W = 0.5$, $H = 0.5$, $m = 2$.

Δt	$|\mu|$
0.0005 ($T/3500$)	0.6240
3.5e-04 ($T/5000$)	0.6521
1.75e-04 ($T/10000$)	0.6654

Table 2.12: The convergence of the Floquet multiplier with Δt using mesh $Mb6$. Parameter settings: $Q1$, $Re = 250$, $Wo = 15$, $W = 0.5$, $H = 0.5$, $m = 1$.

Having established the validity of our flow solver, we now move on to the investigation of the flow dynamics at various parameter conditions. We begin by a discussion on steady flows through AAAs (chapter 3), followed by a discussion on pulsatile base flow characteristics at various flow conditions (chapter 4) and subsequently an investigation of stability characteristics (chapter 5).

Steady Flows Through Model AAAs

3.1   Introduction

In the present chapter we discuss the base flow characteristics and the results of our stability calculations obtained for steady flows through model abdominal aortic aneurysms (AAAs). Specifically, the changes in flow characteristics during the progressive enlargement of an AAA is investigated.

Though the flows encountered in AAAs are highly pulsatile in nature, as a first step it is worthwhile to investigate the flow characteristics encountered in these geometries subject to steady inflow conditions. This will help us in analysing the flow features without the additional complexity introduced by time-periodic inlet waveforms. As mentioned in chapter 1, several studies can be found in the literature aimed towards this objective (Schrader *et al.*, 1992, Budwig *et al.*, 1993, Peattie *et al.*, 1994, 1996, Asbury *et al.*, 1995, Bluestein *et al.*, 1996, Vorp *et al.*, 1998, Yu, 2000). However, no study that examines the stability of steady flows in model AAAs is to be found. Though Sheard & Blackburn (2010) carried out a global and transient stability analysis of a steady flow through a model AAA, information on the mode structures and the instability mechanisms inherent in these geometries presented by them are very limited. Moreover, they do not take into account the progressive enlargement of an AAA by varying the geometrical parameters, namely the bulge height H and the bulge width W. This is the contribution of the present chapter, where we discuss the changes in flow characteristics under varying geometrical parameters and examine the stability of these flows, providing information on the origin of the instability mechanisms. This would also help us in providing answers to another perennial question present in fluid mechanics: the deviation needed from a circular pipe for the flow to become unstable.

The aneurysm is modeled as an inflation of gaussian shape on a vessel of circular cross-section. The fluid is assumed to be Newtonian and the flow far upstream and downstream of the inflation is a Hagen–Poiseuille flow. The model aneurysm is characterized by a maximum height H and width W, made dimensionless by the upstream vessel diameter, and the steady flow is characterized by the Reynolds number of the upstream flow. The base flow through the model aneurysms is determined for non-dimensional heights and widths in the physiologically relevant ranges $0.1 \leq H \leq 1.0$ and $0.25 \leq W \leq 2.0$, and Reynolds numbers up to 7000, which corresponds to peak values recorded during pulsatile flows under physiological conditions. The global linear stability of the base flows is analysed by determining the eigenfrequencies of a modal representation of small-amplitude

perturbations. The nature of instability mechanisms are investigated using the energy transfer between the base flow and the perturbations.

The chapter is organized as follows. We begin by discussing the base flow characteristics observed in a typical AAA and then move on to the effect of geometrical parameters. Following this is a discussion of the stability characteristics of these base flows, concluded by a discussion of the various instability mechanisms.

3.2 Base flow characteristics

3.2.1 Effect of dilatation parameter

3.2.1.1 Base flow fields

First, the flow characteristics are described by considering a typical value of the bulge width $W = 0.5$. The base flow fields at three different bulge heights ($H = 0.3$, $H = 0.5$, $H = 0.8$) are visualized in figure 3.1 at a Reynolds number of 5500 using streamlines and azimuthal component of vorticity. It is to be noted that the typical Reynolds numbers (peak) in the abdominal region of the aorta can vary from 600 at rest to up to 6000 under excercise conditions (Ku, 1997). The base flow consists of a jet of fluid passing through the aneurysm and a slowly recirculating vortex in the outer annulus. The radial velocity component is at least two orders of magnitude lower than the axial component everywhere in the domain except at the downstream end of the bulge where it is around one order of magnitude smaller. This is the region where the vorticity increases. For higher bulge heights the appearance of a secondary recirculation zone is seen which is also observed with increase in Reynolds number at a fixed bulge height. This secondary recirculating zone is observed to move towards the upstream end of the bulge, with increase in Reynolds number, thereby pushing the primary recirculation towards the downstream end. This is further shown in figure 3.2 where the base flow vorticity along with representative streamlines are shown for two different bulge heights at three different Reynolds numbers.

Figure 3.3 shows a map indicating the presence of the number of recirculation zones as a function of the bulge height and the Reynolds number. It is seen that as the bulge height is gradually increased, two recirculation zones are present. The primary recirculation zone with a positive vorticity migrates towards the distal end of the bulge with increase in Reynolds numbers and pushes the secondary recirculation zone with a negative vorticity towards the proximal end of the bulge. This observation is consistent with those provided in the literature (Bluestein *et al.*, 1996) who showed that the recirculation zones formed inside the aneurysm create conditions that promote thrombus formation. As the aneurysm develops, its wall becomes lined with a thrombus: an aggregate of blood cells, platelets, blood protein and cellular debris, which has been considered as an attempt of the body to increase the wall thickness, thereby reducing the likelihood of rupture. It has been argued that the platelets approaching the recirculation zone get trapped in the recirculation zone that allow prolonged contact with the wall, promoting adhesion to the wall.

3.2.1.2 Wall shear stress distributions

The above flow features within the aneurysm impact the WSS distributions. The WSS is computed from our base flow fields using the expression given by equation (2.51). Figure
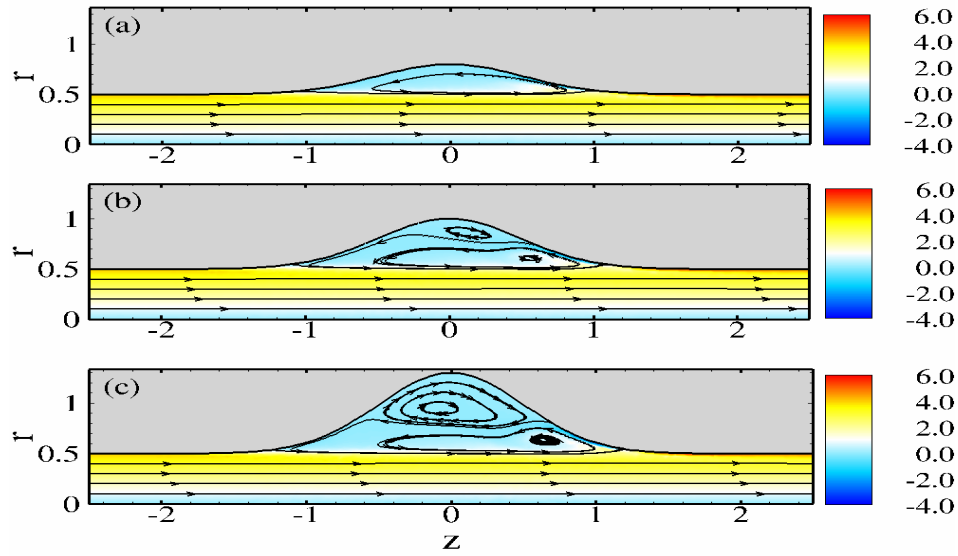
Figure 3.1: Base flow visualized by the vorticity and streamlines at $Re = 5500$ for $W = 0.5$. Parameter settings: (a) $H = 0.3$ (b) $H = 0.5$ (c) $H = 0.8$.
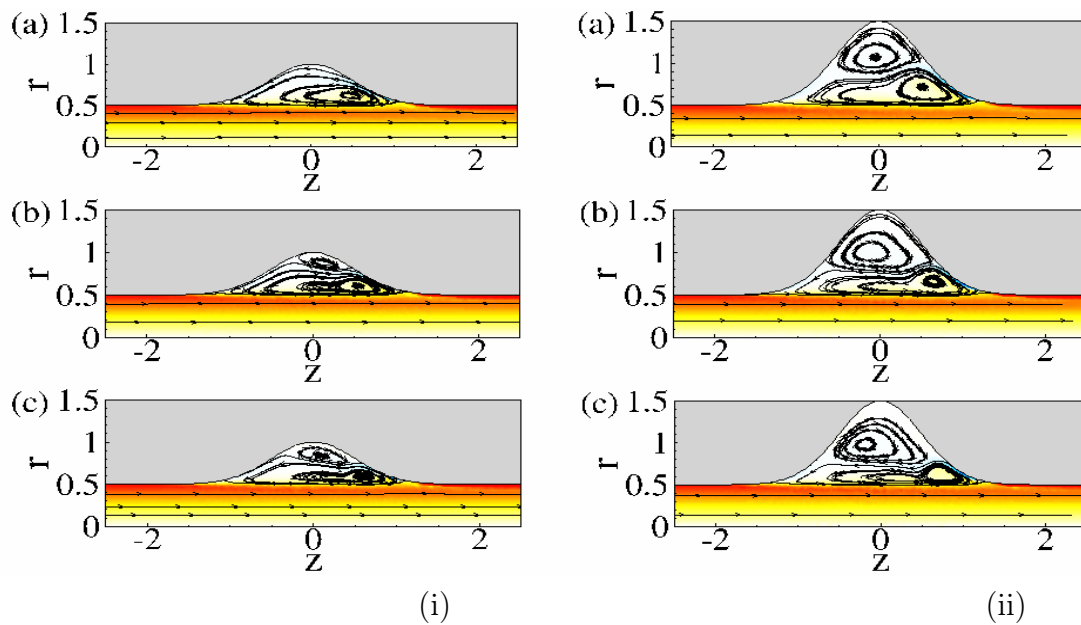

Figure 3.2: Base flow visualized by the vorticity and streamlines for $W = 0.5$ at three different Reynolds numbers. Parameter settings: (i) $H = 0.5$ (ii) $H = 1.0$. (a) $Re = 3000$ (b) $Re = 5000$ (c) $Re = 7000$.
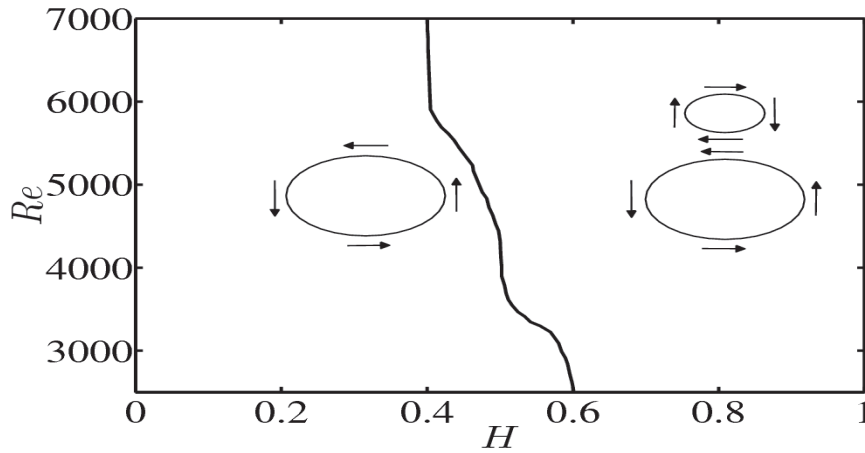
Figure 3.3: The number of recirculation zones as a function of bulge height and Reynolds number. Parameter settings: $W = 0.5$.

3.4 shows the WSS distributions at four different bulge heights as a function of the Reynolds number. The WSS values were normalized with the values present in a circular pipe. The variation in the WSS values with the Reynolds numbers is negligible and only significant differences can be seen at the distal end where WSS values reach a minimum. The WSS values within the bulge region are very low when compared with the value present in the straight sections upstream and downstream of the bulge. They attain a negative value reaching a minimum just upstream of the distal end. This is followed by a sharp gradient resulting in a positive value for the WSS thereby reaching a maximum near the distal end of the bulge. Also further downstream of the bulge, the WSS values slowly converge towards the value observed in a straight circular pipe. Also the changes in the WSS distributions as a function of H are more pronounced at lower values of bulge height.

Figure 3.5 shows the variation in the minima and the maxima of the WSS values as a function of the bulge height H for four different Reynolds numbers. We can see that the minima, given by figure 3.5(a) decrease with the increase in Reynolds number. Also there is a sharp change in the minimum value once H becomes greater than 0.25. This is due to the fact that for small bulge heights the minimum is attained at the upstream end of the bulge whereas at larger bulge heights it is attained at the downstream end. The absolute value of the minimum is an order of magnitude lower from the values in a circular pipe at larger bulge heights. From figure 3.5(b) we can see that the maximum increases with the increase in bulge height and is around 1.5 times greater than the values found in the upstream and downstream of the aneurysm. Such low values for the minimum and high values for the maxima of the WSS, at the downstream end of the bulge, can significantly affect the physiology of the arterial walls as they tend to pull the walls in opposite directions.

The endothelial cells which line the arterial walls are more receptive to changes in the WSS values than to flow rate. As a result, the WSS distributions form an important link between pathological propagation of the disease and hemodynamics. The presence of low WSS regions within the bulge are found to lessen the wall permeability. It is understood that these regions of the wall, with a low wall permeability are favored locations for atherosclerotic
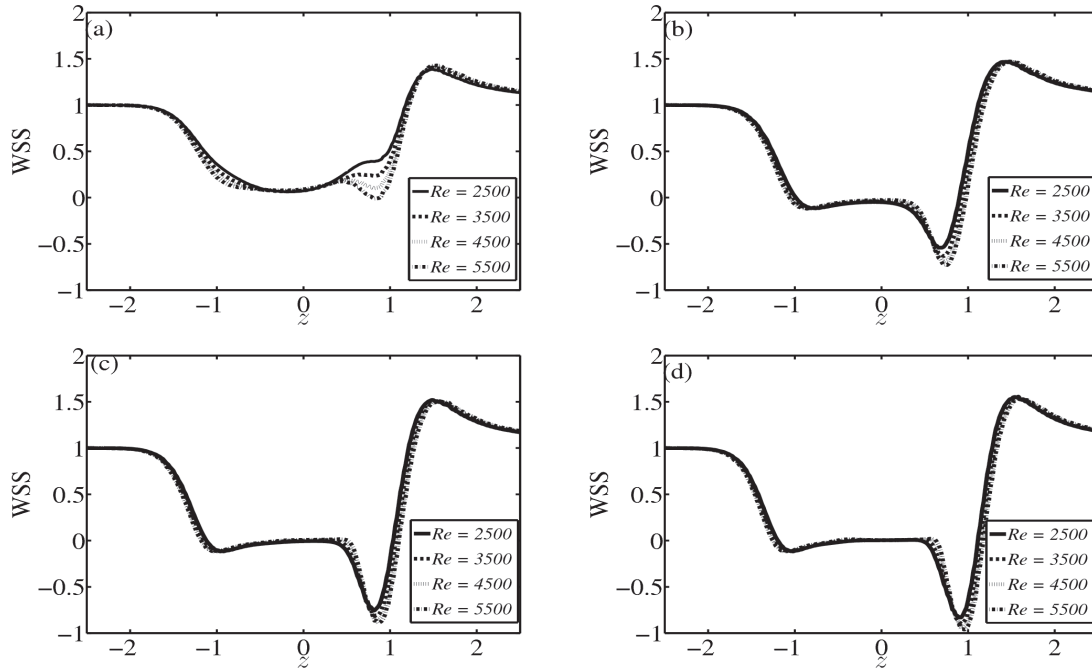
Figure 3.4: The wall shear stress distributions as a function of Reynolds number. (a) $H = 0.1$ (b) $H = 0.3$ (c) $H = 0.5$ (d) $H = 0.7$.
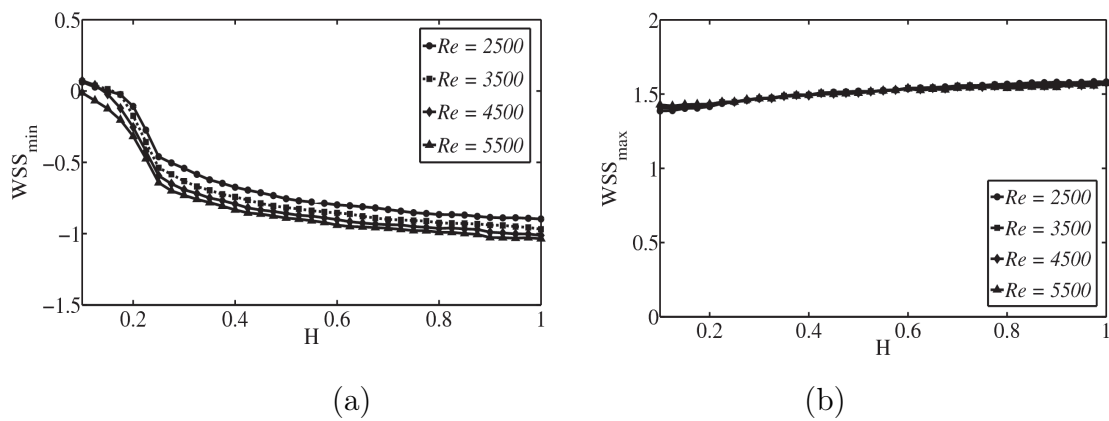
Figure 3.5: The minimum and maximum WSS values as a function of the bulge height H at different Reynolds numbers are shown in (a) and (b) respectively.

plaque deposits (Aird, 2007, Pedley, 1979, Ku, 1997). Also the presence of coexisting regions of low negative WSS and high positive WSS at the distal end of the bulge, tends to pull the walls apart thereby increasing the risk of rupture. The presence of such disturbed flow patterns may induce differential molecular responses in endothelial cells that result in preferential localization of atherosclerotic lesions (Chiu & Chien, 2011).

3.2.2 Effect of W on base flow characteristics

Streamlines and distributions of azimuthal vorticity of the steady axisymmetric base flows through inflated vessels are shown in figures 3.6 – 3.8 for different values of W. In these figures the values of the dimensionless width W and Reynolds number Re are: $W = 0.25$, $Re = 5500$ (figure 3.6); $W = 1.0$, $Re = 5500$ (figure 3.7); $W = 2.0$, $Re = 4000$ (figure 3.8). In each of these figures the dimensionless height H is: $H = 0.3$ in (a); $H = 0.5$ in (b); and $H = 0.8$ in (c). Note that, to bring out details, the horizontal scales in the figures have been chosen differently.

The flow through the model aneurysms is qualitatively similar for all parameter values such that H/W is relatively small: A jet-like core of diameter roughly that of the non-inflated vessel, surrounded by slowly recirculating fluid in the inflation. In the recirculation region the radial velocity is at least two orders of magnitude smaller than the axial velocity, except near the downstream end of the inflation, where it is about one order of magnitude smaller. The vorticity distribution in the core region is uniform with magnitude similar to that in the Hagen–Poiseuille flow far upstream and downstream. The vorticity distribution in the recirculation region is also approximately uniform, but of opposite sign and of smaller magnitude. A stagnation point is observed at the downstream end of the inflation. This flow structure has been observed by Budwig *et al.* (1993) and Bluestein *et al.* (1996) in their experiments and numerical calculations. That a secondary recirculation region, with weak vorticity of opposite sign to that in the primary recirculation zone, appears as the ratio H/W or the Reynolds number Re is increased has not been reported before. The centre of the primary recirculation zone is displaced towards the distal end of the inflation as H/W or Re is increased further, while the centre of the secondary recirculation zone is displaced towards the proximal end of the inflation.

The WSS for two different values of W are shown in figures 3.9 and 3.10. For a small value of $W = 0.25$, the WSS distribution hardly varies with Re and H, and are qualitatively similar to $W = 0.5$ (see figure 3.4). At a larger value of $W = 2.0$, the mimimum value of the WSS is found to be dependent on the Reynolds number, as can be seen from figure 3.10(a). However at larger bulge heights, the WSS variation is minimal as a function of the Reynolds number.

We now move on to the stability analyses of the base flows described above.

3.3 Stability analyses

3.3.1 Stability characteristics in a typical AAA

A typical eigenfrequency spectrum in the complex ω-plane is shown in figure 3.11. In this example $W = 0.5$, $H = 0.5$, $Re = 5500$, parameter values for which the basic flow is shown in figure 3.1(b). Figure 3.11(b) shows a close-up view of the eigenvalue spectrum. Two modes
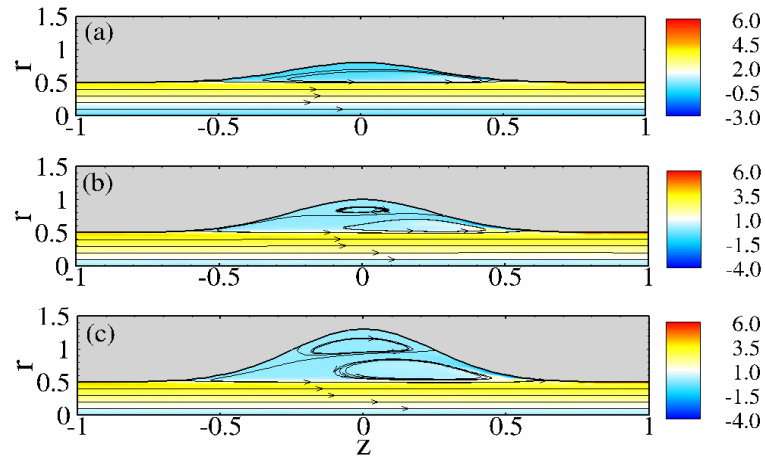
Figure 3.6: Base flow visualized by the vorticity and streamlines at $Re = 5500$ for $W = 0.25$. Parameter settings: (a) $H = 0.3$ (b) $H = 0.5$ (c) $H = 0.8$.
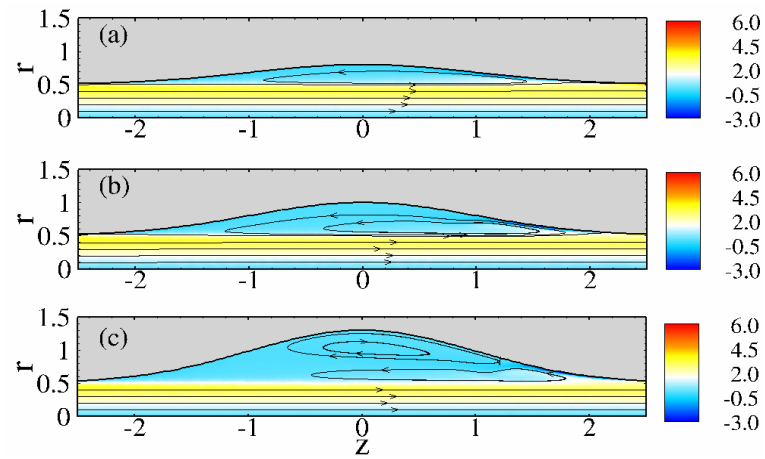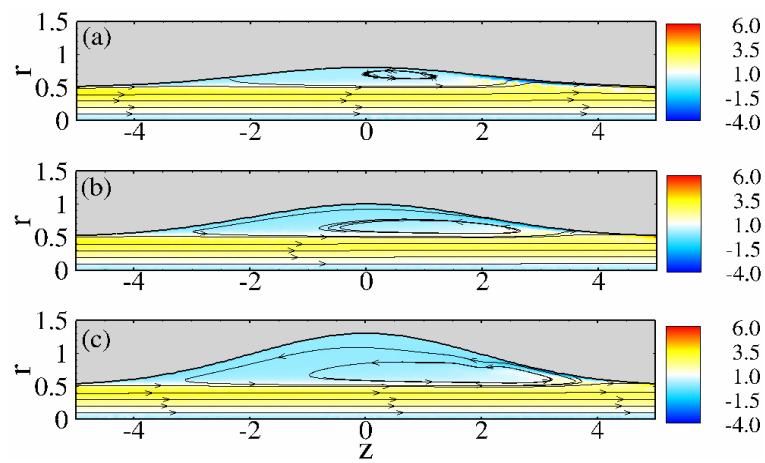

Figure 3.7: As in figure 3.6, but for $W = 1.0$.

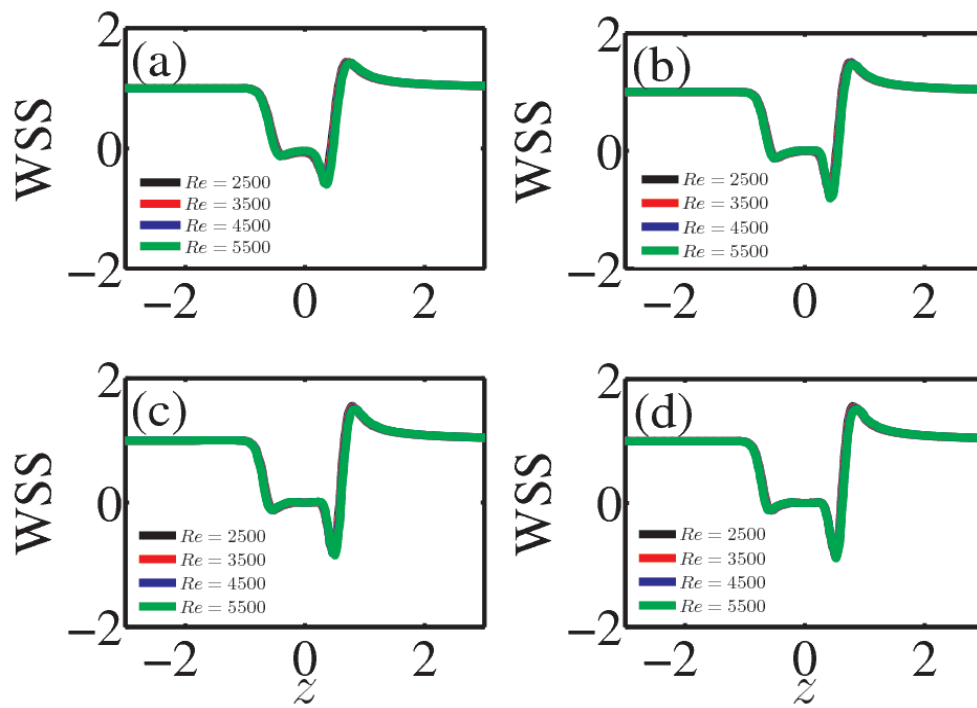Figure 3.8: As in figure 3.6, but for $Re = 4000$ and $W = 2.0$.

Figure 3.9: The wall shear stress distributions as a function of Reynolds number for $W = 0.25$. (a) $H = 0.2$ (b) $H = 0.4$ (c) $H = 0.6$ (d) $H = 0.8$.
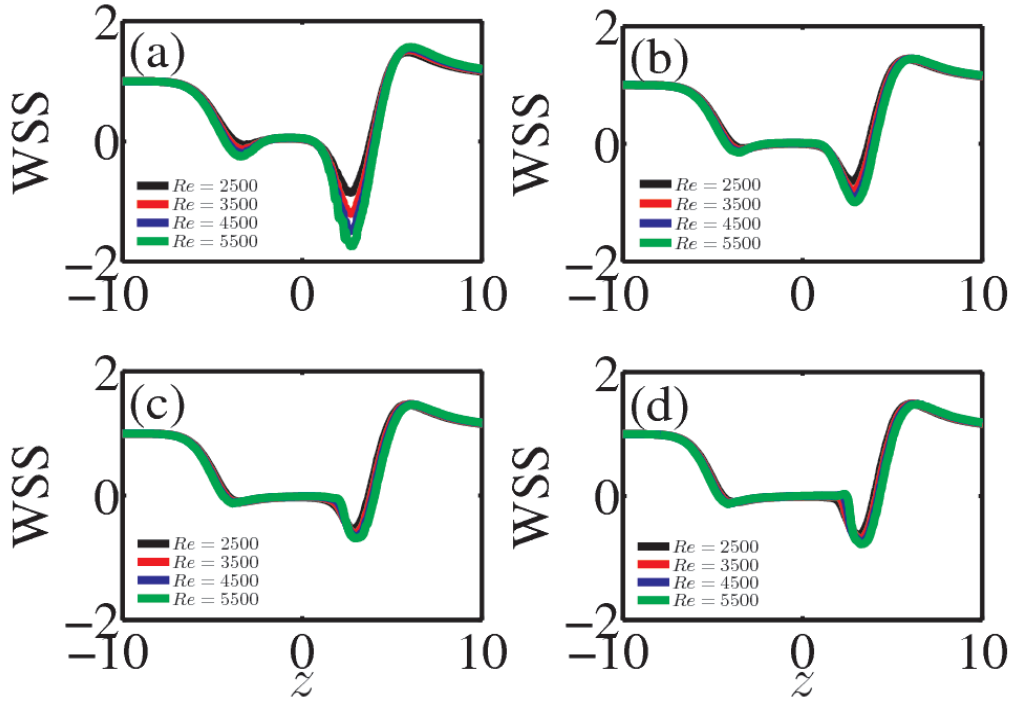
Figure 3.10: As in figure 3.9, but for $W = 2.0$.

with a positive temporal growth rate ω_i can be observed; they are associated with the azimuthal wavenumbers $m = 4$ and $m = 5$. The real parts ω_r of these eigenfrequencies are non-zero, so that the unstable modes represent three-dimensional oscillations. The spatial distribution of the unstable mode corresponding to the azimuthal wavenumber $m = 4$ is shown in figure 3.12. It can be observed that the modes are localized entirely within the bulge region. This also strengthens our argument that larger domain sizes are not needed for stability calculations.

With each azimuthal wavenumber m a leading mode can be associated; this is the mode with the largest imaginary part ω_i of the eigenfrequency. The variation of the temporal growth rate ω_i of these leading modes with Reynolds number is shown in figure 3.13(a), again for $W = 0.5$, $H = 0.5$. Figure 3.13(b) shows the real part ω_r of the leading modes associated with wavenumbers $m = 4$ and $m = 5$. The temporal growth rate of both of these modes become positive at $Re \approx 4875$; both modes are found to switch abruptly from stationary to oscillatory at much smaller Reynolds numbers.

Figure 3.14(i) shows the amplitude of the global mode defined as the square-root of the energy density field at two different Reynolds numbers for the azimuthal mode number $m = 4$. The Reynolds numbers are chosen in such a way that they belong to the two different regimes, corresponding to a dominant stationary critical mode and an oscillatory one, observed in figure 3.13. The bulge height chosen is $H = 0.5$. The amplitude of the leading mode is found to reach its maximum slightly above the free shear layer and slightly upstream of the reattachment point. The maximum is also seen to shift towards
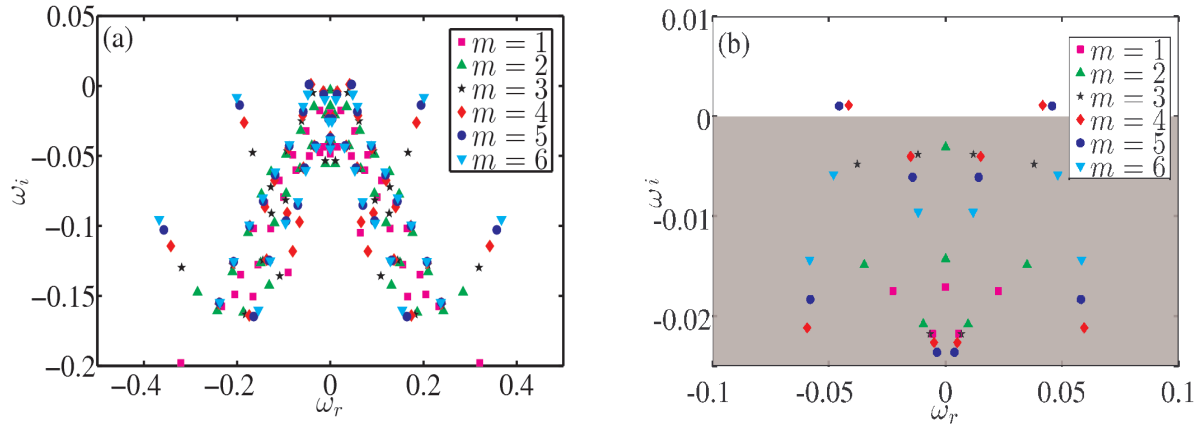
Figure 3.11: (a) Eigenfrequency spectrum for different azimuthal wavenumbers m; $W = 0.5$, $H = 0.5$, $Re = 5500$. (b) A close-up view of the eigenfrequency spectrum showing the unstable modes corresponding to $m = 4$ and $m = 5$. The stable region is shaded in grey.
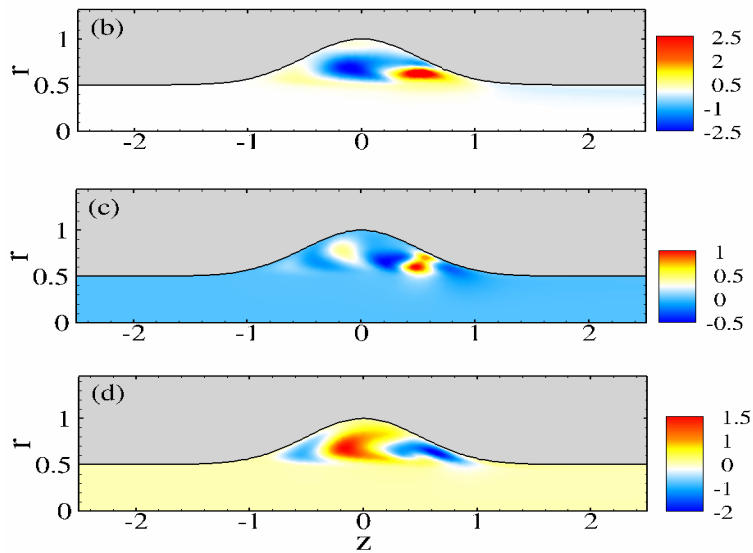

Figure 3.12: Modes visualized by their (b) axial, (c) radial and (d) azimuthal velocity components. Parameter settings: $W = 0.5$, $H = 0.5$, $m = 4$, $Re = 5500$.
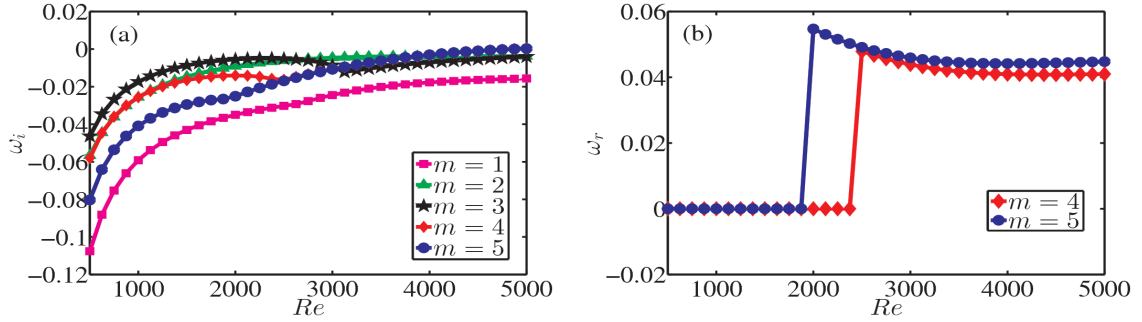
Figure 3.13: (a) Temporal growth rates ω_i and (b) oscillation frequencies ω_r as a function of Reynolds number Re of the leading modes associated with different azimuthal wavenumbers m; $W = 0.5$, $H = 0.5$.
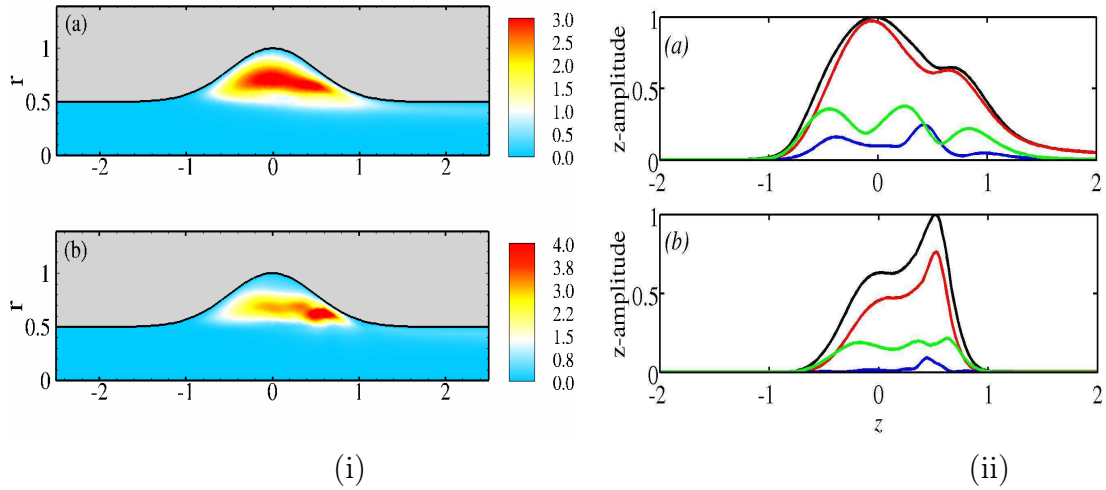
Figure 3.14: (i) The amplitude of the mode defined as the square-root of the energy density field. Parameter settings: $H = 0.5$, $m = 4$; (a) $Re = 2000$ (b) $Re = 5500$. (ii) Magnitude of the velocity of the global mode and of its components integrated over r: black line $(\int |\hat{\mathbf{u}}|^2 dr)^{1/2}$, red line $(\int |\hat{u_z}|^2 dr)^{1/2}$, blue line $(\int |\hat{u_r}|^2 dr)^{1/2}$, green line $(\int |\hat{u_\theta}|^2 dr)^{1/2}$. Parameter settings: $H = 0.5$, $m = 4$; (a)$Re = 2000$ (b) $Re = 5500$.
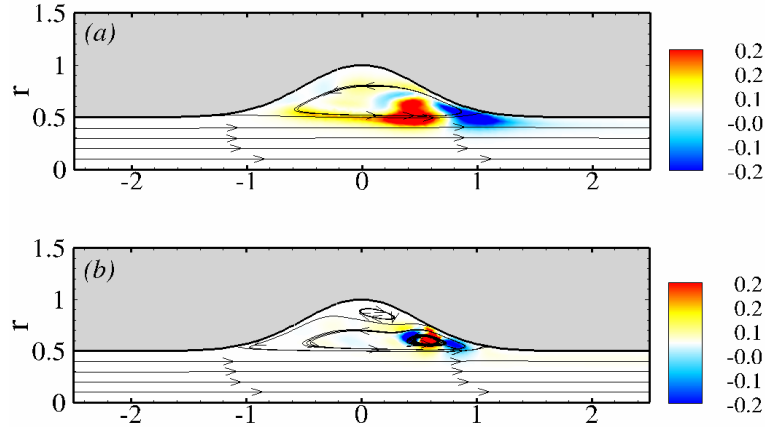
Figure 3.15: Basic streamlines and total local energy production rate $\sum_{i=1}^{4} E_{p,i}$ for $H = 0.5$ at an azimuthal mode number $m = 4$. (a)$Re = 2000$ (b)$Re = 5500$.

the downstream end of the bulge at a higher Reynolds number. The mode amplitude at each axial position z, defined as $(\int |\hat{\mathbf{u}}|^2 dr)^{1/2}$, hereafter referred to as the $z-$amplitude, is presented in figure 3.14(ii). The contribution of each of the velocity components to the energy density field at each axial location is shown using different colored lines (see caption). Three different zones can be noted. In the first zone starting from the inlet to the upstream end of the bulge the mode is almost nil. Within the bulge region the amplitude is maximum. The third region from the downstream end of the bulge to the exit, the amplitude drops off significantly with z. In figure 3.14(iia) where the $z-$amplitude is computed for a Reynolds number 2000 one can see that the axial velocity component of the mode contributes almost entirely to the total energy density. Though the azimuthal velocity component is more significant than the radial one its contribution to the total energy density is minimal. Whereas in figure 3.14(iib) which corresponds to a Reynolds number 5500 we can observe that the contribution coming from the azimuthal velocity component is more significant. We believe that the shift in the flow characteristic from a steady to an unsteady one at a Reynolds number around 2375 is related to the increase in dominance of the azimuthal energy density and as such one may expect different instability mechanisms to be present.

Figure 3.15 shows the regions in the flow where the energy transfer from the base flow to the perturbations take place at two different Reynolds numbers corresponding to a dominant stationary critical mode and an oscillatory one as in figure 3.14. We can see that in the case of a stationary critical mode (figure 3.15(i)), the region of maximum energy transfer is located around the separating streamline, whereas for the oscillatory critical mode (figure 3.15(ii)), the maximum energy transfer takes place within the primary recirculation region. This further suggests that different instability mechanisms are at play at different regimes. We come back to this point shortly when we make a comparison with other bulge heights and discuss the various instability mechanisms.

3.3.2 Stability boundaries and comparison with other AAAs

The stability boundaries in the $H - Re$ plane are shown in figure 3.16 for different azimuthal mode numbers m at four values of the bulge width: $W = 2.0$ (a); $W = 1.0$ (b); $W = 0.5$ (c); $W = 0.25$ (d). For small values of bulge height, the aneurysm geometry can be viewed as a small perturbation to a circular pipe flow which is linearly stable for all Reynolds numbers. We can see that this is indeed the case as the flow is found to be stable to small values of H. Though a critical bulge height cannot be confirmed, as higher Reynolds numbers were not investigated, it is deemed that all the perturbations to the base flow are linearly stable for bulge heights $H < 0.2$. This critical value of bulge height depends on the width W. As the bulge height is increased, the flow is found to become unstable to stationary critical modes shown by dotted lines in figure 3.16. These critical modes are characterized by larger azimuthal mode numbers. As the bulge height is increased further, the flow is found to become unstable to smaller azimuthal mode numbers and these are of oscillatory nature and shown using continuous lines in figure 3.16. Stationary disturbances were also found to be the least stable modes at very large values of H. The critical Reynolds numbers for stationary unstable modes are found to be lower than those for the oscillatory unstable modes. We find qualitatively the same nature of flow instability as in the work carried out by Cho *et al.* (1988) in which stationary disturbances dominated for small bulge heights and the oscillatory disturbances for larger bulge heights.

For the case of $W = 0.25$, figure 3.16(d), the stable region in the $H - Re$ plane is significantly larger. This is expected as the flow passes through the aneurysm without being significantly influenced by the presence of the dilatation. The critical bulge height below which the flow remains stable to all Reynolds numbers and azimuthal mode number is roughly around $H = 0.5$. The critical Re is around 4000 for which the flow becomes unstable to $m = 2$ mode for a bulge height of $H \approx 0.775$. All the unstable modes have a stationary nature.

With the increase in width, W, the stability characteristics remain qualitatively similar, albeit with some exceptions. For $W = 0.5$, the stationary mode corresponding to $m = 4$ is not observed for lower values of bulge height, unlike in the case of $W = 1.0$ and $W = 2.0$. With the increase in width, the stable region is found to increase gradually, though we have not performed calculations for very large values of W to verify the asymptotic features, as such aneurysms are highly unrealistic. As large values of W are not physiologically relevant, we have have not gone beyond $W = 2$ in the present study.

3.3.3 Instability mechanisms

In this section, we attempt to discuss the various stability mechanisms that are at play in these geometries. We use the energy-transfer analysis to decipher the physical nature of instabilities. As shown earlier in figures 3.14 and 3.15, the distribution of the energy-transfer differs when the base flow has a single recirculation region or two recirculation regions. This can happen with the increase in Reynolds number or bulge height. We begin by discussing the stability boundaries for $W = 0.5$ as it is representative of a typical AAA.
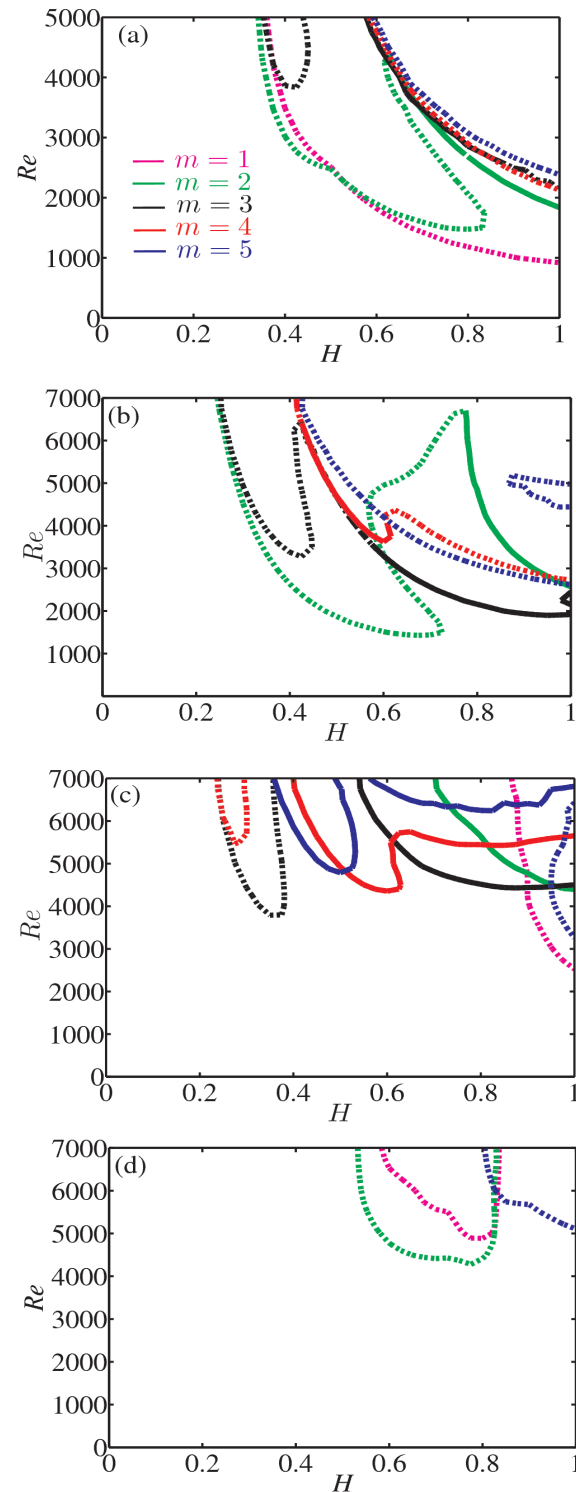
Figure 3.16: Critical curves associated with different azimuthal wavenumbers m in the Reynolds number Re versus inflation height H plane. The pink, green, black, red and blue lines correspond to $m = 1$, $m = 2$, $m = 3$, $m = 4$ and $m = 5$, respectively. The continuous curves indicate oscillatory modes, the dotted lines stationary modes. The bulge width in these figures is: (a) $W = 2.0$; (b) $W = 1.0$; (c) $W = 0.5$; (d) $W = 0.25$.
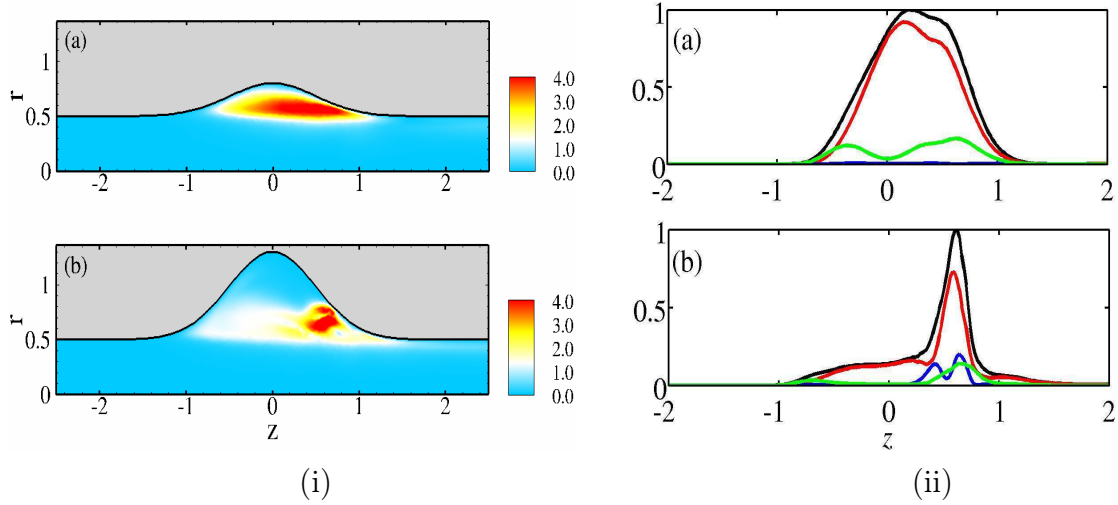
(i)   (ii)

Figure 3.17: *Left column*: Amplitude of the mode defined as the square-root of the perturbation energy density field. *Right column*: Variation with axial distance z of the magnitude of the velocity of the global mode and of its components integrated over r: $(\int |\hat{\mathbf{u}}|^2 \mathrm{d}r)^{1/2}$ (*black*); $(\int |\hat{u}_z|^2 \mathrm{d}r)^{1/2}$ (*red*); $(\int |\hat{u}_r|^2 \mathrm{d}r)^{1/2}$ (*blue*); $(\int |\hat{u}_\theta|^2 \mathrm{d}r)^{1/2}$ (*green*); all normalized with the maximum value of $(\int |\hat{\mathbf{u}}|^2 \mathrm{d}r)^{1/2}$. Parameter values: $Re = 5500$, $m = 3$, $W = 0.5$, $H = 0.3$ (*a*); $H = 0.8$ (*b*).

3.3.3.1 $W = 0.5$

First, two flows are compared at $Re = 5500$ through a model aneurysm with width $W = 0.5$, one with height $H = 0.3$, the other with $H = 0.8$.

Figure 3.17 presents the perturbation energy density distribution associated to the amplitude function $(\hat{u}_r, \hat{u}_\theta, \hat{u}_z)$ for the two different cases, in (*a*) for the basic flow with a single recirculation region ($H = 0.3$) and in (*b*) for the basic flow with also a secondary recirculation region ($H = 0.8$). It is observed (left column) that in the first case the disturbance energy is distributed all along the axis of the inflation, while in the second case it is localized in a small region at the downstream end. This can be seen even more clearly from the $z-$amplitude associated with the individual perturbation velocity components (right column). Note also that in both cases most of the perturbation energy is in the axial perturbation velocity component, and that in the second case there is also a small contribution of the radial velocity component, which is totally absent in the first case; in this first case then, the disturbance motion takes place in circular planes.

That different mechanisms are involved in the instability of the two basic flows, is also clear from figures 3.18 and 3.19, which provide information on the energy transfer between the basic flow and the perturbation flow. Shown here are the total energy transfer rate, in (*d*), and the three separate contributions $E_{p,1}$ (*a*), $E_{p,2}$ (*b*) and $E_{p,4}$ (*c*), which have been defined in expression (2.44). The global picture is the one that also emerges from figure 3.17, but here it is seen further that the main energy transfer mechanism *in both cases* is that represented by $E_{p,2}$; the locations where this mechanism is active are different, though.
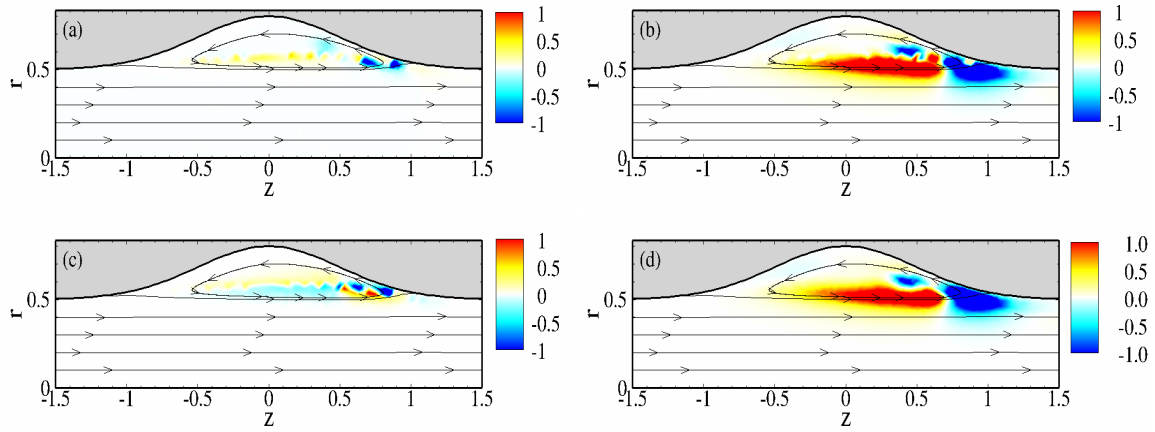
Figure 3.18: Basic streamlines and local energy production rates for $H = 0.3$ at $Re = 5500$ and for an azimuthal mode number $m = 3$. (a) $E_{p,1}$ (b) $E_{p,2}$ (c) $E_{p,4}$ (d) $\sum_{i=1}^{4} E_{p,i}$.
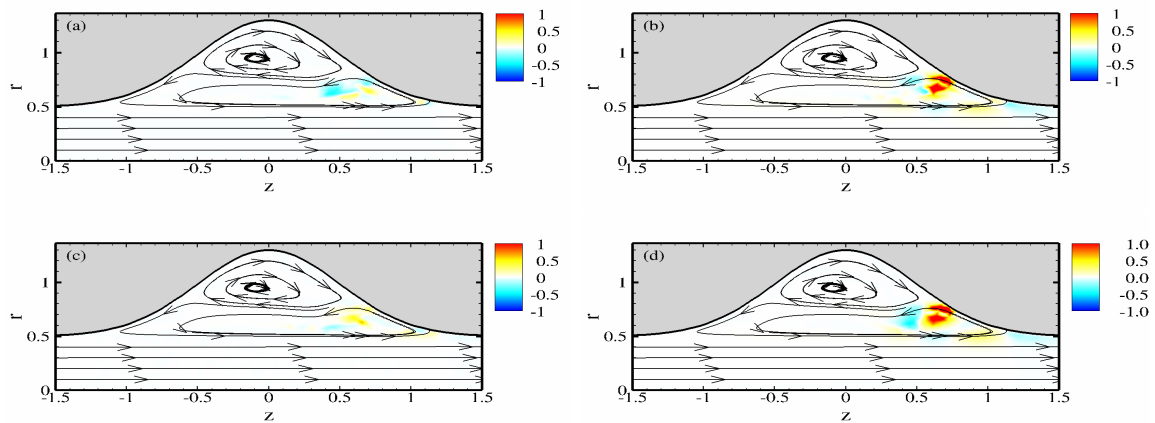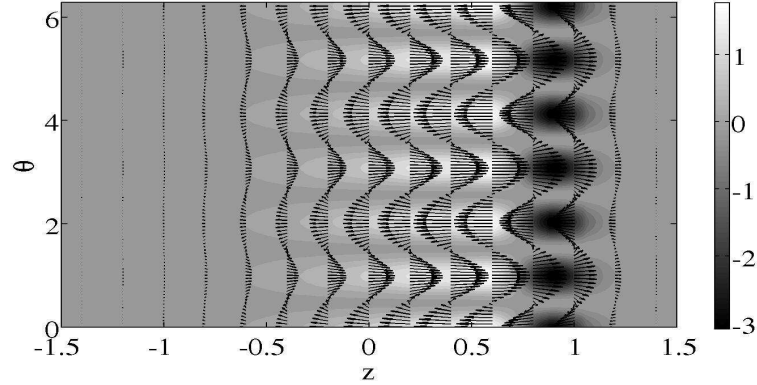

Figure 3.19: Basic streamlines and local energy production rates for $H = 0.8$ at $Re = 5500$ and for an azimuthal mode number $m = 3$. (a) $E_{p,1}$ (b) $E_{p,2}$ (c) $E_{p,4}$ (d) $\sum_{i=1}^{4} E_{p,i}$.

Figure 3.20: Velocity distribution at $r = 0.5$ of the most unstable mode associated with wavenumber $m = 3$ in the form of streaks (arrows) and the total local energy production $\sum_{i=1}^{4} E_{p,i}$ (grey shading); $H = 0.3$, $W = 0.5$, $Re = 5500$.
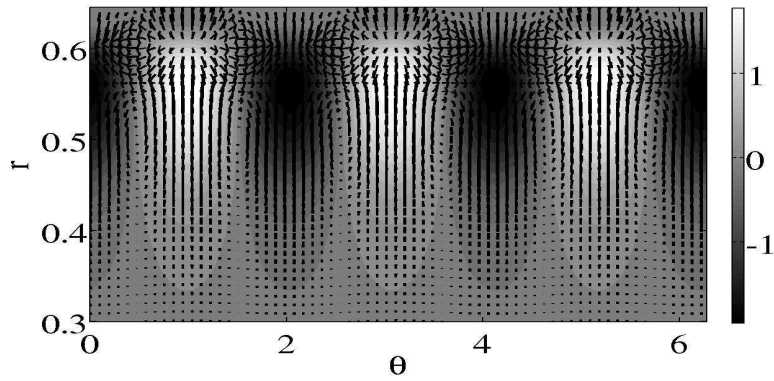
Figure 3.21: Velocity distribution (arrows) and streamwise perturbation velocity u'_z (grey shading) at the axial location of maximum perturbation energy of the most unstable mode associated with wavenumber $m = 3$; $H = 0.3$, $W = 0.5$, $Re = 5500$.

In the case with a relatively shallow inflation ($H = 0.3$), the unstable mode is stationary and the disturbance motion primarily takes place on cylindrical planes. Figures 3.20 and 3.21 provide a more detailed view of this perturbation velocity field. The picture that emerges is that of a flow with alternating slow and fast streamwise streaks (figure 3.20), and an arrangement of alternately rotating vortices distributed in the layer between the core and the recirculation zone (figure 3.21). These vortices transport low-velocity fluid to high-speed regions within the perturbation flow. This is the familiar lift-up mechanism, first described by Orr in 1907 (Schmid & Henningson, 2001). The lift-up mechanism has also been identified by Lanzerstorfer & Kuhlmann (2012a) as governing the instability of two-dimensional flow past a backward-facing step with small expansion ratio; cf. their figure 20 with our figure 3.18(d).

At larger bulge heights, $H > 0.4$, the energy-transfer from the basic flow to perturbation is different, which can be seen from figures 3.14 and 3.19. It is seen that the energy
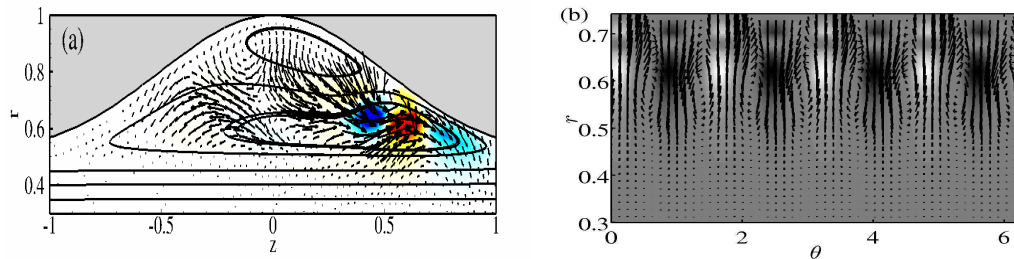
Figure 3.22: (a) Base flow streamlines (continuous lines), critical velocity fields (arrows) and total local energy production $\sum_{i=1}^{4} E_{p,i}$. (b) Critical velocity fields (arrows) and the total local energy production $\sum_{i=1}^{4} E_{p,i}$ (grey shading) at an axial location where the energy transfer reaches its maximum. Parameter settings: $H = 0.5$, $Re = 5500$, $m = 4$.
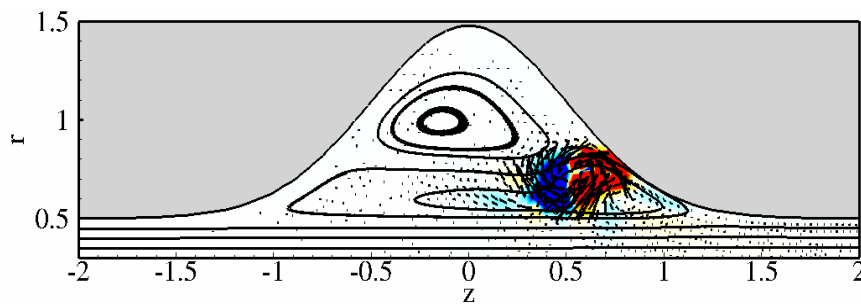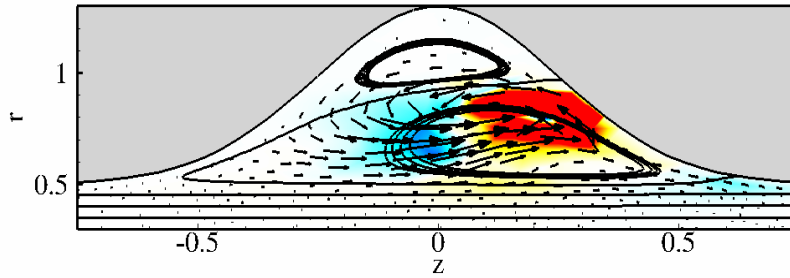

Figure 3.23: Base flow streamlines (continuous lines), critical velocity fields (arrows) and total local energy production $\sum_{i=1}^{4} E_{p,i}$. Parameter settings: $H = 0.975$, $Re = 5500$, $m = 1$.

Figure 3.24: Base flow streamlines (continuous lines), critical velocity fields (arrows) and total local energy production $\sum_{i=1}^{4} E_{p,i}$. Parameter settings: $W = 0.25$, $H = 0.8$, $Re = 5500$, $m = 2$.

transfer occurs only in a small region, namely in the centre of the primary vortex. This is typical for an elliptical instability mechanism. Lanzerstorfer & Kuhlmann (2012a) have also demonstrated that the elliptical instability mechanism is involved in the global instability of flow past a two-dimensional backward-facing step of moderately large expansion rates; note the close correspondence to our figure 3.19(d) and their figures 13 and 14. This is further exemplified in figure 3.22(a) where the total local energy production for $H = 0.5$ at a Reynolds number $Re = 5500$ for an azimuthal mode number $m = 4$ is shown along with the critical velocity field vectors and the basic flow streamlines. The perturbation flow is strongest where the energy transfer is maximum, which is entirely localized in the core region of the primary recirculation region and they are aligned with the principal direction of strain. Figure 3.22(b) shows the resulting perturbation flow that arises as a sequence of counter-rotating vortices in the azimuthal plane. The same features are observed at larger bulge heights (see figure 3.23) which indicates that the instability mechanism is of an elliptic type.

3.3.3.2   Comparison with other widths

We begin by considering $W = 0.25$, by choosing the most unstable mode at $H = 0.8$ at a Reynolds number of 5500 and $m = 2$. Figure 3.24 shows the energy transfer for these parameters, along with the basic flow streamlines and critical perturbations. Once again we can forward the arguments mentioned earlier for the case of elliptic instability mechanism for the present parameters too. However, unlike in the previous cases, the energy transfer is not entirely localized within the primary vortex and is slightly pushed towards the convex streamline. We postulate the possibility of another instability mechanism that is centrifugal in nature that could possibly account for these differences.

Figure 3.25(a) shows the regions where the maximum energy transfer from the basic flow to the perturbation takes place. Unlike in the previous cases where the energy transfer is localized along the separating streamline or within the primary vortex, here the energy transfer is along the convex side of the streamlines, sufficiently displaced from the center of the primary vortex. We believe that in this case, the instability mechanism could be centrifugal in nature.

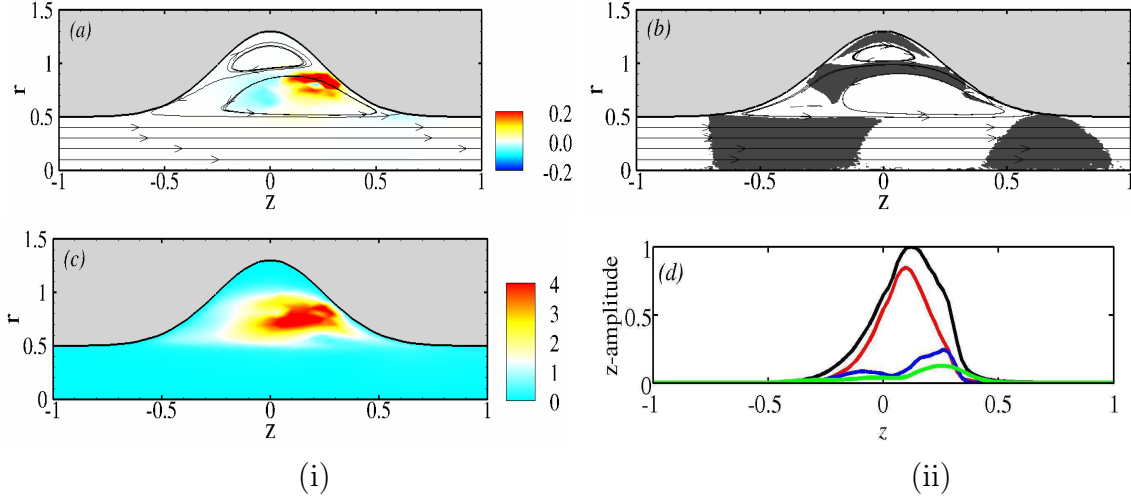Centrifugal instability theory, as first developed by Rayleigh (1917) for axisymmet-

Figure 3.25: (i) (a) Basic streamlines and local energy production rate $\sum_{i=1}^{4} E_{p,i}$. (b) Expression (3.1). (ii) (a) The amplitude of the mode defined as the square-root of the energy density field. (b) Magnitude of the velocity of the mode and of its components integrated over r (normalized with $(\int |\hat{\mathbf{u}}|^2 dr)^{1/2}$) : black line $(\int |\hat{\mathbf{u}}|^2 dr)^{1/2}$, red line $(\int |\hat{u}_z|^2 dr)^{1/2}$, blue line $(\int |\hat{u}_r|^2 dr)^{1/2}$, green line $(\int |\hat{u}_\theta|^2 dr)^{1/2}$. Parameter settings: $W = 0.25$, $H = 0.8$, $Re = 5500$, $m = 2$.

ric inviscid flows with circular streamlines, holds that a potentially unstable condition results from the existence of a decrease in angular momentum of fluid particles, as the radial distance from the centre of rotation of the flow increases, resulting in an imbalance between the radial pressure gradient and the centrifugal force acting on the fluid particles. This unstable condition triggers three-dimensional structures to form, which redistribute the angular momentum between the inner and outer regions of such a vortex. The corresponding perturbations typically consist of a series of counter-rotating azimuthal vortices located in the region of decreasing angular momentum and whose axial wavelength scales on the radial extent of this region.

To support this argument, we use the criterion proposed in Lanzerstorfer & Kuhlmann (2012b), which is a reformulation of Bayly (1988)'s criterion, which is a sufficient condition for centrifugal instability for two-dimensional, inviscid flows. Accordingly, the inviscid flow is centrifugally unstable if

$$\frac{|\mathbf{U}|\zeta}{\alpha} < 0, \tag{3.1}$$

is satisfied all along a closed streamline $\Psi = $ const. Here ζ stands for the vorticity of the basic flow and α for the local algebraic radius of curvature, given by

$$\alpha = \frac{|\mathbf{U}|^3}{(\nabla \Psi) .(\mathbf{U} .\nabla \mathbf{U})}. \tag{3.2}$$

As a result, the quantity from the expression (3.1) is computed and is shown in figure 3.25(b). A good agreement between the regions where one would expect centrifugal instability and the regions where maximum energy transfer takes place can be observed,
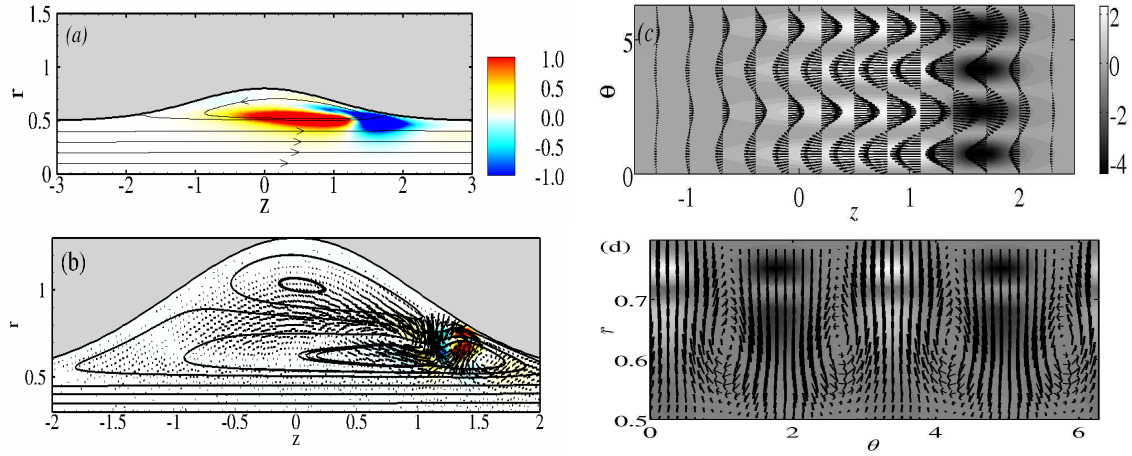
Figure 3.26: (a) Basic streamlines and local energy production rate $\sum_{i=1}^{4} E_{p,i}$. (c) Critical velocity fields in the form of streaks (arrows) and the total local energy production $\sum_{i=1}^{4} E_{p,i}$. Parameter settings: $H = 0.3$, $m = 2$, $Re = 5500$. (b) Base flow streamlines (continuous lines), critical velocity fields (arrows) and total local energy production $\sum_{i=1}^{4} E_{p,i}$. (d) Critical velocity fields (arrows) and the total local energy production $\sum_{i=1}^{4} E_{p,i}$ (grey shading) at an axial location where the energy transfer reaches its maximum. Parameter settings: $H = 0.8$, $m = 2$, $Re = 5500$.

indicating centrifugal instability mechanism. Also, the term given by $E_{p,2}$ dominates over the rest (not shown here). The energy distribution of the mode and the contribution from each component is shown in figure 3.25(c),(d). Also, we can see that the contributions from the radial and the azimuthal components are more pronounced in the regions where the centrifugal effects are more important. We would like to remind that both elliptic and centrifugal mechanisms are dominant at small values of W for large bulge heights.

At a larger value of width, $W = 1.0$, we can see from figure 3.16(b) that at lower bulge heights, the unstable modes are found to be stationary with $m = 2, 3$. The least stable configuration is for $H \approx 0.7$ and $Re \approx 1500$ for $m = 2$. For low values of H, the unstable modes corresponding to $m = 4$ are found to be oscillatory and for higher values of H they are found to be stationary. To compare the differences of the unstable modes at different points in the parameter space, we consider the modes $m = 2, 3$ for the bulge heights $H = 0.3$ and $H = 0.8$ at a Reynolds number $Re = 5500$. Figure 3.26 shows the regions where the energy transfer from the basic flow to the perturbations takes place giving insight into the instability mechanisms. We can see that the energy distributions at small and large values of H are qualitatively the same as in the case of $W = 0.5$. The maximum energy transfer for stationary modes at small bulge heights are found to take place along the separating streamline. For larger bulge heights, the energy transfer is more pronounced within the primary vortex. Once again, one expects a lift-up mechanism to be present at small bulge heights and elliptical mechanism to be dominant at large bulge heights. This is verified in figure 3.26 where the formation of streaks and the regions of energy transfer are shown, indicating lift-up mechanism at small heights and elliptic mechanism at larger heights. The same features are also observed for $W = 2.0$.

3.4   Conclusions

The steady axisymmetric flow through the model aneurysm studied here is unstable for Reynolds numbers that correspond to the peak values observed during physiological conditions. This occurs for dimensionless aneurysm 'heights' of about $H = 0.3$. Also, the flow in relatively long aneurysms (i.e. with large widths W) is more susceptible to instability than that through more localized aneurysms. The base flow in these extended aneurysms is characterized by a single large recirculation region; this flow becomes unstable to a stationary mode by the lift-up mechanism. Steady flows through shorter aneurysms also include a secondary recirculation zone; these flows become unstable to oscillatory modes which involve energy transfer from the base flow to perturbations in a small region at the downstream end of the aneurysm, presumably by an elliptical instability mechanism.

It may be tempting to draw conclusions concerning the pathophysiology of abdominal aortic aneurysms from the results found in this study. However, in our opinion this idealized model is too far removed from reality to do so. The motivation for the present study is to provide a basis for further more realistic studies, which should permit to quantify the effects of pulsatility of the flow (discussed in the following chapters), the non-axisymmetry and other characteristics of the geometry of aneurysms, the presence of the iliac bifurcation and other vasculature downstream of the aneurysm. Nevertheless, the present study does suggest that in inflated arteries regions with slowly recirculating fluid occur, with very low wall shear stresses.

Pulsatile flows: Flow characteristics

4.1 Introduction

The present chapter extends the work presented in the previous chapter by taking into account pulsatile flow. Specifically, the changes in flow characteristics under varying flow conditions and during the progressive enlargement of an abdominal aortic aneurysm (AAA) are investigated.

One of the most fundamental questions that is still staring at researchers in the field of bio-fluidmechanics of aneurysms is whether an aneurysm forms as a result of a degradation process in the wall, or by anomalous changes in the hemodynamic stimuli resulting in an unstable degenerative process on the vessel wall, or by a combination of both. The prevailing consensus is that the cause is more likely to result from a coupling between structural changes of the arterial wall and disturbed patterns of hemodynamic stresses acting on the vessel wall. Changes in structure and etiology of the arterial wall influences the flow through the arterial segment. Conversely, changes in flow characteristics alter the pressure and shear stresses acting on the arterial wall, in turn resulting in wall degradation. Thus, once an aneurysm is formed, the expansion process depends on an interplay between mechanical stimuli exerted by the pulsatile blood flow and physiological wall changes.

Several works probing at different points of view have been carried out, a review of which is provided in Lasheras (2007), Humphrey & Taylor (2008). Many of these have used patient-specific models of AAA to investigate the distribution of wall shear stresses (WSS) along the arterial wall. Some of the more recent works are Raghavan *et al.* (2000), Stamatopoulos *et al.* (2011), Les *et al.* (2010), Suh *et al.* (2011), Sheidaei *et al.* (2011), Vorp (2007). All of these studies have provided a good qualitative description of the flow in an AAA, and the most relevant features like the concentration of WSS at the distal end, low oscillatory WSS within the AAA cavity and the presence of disturbed flow conditions, were captured. These studies are highly relevant as they help us to get a clear picture of the complexity present *in vivo* AAAs. However, a major drawback is that it is often difficult to derive general conclusions using this approach due to the complexity of geometries used in these studies. To overcome this, studies have also been carried out using model AAA geometries, some of which are Taylor & Yamaguchi (1994), Salsac *et al.* (2004), Salsac (2005), Sheard (2009), Duclaux *et al.* (2010), Deplano *et al.* (2007, 2013). Of these, the most comprehensive study on the evolution of the flow field during AAA enlargement was reported by Salsac (2005), who provided changes in spatial and temporal changes in WSS acting on the endothelial cells as the AAA grows. However, a

minor limitation of that study was that the WSS distributions at the arterial wall were underestimated, particularly at the point of impact of the primary vortex, because of the very small size of the Stokes layer and of the resolution of their measurements, as was pointed out by them. Hence, in the present work we have used a model AAA geometry, as the various geometrical parameters, namely the bulge height H and bulge width W of the AAA, can be varied systematically and a precise description of the various flow characteristics can be provided.

As reported in Salsac (2005), it has been observed that aneurysms tend to be symmetric at the early stages of the disease, but may become non-symmetric when they reach larger sizes. Also, as the AAA shapes observed *in vivo* are complex in nature, some studies have concentrated on comparing the flow features observed in a symmetrical AAA with an asymmetrical one (Taylor & Yamaguchi, 1994, Salsac, 2005, Deplano *et al.*, 2007, Vorp, 2007, Deplano *et al.*, 2013). Some of the typical flow features observed in symmetric AAAs persisted in non-symmetric models, with significant deviations only observed for large values of asymmetry. With these observations in mind, we have used a symmetric model of AAA in our study with the primary focus being on characterising the flow fields during the early stages of growth of an AAA.

Another aspect that has received much attention in recent years is to understand the changes in flow hemodynamics under varying conditions of physical activity, i.e. under rest and exercise conditions. The flow rates and associated flow parameters, namely the Reynolds number Re, the Womersley number Wo and the waveform significantly depend on these conditions. Some of the notable works are those by Taylor *et al.* (1999), Egelhoff *et al.* (1999), Deplano *et al.* (2007), Les *et al.* (2010), Suh *et al.* (2011). The hypothesis that prolonged exercise may eventually slow AAA growth has been mainly supported using the following arguments: studies on animals have shown that artificial augmentation of blood flow led to smaller sized aneurysms (Hoshina *et al.*, 2003), elevation of blood flow rate and WSS resulted in release of athero-protective factors such as nitric oxide (Taylor *et al.*, 1999), reduction in stagnation and recirculation of blood flow (factors related to thrombosis (Reininger *et al.*, 1994, Vorp *et al.*, 2001)), reduction in incidence of platelet aggregation (Suh *et al.*, 2011), to name some. However, no study has been carried out that looked into varying flow characteristics in an AAA under exercise conditions. This is another aspect that we have investigated in our present work.

The chapter begins with a brief description of flow characteristics in a healthy abdominal aorta under rest and exercise conditions. The observations are then compared with the case of a typical AAA under resting conditions. The effect of varying geometrical parameters, H and W, is then provided. As the flow parameters, Re and Wo, are found to vary from person to person, even during resting conditions, we have investigated the sensitivity of our observations, by varying Reynolds number and Womersley number for a waveform characteristic of resting conditions. Then some results for exercise conditions are obtained. The chapter concludes with a discussion on physiological implications of our observations under varying flow conditions at various stages of growth of an AAA.
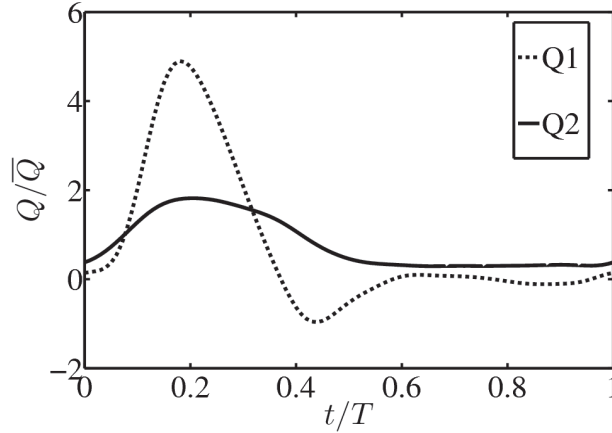
Figure 4.1: Waveform $Q1$ and $Q2$ corresponding to rest and exercise conditions respectively.

4.2 Flow characteristics in a healthy abdominal aorta

The healthy abdominal aorta is idealized as a straight circular pipe with no inflation. Two types of physiological flow rate waveforms were considered in our study, corresponding to rest ($Q1$) and exercise ($Q2$) conditions. These waveforms are taken from the article by Suh *et al.* (2011), were measured for patients suffering from AAAs during resting and exercise conditions and are summarized in figure 4.1. More details on the waveforms used in our analysis and the Fourier coefficients corresponding to these waveforms are provided in chapter 1 (see section 1.2.3). The important flow parameters that are investigated in the present chapter are the Womersley number Wo and the Reynolds number Re, defined as

$$Wo = \frac{D}{2}\sqrt{\frac{\omega}{\nu}}, \tag{4.1a}$$

$$Re = \frac{\overline{U}D}{\nu}, \tag{4.1b}$$

where D is the vessel diameter at the inlet, ω the frequency of the pulsation, ν the kinematic viscosity, and $\overline{U}$ the mean axial velocity. The Womersley number Wo can be interpreted as the ratio of the radius $D/2$ to the oscillating boundary-layer thickness $\sqrt{\frac{\nu}{\omega}}$. Typical flow parameters for the present analysis derived from the physiological values provided in Suh *et al.* (2011) are given in table 4.1.

As seen in figure 4.1, under resting conditions, the peak flow rate during systole ($t = 0.18T$) goes up to 5 times the mean value. After this the flow rate decelerates and becomes negative during peak diastole ($t = 0.44T$). At the end of the diastole, the flow sets forward again and relaxes to zero during the resting period, before being accelerated again at the beginning of the next cardiac cycle. Figure 4.2(a) shows the corresponding axial velocity profiles across the aorta during various instants of the cycle. At the beginning of the cycle, the fluid is almost at rest ($t = 0.0T$). During the acceleration portion of the systole, the

Waveform	Re	Wo
$Q1$(rest)	264	12
$Q2$(exercise)	1700	13.8

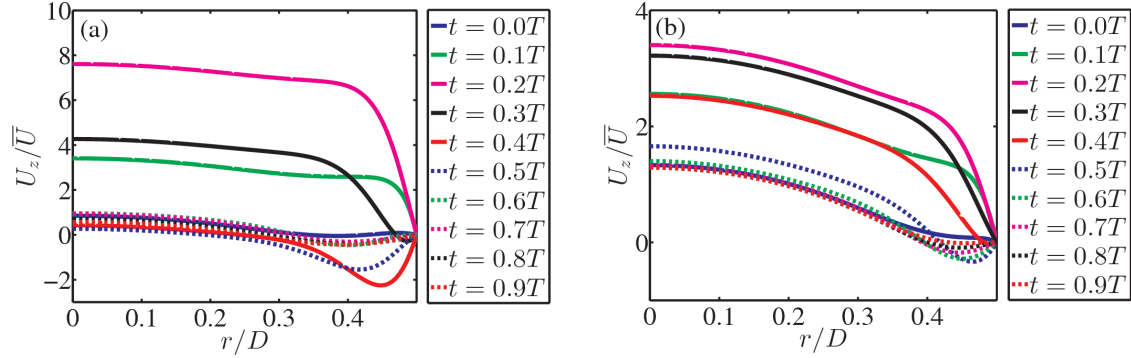Table 4.1: Typical values of the flow parameters considered in our study.

Figure 4.2: Axial velocity profiles across the healthy abdominal aorta at several instants of time in one cardiac cycle calculated under (a) rest and (b) exercise conditions.

flow develops into a characteristic top-hat velocity profile. For small Womersley numbers, viscous forces dominate and the velocity profiles would be parabolic in shape. However, the Womersley numbers observed in the abdominal aorta are in the range of $10-15$, and hence the unsteady forces dominate, and the flow is nearly top hat with thin boundary layers. The thickness of the boundary layer scales as D/Wo. After the peak systole, the flow decelerates first along the walls and the bulk of the flow reverses at peak diastole. Similar flow features were observed by Salsac *et al.* (2006), though a slightly different waveform was considered in their study.

During exercise conditions different flow characteristics prevail. Unlike in the case of rest, the flow rate remains positive throughout the cardiac cycle and does not reverse during diastole (see figure 4.1). Also, at the beginning of the cardiac cycle at $t = 0.0T$, the flow rate is significant and never vanishes during the entire cardiac cycle. The axial velocity profiles across the aorta at different time instants are shown in figure 4.2(b). As the flow rate reaches its maximum during the peak systole, the velocity profile resembles a top-hat profile like in the case of rest. Another difference from the rest condition is that the axial velocity remains positive throughout the cycle with the exception during diastole, where negative values are observed close to the wall.

Wall shear stresses in a healthy abdominal aorta

The wall shear stress (WSS) has been established as the primary fluid mechanical characteristic affecting biological arterial responses (Ku, 1997). The wall shear stresses were

Condition	$\text{WSS}_{\text{peak}}(\text{Pa})$	$\text{WSS}_{\text{min}}(\text{Pa})$	$\overline{\text{WSS}}(\text{Pa})$	OSI
Rest	2.75	-1.37	0.11	0.41
Exercise	5.26	-1.85	0.71	0.27

Table 4.2: WSS characteristics under varying physiological conditions in a healthy abdominal aorta.

calculated as a function of time from the velocity profiles described above as

$$\text{WSS}(z,t) = -\frac{\partial U_z}{\partial r}|_{r=\text{wall}}. \tag{4.2}$$

The temporal evolution of the WSS under rest and exercise conditions is shown in figure 4.3 and follows the evolution of the flow rate. The convention is to assign a negative value to WSS corresponding to reversed flow.

The various quantities used by different authors to investigate the effect of WSS on endothelial cells are the time-averaged WSS ($\overline{\text{WSS}}$) and magnitude of the time-averaged WSS magnitude ($\overline{|\text{WSS}|}$). These quantities are defined as

$$\overline{\text{WSS}} = \frac{1}{T} \int_0^T \text{WSS} dt, \tag{4.3}$$

$$\overline{|\text{WSS}|} = \frac{1}{T} \int_0^T |\text{WSS}| dt. \tag{4.4}$$

The pulsatility of the flow and the unidirectionality of the WSS is quantified using the oscillatory shear index, defined as

$$\text{OSI} = \frac{1}{2}\left(1 - \frac{\overline{\text{WSS}}}{\overline{|\text{WSS}|}}\right). \tag{4.5}$$

OSI ranges from 0 to 1, where 0 indicates that the WSS is unidirectional. An OSI index of 0.5 indicates that the flow is purely oscillatory with $\overline{\text{WSS}} = 0$.

Figure 4.3 shows the WSS corresponding to rest (dotted lines) and exercise (solid lines) conditions. The dimensionless WSS values plotted in figure 4.3(a) can be converted to dimensional values by multiplying by $\mu \overline{U}/D$. These WSS characteristics are summarized in the table 4.2. As we have carried out computations using the waveforms presented by Suh *et al.* (2011), it is reasonable to make a comparison with the values presented by them. Their analysis based on realistic patient-specific AAA models predicted a mean WSS value of 0.29 Pa and 1.54 Pa, under resting and exercise conditions respectively. The values presented in table 4.2 are roughly half of their values, as they were obtained using calculations made in a healthy abdominal aorta (without any aneurysm). This would indicate that the presence of an aneurysm significantly elevates the WSS values. The OSI index in their study was 0.29 and 0.15 under resting and exercise conditions respectively. Once again differences could be due to the difference in geometries. The maximum and minimum values of WSS predicted by Salsac *et al.* (2006) were -3 Pa and 4.9 Pa
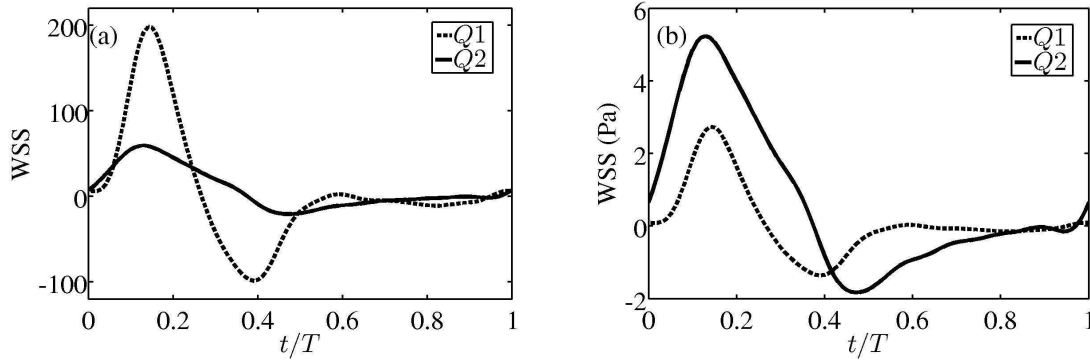
Figure 4.3: WSS during one cardiac cycle calculated using the Womersley solution. Dotted and continuous lines correspond to rest ($Q1$) and exercise ($Q2$) conditions respectively. The non-dimensional values are shown in (a) and physiologically relevant values obtained using the data shown in table 1.1 are shown in (b).

respectively. However, different waveforms and physiological conditions were employed in their study.

Despite intensive investigation over the past four decades, a definitive correlation between arterial fluid mechanics and arterial wall dysfunction has remained elusive (Barakat, 2013). Arterial wall dysfunction due to atherosclerotic lesions have been correlated with the formation and growth of an aneurysm (Lasheras, 2007). As discussed in Barakat (2013), the earliest investigations concluded that atherosclerotic lesions developed in arterial regions where the WSS is particularly high, as high levels of WSS are damaging to endothelial cells, thereby promoting the development of lesions. However, a competing theory that rapidly emerged claimed that atherosclerosis developed in arterial regions subjected to particularly low levels of shear stress. The thinking was that low shear regions increase the residence time of molecules near the arterial wall, thus increasing mass transport into the wall and leading to progressive accumulation of deposits. Further fluid mechanical studies have demonstrated that the regions of low WSS oscillate in time and have revealed that the endothelial cells are more receptive to spatial and temporal gradients (Jilkova *et al.*, 2013).

One can see from table 4.2 that the peak WSS under exercise conditions is almost twice that of rest conditions. Though the minimum value of WSS does not change drastically under varying conditions, the mean WSS is roughly 7 times higher during exercise conditions than under resting conditions, as it is directly proportional to Re. However, peak to mean ratio under resting conditions are almost 4 times higher than under exercise. As a result, even though significantly higher WSS values are recorded during exercise conditions, the temporal variations are significantly lower. Also OSI value during exercise conditions are significantly lower than under resting conditions, thereby reducing the oscillatory stresses experienced by the arterial wall. The effect of exercise on the reduction of oscillatory shear stresses suggests one possible direct benefit of exercise – namely, the elimination of hemodynamic conditions known to correlate with the location of atherosclerotic plaques (Taylor *et al.*, 1999). We now discuss the flow characteristics in an AAA and compare the differences that arise from a flow through a healthy abdominal
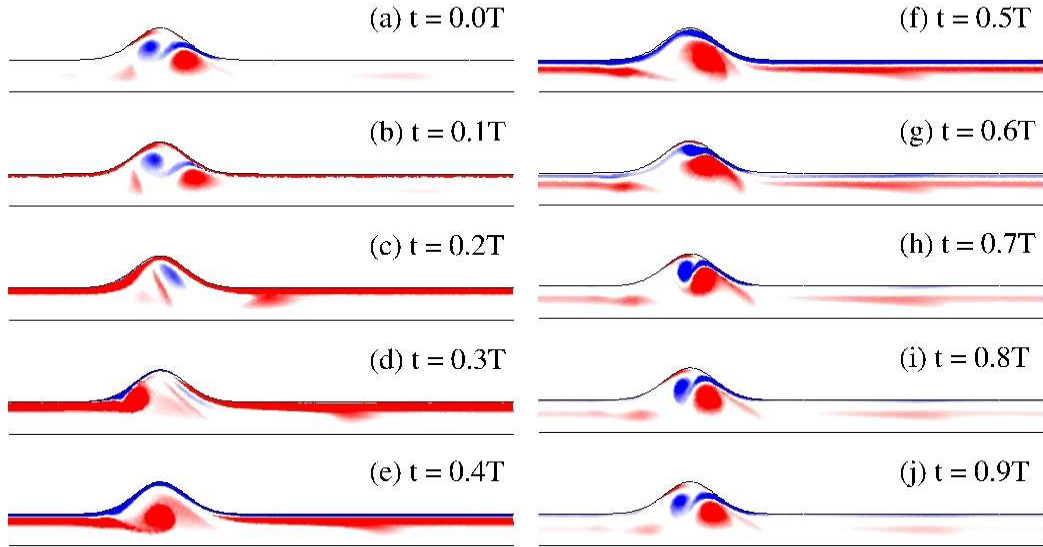
Figure 4.4: Dimensionless out-of-plane vorticity contours plotted at different time instants in a pulse cycle. Contours are plotted between -20(blue) and +20(red) within the axial range $-3 < z < 7$. Parameter settings: $Q1$, $Re = 264$, $Wo = 12$, $W = 0.5$, $H = 0.5$.

aorta.

4.3 Flow characteristics in an AAA during rest conditions

The flow characteristics in an AAA under resting conditions are presented in this section beginning with a description of spatial and temporal features characterising the typical flow field in an AAA. Subsequently, the parametric study of the flow characterisitics in an AAA is presented, specifically the effects of varying the geometry, Reynolds number and Womersley number.

4.3.1 Typical flow in an AAA

As in the case of steady flows, we consider an AAA with $W = 0.5$ and $H = 0.5$ to discuss the typical flow features in an AAA. The flow conditions are chosen such that $Re = 264$ and $Wo = 12$, and the rest waveform $Q1$ is chosen (see figure 4.1).

Figure 4.4 shows the azimuthal vorticity component of the flow field at various time instants in a pulse cycle. As the flow rate increases and reaches the peak systole ($t \approx 0.2 \ T$), the presence of positive vorticity near the walls can be seen. Subsequently, as the flow rate begins to decrease, the vorticity rolls up into a vortex located just downstream of the middle of the aneurysm, as shown in frames 4.4(d) and 4.4(e). This vortex enlarges with time, and results in a weaker vortex of opposite rotational direction located near the
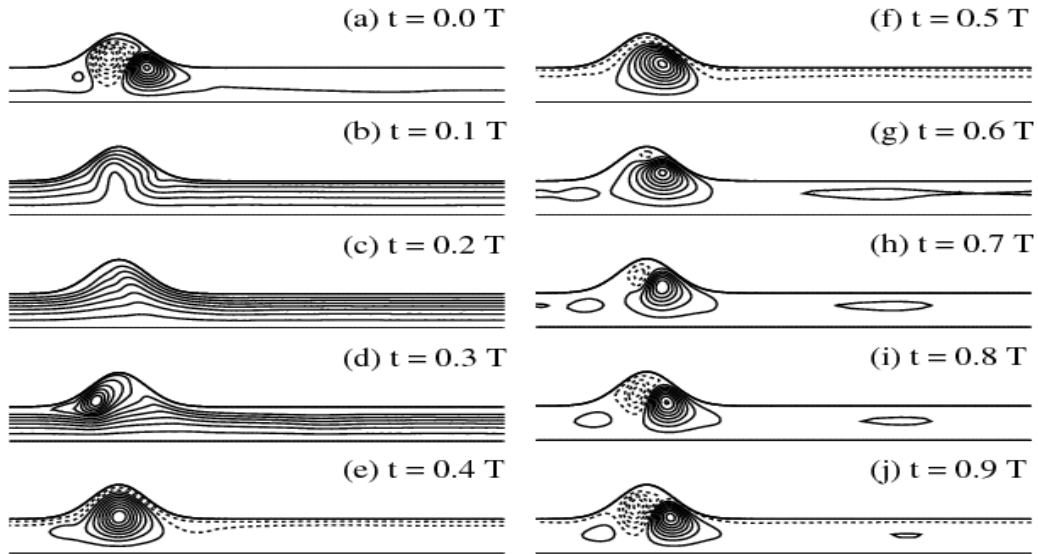
Figure 4.5: Streamlines at different time instants in a pulse cycle. Parameter settings: $Q1$, $Re = 264$, $Wo = 12$, $W = 0.5$, $H = 0.5$.

proximal (upstream) end of the bulge. This is a manifestation of the anti-clockwise rotation of the primary vortex coupled with reversed flow in the aneurysm. This can be observed in frames 4.4(g) and 4.4(h). The secondary vortex persists in the bulge, and as the flow rate completes the pulse cycle, bulk of the primary vorticity is convected out of the aneurysm, and the cycle repeats itself.

The above process is further illustrated using the basic flow streamlines at various instants within the pulse cycle, which are shown in figure 4.5. It shows the complex flow patterns that are generated during a cardiac cycle due to the presence of an aneurysm. During the initial phase of the cycle, the flow within the aneurysm is mainly forward, as shown in figures 4.5 (a–d). However, as the flow rate begins to decrease after the peak systole, the direction of the flow reverses suddenly, especially near the walls, as seen in frames 4.5 (e–f). Subsequently, as the flow rate begins to increase again, there is forward flow at the upstream end, coupled with reversed flow downstream of the aneurysm.

Before analysing the effects of these complex flow patterns on WSS distributions, it is interesting to look at the variation of the axial velocity profiles across the AAA at various axial locations, during various time instants in a pulse cycle. This is shown in figure 4.6. The first observation is that the departure from the Womersley solutions is highly localized to the bulge region. This can be seen by observing the variations recorded at points (a)–(b) and (f)–(g), which roughly correspond to proximal and distal ends of the aneurysm. The dotted lines shown at points (a) and (g) are the Womersley solutions calculated in a straight circular pipe. Secondly, the bulge region is associated with not only spatial variations in velocity profiles but also with significant temporal variations. Thirdly, these spatial and temporal variations are dominant at the near wall region, inducing thin layers with high stresses. Complex flow patterns due to the presence of disordered vortices within the aneurysm bulge have been associated with weak turbulence, even during resting conditions
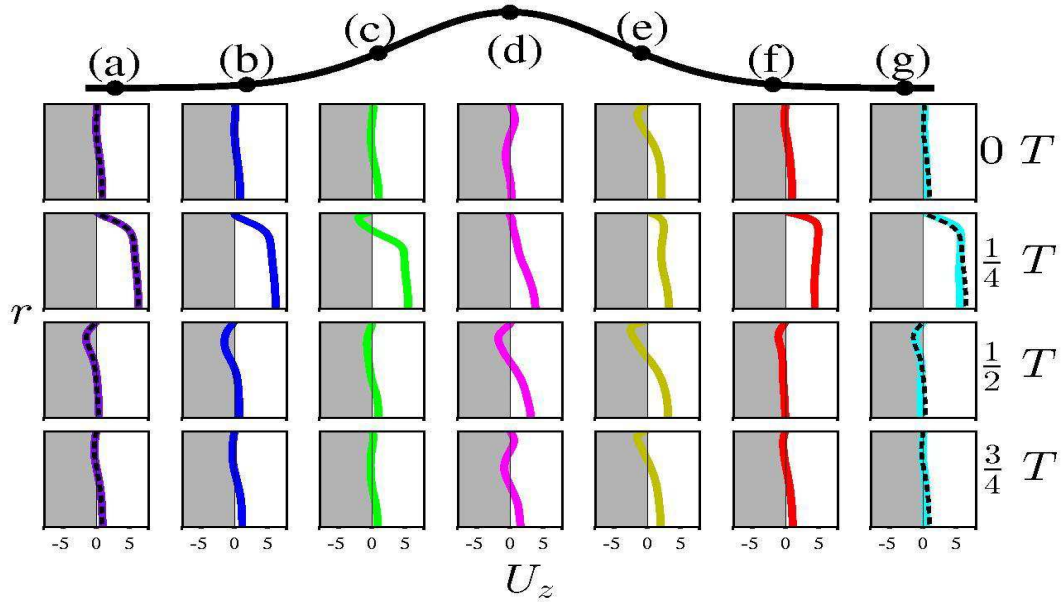
Figure 4.6: Axial velocities across a transverse cut at various axial locations ((a) $z = -1.86$ (b) $z = -1.24$ (c) $z = -0.62$ (d) $z = 0$ (e) $z = 0.62$ (f) $z = 1.24$ (g) $z = 1.86$) during a pulse cycle. It is to be noted that the radial extent is from the vessel centerline to the AAA wall and hence varies across the AAA dilatation. Parameter settings: $Q1$, $Re = 264$, $Wo = 12$, $W = 0.5$, $H = 0.5$.

(Salsac *et al.*, 2006).

The complex vorticity patterns and flow fields result in interesting WSS distributions. This is shown in figure 4.7 at four different time instants within the cycle. With the increase in flow rate, WSS reaches its maximum at the downstream end of the aneurysm. At peak systole, the maximum value of WSS observed at the downstream end is about 1.7 times the value recorded in a healthy abdominal aorta. The minimum value of WSS is observed roughly at the center of the aneurysm, just upstream of the distal end. Close proximity of peak low WSS values followed by peak maximum WSS values affect the physiology of the arterial walls as it tends to pull the walls in opposite directions. As the pulse cycle advances, the WSS values diminish. Sheard (2009) observed a peak WSS value that was 2.4 times that recorded in a healthy vessel at peak systole, using the waveform used in the study carried out by Salsac *et al.* (2006) for a flow through a typical AAA during resting conditions. The differences in the observations could be associated to different flow rate waveform and geometry used in their study.

To determine how the WSS values in the aneurysm bulge differ from the levels recorded in healthy vessels, the mean WSS values are shown in figure 4.8(a). It is interesting to note that significant deviation from the values obtained in the straight tube sections are isolated to the aneurysm bulge, roughly $-1 < z < 1$. The minimum and maximum values of the magnitude of the WSS are 36% and 197% of the values found in the non-dilated tube sections, respectively. However, when considering the mean of the WSS itself, a peak is found 2.8 times greater than the mean level in the healthy vessel, and an opposite-signed
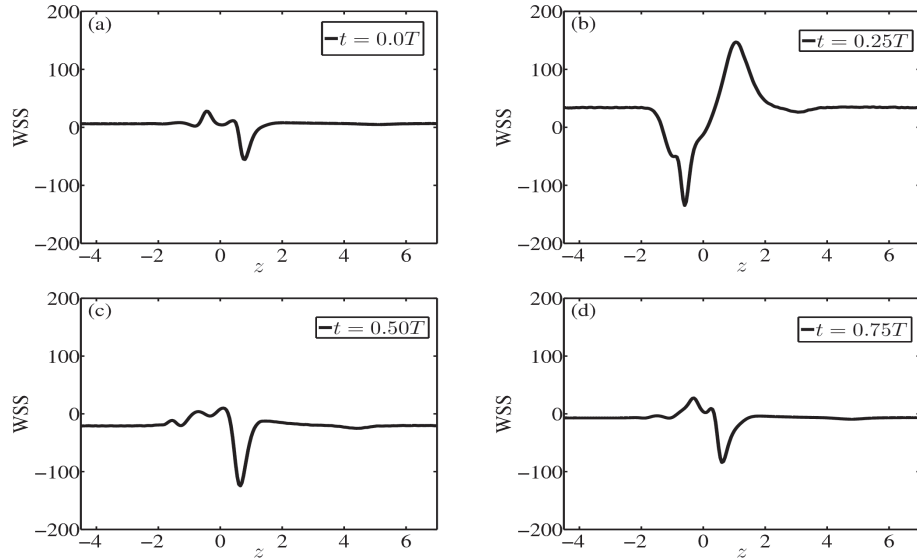
Figure 4.7: WSS distributions at various instants in a pulse cycle. Parameter settings: $Q1$, $Re = 264$, $Wo = 12$, $W = 0.5$, $H = 0.5$.
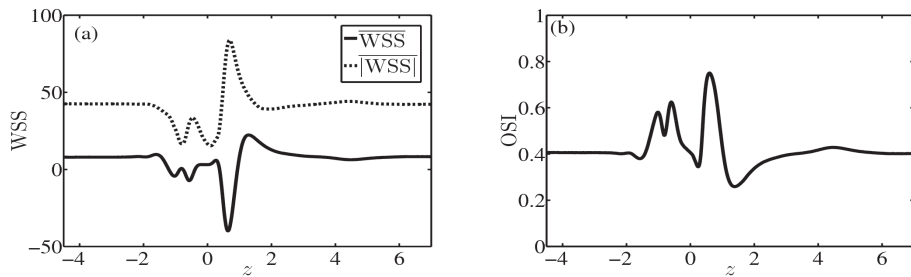

Figure 4.8: (a) Mean WSS ($\overline{\text{WSS}}$; solid line) and mean WSS magnitude ($\overline{|\text{WSS}|}$; dotted line). (b) Oscillatory shear index, OSI, given by equation (4.5). Parameter settings: $Q1$, $Re = 264$, $Wo = 12$, $W = 0.5$, $H = 0.5$.
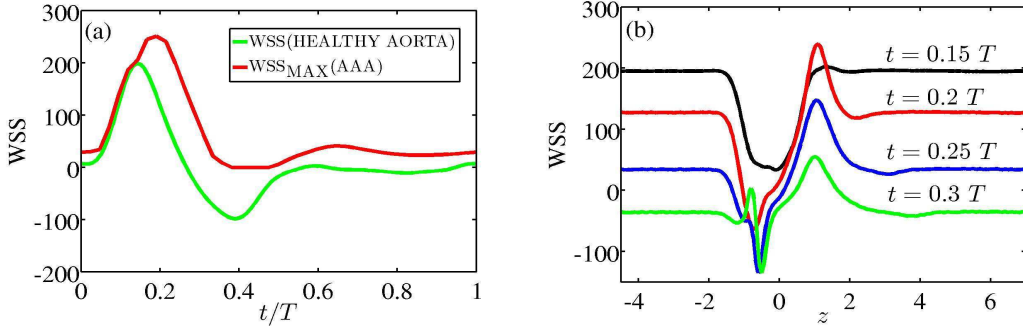
Figure 4.9: (a) Maximum WSS values computed in a healthy abdominal aorta compared with the values observed in the presence of an AAA during a pulse cycle. (b) WSS distributions at various instants around the accelerating and decelerating phases in a pulse cycle. Parameter settings: $Q1$, $Re = 264$, $Wo = 12$, $W = 0.5$, $H = 0.5$.

peak is found with a level 4.8 times greater than the healthy vessel. These extrema are located along adjacent sections on the wall of the AAA at the downstream end. Atherosclerotic lesions have usually been observed in the presence of an AAA (Lasheras, 2007). The presence of sharp spatial gradients along the aneurysmal wall caused due to the presence of an AAA may damage the endothelial cells, providing a possible explanation for the above observation (Jilkova *et al.*, 2013).

The oscillatory shear index, OSI, is shown in figure 4.8(b). The OSI index points out the regions of oscillatory WSS (OSI $\cong 0.5$) as well as the regions of mean forward (OSI < 0.5) or reversed (OSI > 0.5) WSS. Fluctuations in the OSI index were confined within the bulge region. In the straight tube sections, the OSI index was 0.41. Moving further down to the point where the mean WSS reaches its minima, the OSI index is found to attain its maximum of 0.75. Further downstream at the distal end, where the WSS mean reaches its maxima, the OSI index value drops again. Most of the aneurysm wall experiences an OSI index larger than 0.5, which indicates that significant reversal of WSS occurs during the cycle. This further corroborates our earlier observation on damaging hemodynamic conditions, favorable for atherosclerosis, present within an AAA.

It is important to note that though the maximum WSS at peak systole is 1.7 times that of the value observed in a healthy vessel, the maximum WSS observed in the presence of an AAA is only 1.26 times the peak WSS observed in a healthy abdominal aorta. This is due to the fact that the maximum WSS observed in a healthy abdominal aorta occurs slightly before peak systole (Pedley, 1979)(see figure 4.9(a)). The slow-moving fluid near the wall responds more readily to variations in the driving pressure gradient than the faster-moving fluid in the core. This observation is further elucidated in figure 4.9(b) where the WSS distributions around peak systole ($t = 0.18\ T$) are shown. The maximum value observed in the presence of an AAA is found to occur at peak systole. It has to be kept in mind that the peak WSS values observed in the presence of an AAA (particularly at the distal end) are significantly higher during most of the cycle, than when compared to the values observed in a healthy abdominal aorta (see figure 4.9(a)). As mentioned earlier, dynamic low oscillatory WSS distributions along with spatial gradients over the wall could contribute to an unstable
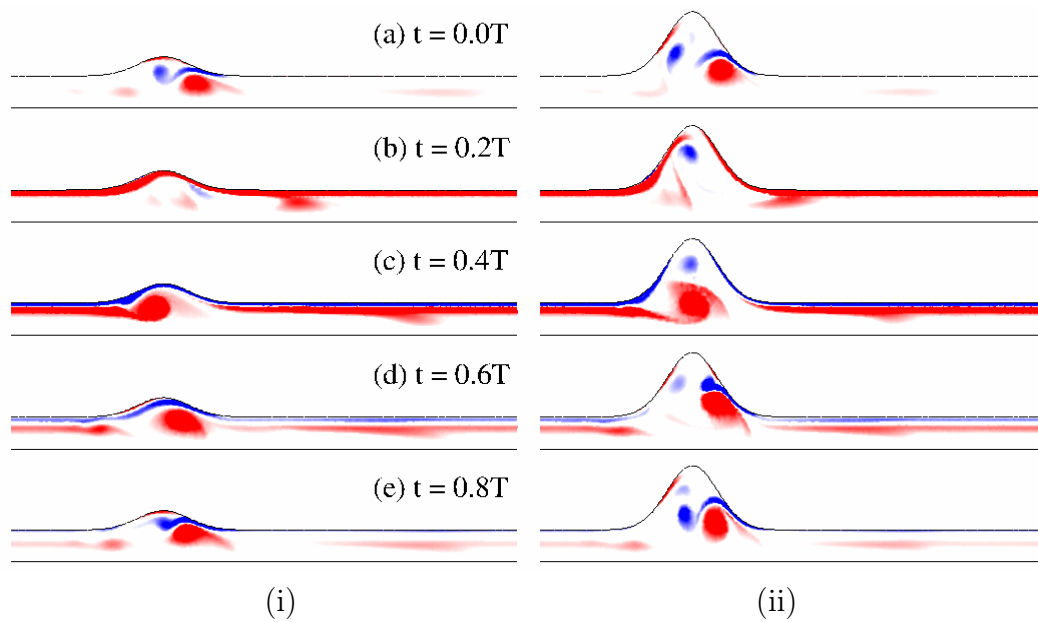
Figure 4.10: Dimensionless out-of-plane vorticity contours plotted at different time instants in a pulse cycle. Contours are plotted between -20(blue) and +20(red). Parameter settings: $Q1$, $Re = 264$, $Wo = 12$, $W = 0.5$. (i) $H = 0.3$ (ii) $H = 1.0$.

progressive degradation of the arterial wall and to the formation of atherosclerotic lesions (Lasheras, 2007, Barakat, 2013).

4.3.2   Effect of dilatation parameter

Flow fields

The effect of dilatation ratio, D_R, which is the ratio of the maximum diameter to the inlet diameter and given by $D_R = 1 + 2H^\star/D^\star$, is investigated by varying the non-dimensional bulge height H. For this the width of the aneurysm, W, is kept the same as the value used for a typical AAA ($W = 0.5$). Figure 4.10 shows the vorticity at various time instants for two different values of height: $H = 0.3$ and $H = 1.0$. A remarkable feature is that the clinically relevant flow characteristics of aneurysmal flows, i.e. detachment of the flow and impingement on the distal neck, occur even for a dilatation parameter as low as 1.6 ($H = 0.3$). However, for $H = 0.3$ as the bulge is shallow, the primary vortex is less localized within the bulge and subsequently the primary vorticity gets convected out of the bulge more easily. Also as there is less space within the bulge, the formation of a secondary vortex is delayed further. On the other hand, for the case of $H = 1.0$, as the bulge is relatively deeper, the vortices are trapped within the bulge. One can observe the presence of the secondary vortex persisting at all times within the bulge, even during the peak systole, due to the deeper cavity.

Figure 4.11 shows the streamlines at different time instants in a pulse cycle for two bulge heights: $H = 0.3$ and $H = 1$. Once again it is seen that even an incipient aneurysm is characterized by the formation of recirculating zones close to the wall. Flow separation occurs around the peak systole for both the aneurysms. These observations are in congruence
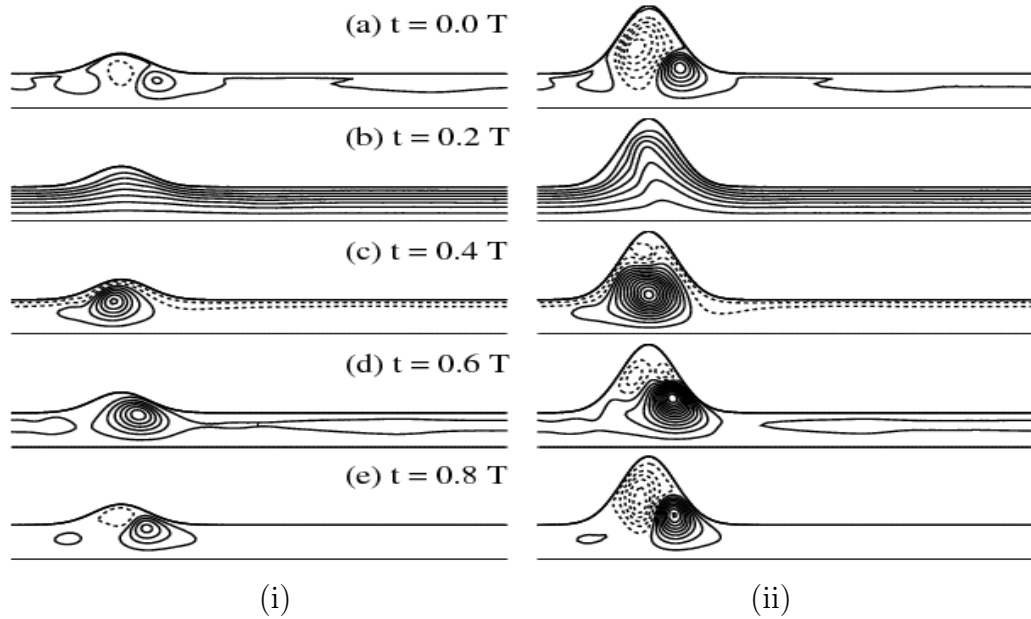
Figure 4.11: Streamlines at different time instants in a pulse cycle. Parameter settings: $Q1$, $Re = 264$, $Wo = 12$, $W = 0.5$. (i) $H = 0.3$ (ii) $H = 1.0$.

with the experiments carried out by Salsac (2005). However, at larger heights, multiple recirculating regions close to the wall can be observed. The presence of recirculating regions of flow and stagnation points are known to promote thrombosis (Vorp *et al.*, 2001). In the region of stagnant fluid zone of low WSS, cholesterol may tend to accumulate, leading to intimal thickening (Deplano & Siouffi, 1999).

We now take a closer look at the dynamics near the wall within the aneurysm. Figures 4.12 – 4.13 show the axial velocity across a transverse cut at various axial locations (same as in figure 4.6 across the aneurysm for $H = 0.3$ and $H = 1$, respectively. Once again the departure from the Womersley solution in a circular pipe is weak at the proximal and distal ends of an AAA, which is shown using dotted lines at points (a) and (g) respectively. As mentioned earlier, the features observed at a typical AAA persist even for shallow aneurysms. However, at axial points within the aneurysm ((c)–(e)), the temporal fluctuations near the wall are significant even for shallow aneurysms. These observations indicate that the disturbed flow conditions that play a role in degradation of the arterial wall and in the localization of atherosclerotic lesions are already present during the incipient stages of an AAA and could play a role in its progression. The effect of different velocity gradients close to the wall can lead to different WSS distributions, which is discussed in the subsequent section.

WSS distributions

The WSS distributions at various instants in a pulse cycle are shown for $H = 0.3$ and $H = 1$ in figure 4.14(a) and (b) respectively. It is found that the WSS variation along the aneurysm wall is similar to that observed for $H = 0.5$ (see figure 4.7).
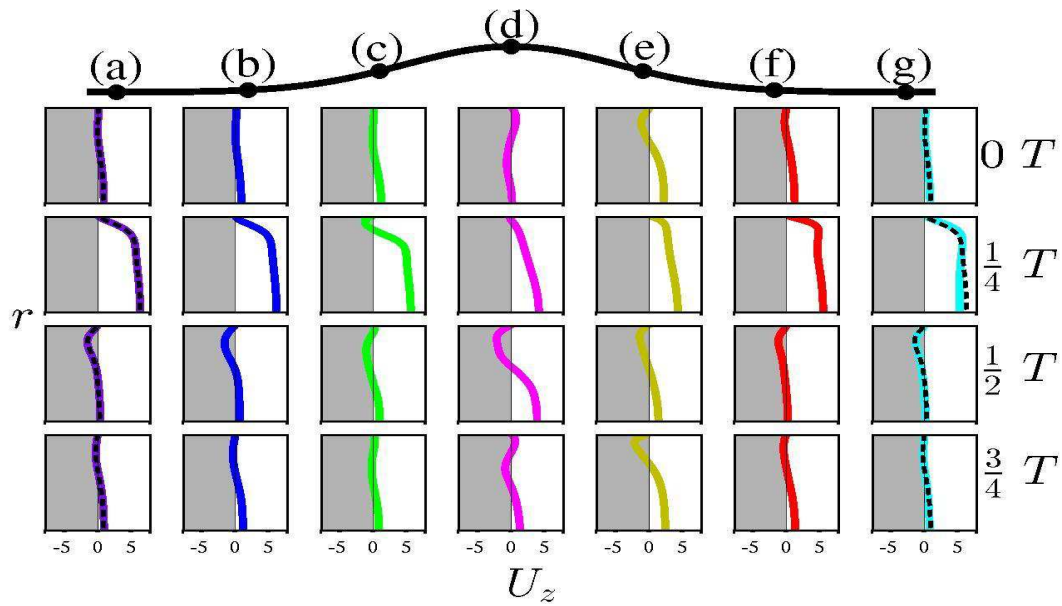
Figure 4.12: Axial velocities across a transverse cut at various axial locations ((a) – (g), same as in figure 4.6) during a pulse cycle. Parameter settings: $Q1$, $Re = 264$, $Wo = 12$, $W = 0.5$, $H = 0.3$.
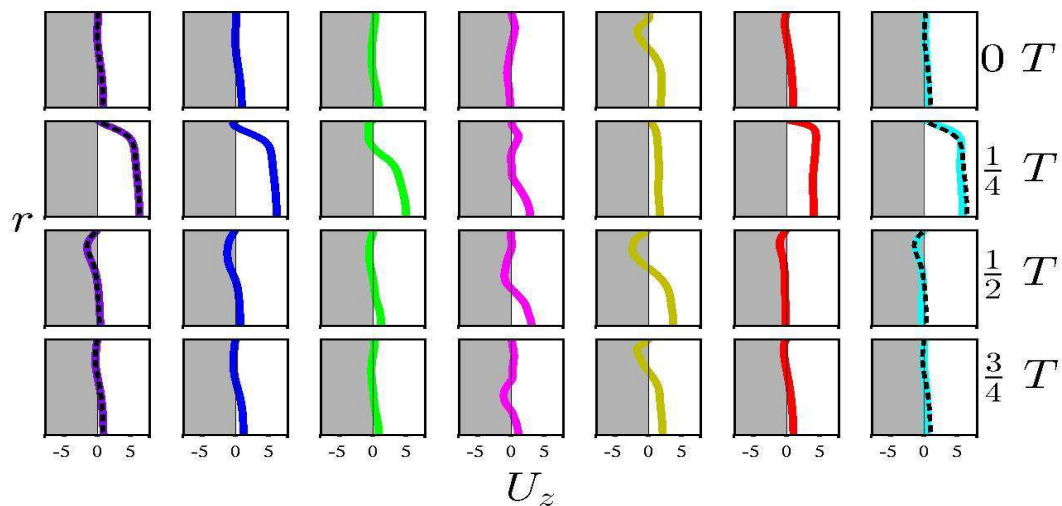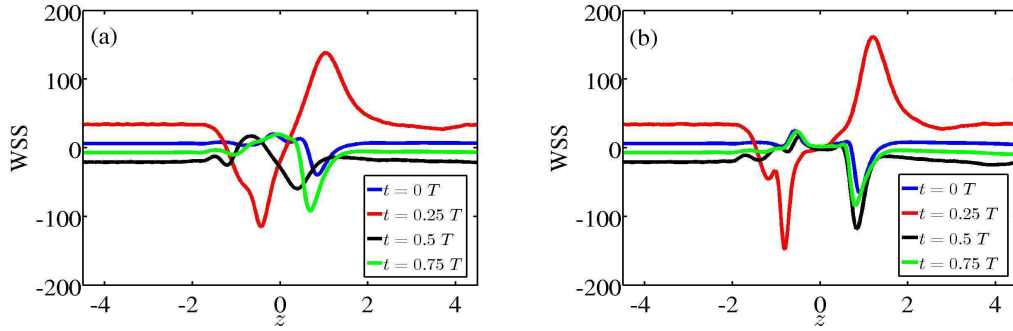

Figure 4.13: Same as in figure 4.12 but for $H = 1$.

Figure 4.14: WSS distributions at various instants in a pulse cycle. Parameter settings: $Q1$, $Re = 264$, $Wo = 12$, $W = 0.5$ (a) $H = 0.3$ (b) $H = 1$.
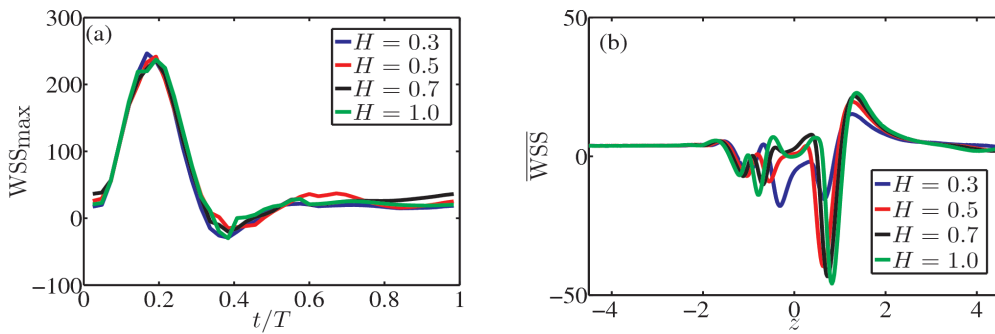

Figure 4.15: (a) Maximum WSS during a pulse cycle for various bulge heights. (b) Time-averaged WSS along the aneurysm wall for various bulge heights. Parameter settings: $Q1$, $Re = 264$, $Wo = 12$, $W = 0.5$.

During the deceleration phase just after peak systole ($t = 0.25\ T$), the minimum WSS value is observed at the proximal end, which slowly migrates towards the distal end during the pulse cycle. The principal effect of increasing H is that the spatial gradients along the wall are enhanced. However, the recirculation region does vary much with H.

The peak WSS observed along the aneurysm wall as function of time is shown in figure 4.15(a) for different values of H. The peak WSS value which is observed at the distal end of the aneurysm is seen to be largely independent of bulge height. The spatial distribution of the time-averaged WSS is shown in figure 4.15(b). Once again the spatial distributions are found to remain qualitatively similar for different H. Though the minimum value of WSS which is usually observed slightly upstream of the distal end is seen to increase sharply initially, when H is increased from 0.3 to 0.5. Two things emerge from the above discussion. Firstly, peak WSS value does not seem to be a significant quantity to be monitored during the growth of an aneurysm as it remains relatively constant. Secondly, as the WSS distributions remain qualitatively similar for shallow and deep aneurysms, it appears that the flow shear stresses may not be the determinant factor controlling the expansion of fusiform aneurysms, especially during the later stages. However, spatial distribution of WSS, particularly dynamic low oscillatory shear stresses and sharp spatial gradients, could play a key role during the incipient stages of growth, as these are associated with atherosclerotic plaque deposition and intimal thickening (Ku, 1997, Deplano & Siouffi, 1999).

4.3.3 Effect of aspect ratio

Flow fields

A large value of W and a small value of H is representative of an AAA during its initial stage and hence it is important to understand the dynamics at larger W. The aspect ratio is varied here by changing the value of bulge width W from 0.5 to 1. Figure 4.16 shows the vorticity distributions at various instants in a cycle for two different bulge heights ($H = 0.3$ and $H = 1$) at $W = 1$.

It is seen that the vorticity distributions are very different from those observed for $W = 0.5$ (see figure 4.10). Firstly, the flow remains attached for longer times even after the peak systole unlike at $W = 0.5$. Hence the primary vortex is formed much later during the decelerating phase after peak systole and is hence much weaker. Due to this the primary vortex does not travel till the downstream end and is not strong enough to induce vortices of opposite sign within the bulge during the diastolic phase. Also, since it is weak by the time it impinges at the distal end, the roll-up of the shear layer is absent. A similar observation has been made by Salsac (2005) who found out the length traveled by the vortex ring scales inversely with the aspect ratio. They also observed that the time at which flow separation occurred during the pulse cycle is delayed with increasing aspect ratio. The above phenomenon is further illustrated using some representative streamlines shown in figure 4.17 at the same parameter settings. It is clearly seen that the flow remains attached even after the systolic phase. The above discussion implies that longer aneurysms are less pathological than short ones, even though the disturbed flow conditions are already present for an incipient AAA.

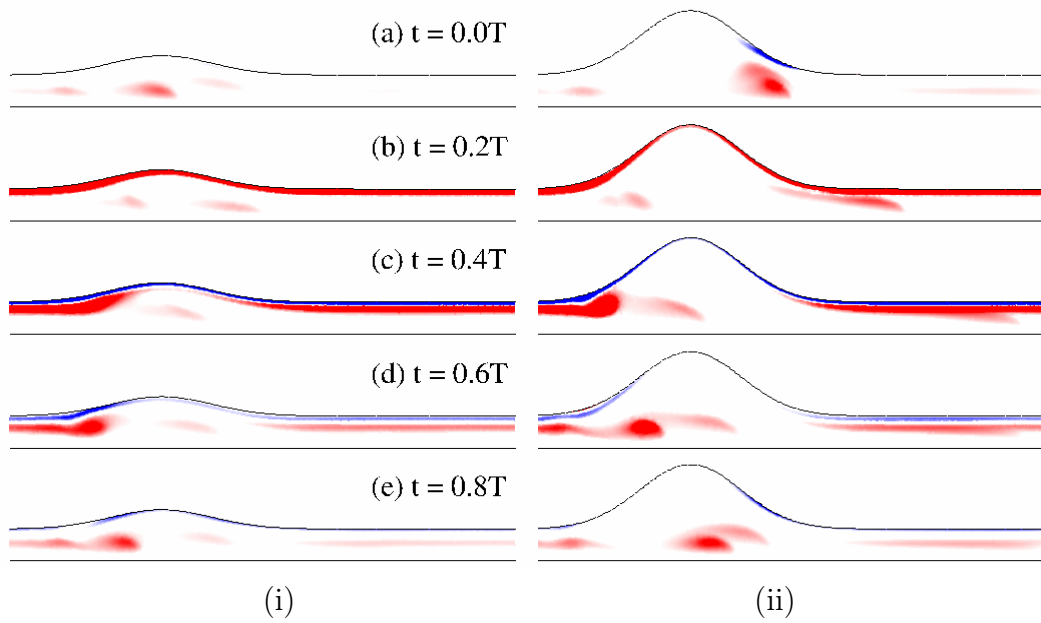Similarly, the near wall dynamics illustrated by transverse cuts of axial velocity at

Figure 4.16: Dimensionless out-of-plane vorticity contours plotted at different time instants in a pulse cycle. Contours are plotted between -20(blue) and +20(red). Parameter settings: $Q1$, $Re = 264$, $Wo = 12$, $W = 1.0$. (i) $H = 0.3$ (ii) $H = 1.0$.
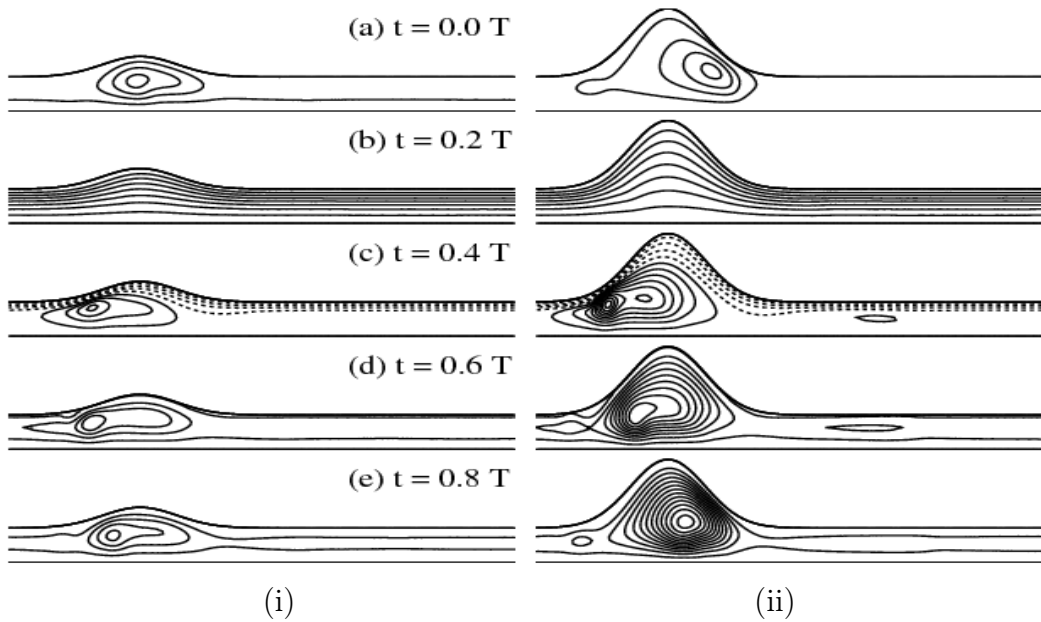

Figure 4.17: Streamlines at different time instants in a pulse cycle. Parameter settings: $Q1$, $Re = 264$, $Wo = 12$, $W = 1.0$. (i) $H = 0.3$ (ii) $H = 1.0$.
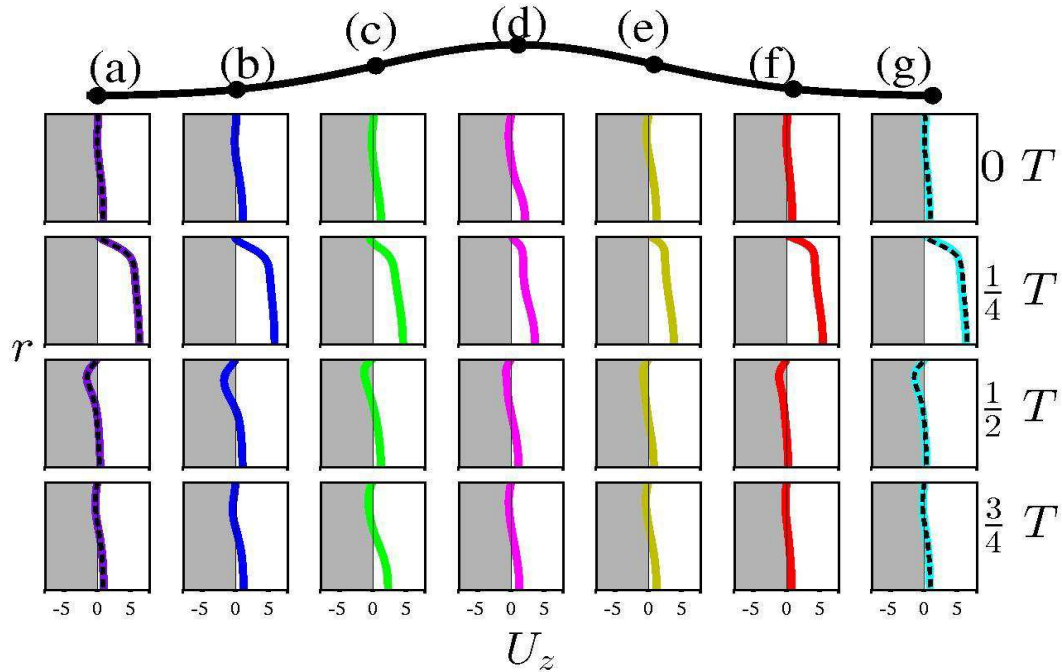
Figure 4.18: Axial velocities across a transverse cut at various axial locations ((a) $z = -3$ (b) $z = -2$ (c) $z = -1$ (d) $z = 0$ (e) $z = 1$ (f) $z = 2$ (g) $z = 3$) during a pulse cycle. Parameter settings: $Q1$, $Re = 264$, $Wo = 12$, $W = 1$, $H = 0.3$.
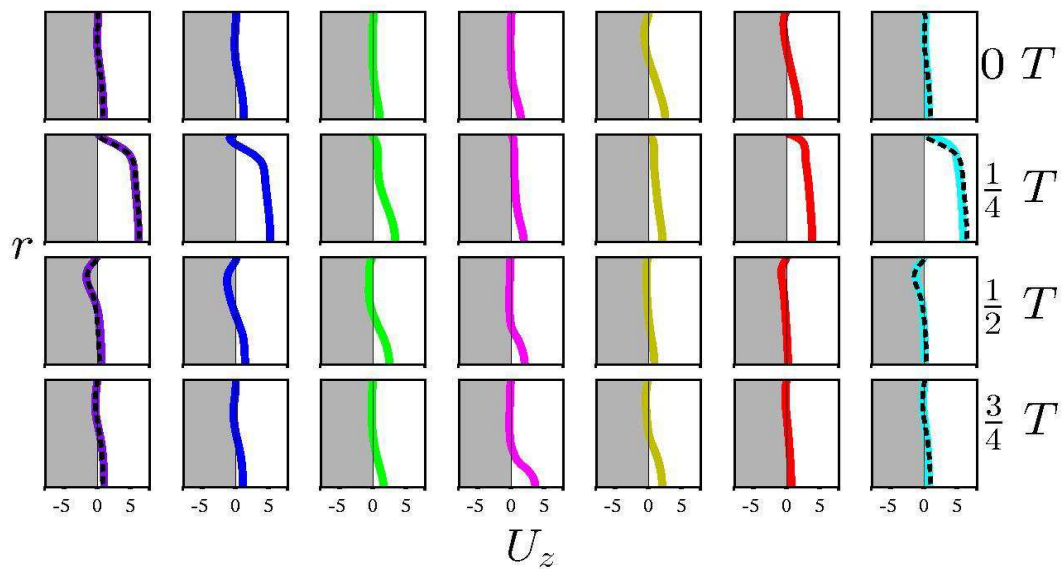

Figure 4.19: Same as in figure 4.18 but for $H = 1$.
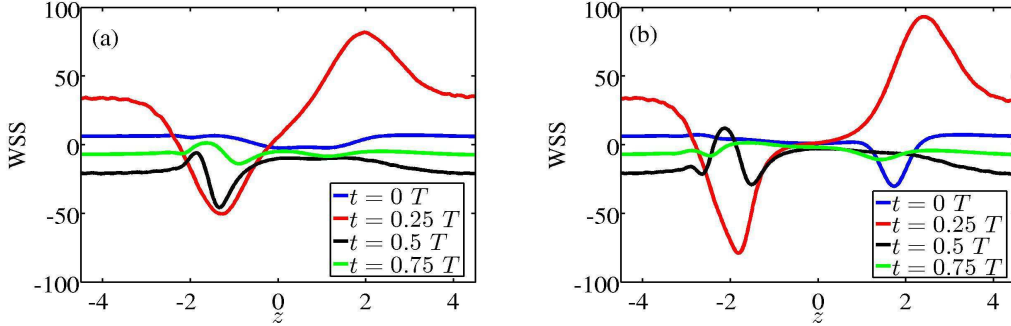
Figure 4.20: WSS distributions at various instants in a pulse cycle. Parameter settings: $Q1$, $Re = 264$, $Wo = 12$, $W = 1$ (a) $H = 0.3$ (b) $H = 1$.

different axial locations within an aneurysm, differ from the situation at $W = 0.5$. This is shown in figures 4.18 – 4.19 for $H = 0.3$ and $H = 1$ respectively. The axial locations are mentioned in the caption. Note again that as the bulge height varies along an AAA in the plots, the radial extent from the vessel centerline to the AAA wall is different for different axial locations in the plots. Firstly, the temporal fluctuations near the wall are less prominent. Secondly, variation along the aneurysm wall is also markedly less, and is confined to the AAA cavity, as can be deduced from the Womersley flow profiles shown at points (a) and (g) obtained from calculations made in a circular pipe. These observations once again suggest that longer aneurysms are less pathological. Also the temporal variations are more prominent at lower H as also seen at $W = 0.5$. This can be clearly observed at the axial location (d). For $H = 1$, the temporal variation near the wall is practically zero, unlike at $H = 0.3$. This indicates that the changes experienced on the aneurysm wall during its incipient stages could have a higher influence on the arterial wall, particularly with regards to endothelial cell alignment.

WSS distributions

The WSS distributions at two characteristic bulge heights $H = 0.3$ and $H = 1$ are shown in figure 4.20(a) and (b) respectively, at a bulge width $W = 1$. The first striking difference from the distributions observed at smaller widths (see figure 4.14) is that the spatial variations along the arterial wall are weaker. The minimum and maximum values are observed at the proximal and distal end respectively, though their values are significantly smaller than at $W = 0.5$. Secondly, the temporal variations are also weaker during the pulse cycle at larger widths. Except during the systolic phase, the WSS values are approximately the same as the ones observed in a healthy abdominal aorta.

As seen earlier at $W = 0.5$, even for longer aneurysms the peak WSS value hardly depends on bulge height as shown in figure 4.21(a). It is to be noted that the peak WSS value is lower than at $W = 0.5$ and is close to the values observed in a healthy abdominal aorta. The time-averaged WSS along the aneurysmal wall remains qualitatively similar at all H's at $W = 1$. Unlike at $W = 0.5$ where the minimum WSS value was observed slightly upstream of the distal end, at $W = 1$ the minimum and maximum values of WSS are well separated and are observed at proximal and distal ends respectively. This is another favorable indication in relation to the effect of mechanical stimuli on arterial wall, as the spatial gradients are weaker for longer aneurysms.
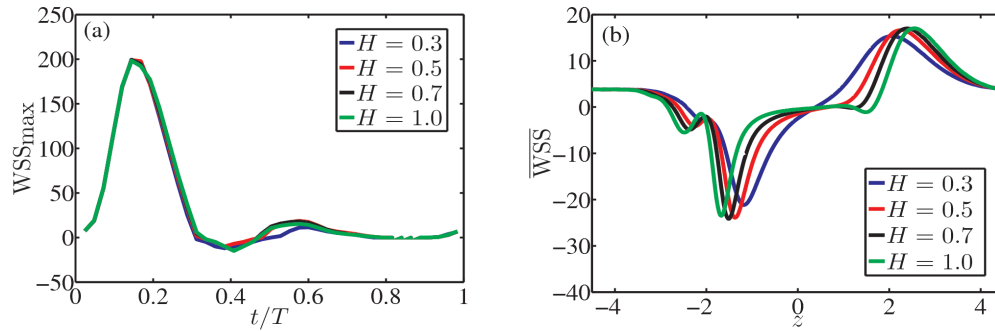
Figure 4.21: (a) Maximum WSS during a pulse cycle for various bulge heights. (b) Time-averaged WSS along the aneurysm wall for various bulge heights. Parameter settings: $Q1$, $Re = 264$, $Wo = 12$, $W = 1$.
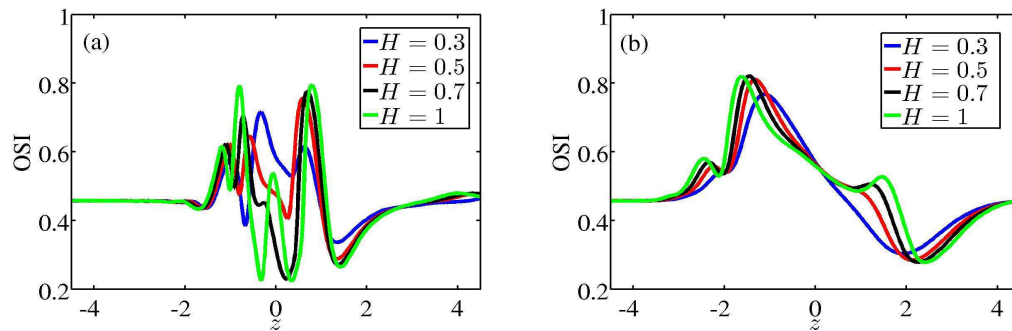

Figure 4.22: Comparison of OSI values at two different bulge widths for various bulge heights. Parameter settings: $Q1$, $Re = 264$, $Wo = 12$ (a) $W = 0.5$ (b) $W = 1$.
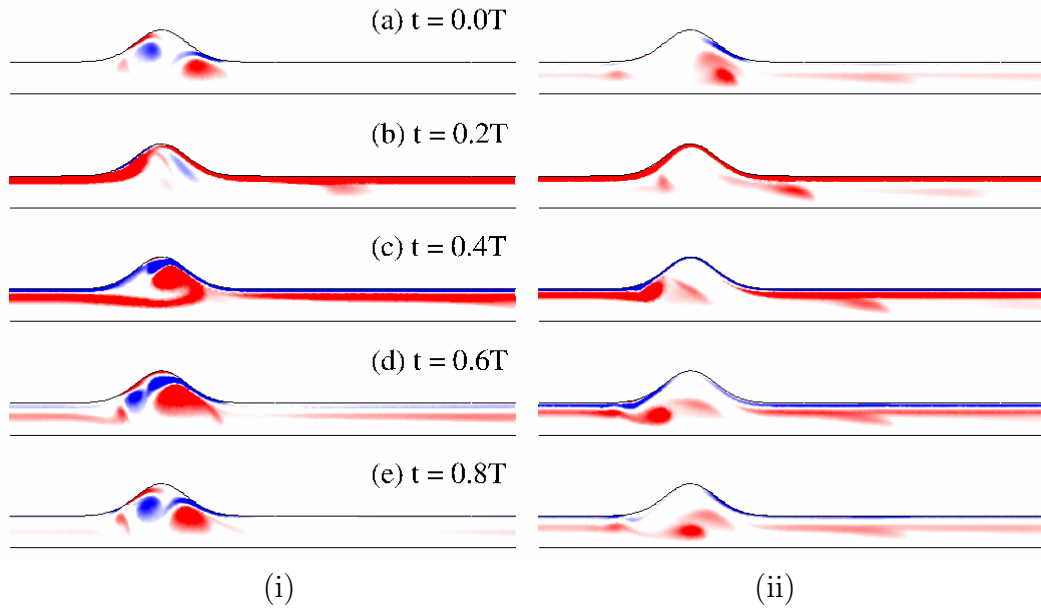
Figure 4.23: Dimensionless out-of-plane vorticity contours plotted at different time instants in a pulse cycle. Contours are plotted between -20(blue) and +20(red). Parameter settings: $Q1$, $Re = 264$, $H = 0.5$, $W = 0.5$ (i) $Wo = 10$ (ii) $Wo = 15$.

The OSI parameters, indicative of oscillatory flow conditions, along the AAA wall at two different widths $W = 0.5$ and $W = 1$ are shown in figure 4.22(a) and (b) respectively. These figures once again show that shorter aneurysms have higher stress fluctuations within the aneurysm bulge than longer aneurysms. All of the above discussion points to the fact that longer AAAs are less pathological and have weaker effect on physical processes that occur inside the AAA. These observations are in good agreement with those made by Salsac (2005).

4.3.4   Effect of Womersley number

Flow fields

The flow characteristics in the abdominal aorta vary substantially over time, depending on the physical activity that a person is engaged in. In this section we discuss how the Womersley number Wo, influences the flow characteristics discussed in previous sections. One of the principal parameters that change with physical activity is the pulsation frequency that is directly related to the Womersley number. However, a change in Womersley number is usually accompanied by a change in the flow rate waveform and the Reynolds number. But in order to isolate the effects of various flow parameters, it has been decided to keep the Reynolds number and the flow rate waveform fixed for the present discussion. The Reynolds number and the geometrical parameters are those used to model a typical AAA: $Re = 264$, $W = 0.5$ and $H = 0.5$. The Womersley number is varied between 5 to 15. The range of Wo usually observed in the abdominal aorta is 10 and 15, and hence forms the main focus of our discussion.
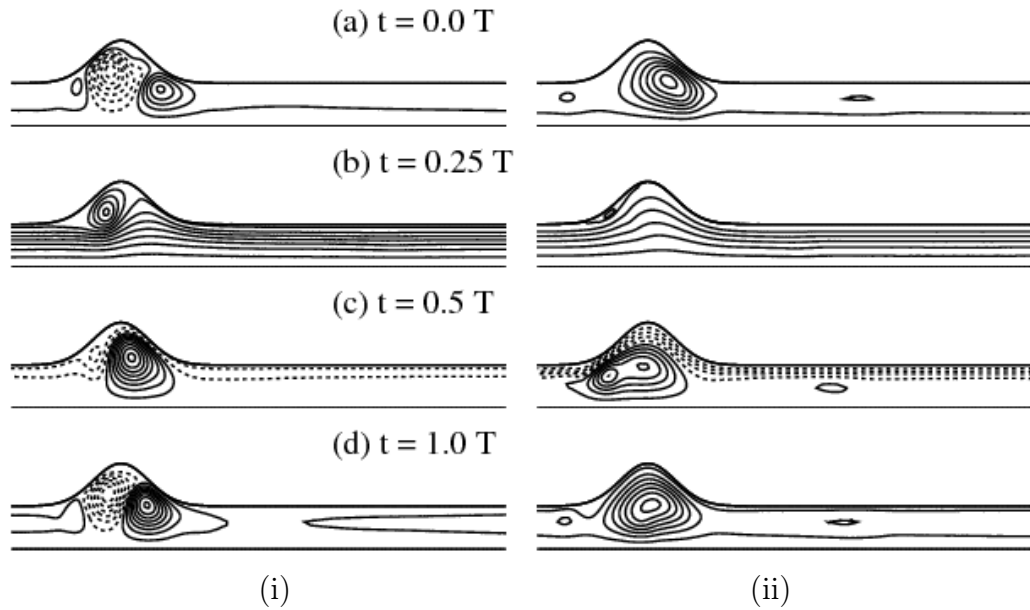
Figure 4.24: Streamlines at different time instants in a pulse cycle. Parameter settings: $Q1$, $Re = 264$, $H = 0.5$, $W = 0.5$ (i) $Wo = 10$ (ii) $Wo = 15$.

Figure 4.23 shows the vorticity evolution at various time instants during the pulse cycle for two different values of Wo, 10 and 15. It can be seen that the characteristics are very different as the Womersley number is increased. When all the other parameters are kept fixed, an increase in Wo corresponds to an increase in the frequency of pulsation (as Wo^2). In that case, an increase in Womersley number from 10 to 15, results in an increase in frequency by more than a factor of 2. At a lower frequency, the shear layer is seen to roll up forming a primary vortex within the bulge, similar to the features observed at $Wo = 12$. However with increase in frequency, the roll-up of the shear layer is less prominent and an opposite signed vortex is not formed within the bulge. This is also due to the fact that the flow separation is delayed at higher Womersley numbers. This once again indicates that the primary vortex formed at a higher Wo is much weaker. These arguments are further exemplified using snapshots of some representative streamlines at these two Womersley numbers in figure 4.24. Higher spatial fluctuations within the aneurysm are observed at lower Womersley numbers.

The dynamics prevailing near the wall are illustrated by transverse cuts of the axial velocity, shown in figures 4.25 – 4.26. Firstly, when considering the spatial variations along the wall at a fixed instant in the pulse cycle, it is seen that the fluctuations are more pronounced at a lower Wo. Secondly, when considering the temporal changes at a fixed location along the wall, it is also seen that these are higher at a lower Wo. The above discussion points that the disturbed flow conditions within an AAA are reduced with an increase in Wo. As an increase in Wo is usually associated with an increase in physical activity, these observations point to one possible benefit of exercise.

Finally, streamlines and vorticity distribution at various instants in a pulse cycle for $Wo = 5$
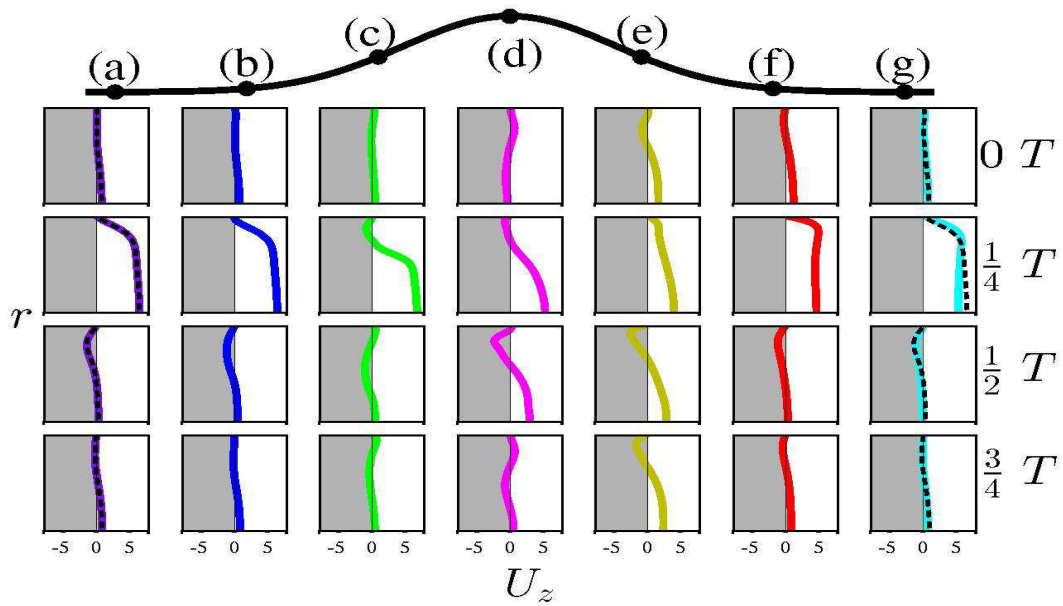
Figure 4.25: Axial velocities across a transverse cut at various axial locations ((a) – (g), same as in figure 4.6) during a pulse cycle. Parameter settings: $Q1$, $Re = 264$, $W = 05$, $H = 0.5$, $Wo = 10$.
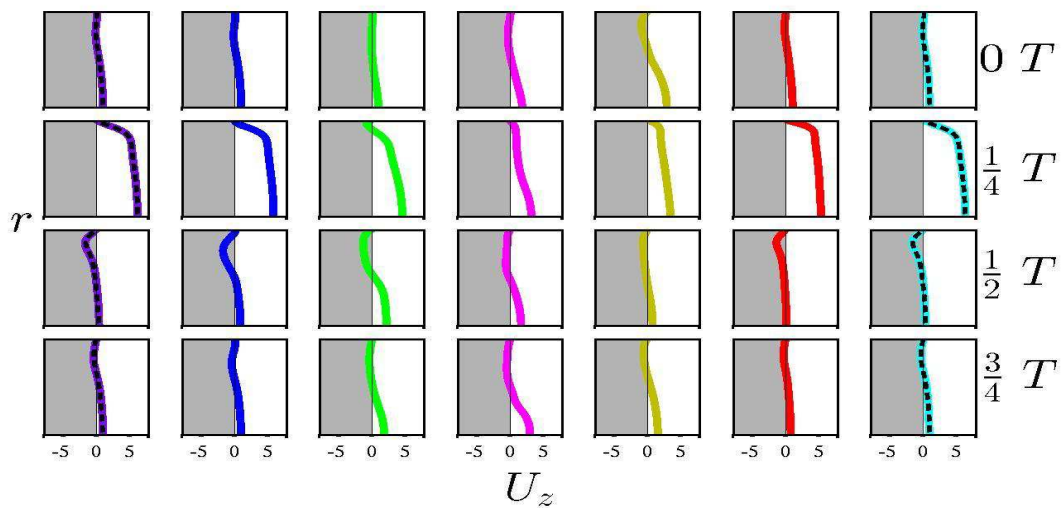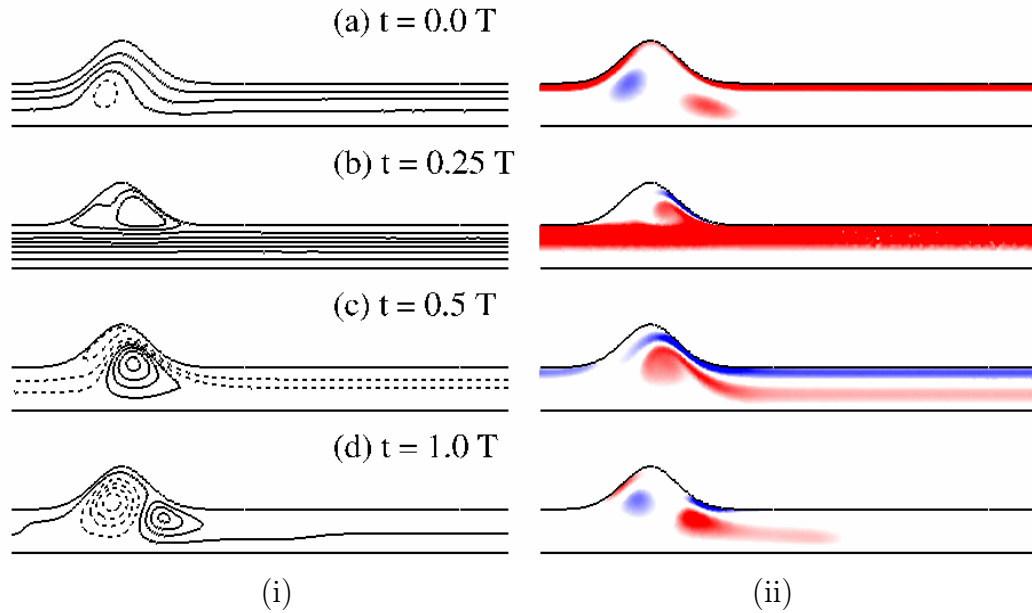

Figure 4.26: Same as in figure 4.25 but for $Wo = 15$.

Figure 4.27: (i) Streamlines and (ii) vorticity snapshots at different time instants in a pulse cycle (contours are plotted between -20(blue) and +20(red)). Parameter settings: $Q1$, $Re = 264$, $H = 0.5$, $W = 0.5$, $Wo = 5$.

are shown in figure 4.27. Note that the vorticity contour levels are chosen differently at different time instants. This is due to the fact the vorticity values observed are significantly lower for such a small Wo. The flow remains attached for a longer duration and the roll-up of the shear layer during the decelerating phase after the peak systole is weak. During this phase, the streamlines and vorticity distributions resemble that of the limiting steady flow case, where a jet-like flow is observed through the bulk of the AAA with a slowly rotating vortex in the cavity.

WSS distributions

WSS distributions at Womersley numbers for the different flow conditions are shown in figure 4.28. Notable difference is mainly during the diastolic phase at $t = 0.5\ T$ where for $Wo = 10$, a minimum is observed slightly upstream of the distal end due to the formation of the negative vortex. Whereas for $Wo = 15$, as no negative vortex is formed, a minimum in the WSS is not observed. Also the WSS values within the AAA are comparable to the levels found in a healthy abdominal aorta at a higher Wo during most of the pulse cycle. Both the spatial and temporal oscillations of WSS are weaker at higher Wo. As usually higher Womersley numbers are encountered during exercise conditions, this may be an indication of the usefulness of doing exercise, though the waveform indeed would be different.

The above observations are again reflected in figure 4.29 where the time-averaged WSS along the arterial wall along with OSI parameter are shown. Figure 4.29(a) shows that the maximum and minimum values of the time-averaged WSS are lower at higher Wo. The OSI parameter shown in figure 4.29(b) also points towards a weaker oscillatory flow component in an AAA, at higher Wo. All the above observations point towards the
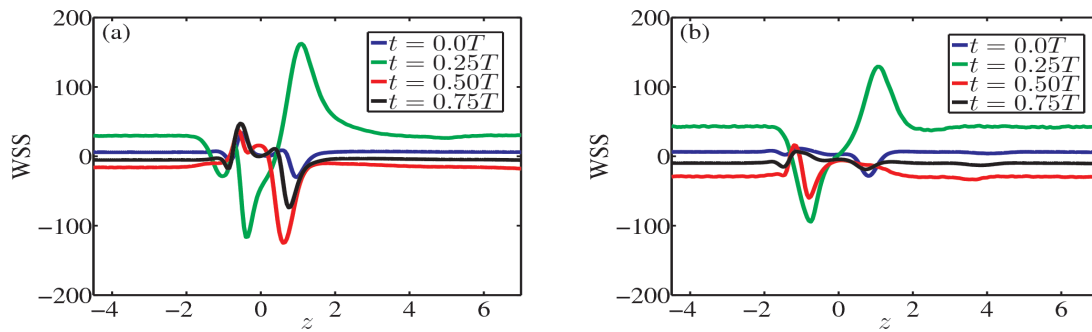
Figure 4.28: WSS at different time instants during a pulse cycle for two different Womersley numbers. Parameter settings: $Q1$, $Re = 264$, $H = 0.5$, $W = 0.5$. (a) $Wo = 10$ (b) $Wo = 15$.
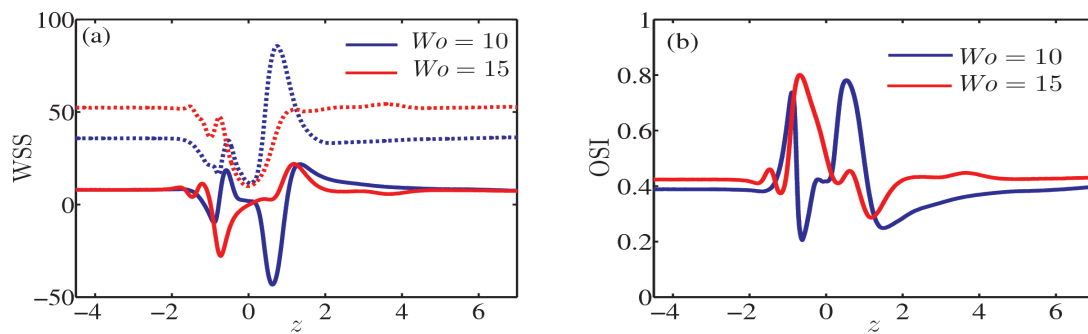

Figure 4.29: (a) Mean WSS ($\overline{\mathrm{WSS}}$; solid line) and its magnitude ($|\overline{\mathrm{WSS}}|$; dotted line). (b) OSI. Parameter settings: $Q1$, $Re = 264$, $H = 0.5$, $W = 0.5$.
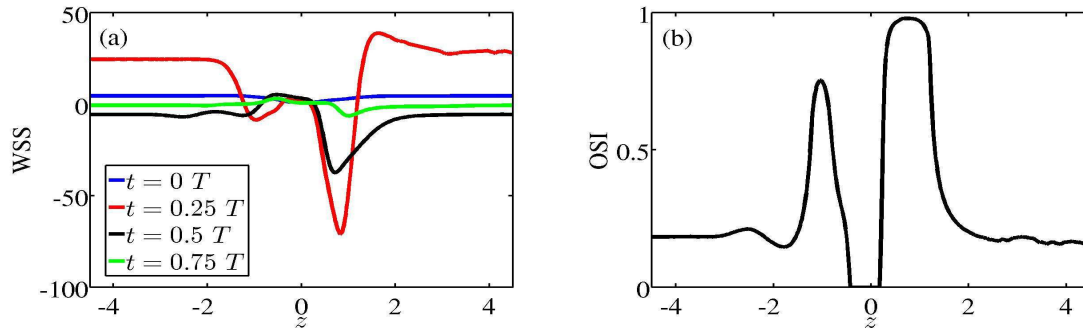
Figure 4.30: (a) WSS distributions at different time instants. (b) OSI. Parameter settings: $Q1$, $Re = 264$, $H = 0.5$, $W = 0.5$, $Wo = 5$.

fact that at higher Womersley numbers, usually observed during exercise conditions, the oscillatory shear stresses are reduced, thereby reducing hemodynamic conditions known to correlate with the location of atherosclerotic plaques and degradation of arterial wall. Though one has to keep in mind that along with an increase in Wo, the Reynolds number also increases with physical activity along with a change in flow rate waveform. Hence, these observations do not directly correspond to exercise conditions, which are discussed in the latter part of this chapter.

We conclude this section by a brief discussion on WSS characteristics observed at a low Womersley number, $Wo = 5$. Note that $Wo = 5$ is below the relevant range observed in the abdominal aorta. Figure 4.30(a) shows the WSS distributions at various time instants. It is seen that the WSS values are smaller at $Wo = 5$. However, deviations from a healthy abdominal aorta still prevail within the aneurysm cavity, though mainly during the systolic phase. During the major part of the cycle the WSS values within the aneurysm are hardly different from the upstream and downstream straight circular sections. The OSI parameter shown in figure 4.30(b) indicates the presence of entirely forward and reverse flows within the center of the aneurysm and at distal ends respectively. This is due to the low levels of oscillations at such a low Womersley number as the flow moves slowly forward and backward.

4.3.5   Effect of Reynolds number

Flow fields

As mentioned earlier, the Reynolds numbers observed in the abdominal aorta can vary from 600 at rest up to 6000 under exercise conditions. Similar to our analysis of the effect of Womersley number on flow characteristics, we fix all the other parameters in our study and vary the Reynolds number to isolate its effect. For this, the flow rate waveform corresponding to rest conditions is chosen, the geometry is the configuration corresponding to a typical AAA, the Womersley number is fixed at a value of 12, and the mean Reynolds number is varied from 200 to 500. This corresponds to a range of 1500 – 4000 for the peak Reynolds number.

Figure 4.31 shows the flow characteristics at $Re = 200$ and $Re = 500$. The principal effect
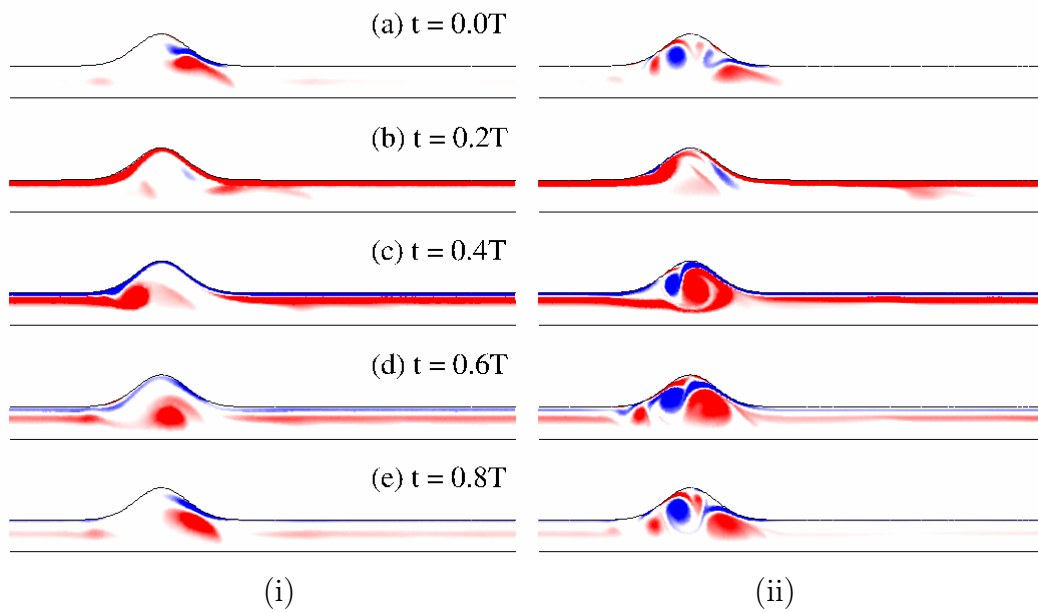
Figure 4.31: Dimensionless out-of-plane vorticity contours plotted at different time instants in a pulse cycle. Contours are plotted between -20(blue) and +20(red). Parameter settings: $Q1$, $Wo = 12$, $H = 0.5$, $W = 0.5$ (i) $Re = 200$ (ii) $Re = 500$.

Figure 4.32: Streamlines at different time instants in a pulse cycle. Parameter settings: $Q1$, $Wo = 12$, $H = 0.5$, $W = 0.5$ (i) $Re = 200$ (ii) $Re = 500$.

Figure 4.33: Axial velocities across a transverse cut at various axial locations ((a) – (g), same as in figure 4.6) during a pulse cycle. Parameter settings: $Q1$, $Wo = 12$, $W = 05$, $H = 0.5$, $Re = 200$.

Figure 4.34: Same as in figure 4.33 but for $Re = 500$.

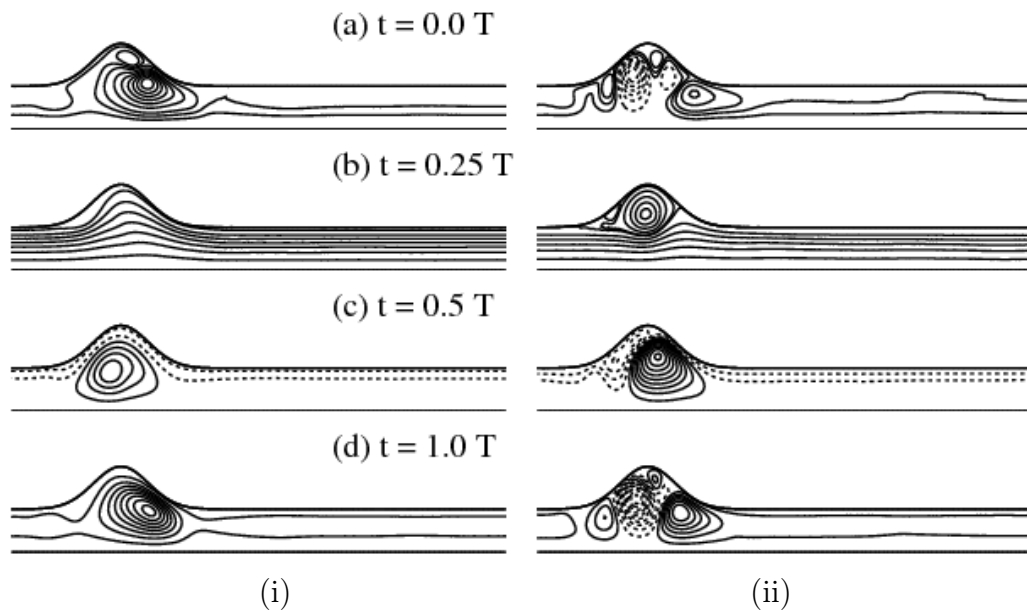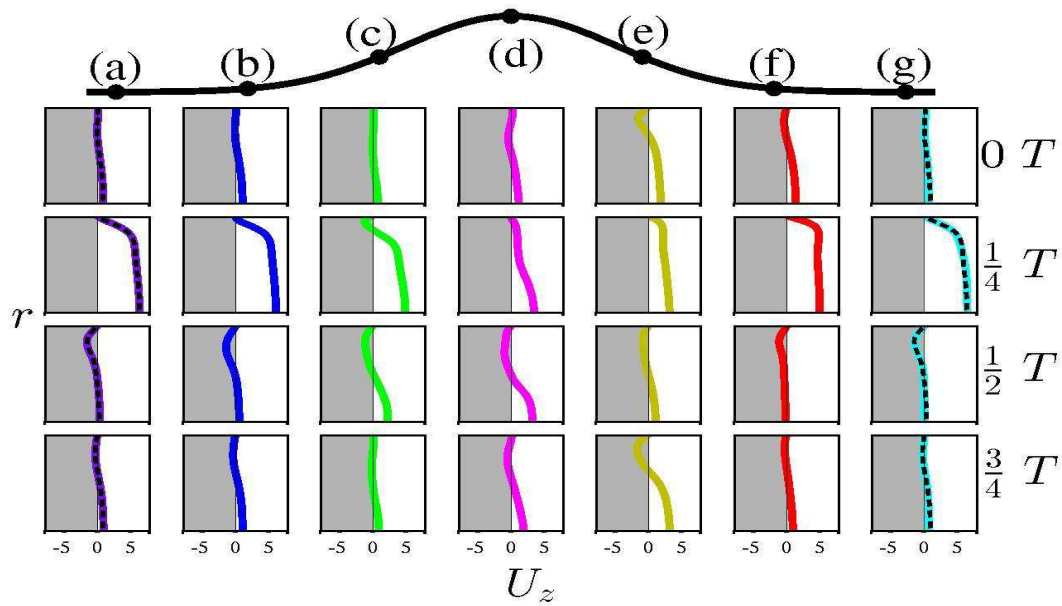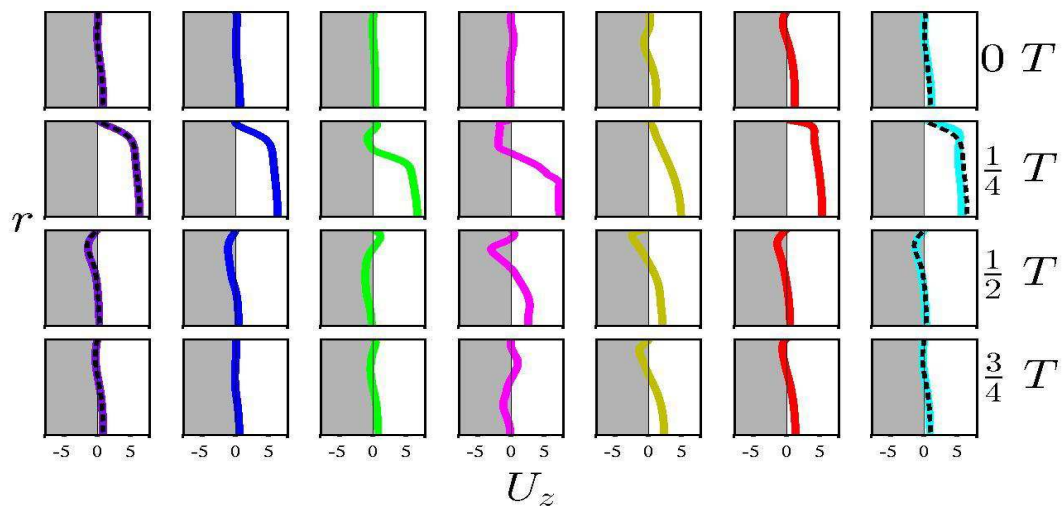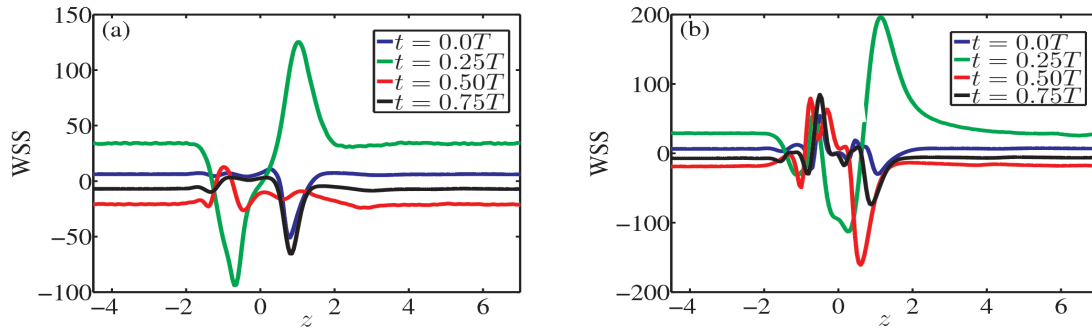Figure 4.35: WSS at different time instants during a pulse cycle for two different Reynolds numbers. Parameter settings: $Q1$, $Wo = 12$, $H = 0.5$, $W = 0.5$. (a) $Re = 200$ (b) $Re = 500$.

of increasing Reynolds number is that the primary vortex formed during the decelerating phase after peak systole is stronger. This is probably due to the flow separation taking place earlier at higher Reynolds numbers. The rolling up of the shear layer is more pronounced at higher Re. The primary vortex impinges at the distal end and is strong enough to induce vortices of opposite signs at higher Re. One can see from the snapshots of streamlines shown in figure 4.32 the absence of secondary vortices at a lower Re. Also the flow remains attached for a longer time at a lower Re. All these observations point out that the disturbed flow conditions are increased significantly with increasing Reynolds number.

Transverse cuts of axial velocity profiles shown in figures 4.33 – 4.34 reveal that both the spatial and temporal oscillations of the velocity gradients close to the wall are more prominent at a higher Reynolds number. Thus the flow characteristics at a higher Re are probably more detrimental to the arterial wall.

WSS distributions

The WSS distributions at $Re = 200$ and $Re = 500$ are shown in figure 4.35(a) and (b) respectively. Firstly, the peak WSS value observed during the systolic phase is higher at a higher Reynolds number. Secondly, significant positive WSS values appear near the proximal end (between $-1 < z < 0$) during diastolic phase at a higher Re which are absent at $Re = 200$. Thirdly, the peak minimum value observed upstream of the distal end is also higher with increasing Re. These observations mean that both the temporal and spatial gradients of WSS within the AAA increase with increase in Re.

The above observations are reflected in the time-averaged WSS distributions along the aneurysmal wall, shown in figure 4.36(a). The OSI parameter shown in figure 4.36(b) corresponds to highly oscillatory flow conditions within the AAA at a higher Re. These flow conditions are known to affect the etiology of the arterial wall leading to its degradation and formation of atherosclerotic lesions and could also play a role in the development of an AAA.
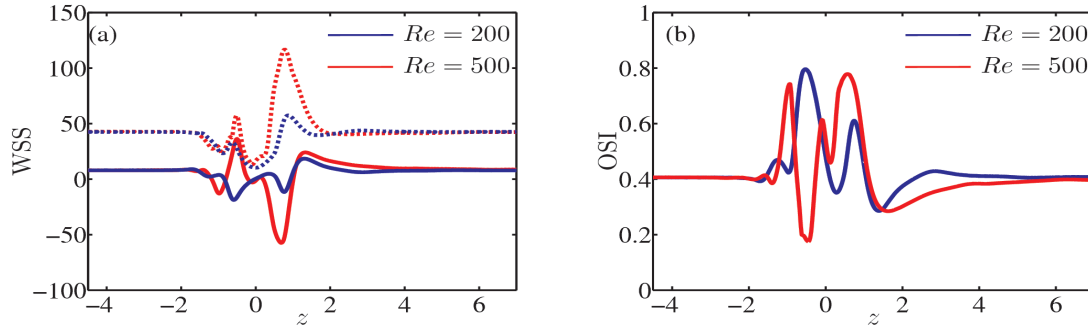
Figure 4.36: (a) Mean WSS ($\overline{\text{WSS}}$; solid line) and its magnitude ($\overline{|\text{WSS}|}$; dotted line). (b) OSI. Parameter settings: $Q1$, $Wo = 12$, $H = 0.5$, $W = 0.5$.

4.4   Flow characteristics in an AAA during exercise conditions

The flow characteristics in an AAA for a person in exercise conditions are presented in this section. The flow features in a typical AAA are presented first, followed by an investigation of the dependence of flow characteristics on geometrical configurations. The waveform used in this analysis corresponds to $Q2$ shown in figure 4.1. The associated Reynolds and Womersley numbers are $Re = 1700$ and $Wo = 13.8$, as derived from the physiological values provided in Suh *et al.* (2011) .

4.4.1   Typical flow in an AAA

First, the prominent features observed in a typical geometrical configuration are discussed, with the bulge width and height both fixed at a value of 0.5. Figure 4.37 shows the vorticity distribution during various instants in a pulse cycle. As the Reynolds number is high, a strong vortex is formed at the proximal end during flow deceleration after peak systole. The impingement of this strong vortex at the distal end results in high stresses along the arterial walls, particularly at the distal end. Then, an oppositely signed secondary vortex is formed similar to those observed during rest conditions in a typical AAA. However, as these vortices are much stronger, even a tertiary vortex, similar in sign to the primary vortex is formed within the bulge during the diastolic phase. This can be seen clearly in frame (f) corresponding to $t = 0.5\,T$, where the negative vortex pulls the vorticity in the shear layer to form a positive signed vortex. These positive vortices persist within the bulge during the major part of the pulse cycle. These observations are further illustrated in figure 4.38, where some representative streamlines are shown during the pulse cycle. The most significant result from these observations is that due to the increase in strength of the vortices at these elevated Reynolds numbers, along with the absence of reversed flow during the pulse cycle, the resulting flow fields are highly complex and the mixing of aneurysmal blood appears to be enhanced. Moderate levels of turbulence have been observed under exercise conditions (Les *et al.*, 2010). Such exercise-induced flow patterns with increased flow magnitude and moderate turbulence reduce regions of flow stasis that have been correlated with thrombus formation (Salsac *et al.*, 2004, Deplano & Siouffi, 1999, Reininger *et al.*, 1994).
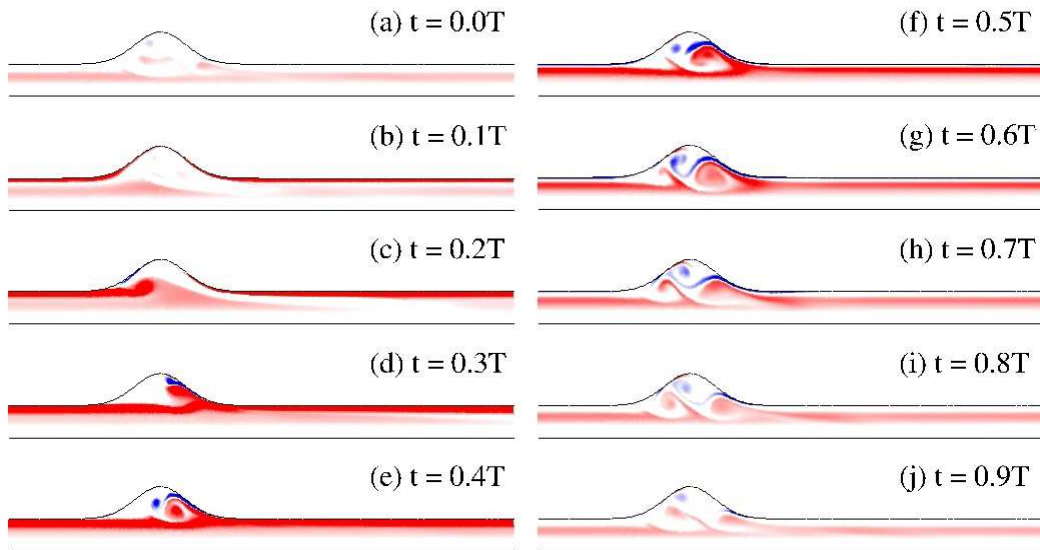
Figure 4.37: Dimensionless out-of-plane vorticity contours plotted at different time instants in a pulse cycle. Contours are plotted between -15(blue) and +15(red). Parameter settings: $Q2$, $Re = 1700$, $Wo = 13.8$, $H = 0.5$, $W = 0.5$.
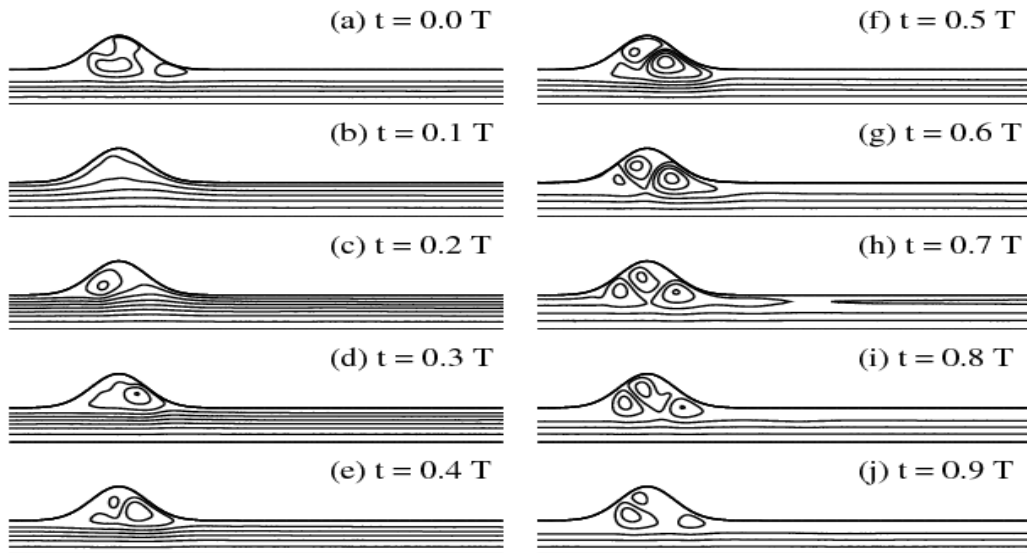

Figure 4.38: Streamlines at different time instants in a pulse cycle. Parameter settings: $Q2$, $Re = 1700$, $Wo = 13.8$, $H = 0.5$, $W = 0.5$.
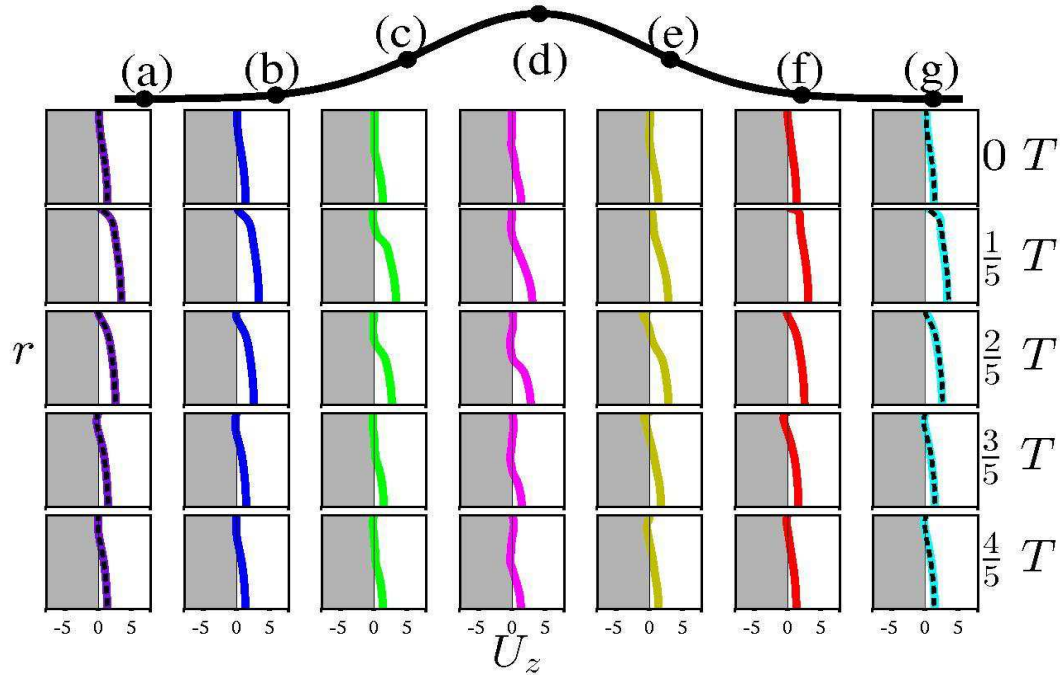
Figure 4.39: Axial velocities across a transverse cut at various axial locations ((a) – (g), same as in figure 4.6) during a pulse cycle. Parameter settings: $Q2$, $Re = 1700$, $Wo = 13.8$, $H = 0.5$, $W = 0.5$.

Since the flow fields observed within the AAA cavity appear to be complex, the near wall dynamics needs to be further investigated, as it is expected to govern the response of endothelial cells and subsequent degradation of the arterial wall. Figure 4.39 shows transverse cuts of axial velocity profiles along the AAA (same locations as in figure 4.6) at various instants in the pulse cycle. The first striking feature is that the velocity distribution near the wall hardly changes within the AAA cavity. Secondly, for profiles at locations (c) – (e), velocities are small near the wall and hardly depend on time. Hence, in this regard the magnitude of the fluctuations seems to be lower during exercise conditions than observed during resting conditions. Also, as expected, the deviation from a healthy abdominal aorta is confined to the AAA cavity as illustrated using the Womersley flow solutions shown using dotted lines at proximal (a) and distal ends (g).

To put these observations into perspective, the WSS distributions are monitored. The WSS variation during a pulse cycle is shown in figure 4.40. It is seen that both the peak maximum and minimum WSS values are localized at the downstream end. The spatial variations are highly localized within the AAA cavity. Once again sharp temporal and spatial changes in WSS occur along the wall. However, these changes prevail mainly at the distal end unlike the case of rest conditions where the fluctuations were spread over the entire AAA cavity.

To determine how the WSS measured in the aneurysm bulge differs from the levels recorded in healthy vessels, the mean WSS values are shown in figure 4.41(a). It is interesting to note that significant deviation from the values obtained in the straight tube sections are
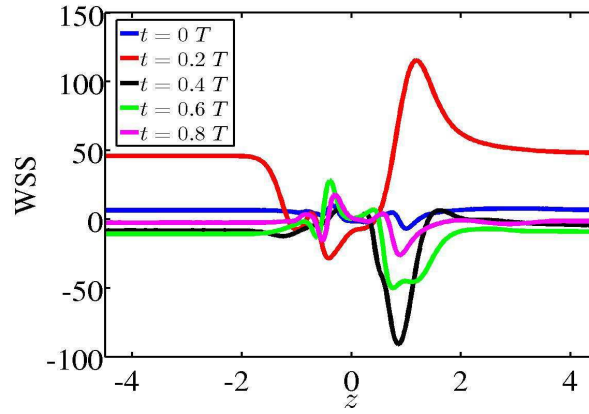
Figure 4.40: WSS distributions during a pulse cycle. Parameter settings: $Q2$, $Re = 1700$, $Wo = 13.8$, $H = 0.5$, $W = 0.5$.

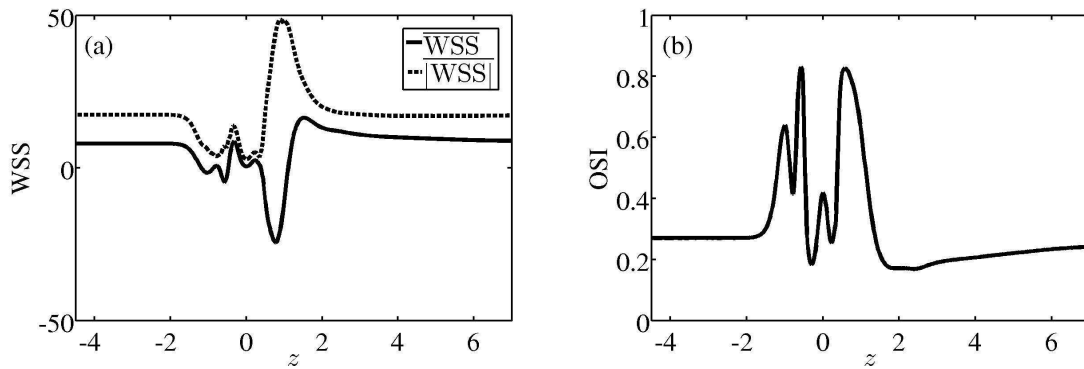Figure 4.41: (a) Mean WSS ($\overline{\text{WSS}}$; solid line) and its magnitude ($\overline{|\text{WSS}|}$; dotted line). (b) OSI. Parameter settings: $Q2$, $Re = 1700$, $Wo = 13.8$, $H = 0.5$, $W = 0.5$.

Figure 4.42: Dimensionless out-of-plane vorticity contours plotted at different time instants in a pulse cycle. Contours are plotted between -15(blue) and +15(red). Parameter settings: $Q2$, $Re = 1700$, $Wo = 13.8$, $W = 0.5$ (i) $H = 0.3$ (ii) $H = 1.0$.

confined to the aneurysm bulge, roughly $-1 < z < 1$. The minimum and maximum values of the magnitude of the WSS are 17% and 279% of the values found in the non-dilated tube sections, respectively. However, when considering the mean of the WSS itself, a peak is found double than the mean level in the healthy vessel, and an opposite-signed peak is found with a level 3 times greater than the healthy vessel. The spatial distribution of the OSI values shown in figure 4.41(b) were similar to those observed during rest conditions. Though the OSI values reached a maximum value of 0.8, they were not reduced to zero in the aneurysm in coherence with the observations made by Les *et al.* (2010).

4.4.2   Effect of variation in geometry

To begin with, the bulge height is increased while keeping the width fixed. The differences in vorticity evolution at two bulge heights $H = 0.3$ and $H = 1.0$ are shown for $W = 0.5$ in figure 4.42. Even at a low bulge height, $H = 0.3$, flow characteristics are found to be similar to those observed in a typical AAA during exercise conditions, namely strong vortices, persistence of positive vorticity at the downstream end, formation of multiple vortices within the cavity. The principal difference is that due to the deeper cavity at $H = 1.0$, the negative vortex persists within the bulge for longer times, whereas at $H = 0.3$, it gets flushed out of the aneurysm, when the flow rate increases in the beginning of the cycle. In both the cases, the vortex impinges at the downstream end and rolls up, as in the previous situation.

Now the above observations are compared to a longer AAA, at $W = 1$. The effect of increase in width is illustrated in figure 4.43 for $W = 1$, using the same bulge heights. At a lower bulge height, $H = 0.3$, the flow remains attached for a longer time as for rest conditions.
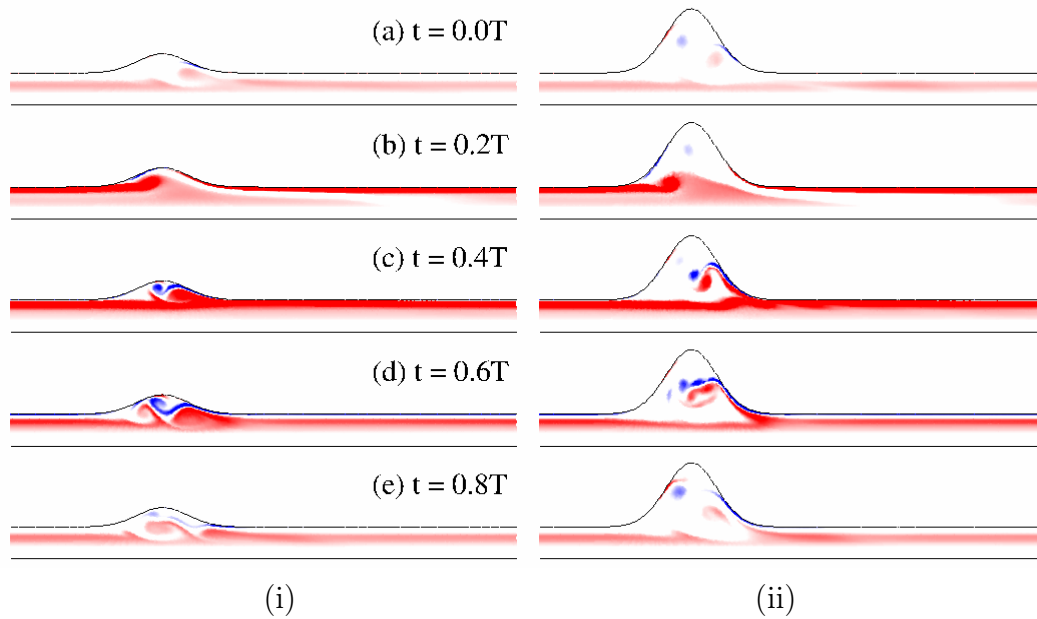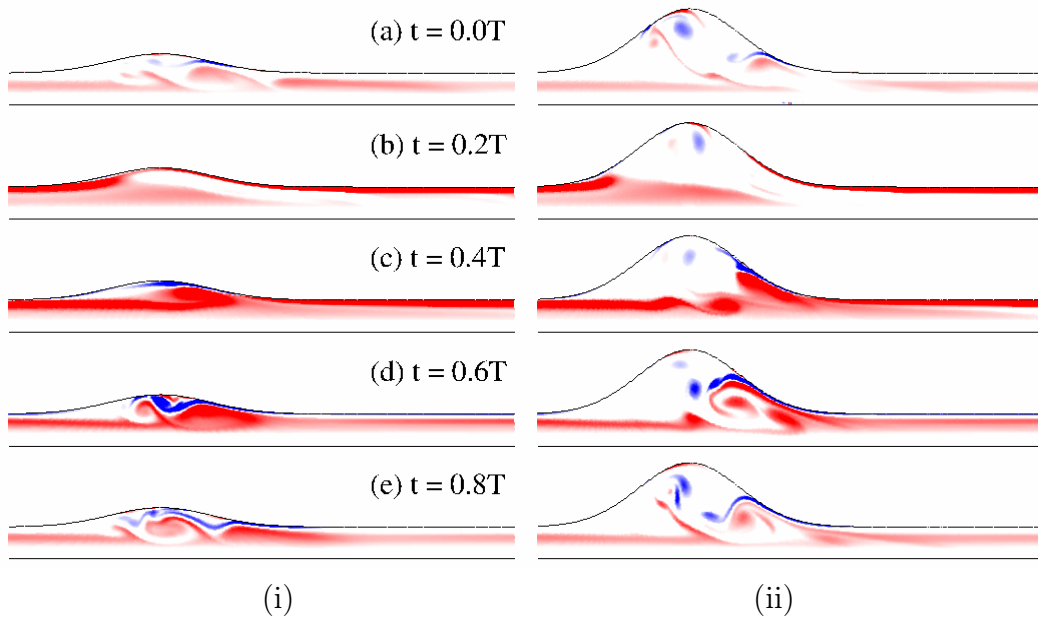
Figure 4.43: Dimensionless out-of-plane vorticity contours plotted at different time instants in a pulse cycle. Contours are plotted between -15(blue) and +15(red). Parameter settings: $Q2$, $Re = 1700$, $Wo = 13.8$, $W = 1.0$ (i) $H = 0.3$ (ii) $H = 1.0$.

The main difference from rest conditions for longer aneurysms under exercise conditions is that the vortex formed during the deceleration phase of the pulse cycle is strong enough, and travels till the distal end creating multiple vortices. Also, due to the larger space within the AAA cavity, these disturbed flow conditions persist for longer times. Hence, it is not evident that longer AAAs are less pathological under exercise conditions, in contrast to the observations made under rest conditions.

The distribution of WSS for the different geometries considered is summarized in figure 4.44. The bulge height appears to have a weak influence, except for the peak minimum value of the WSS. With an increase in H, the negative vorticity formed within the aneurysm is able to persist for longer periods, thereby influencing the minimum value, as larger bulge heights result in higher minima. The effect of width is to shift the spatial locations of the maximum and minimum values observed in the aneurysm. The OSI values are summarized in figure 4.45. It is seen that within the undilated sections of the aneurysm, the OSI values are small indicating a uni-directional flow. With an increase in bulge height, the range of fluctuation of the OSI value was found to increase with a mainly uni-directional flow observed at the center of the bulge, indicated by an OSI value ≈ 0, and reversed flow observed at the upstream and downstream end, indicated by large (≈ 1) values.

4.5   Effect of wall modeling on flow dynamics

The effect of modeling the aneurysm geometry using different functions is briefly investigated in the present section. As a study on flow characteristics in an AAA using a sinusoidal function was carried out recently by Sheard (2009), we consider the same geometrical and
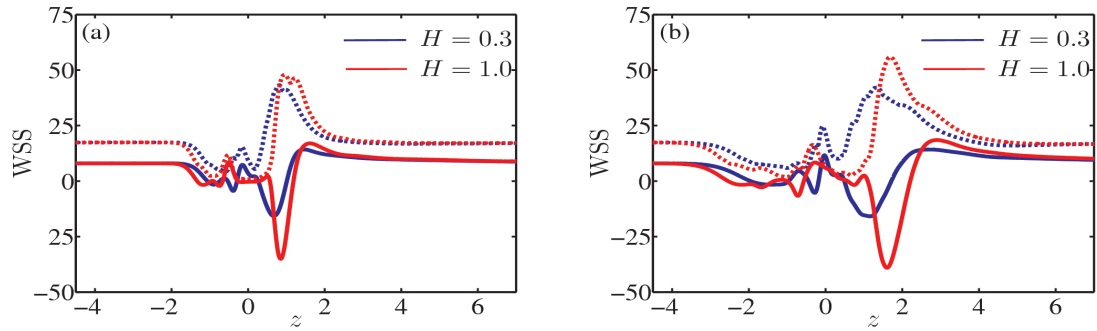
Figure 4.44: Mean WSS ($\overline{\text{WSS}}$; solid line) and its magnitude ($|\overline{\text{WSS}}|$; dotted line) for two different bulge heights and widths. Parameter settings: $Q2$, $Re = 1700$, $Wo = 13.8$ (a) $W = 0.5$ (b) $W = 1.0$.
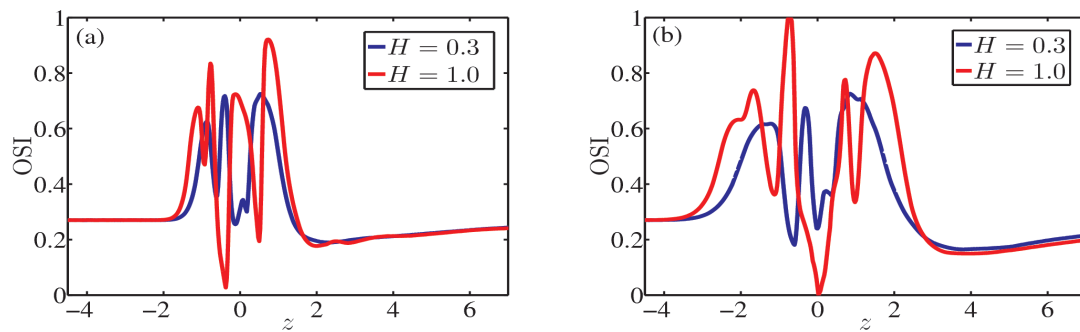
Figure 4.45: OSI values for two different bulge heights and widths. Parameter settings: $Q2$, $Re = 1700$, $Wo = 13.8$ (a) $W = 0.5$ (b) $W = 1.0$.
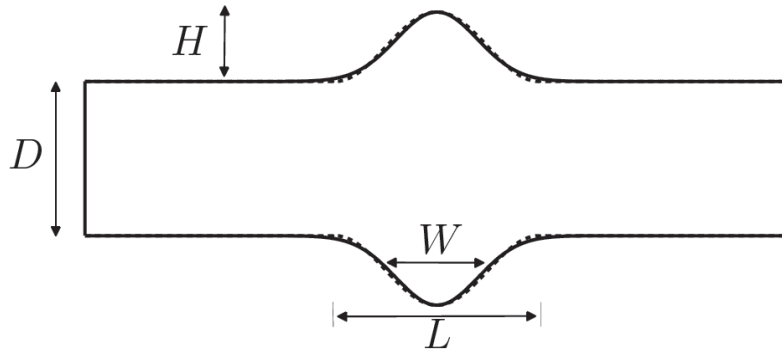
Figure 4.46: The geometry considered in the study by Sheard (2009) is shown using dotted lines, where the dilatation was modeled as a sinusoidal function. The corresponding gaussian equivalent geometry is shown using continuous lines. Parameter settings: $H = 0.45$, $L = 2.9$, $W = 0.58$.
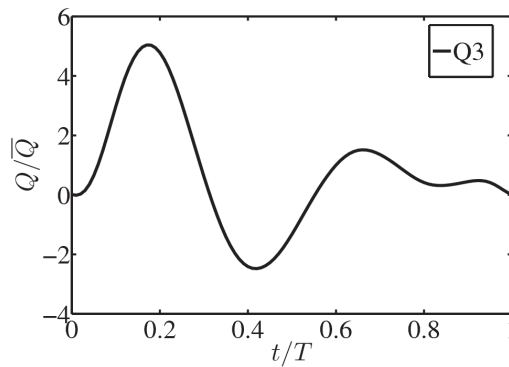
Figure 4.47: The waveform considered in the study by Salsac *et al.* (2006), Sheard (2009).

flow characteristics as in their study. For this, an aneurysm modeling using a sinusoidal function (equation (2.4.2)) and an aneurysm modeled using an equivalent gaussian function (equation (2.49)) is used. The geometries considered in the investigation are shown in figure 4.46.

The flow conditions correspond to the waveform $Q3$ shown in figure 4.47 and the flow parameters are $Re = 330$ and $Wo = 10.7$. The same geometry and flow conditions were also employed in the study by Salsac *et al.* (2006). An important difference when comparing the waveform $Q3$ with the waveform $Q1$ is that larger negative flow rates occur for $Q3$ as opposed to $Q1$.

Figure 4.48 shows the evolution of azimuthal vorticity over a pulse cycle at different time instants in an AAA modeled using a sinusoidal and a gaussian function. For both cases, as seen earlier for the case of $Wo = 10$, due to the smaller frequency, the vorticity rolls-up within the bulge and is strong enough to induce secondary vortices. This is also aided by
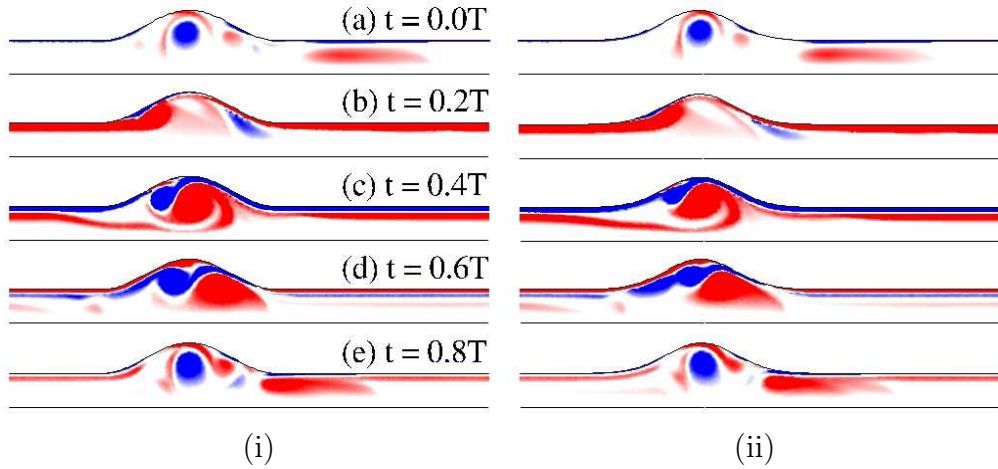
Figure 4.48: Dimensionless out-of-plane vorticity contours plotted at different time instants in a pulse cycle computed using a (i) sinusoidal and a (ii) gaussian function. Parameter settings: $Q3$, $Re = 330$, $Wo = 10.7$.

the fact that the waveform $Q3$ has a larger reversed flow rate, resulting in larger temporal gradients. At the end of the cycle, as the flow rate once again starts to increase, the primary vortices are flushed out of the domain, even further, due to the significant differences between diastolic and systolic flow rates. However, close inspection of figure 4.48 reveals that the vorticity obtained in a gaussian AAA seems to be lagging slightly in phase when compared with a sinusoidal AAA. This may be due to the fact that flow separation occurs earlier in a sinusoidal AAA, as a gaussian AAA is smoother at the proximal and distal ends of the AAA. Frame corresponding roughly to peak systole ($t = 0.2\ T$) shows that the flow remains attached at the proximal end for a gaussian AAA unlike in a sinusoidal AAA for a longer time. As peak wall shear stress values in an AAA are usually observed at the downstream end of an AAA, slight differences in the vorticity distributions arising as a consequence of differences in the functions used to model an AAA could lead to rather different WSS distributions.

Though roughly similar base flow fields are obtained for sinusoidal and gaussian AAAs, some differences are observed in the WSS distributions shown in figure 4.49. The differences are marked at the upstream and downstream end of the bulge, particularly during the systolic phase (frame (b)), as expected from the discussion on the vorticity distributions. This is probably due to the fact that a gaussian function converges more smoothly from the bulge region to the straight circular pipe region, both at the upstream and downstream ends. The distribution of WSS for the different geometries considered is summarized in figure 4.50 using the mean WSS and its magnitude. The differences are confined entirely to the bulge region, with the differences in absolute value being more prominent. Although the AAA geometries corresponding to a sinusoidal and a gaussian function are almost indistinguishable (figure 4.46), there are small but significant differences in the dynamics. Thus the flow features appear to be very sensitive to geometrical details. We will see in the next chapter that also differences arise in the stability characterisitics of the flows, while modeling AAA shapes using different functions.
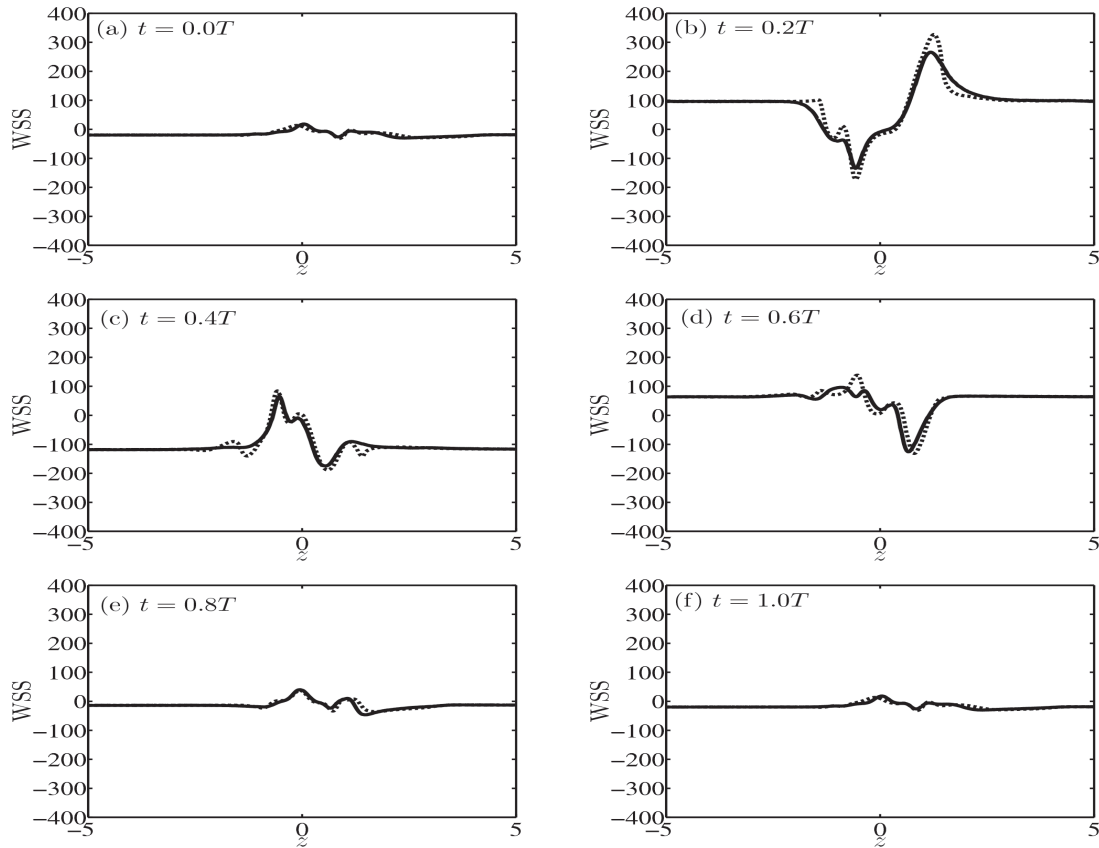
Figure 4.49: The WSS (dimensionless) distributions at different time instants are shown in frames (a) - (f) obtained using gaussian (continuous lines) and sinusoidal (dotted lines) functions. Parameter settings: $Q3$, $Re = 330$, $Wo = 10.7$, $W = 0.58$, $H = 0.45$.
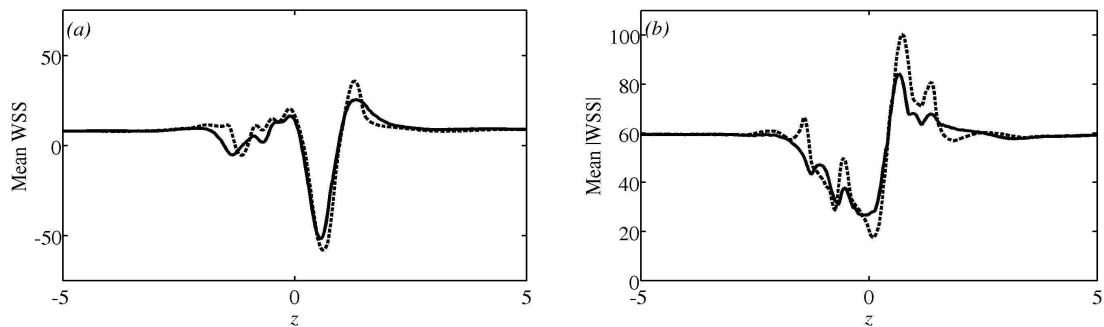
Figure 4.50: (a) Mean WSS ($\overline{\text{WSS}}$) and its magnitude (b) ($|\overline{\text{WSS}}|$) obtained using gaussian (continuous lines) and sinusoidal (dotted lines) functions. Parameter settings: $Q3$, $Re = 330$, $Wo = 10.7$, $W = 0.58$, $H = 0.45$.

4.6   Discussion

The past two decades have witnessed a large number of studies aimed at improving our understanding of the relevant biomechanical processes that take place in the vascular system. Studies have shown that the endothelial cells lining the walls of the abdominal aorta are sensitive to local hemodynamic variations. Among the various flow characteristics, the endothelial cells are known to have been most affected by the wall shear stresses (WSS), not only on their magnitude, but also on their spatial and temporal variations. The presence of "disturbed flow conditions", i.e. regions where the WSS differ from healthy conditions have been postulated to play a key role in the formation of atherosclerotic lesions, associated with degradation of the arterial wall. Hence, the characterisation of WSS during the progressive enlargement of an AAA, under varying flow conditions is essential in understanding the etiology of AAAs, as well as the role that the hemodynamics play in the progression of this disease.

Characterising the flow properties observed in a healthy abdominal aorta under varying conditions is an important step to begin with. Our studies have shown that the peak WSS value under exercise conditions is almost twice that observed during rest. Though the minimum value of WSS does not change drastically, the mean WSS is roughly 7 times higher during exercise conditions. However, peak to mean ratio under resting conditions is observed to be 4 times higher than under exercise. As the mechanisms involved in the regularisation and alignment of the endothelial cells are known to be receptive to temporal changes in WSS, rather than the magnitude, these studies have shown a reduction in hemodynamic conditions known to promote atherosclerotic plaques as a consequence of exercise.

Our computations of flow fields in idealized AAA models have shown that the flow inside the aneurysm is characterized by the formation of regions of larger and lower amplitude of WSS than in the healthy vessel. Regions with large spatial gradients in WSS distributions are observed, particularly at the distal end of the AAA. These are not present in the healthy aorta. The flows were observed to remain attached to the walls during the systolic phase, with flow separation generally observed during the deceleration after the peak systole. During this phase, the vorticity is found to roll-up into a vortex at the proximal end. This vortex enlarges with time and impinges at the downstream end of the AAA, resulting in large spatial gradients of WSS along the wall. Depending on the strength of this primary vortex, even secondary vortices of opposite signs were observed within the AAA. For a typical AAA under rest conditions, at peak systole, the maximum WSS observed at the downstream end is about 1.7 times the value recorded in a healthy abdominal aorta. However, when considering the time-averaged mean WSS, a peak is found 2.8 times larger than the mean level in the healthy vessel, and an opposite-signed peak that was 4.8 times greater. The oscillating shear index value, used to characterise the oscillatory nature of the flow, is larger than 0.5 showing that reversed flow conditions are dominant within the AAA. Such dynamic low oscillatory WSS distributions, along with spatial gradients over the aortic wall, contribute to an unstable progressive degradation of the arterial wall and to the formation of atherosclerotic lesions and aneurysm.

To investigate AAAs at different stages of their growth and progression, the geometrical parameters, namely the bulge height H and bulge width W were varied. It is seen that the clinically relevant flow characteristics of aneurysmal flow, i.e. detachment of flow

and impingement on the distal neck, presence of low oscillatory WSS within the AAA, are observed even for very shallow aneurysms. For shallow aneurysms, the primary vortex formed during the deceleration phase is seen to be convected out of the bulge more easily. For deep aneurysms, the presence of multiple vortices within the AAA cavity is observed throughout the cycle. More importantly, the peak WSS hardly changes with increase in bulge height and qualitatively similar WSS distributions are observed. However, the minimum value of WSS, usually observed slightly upstream of the distal end, is seen to increase sharply during the initial growth of an AAA. These studies indicate that the spatial distributions of WSS and their gradients are relevant for AAAs during the incipient stages, but may be less important during the latter stages. The minimum and maximum values of WSS are found to decrease with increase in width of an AAA. Also, the spatial variations along the arterial wall are weaker for longer aneurysms and, more importantly, temporal fluctuations also diminish. Except during the systolic phase, the WSS values observed in a long AAA are close to the values observed in a healthy abdominal aorta. Our analysis suggests that longer AAAs are less pathological than shorter ones.

The flow conditions are known to vary from person to person, even under resting conditions. The Womersley number usually varies within the range 10–15 in the abdominal aorta. It is observed that the flow remains attached to the walls for longer times, with an increase in Womersley number, Wo. Due to this, the primary vortex formed during the deceleration phase is weaker and secondary vortices are not formed within the AAA cavity at higher Wo. Inspection of axial velocity profiles close to the wall, also shows that the spatial variations along the wall and temporal fluctuations at a fixed point are more marked at lower Womersley numbers. These observations are reflected in the WSS distributions which reveal that the peak maximum and minimum values increase with a decrease in Wo. Also, the Reynolds number Re may vary from 600 up to 6000 within the abdominal aorta. The principal effect of increasing Re is that the primary vortex formed after peak systole is stronger. This was compounded with flow separation taking place earlier in the pulse cycle. Hence, the disturbed flow conditions observed within the AAA are stronger for higher Re. The peak WSS and spatial gradients of WSS along the arterial wall are also found to increase with Re.

Another important aspect that has received much attention in recent years is to understand the hemodynamic changes taking place during exercise conditions. Hence, we have carried out studies using physiological waveforms observed during exercise conditions to compare the observations with resting conditions. The most significant result from our observations are an increase in the strength of vortices under exercise conditions and the absence of reversed flow during the pulse cycle. Moreover, the flow fields are highly complex and the mixing of aneurysmal blood appears to be enhanced. Such exercise-induced flow patterns with increased flow magnitude and moderate turbulence reduce the regions of flow that have been correlated with thrombus formation. An investigation of velocity profiles close to the arterial wall reveals that the spatial and temporal gradients are significantly lower during exercise conditions, thereby reducing hemodynamic flow conditions known to promote arterial wall degradation. The WSS distributions observed are similar with a peak maximum value observed at the distal end and a minimum value observed slightly upstream. The effect of varying geometry on flow dynamics and changes in WSS is weaker during resting conditions.

The effect of choice of functions used to model an AAA shape has also been inves-

tigated in the present analysis. For this, AAAs modeled using a sinusoidal and a gaussian function are considered, as a sinusoidal AAA is used in the recent study by Sheard (2009). For this analysis, the flow conditions and geometrical parameters are chosen as in the recent works by Salsac *et al.* (2006), Sheard (2009). The flow rate waveform $Q3$ obtained from Salsac *et al.* (2006), Sheard (2009) corresponds to $Re = 330$ and $Wo = 10.7$. Though both AAA geometries almost superpose, small but significant differences in flow dynamics are observed. Flow separation is found to occur earlier in the pulse cycle in a sinusoidal AAA, with the flow field obtained in a gaussian AAA lagging in phase in comparison to a sinusoidal AAA. This is due to the fact that a gaussian function converges more smoothly at the proximal and distal ends of the AAA cavity. As a result, the WSS distributions are found to be different, particularly at the upstream and downstream ends of the aneurysm. These observations point out the need to model an AAA wall more precisely and put forward the question of what the choice of function needs to be.

Although this study is conducted using simplified models of AAAs, the changes in flow characteristics under varying flow conditions, and during the growth of an AAA are captured. Our computations provide a reference framework, to analyse quantitatively the effects of the modifications in the mechanical stimuli on the formation and growth of AAAs.

Pulsatile flows: Stability analysis

5.1 Introduction

The stability of the pulsatile base flows discussed in the previous chapter is examined in this chapter. The various geometrical parameters and flow conditions are varied systematically, revealing a range of unstable modes.

Following the observation of transition to turbulence in the aorta by Nerem *et al.* (1972), understanding flow transition has emerged as a common theme in studies of flows at Reynolds numbers relevant to the larger arteries of the human physiology. The desire to understand the dynamics of arterial flows has stimulated the interest of researchers to study the stability of oscillatory and pulsatile flows in pipes (Yang & Yih, 1977, Grosch & Salwen, 1968, Stettler & Hussain, 1986, Tozzi & von Kerczek, 1986, Fedele *et al.*, 2005) to name a few (more details can be found in chapter 1). One interesting observation made by Tozzi & von Kerczek (1986), who studied the stability of an oscillatory pipe flow, was that the time-periodic flow was more stable than its steady counter part, with transition to a turbulent regime being suppressed. This observation is further supported by the study of Fedele *et al.* (2005), which revealed that the transient energy growth was smaller in oscillatory flows. However, both these studies were based on axisymmetric disturbances and on purely oscillatory flows. The addition of a mean flow component is known to drastically change the stability characteristics (Thomas *et al.*, 2011). Apart from these, the desire to understand the flow characteristics in the human aorta during various pathologies, especially with regards to stenosis, has also lead to many stability analyses of these flows (Sherwin & Blackburn, 2005, Blackburn & Sherwin, 2007, Griffith *et al.*, 2009, 2013), including some studies carried out using physiological waveforms (Mao *et al.*, 2011). More literature on stability analyses carried out on relevant geometrical configurations can be found in the introduction (chapter 1).

It has been observed that the flow remains laminar during resting conditions and becomes moderately turbulent during exercise conditions (Les *et al.*, 2010). However, the presence of an abdominal aortic aneurysm (AAA) promotes the onset of turbulence, even under resting conditions, enhancing the mixing of aneurysmal blood. These flow patterns with increased flow magnitude and moderate turbulence reduce regions of flow stasis that have been correlated with thrombus formation (Salsac *et al.*, 2004, Deplano & Siouffi, 1999, Reininger *et al.*, 1994). We have seen in the previous chapter that there has been a lot of attention on understanding flow characteristics in AAAs, though nowhere in the literature can be found a fundamental study that examines the stability of these flows, even using model configurations. This is the main contribution of the present work. We examine the stability of pulsatile base flows in model axisymmetric AAAs, under varying geometrical configurations and for different flow conditions. This would give us an idea of

the regions that are sensitive to fluctuations and disturbances at different flow conditions during the growth and progression of an AAA. It is important to first address relatively simple geometries: after understanding the dynamics that prevail in these idealized cases we will be in a position to provide plausible explanations in more realistic configurations.

The present chapter is structured in the following manner: the effect of the flow parameters (Reynolds number Re, and Womersley number Wo) are examined first, followed by an investigation on the effect of geometry. This is followed by a brief discussion on the stability characteristics of flows in an AAA under exercise conditions. A comparison on stability characteristics observed while modeling an AAA using a sinusoidal and a gaussian function is also provided. The chapter concludes with a discussion on physiological implications of our observations.

5.2   Methodology

In this section a brief reminder of the various tools used in the stability analysis is provided (more details can be found in chapter 2). In order to study the stability of the axisymmetric time-periodic base flow to three-dimensional disturbances, the Navier–Stokes equations are linearized around the base flow. The pulsatile base flows are time periodic with period T such that $\mathbf{U}(r, z, t) = \mathbf{U}(r, z, t + T)$. To this a three-dimensional perturbation field $\mathbf{u}'(r, z, \theta, t)$ is added to form the composite field:

$$\mathbf{u}(r, z, \theta, t) = \mathbf{U}(r, z, t) + \mathbf{u}'(r, z, \theta, t). \tag{5.1}$$

Substituting the above expression in the Navier–Stokes equations and neglecting nonlinear terms in the perturbations, we get the linearized Navier–Stokes equations

$$\frac{\partial \mathbf{u}'}{\partial t} + (\mathbf{U}.\nabla)\mathbf{u}' + (\mathbf{u}'.\nabla)\mathbf{U} \quad = \quad -\nabla p' + \frac{1}{Re}\Delta\mathbf{u}', \tag{5.2a}$$

$$\nabla.\,\mathbf{u}' \quad = \quad 0. \tag{5.2b}$$

The perturbations are chosen as normal modes with explicit time-dependence as

$$\begin{pmatrix} u_r'(r, \theta, z, t) \\ u_\theta'(r, \theta, z, t) \\ u_z'(r, \theta, z, t) \\ p'(r, \theta, z, t) \end{pmatrix} = \begin{pmatrix} \hat{u}_r(r, z, t) \\ \hat{u}_\theta(r, z, t) \\ \hat{u}_z(r, z, t) \\ \hat{p}(r, z, t) \end{pmatrix} \exp \mathrm{i}(m\theta) + \text{c.c.} \tag{5.3}$$

where m is the azimuthal mode number. The above expression is substituted into equations (5.2). For the present computations a plane of symmetry for the perturbations is assumed by considering $(\hat{u}_r(r, z, t), \hat{u}_z(r, z, t), \hat{p}(r, z, t))$ to be purely real, and $\hat{u}_\theta(r, z, t)$ to be purely imaginary. This permits us to rewrite the above equations in terms of purely real variables, thereby reducing the computational cost.

To analyse the stability of the time-periodic base flows, the linearized Navier–Stokes equations are time-marched for a suitable number of pulse cycles and the perturbation fields are monitored till they converge. Once the perturbations have converged, the

evolution of the perturbation velocity fields at specific points in the computational domain is recorded to determine the Floquet multiplier μ. According to Floquet theory, the velocity and pressure perturbations grow or decay exponentially from period to period. Thus, the perturbation fields satisfy the relationship

$$\hat{u}(r, z, t + T) = \exp(\sigma T)\hat{u}(r, z, t). \tag{5.4}$$

The coefficient $\mu = \exp(\sigma T)$ is often called the Floquet multiplier, where T is the time period of the pulsatile base flow and $\sigma = \lambda + \mathrm{i}\omega$ is the complex growth rate. The absolute value of the Floquet multiplier $|\mu|$ is computed as

$$|\mu| = E_k(t + T)/E_k(t). \tag{5.5}$$

where $E_k(t)$ is defined as,

$$E_k(t) = \sqrt{\int_\Omega [u'_r(t)^2 + u'_\theta(t)^2 + u'_z(t)^2]d\Omega}. \tag{5.6}$$

A Floquet multiplier $|\mu| > 1$ indicates an unstable flow, while $|\mu| < 1$ indicates a stable one. A Floquet multiplier $|\mu| = 1$ represents neutral stability. Also, depending on the value of the Floquet multiplier μ, several mode classifications are possible. A real bifurcation ($\mu = 1$) has the same period as the base flow. A subharmonic bifurcation is indicated by a negative Floquet multiplier ($\mu = -1$), where the perturbation is period-doubling, operating at a period twice that of the base flow. A subharmonic bifurcation can be detected by investigation of the perturbation field, as the sign of a period-doubling bifurcation will alternate from one base flow period to the next. A third-type, complex-conjugate bifurcations, consist of standing- or travelling-wave solutions. A complex Floquet multiplier can be identified using the evolution of the absolute value of Floquet multiplier, $|\mu|$. An oscillation around a mean value indicates a complex Floquet multiplier (Robichaux *et al.*, 1999, Sheard *et al.*, 2005). However, most of the Floquet multipliers observed in this study are real, with only a few exceptions.

5.3 Effect of flow parameters

As seen in detail in the previous chapter 4, the flow characteristics significantly depend on Womersley number Wo and Reynolds number Re. So we begin by discussing the effect of these parameters on the flow stability characteristics. For the present discussion, the AAA geometry is fixed, using a value of 0.5 for both the bulge width W and bulge height H, and flow rate waveform $Q1$ corresponding to resting conditions is used. Recall that this waveform is obtained from the data presented in the article by Suh *et al.* (2011) where the flow rate was measured in patients with AAAs. The Reynolds number was varied between 200–300 and the Womersley number from 10–15, which covers the physiologically relevant range.

5.3.1 Stability analysis: $Wo = 15$

The first section of the stability analysis focuses on flows at Womersley number $Wo = 15$, which are already discussed in detail in the previous chapter (see section 4.3.4). Figure 5.1
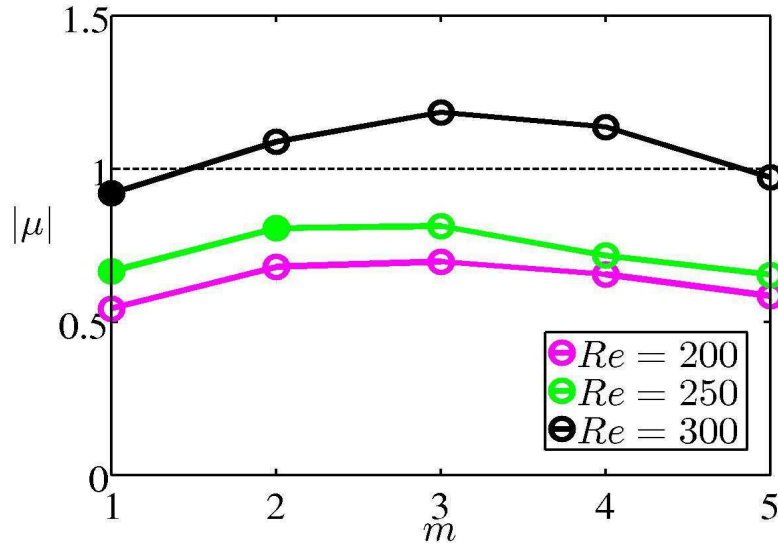
Figure 5.1: Floquet multiplier at $Wo = 15$ for different Reynolds numbers. Subharmonic modes are shown using filled circles. The dotted line demarcates the stable region from the unstable one. Parameter settings: $Q1$, $H = 0.5$, $W = 0.5$, $Wo = 15$.

summarizes the results obtained at $Wo = 15$ for different Reynolds numbers. The flow is stable at all Reynolds numbers except at $Re = 300$, where it is unstable to mode numbers $m = 2$, 3, 4, with $m = 3$ being the most unstable. Sub-harmonic modes have a negative Floquet multiplier and are shown using filled circles. The modes observed clearly arise from two different sets of eigenmodes, with sub-harmonic modes dominating at small azimuthal mode numbers and harmonic modes, at higher values. A similar trend was observed for the case of stenotic flows (Sherwin & Blackburn, 2005, Blackburn & Sherwin, 2007, Griffith *et al.*, 2009) where the mode corresponding to $m = 1$ arose as a period-doubling bifurcation.

The spatial distribution of the modes at $Re = 300$ for various azimuthal mode numbers are visualized using the contours of azimuthal vorticity in figure 5.2. The spatial structure corresponding to mode $m = 1$ is different, as the perturbations are observed to extend further downstream of the aneurysm bulge and the sign of the azimuthal vorticity changes along an axial cut at a fixed radius downstream of the AAA dilatation. This seems to be characteristic of subharmonic modes. It is interesting to see from figure 5.2 that though the modes are dominant within the AAA cavity, they extend beyond the AAA. This is different from the spatial distributions seen for steady flows, where the perturbations were confined entirely to the AAA. As seen in figure 4.23, where the base flow for $Wo = 15$ is shown, the primary vortex forms during the deceleration phase at a later instant in the pulse cycle and is hence weaker. Subsequently, no secondary vortices are formed within the cavity and the vortex passes through the AAA with less interaction with the distal end of the AAA wall. This in effect results in less localization of the perturbations within the AAA dilatation, and hence they are more prominent outside. What this implies is that the presence of an AAA creates disturbed flow conditions that are not entirely restricted to the AAA dilatation but rather extend even to the undeformed healthy region. AAA dilatation acts as a wavemaker region causing the growth of disturbances downstream of it. As a
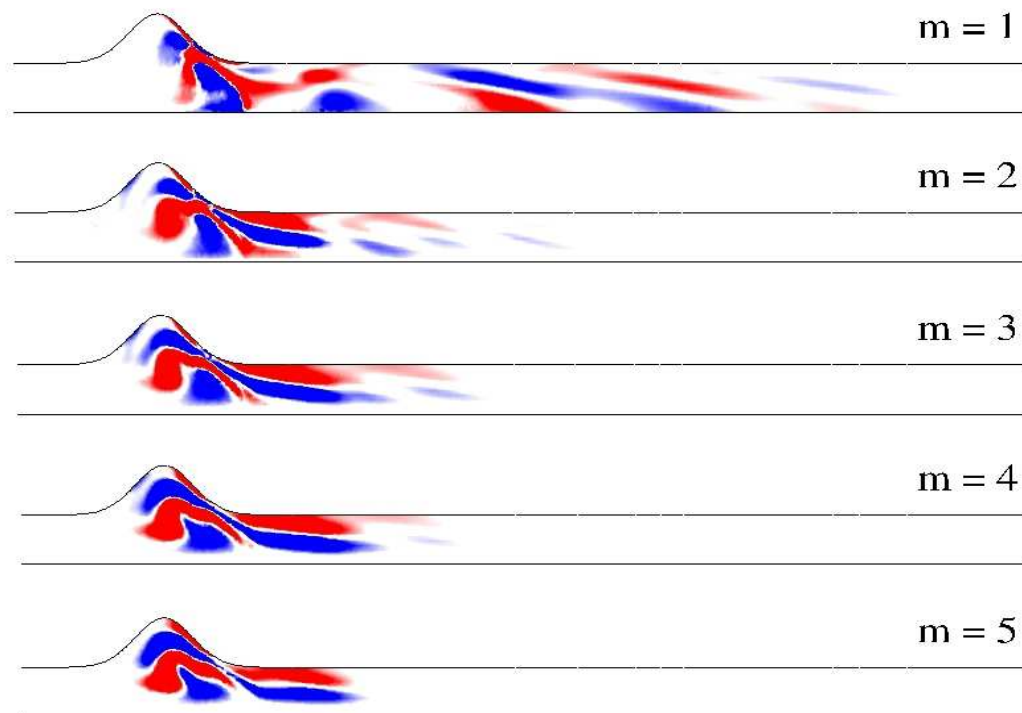
Figure 5.2: Contours of azimuthal vorticity of the perturbation corresponding to different azimuthal mode numbers at phase $t = 0.0T$ within the axial extent $-2.5D \leq z \leq 15D$. Parameter settings: $Q1$, $H = 0.5$, $W = 0.5$, $Re = 300$, $Wo = 15$.
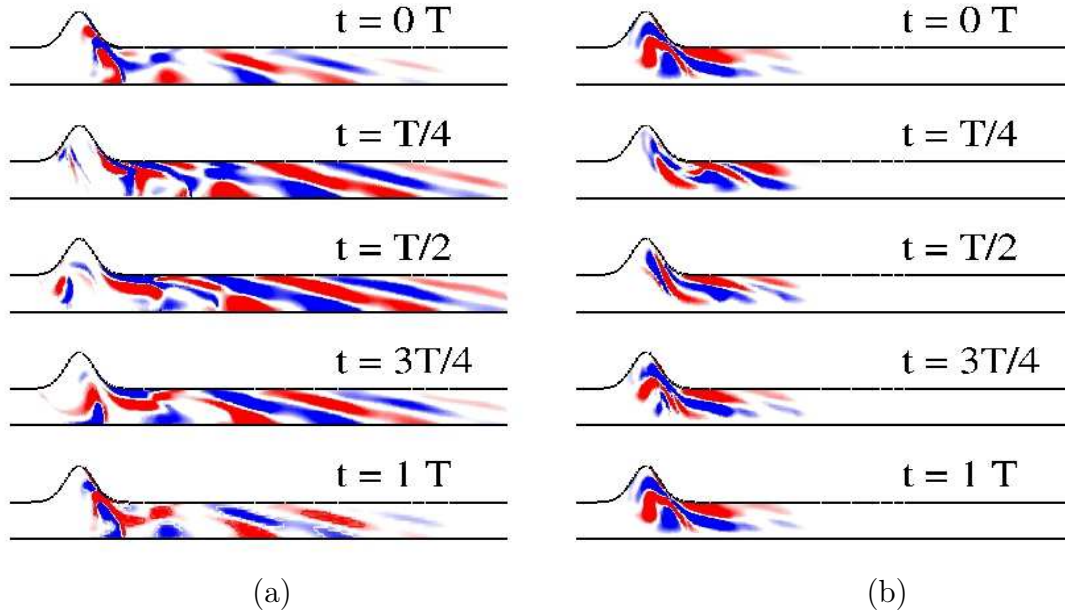
(a)   (b)

Figure 5.3: Contours of azimuthal vorticity of the perturbation at various instants in a pulse cycle corresponding to (a) $m = 1$ (b) $m = 3$. Parameter settings: $Q1$, $H = 0.5$, $W = 0.5$, $Re = 300$, $Wo = 15$.

result, even the undeformed arterial wall might experience undesirable fluctuations of the flow field, that could play part in thrombosis formation and platelet activation, and in turn damage the endothelial cells leading to atherosclerosis (Deplano & Siouffi, 1999, Reininger *et al.*, 1994, Barakat, 2013).

These observations are further illustrated in figure 5.3 where the evolution of modes $m = 1$ and $m = 3$ during a pulse cycle is shown. During the systolic phase ($\approx t = 0.25T$) the perturbations are less localized within the AAA cavity and are more prominent downstream of it. The sign of the spatial distribution of vorticity corresponding to the stable sub-harmonic mode $m = 1$, switches at the end of a pulse cycle and extends far more downstream than the unstable $m = 3$ mode. However, as the mode $m = 1$ is stable, any noise present in the flow through the AAA would eventually decay asymptotically, with the flow being dominated by the unstable $m = 3$ mode.

The spatial structure of the harmonic $m = 1$ and $m = 2$ modes at $Re = 200$ is illustrated in figure 5.4. Though the flow is stable to these perturbations at these parameter conditions, it is seen that the axial velocity contours seem to be spatially growing, which is different from those observed at higher Reynolds numbers. However, to verify this phenomenon, some further tests were conducted by analysing the response of the system to an impulse forcing, which is described in the following section.

Response to impulse forcing

The spatial distribution of the global modes downstream of the AAA dilatation could be expected to be the same as those observed in a straight circular pipe, provided, at the
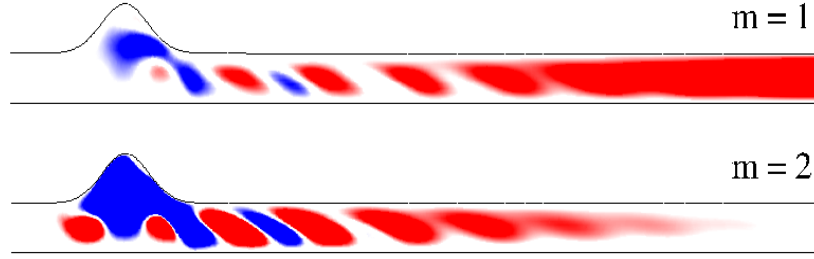
Figure 5.4: Contours of axial velocity of the perturbation corresponding to $m = 1$ and $m = 2$ at phase $t = 0.0T$. Parameter settings: $Q1$, $H = 0.5$, $W = 0.5$, $Re = 200$, $Wo = 15$.

entrance of the circular pipe a harmonic forcing, to mimick the AAA cavity is applied. In effect, the AAA cavity could be thought of as a wavemaker region that forces the dynamics downstream in the straight circular pipe region. Using this idea, we investigate whether the spatial structures observed downstream of the AAA dilatation for $m = 1$ at $Re = 200$ (see figure 5.4) are indeed correct. For this, we consider a straight circular pipe of sufficient length (40 D units), and apply a harmonic forcing, with a frequency derived from from our linear stability analysis in the presence of an AAA, at an upstream axial location, and observe the linear dynamics. The basic flow applied within the circular pipe corresponds to the analytical Womersley flow solution, since the basic flow well downstream of an AAA returns to this.

The external forcing can be modeled as a body force $\mathbf{f}(\mathbf{x}, t)$ added to the linearized Navier–Stokes equations (5.2) as

$$\frac{\partial \mathbf{u}'}{\partial t} + (\mathbf{U}.\nabla)\mathbf{u}' + (\mathbf{u}'.\nabla)\mathbf{U} = -\nabla p' + \frac{1}{Re}\Delta \mathbf{u}' + \mathbf{f}(\mathbf{x}, t), \qquad (5.7a)$$

$$\nabla.\mathbf{u}' = 0, \qquad (5.7b)$$

with $\mathbf{f}(\mathbf{x}, t) = \psi(\mathbf{x}) \exp(-\mathrm{i}\omega t)$. The weight function $\psi(\mathbf{x})$ is used to restrict the flow region where the forcing is applied and the forcing is time-harmonic, where the frequency ω is real. This frequency is chosen as the real part of the complex frequency obtained previously from the linear stability analysis in the presence of an AAA.

Figure 5.5(b) shows the response of the Womersley solution in a straight pipe to such a harmonic forcing. The spatial location where the harmonic forcing is applied is shown using a filled black circle. It is seen that the spatial distribution of the perturbation observed within the straight circular sections downstream of the aneurysm bulge in figure 5.5(a) is the same as seen in a straight circular pipe forced harmonically using the same frequency as of the perturbation. Though the perturbation is temporally stable, we can see that there is a spatial growth as remarked earlier. However, this phenomenon is observed only at low Reynolds numbers for which the flows are stable.
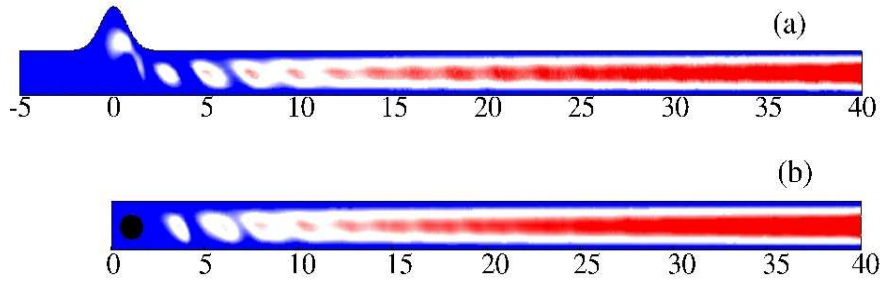
Figure 5.5: (a) Energy of the axial velocity component of the leading critical mode corresponding to $m = 1$. (b) Flow through a straight circular pipe with the corresponding harmonic forcing applied upstream of the domain (shown using a black circle). Parameter settings: $H = 0.5, W = 0.5, Re = 200, Wo = 15$.

	$Wo = 12$	$Wo = 15$
$Re = 200$	-0.0988	-0.2590
$Re = 250$	0.4073	-0.1185
$Re = 300$	0.3554	0.0809

Table 5.1: Growth rate $\sigma = \frac{1}{T} \log \mu$ of the least stable mode.

5.3.2   Stability analysis: $Wo = 12$

We now explore the effect of lowering the Womersley number to 12 on the stability characteristics. The base flows at $Wo = 12$ have been discussed in detail in the previous chapter 4. The first significant difference of the base flows in comparison with $Wo = 15$ is that the primary vortex forms earlier during the deceleration phase after peak systole, and subsequently is stronger. As a result, once it impinges at the distal end of the AAA, secondary vortices are formed that persist within the cavity for longer times in the pulse cycle.

Figure 5.6 summarizes the stability characteristics at $Wo = 12$ for various Reynolds numbers. The first significant observation is that the flows at $Wo = 12$ are way more unstable than those at $Wo = 15$, with the only stable configuration occurring for $Re = 200$. As already discussed, the base flows at these two Womersley numbers are very different. Secondly, the most unstable mode corresponds to $m = 2$. Though the absolute values of Floquet multipliers $|\mu|$ are much higher than at $Wo = 15$, one has to keep in mind that the time-period at $Wo = 12$ is higher than that at $Wo = 15$. As the instability develops over a time period, the growth rates ($\sigma = \frac{1}{T} \log \mu$) are significantly higher but not by orders of magnitude, which is shown in table 5.1.

Figure 5.7 shows the modes visualized by their azimuthal vorticity at various azimuthal mode numbers at $Re = 250$. The first significant difference from $Wo = 15$ is that the perturbations are slightly more localized within the bulge region, though they still extend downstream of the AAA cavity. This is probably due to the difference in base flow dynamics at $Wo = 12$ where multiple vortices were formed within the cavity that persisted throughout the pulse cycle.

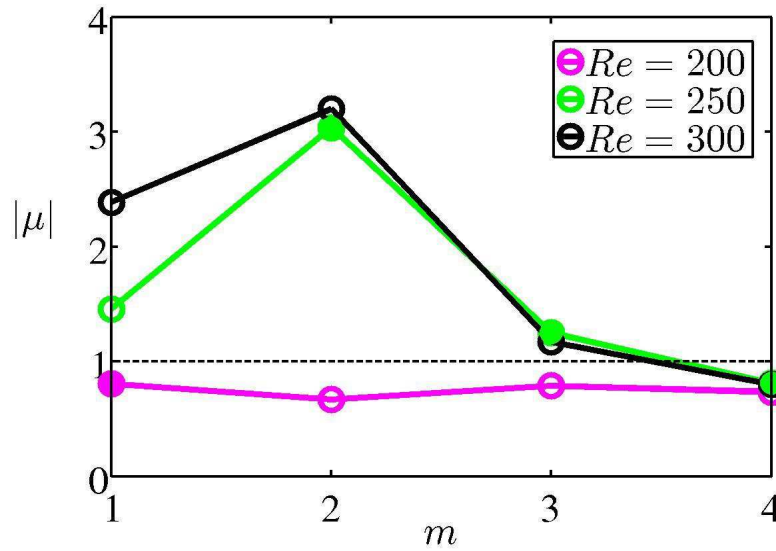Figure 5.6: Floquet multiplier at $Wo = 12$ for different Reynolds numbers. Subharmonic modes are shown using filled circles. The dotted line demarcates the stable region from the unstable one. Parameter settings: $Q1$, $H = 0.5$, $W = 0.5$, $Wo = 12$.
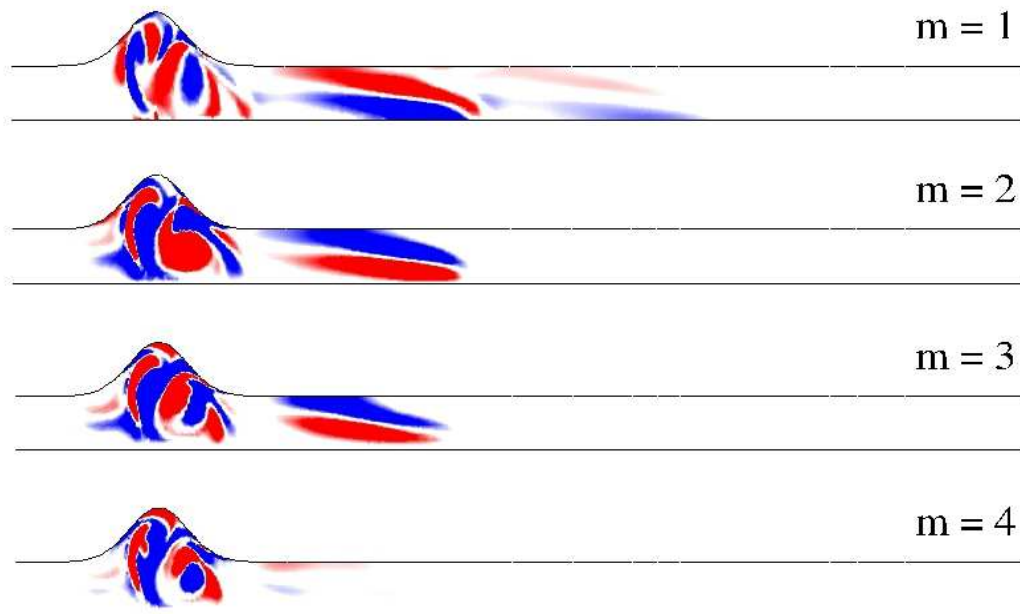

Figure 5.7: Contours of azimuthal vorticity of the perturbations at various azimuthal mode numbers. Parameter settings: $Q1$, $H = 0.5$, $W = 0.5$, $Re = 250$, $Wo = 12$.
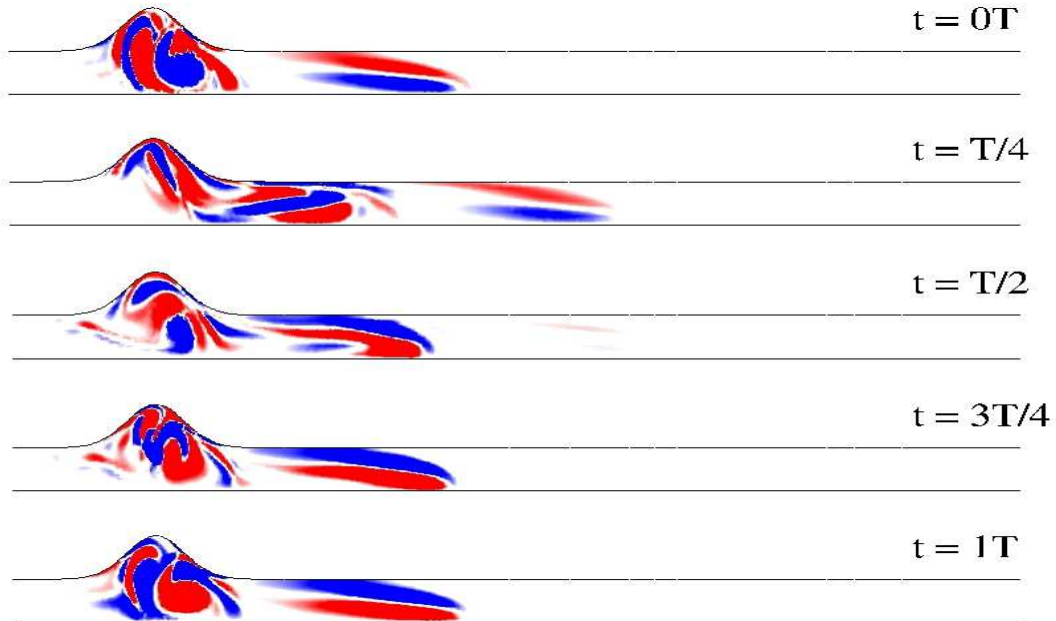
Figure 5.8: Contours of azimuthal vorticity of the perturbations at $m = 2$ at various instants in a pulse cycle. Parameter settings: $Q1$, $H = 0.5$, $W = 0.5$, $Re = 250$, $Wo = 12$.

As remarked earlier, the dominant perturbations have an effect on the undeformed arterial wall downstream of the AAA cavity as can be seen from figure 5.7. The evolution of the mode at $m = 2$ during a pulse cycle is shown in figure 5.8. From the frame corresponding to $t = T/4$, one can observe that the perturbations are pushed out of the cavity during the systolic phase. The period-doubling nature of $m = 2$ mode is also observed as the positive and negative regions are swapped at each successive pulse cycle. Figures 5.7 – 5.8 reveal that the modes extend downstream of the AAA cavity. This could be a significant observation while extending these results to reality, as usually an AAA is observed upsteam of the iliac bifurcation in the abdominal region. The presence of perturbations extending downstream of the AAA dilatation to the regions where the bifurcation is observed indicates that this bifurcation could have an important part to play in the pathology of AAAs (Deplano *et al.*, 2013). A closer look at the spatial distributions downstream of the AAA cavity for the mode numbers $m = 2$ and $m = 4$ are shown in 5.9. Figure 5.9 shows the velocity vectors of the eigenmode at a downstream location of the aneurysm bulge, superimposed on the axial velocity contours of the base flow, for modes $m = 2$ and $m = 4$. For the case of $m = 2$, the perturbation results as counter-rotating vortices downstream of the AAA as can be seen from the perturbation velocity vectors, shown in figure 5.9(a). Whereas for the harmonic $m = 4$ mode, the perturbation vectors are aligned with the axial velocity of the basic flow, and hence the absence of counter-rotating flow.

Before moving on to flows at even lower Womersley numbers, we discuss the fact that at $Re = 300$, the most unstable mode is a harmonic mode corresponding to $m = 2$ shown in
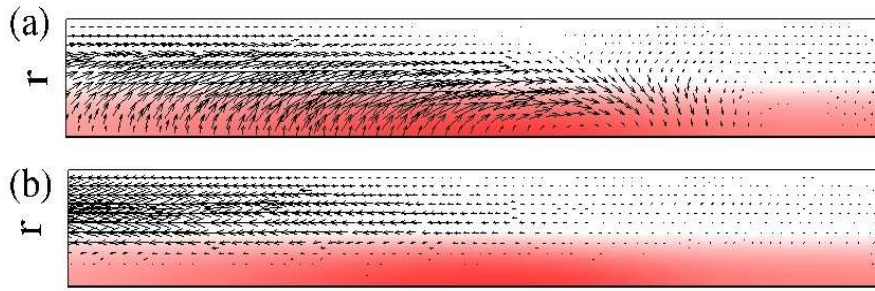
Figure 5.9: The velocity vectors of the eigenmode at a downstream location of the bulge ($3D \leq z \leq 6D$), superimposed on contours of axial veloctiy of the base flow. Parameter settings: $Q1$, $H = 0.5$, $W = 0.5$, $Re = 250$, $Wo = 12$ (a) $m = 2$ (b) $m = 4$.
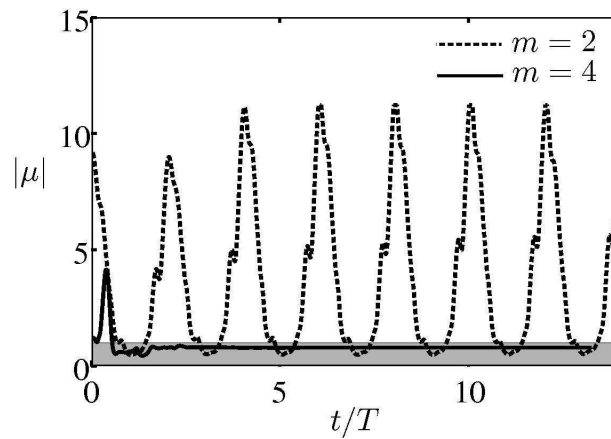
Figure 5.10: Evolution of the absolute value of the Floquet multiplier for azimuthal mode numbers $m = 2$ and $m = 4$. The shaded region indicates the stable region. Parameter settings: $Q1$, $W = 0.5$, $H = 0.5$, $Re = 300$, $Wo = 12$.
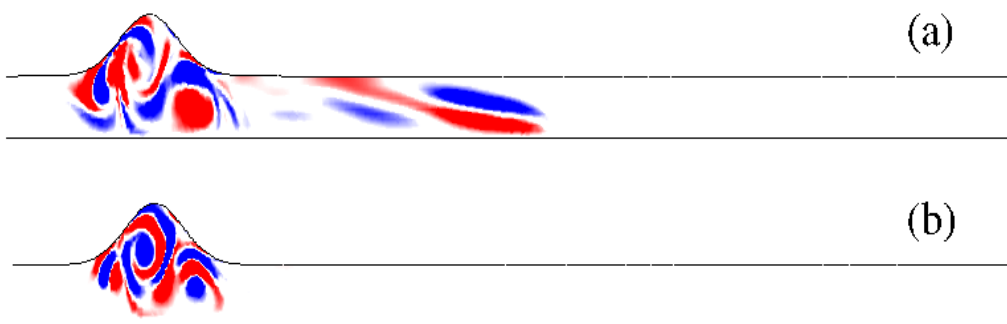
Figure 5.11: Contours of azimuthal vorticity of the perturbation corresponding to $m = 2$ and $m = 4$ at phase $t = 0.0T$. Parameter settings: $Q1$, $H = 0.5$, $W = 0.5$, $Re = 300$, $Wo = 12$ (a) $m = 2$ (b) $m = 4$.
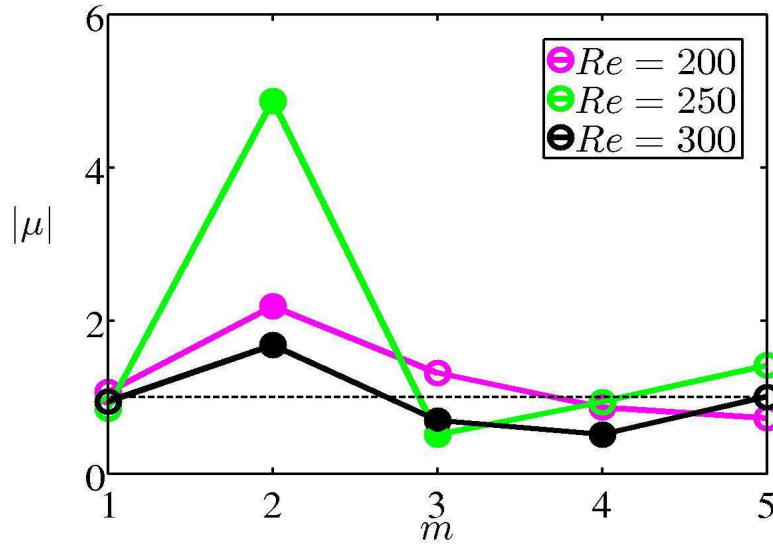
Figure 5.12: Floquet multiplier at $Wo = 10$ for different Reynolds numbers. Sub-harmonic modes are shown using filled circles. The dotted line separates the stable region from the unstable one. Parameter settings: $Q1$, $H = 0.5$, $W = 0.5$, $Wo = 10$.

figure 5.6. This is different from $Re = 250$ where a sub-harmonic mode was found. Figure 5.10 shows the evolution of the absolute value of the Floquet multiplier $|\mu|$ for $m = 2$ and $m = 4$. $|\mu|$ oscillates around a mean value for $m = 2$, whereas for $m = 4$ (and other azimuthal mode numbers), it converges to a constant value. This indicates that the Floquet multiplier is a complex value, as suggested by Robichaux *et al.* (1999). As a result, $m = 2$ corresponds to a quasi periodic mode, with a complex Floquet multiplier (Sheard *et al.*, 2005).

The spatial distribution of the azimuthal component of the vorticity of the eigenmodes $m = 2$ and $m = 4$ are shown in figure 5.11. The spatial distribution is similar to the that observed at $Re = 250$, with $m = 2$ mode extending downstream of the bulge region. The spatial distribution reveals that the perturbations arise in the form of counter rotating vortices downstream of the AAA cavity. This is illustrated by the presence of alternating positive and negative vorticity along the domain.

5.3.3   Stability analysis: $Wo = 10$

The effect of lowering the Womersley number even further to 10 on the stability characteristics is discussed in this section, the base flows of which are already discussed in detail in the previous chapter 4. As at $Wo = 12$, the primary vortex formed during the deceleration phase after peak systole, that impinges at the distal end of the AAA, is much stronger resulting in secondary vortices within the AAA cavity.

The results from our stability calculations are summarized for the case of $Wo = 10$ at various Reynolds numbers in figure 5.12. The flow corresponding to $Re = 200$, 250 are more unstable, when compared with the results obtained for $Wo = 12$ (see figure 5.6).

	$Wo = 10$	$Wo = 12$
$Re = 200$	0.6956	-0.0988
$Re = 250$	1.2398	0.4073
$Re = 300$	0.3559	0.3554

Table 5.2: Growth rate $\sigma = \frac{1}{T}\log\mu$ of the least stable mode.

Figure 5.13: Contours of azimuthal vorticity along with the velocity vectors of the perturbations corresponding to the mode $m = 2$ at various Reynolds numbers. Parameter settings: $Q1$, $H = 0.5$, $W = 0.5$, $Wo = 10$, $m = 2$.
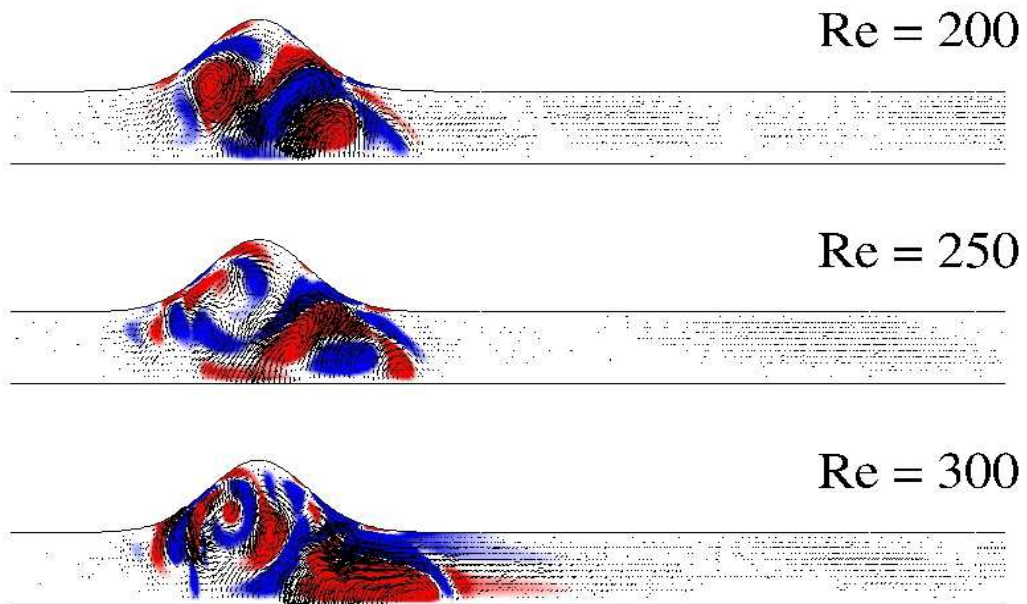
However, the Floquet multipliers obtained for the case of $Re = 300$ are smaller and the flow is observed to be more stable than at slightly lower Reynolds numbers. Mode $m = 2$ is observed to be subharmonic in nature for all the Reynolds numbers investigated. The Floquet multiplier corresponding to $m = 1$ for $Re = 300$ is complex. The values of Floquet multipliers are considerably higher resulting in large values of growth rates (though the time period is higher too), that are summarized in table 5.2. The vorticity distributions of the unstable mode $m = 2$ for various Reynolds numbers are shown in figure 5.13. Unlike in the earlier cases at higher Womersley numbers, the perturbations are entirely localized within the AAA cavity. With an increase in Re, the maximum value of perturbations are seen to be more localized at the distal end.

5.3.4   Stability analysis: $Wo = 5$

To conclude this section on the effect of flow parameters on stability characteristics, we present some results obtained at $Wo = 5$. As mentioned in the previous chapter, the Womersley numbers usually observed in the abdominal aorta are within the range 10–15. Hence the investigation of stability characteristics at $Wo = 5$ is carried out mainly from an academic point of view. We have seen that the flows are more and more unstable with decreasing Womersley numbers, due to the differences in the base flow characteristics. However, one would expect that the flows return to stability at sufficiently low values of Womersley numbers.

Figure 5.14 shows the corresponding Floquet multipliers for $Re = 200$. Only a single value of Reynolds number was chosen as it should provide us with sufficient qualitative information. As expected, the flow is stable for all azimuthal mode numbers, with the values of Floquet multipliers being very low (note the scale of the vertical axis in these plots). This agrees with the fact that the flow remains attached during the major part of the cycle and the vortices that are formed are very weak. The values of growth rates σ, are given in table 5.3. Only the mode associated with $m = 1$ is observed to be sub-harmonic and the least stable mode corresponds to $m = 2$.

The spatial distribution of the modes for various values of m are shown in figure 5.15 using the azimuthal component of the vorticity. As seen at other Womersley numbers, the sub-harmonic mode corresponding to $m = 1$ extends downstream of the AAA dilatation. However, all the other modes are found to be localized within the cavity. This is interesting, as by reducing the Womersley number, one can think that asymptotically one would converge to the case of steady flows, where the perturbations are entirely confined to the AAA cavity.

5.4   Effect of dilatation parameter on stability characteristics

Throughout the discussion so far, the bulge height, H, and the bulge width, W, were fixed at a value of 0.5. However, as seen in the previous chapter (section 4.3.2), the base flow characteristics considerably depend on bulge height. Hence it is interesting to see how the stability characteristics of the flows in AAA vary during the growth of an AAA. For this investigation, we choose the waveform corresponding to the rest conditions, and the flow

m	σ
1	-0.2872
2	-0.2004
3	-0.2339
4	-0.2872
5	-0.4287

Table 5.3: Growth rate $\sigma = \frac{1}{T} \log \mu$ for various azimuthal mode numbers.
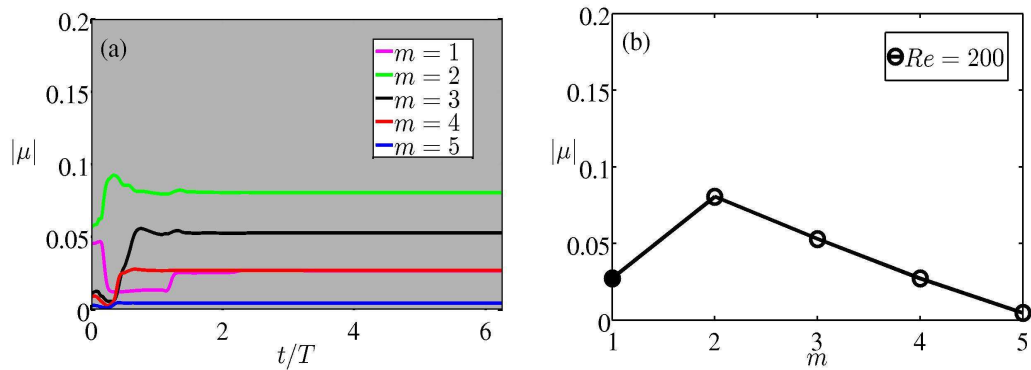
Figure 5.14: (a) Temporal evolution of the maximum value of Floquet multiplier. (b) Converged values of the Floquet multiplier. Sub-harmonic modes are showed using filled circles. Parameter settings: $Q1$, $H = 0.5$, $W = 0.5$, $Re = 200$, $Wo = 5$.
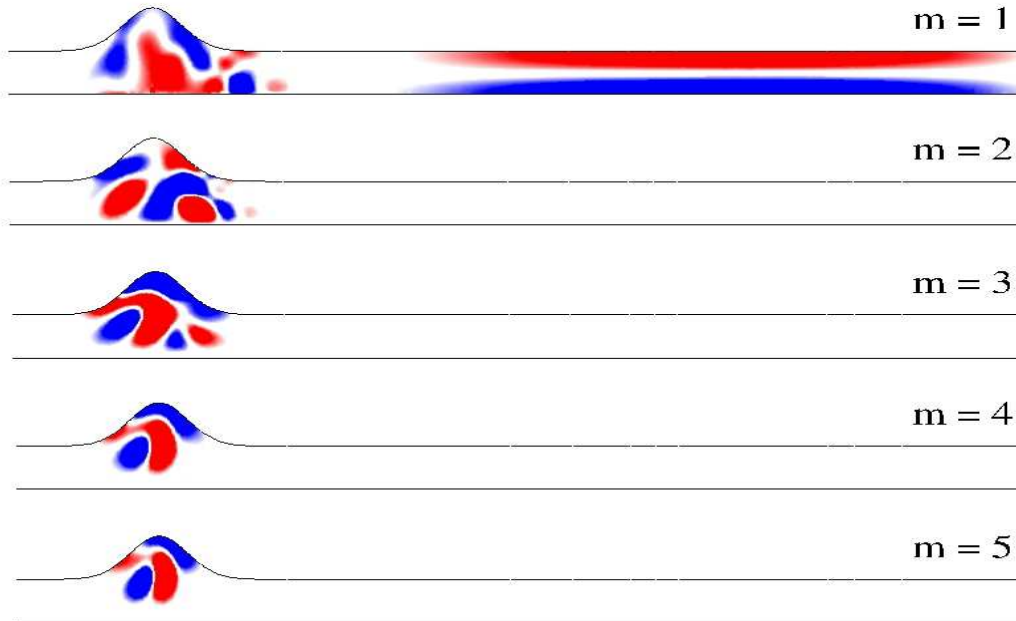
Figure 5.15: Contours of azimuthal vorticity of the perturbation at phase $t = 0.0T$ for various values of m. Parameter settings: $Q1$, $H = 0.5$, $W = 0.5$, $Re = 200$, $Wo = 5$.

parameters chosen are: $Re = 264$ and $Wo = 12$. The values of bulge height investigated are $H = 0.3$, 0.4, 0.5, 1 and the bulge width was fixed at 0.5.

Figure 5.16 summarizes the results of our stability calculations at various bulge heights. For small values of H, the dominant modes are observed to be sub-harmonic. The first striking result is that even at a very small value of H, the flow is not far from marginal stability. The least stable mode at $H = 0.3$ corresponds to $m = 1$ arising through a period-doubling bifurcation, with an absolute value of Floquet multiplier of 0.96. However, with increase in H, the contribution from the $m = 1$ sub-harmonic mode is found to diminish, and for higher values of H, $m = 1$ mode is harmonic, indicating that the eigenmodes are from different branches in the spectrum. At higher values of H, the dominant mode corresponds to a sub-harmonic mode of azimuthal mode number 2. The calculation at $H = 0.4$ was carried out in addition as the change in values of Floquet multipliers from $H = 0.3$ to $H = 0.5$ was significant. As seen in the previous chapter, the flow characteristics persistent in large AAAs are present even during the incipient stages. Here, the observed instability threshold observed roughly corresponds to $H = 0.4$.

The least stable modes obtained for various values of H are shown in figure 5.17 using azimuthal vorticity of the perturbations. Except for the case $H = 0.3$, the dominant mode at other bulge heights corresponds to $m = 2$. It is interesting to see that even at a small value of $H = 0.3$, the dominant mode extends downstream of the AAA cavity, affecting even the healthy undeformed arterial wall. As remarked earlier, in reality, the presence of the iliac artery bifurcation downstream of an AAA modifies the flow characteristics within
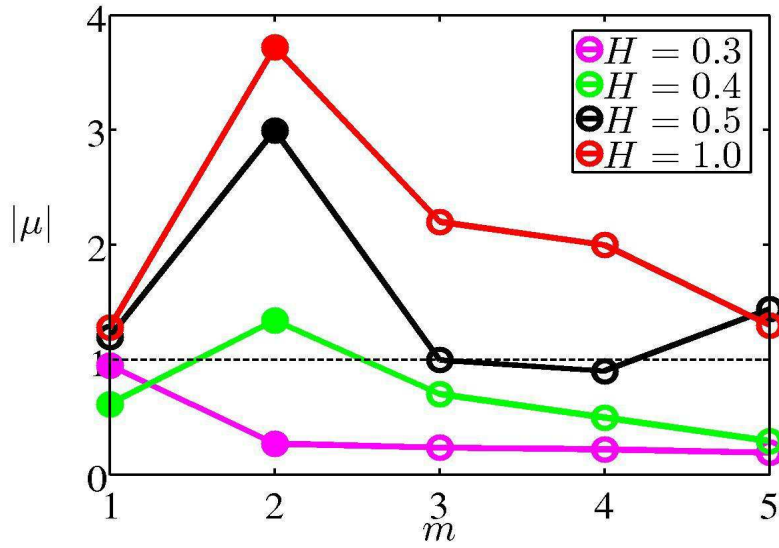
Figure 5.16: Absolute value of the Floquet multiplier at various values of H. Parameter settings: $Q1$, $W = 0.5$, $Re = 264$, $Wo = 12$.

Figure 5.17: Azimuthal vorticity contours of the least stable eigenmode for various bulge heights within an axial range $-1.5D \leq z \leq 7D$. Parameter settings: $Q1$, $Re = 264$, $Wo = 12$, $W = 0.5$.

Figure 5.18: Azimuthal vorticity contours of the least stable eigenmode for various bulge heights within an axial range $-1.5D \leq z \leq 10D$. Parameter settings: $Q1$, $Re = 264$, $Wo = 12$, $W = 0.5$ (a) $H = 0.4$ (b) $H = 1$.

an AAA. This points out that modeling an AAA along with the downstream bifurcation might provide us with more realistic flow features to help us to understand the pathology of AAAs.

The evolution of the unstable modes ($m = 2$) for two values of bulge height $H = 0.4$ and $H = 1$ are shown in figure 5.18 at various instants in a pulse cycle. Note that the axial scale corresponds to $-1.5D \leq z \leq 10D$. It is seen that the stability characteristics pointed out so far in this chapter are present even at a small value of $H = 0.4$. And more importantly, the unstable mode is found to extend far more downstream of the AAA dilatation at a smaller value of H, especially during the systolic phase (roughly around $t = 0.25\ T$). This is in coherence with our discussion on base flow characteristics. At a larger bulge height, the base flow vortices are trapped within the AAA cavity for longer times before getting advected out downstream. Firstly, this reinforces the significance of understanding the effect of an AAA on the downstream segment of the arterial wall, in the presence of an iliac bifurcation. Secondly, the role of fluid mechanical observations are more pertinent during the initial stages of growth of an AAA, in coherence with our observations made on base flow characteristics (see section 4.3.2).
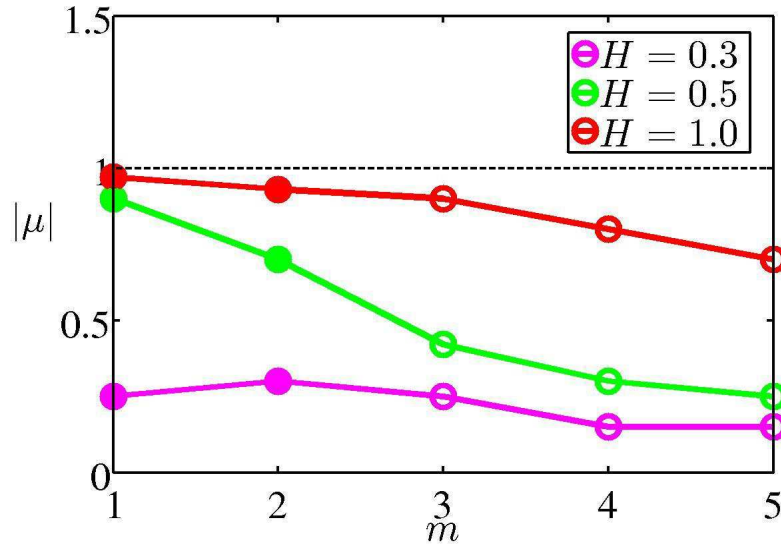
Figure 5.19: Floquet multiplier at $W = 1.0$ for different bulge heights. Subharmonic modes are shown using filled circles. The dotted line demarcates the stable region. Parameter settings: $Q1$, $W = 1.0$, $Re = 264$, $Wo = 12$.

5.5 Effect of aspect ratio on stability characteristics

The results of stability calculations performed at a larger value of bulge width, $W = 1$, are discussed now. It was shown in the previous chapter (see section 4.3.3) that for longer AAAs the vortices formed within the AAA cavity after peak systole are much weaker, coupled with the fact that the flow remains attached for longer times. Also, the oscillatory flow conditions within the AAA are weaker for longer aneurysms. These facts indicate that the flows in longer AAAs might be more stable than short aneurysms.

Longer AAAs with a small dilatation ratio are more resemblent of AAAs during the incipient stages. The summary of our results made at $W = 1$ are shown in figure 5.19. As expected, the flows are stable in comparison with the values observed for $W = 0.5$. This could be primarily attributed to the weak primary vortex formed within the AAA cavity, resulting in the absence of secondary vortices within the AAA dilatation. Once again, the dominant modes correspond to smaller values of m that are sub-harmonic. The mode corresponding to $m = 2$ at $H = 1$ is associated with a complex Floquet multiplier.

The spatial distribution of the modes at $W = 1$ for various values of H are shown in figure 5.20. The spatial distribution of the azimuthal vorticity shows that the perturbations are less localized within the AAA cavity. The perturbations within the AAA dilatation have their maxima at the same radial extent as the undeformed arterial wall. What this implies is that the disturbances close to the wall are weaker. As the endothelial cells lining the arterial wall are sensitive to disturbed flow conditions near the wall, these observations indicate that longer AAAs would be less pathological. However, even these computations show that the perturbations are not entirely limited to the AAA cavity. The presence of an
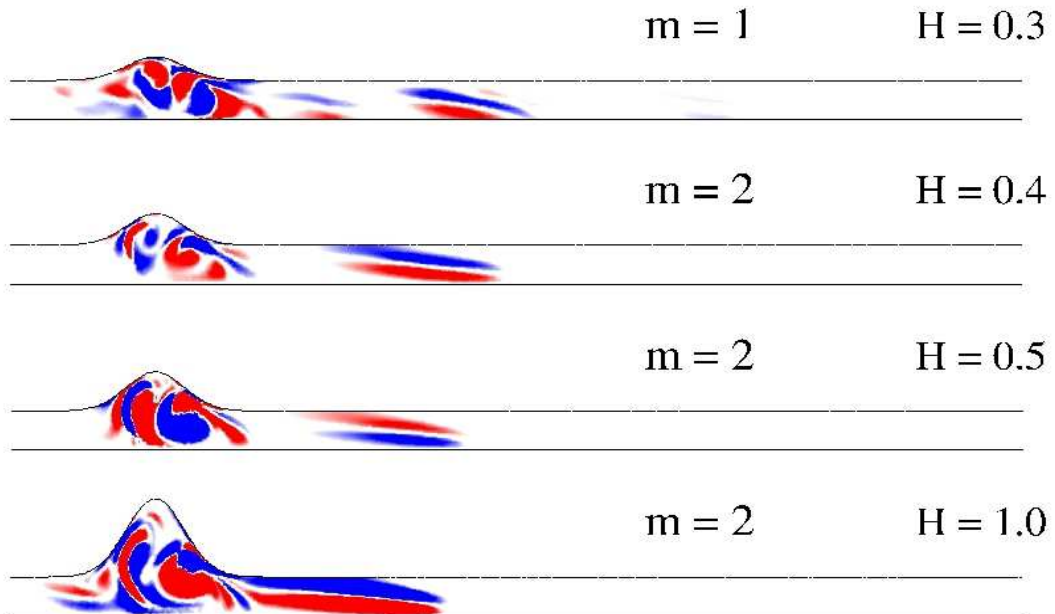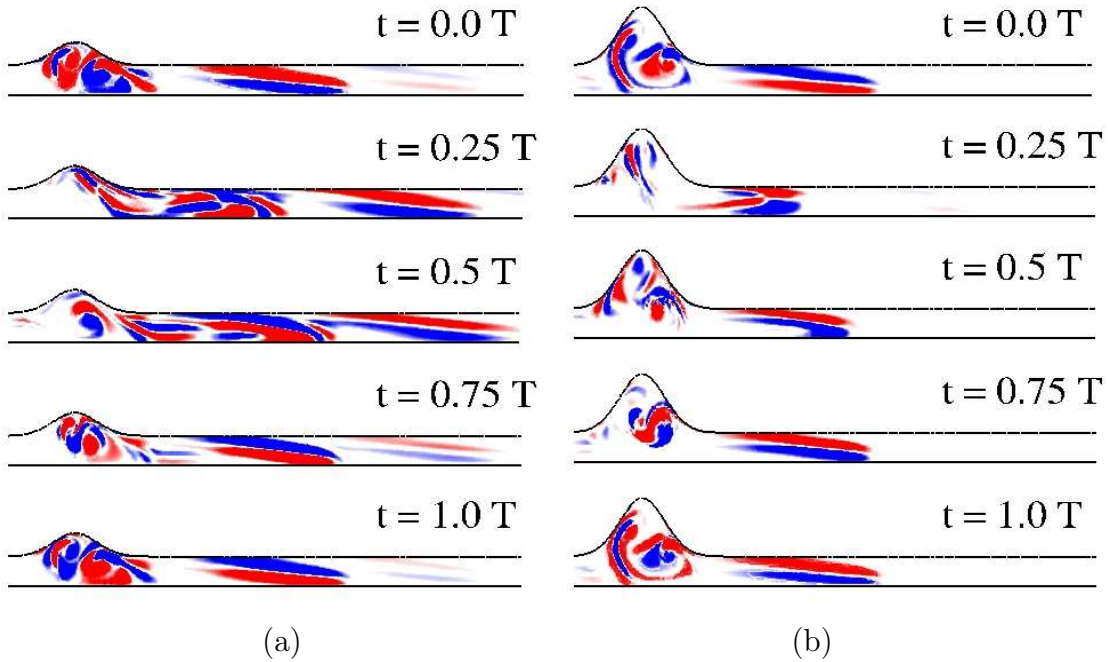
Figure 5.20: Azimuthal vorticity contours of the least stable eigenmode for various bulge heights within an axial range $-1.5D \leq z \leq 10D$. Parameter settings: $Q1$, $Re = 264$, $Wo = 12$, $W = 1$.

AAA initiates disturbed flow conditions on the healthy segment of the arterial walls even in an incipient aneurysm, characterised by a large value of W and a small value of H.

5.6   Stability characteristics during exercise conditions

The results of a linear stability analysis of flows in AAAs under exercise conditions is discussed here. A high peak velocity, fine mesh structure within the AAA cavity and large Reynolds numbers have meant that a very small time-step is required to satisfy CFL-type stability restrictions, and hence requiring more time. Due to this reason, we present only some preliminary results obtained for exercise conditions.

The $Q2$ waveform used is (see figure 4.1, chapter 4), obtained from the data provided in Suh et al. (2011) where the flow rate waveforms were measured in patients with abdominal aortic aneurysms (AAA) during exercise conditions. The Reynolds number corresponding to this waveform is 1700 and the Womersley number is 13.8. To simplify the computations, we have lowered the value of Reynolds number to 500. However, we expect that the characteristics of the perturbations observed for these flow parameters would be qualitatively similar even at a higher value of Re thereby providing us with sufficient information. Another interesting aspect of this analysis is that it helps us in identifying the differences that arise due to a change in the flow rate waveform. The geometry considered corresponds to a typical AAA, where the bulge width and height are fixed at 0.5.

The stability characteristics at $Re = 500$ are summarized in figure 5.21. Figure 5.21(a) shows the evolution of $|\mu|$, whose converged values are shown in figure 5.21(b). The flow
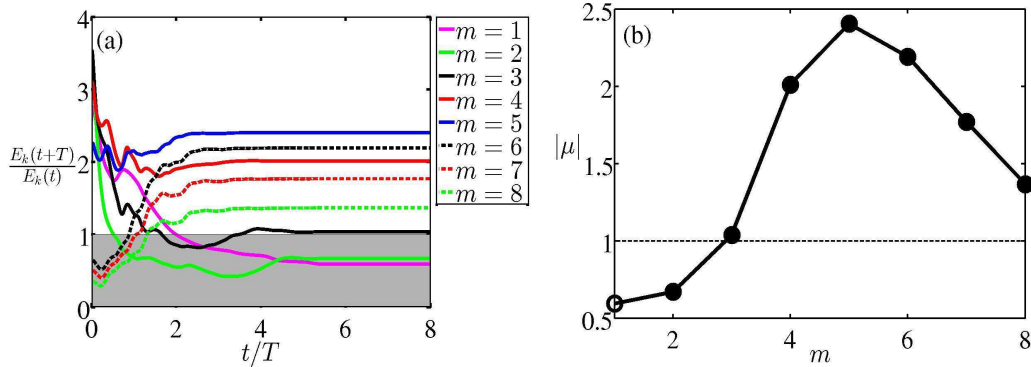
Figure 5.21: (a) Evolution of the absolute value of Floquet multiplier. (b) Absolute values of the Floquet multiplier. Sub-harmonic modes are showed using filled circles. Parameter settings: $Q2$, $H = 0.5$, $W = 0.5$, $Re = 500$, $Wo = 13.8$.

is unstable for the azimuthal mode numbers 3–8. All the Floquet multipliers are real, as $|\mu|$ converges to a constant value. The trend of the Floquet multiplier with respect to the azimuthal mode number, shown in figure 5.21(b), shows that $m = 5$ corresponds to the mode having the highest temporal growth rate. Also, for all the higher values of m starting with $m = 2$ the global modes are sub-harmonic in nature with a negative value for the Floquet multiplier. The period-doubling modes have a negative Floquet multiplier, μ, and are indicated using filled circles. This also indicates that the flows at $Re = 1700$ are more likely to be unstable with even higher values of Floquet multipliers.

The spatial distributions of the perturbations for different azimuthal mode numbers are shown in figure 5.22 using the azimuthal vorticity. Modes corresponding to $m = 1$ and $m = 2$ are stable whereas modes 3, 4 and 5 are unstable. The distributions corresponding to modes 6–8 are not shown as they resemble those seen at $m = 5$. Though the perturbations are concentrated within the AAA cavity, they do extend downstream of the AAA to the healthy undeformed sections of the arterial wall. These observations indicate that once an aneurysm is present, the disturbed flow conditions affect even the undeformed AAA wall which could be damaging and aiding in further progression of this disease. An observation of interest is that the mode $m = 3$ is marginally unstable and extends further downstream of AAA. Whereas modes 4 and 5 that have even higher temporal growth rates are more localized within the AAA cavity. However, these snapshots present the picture only at phase $t = 0T$.

The distributions at various instants in a pulse cycle for modes $m = 3$ and $m = 5$ are shown in figure 5.23. The spatial distributions corresponding to both the azimuthal mode numbers are very similar. These snapshots show that during a pulse cycle the disturbances created by the presence of an AAA extend far downstream of the AAA dilatation. The presence of these disturbed flow conditions may promote thrombosis formation and platelet activation even in the sections of healthy arterial walls. In stark contrast, for the case of steady flows, where even at high Reynolds numbers, the modes were confined entirely to the AAA cavity.
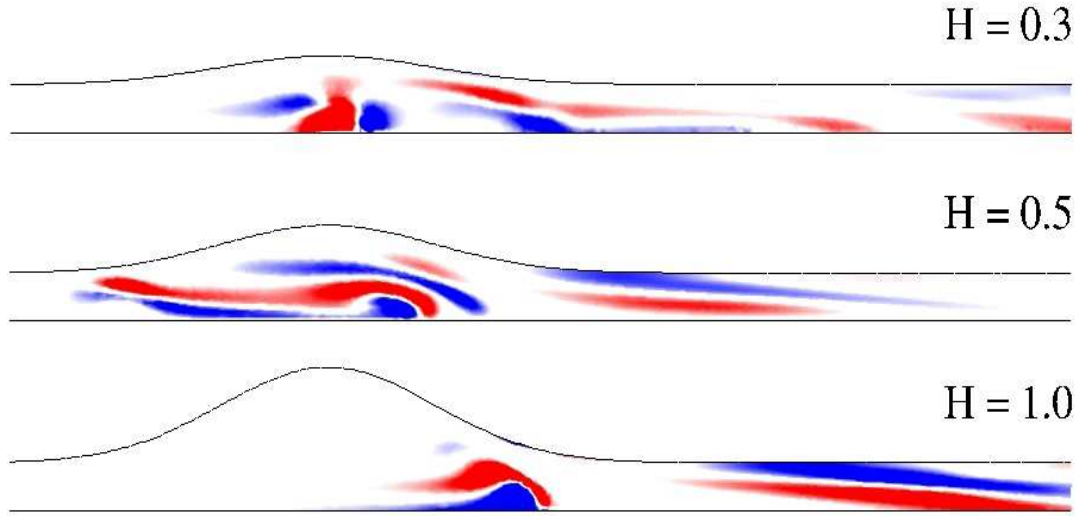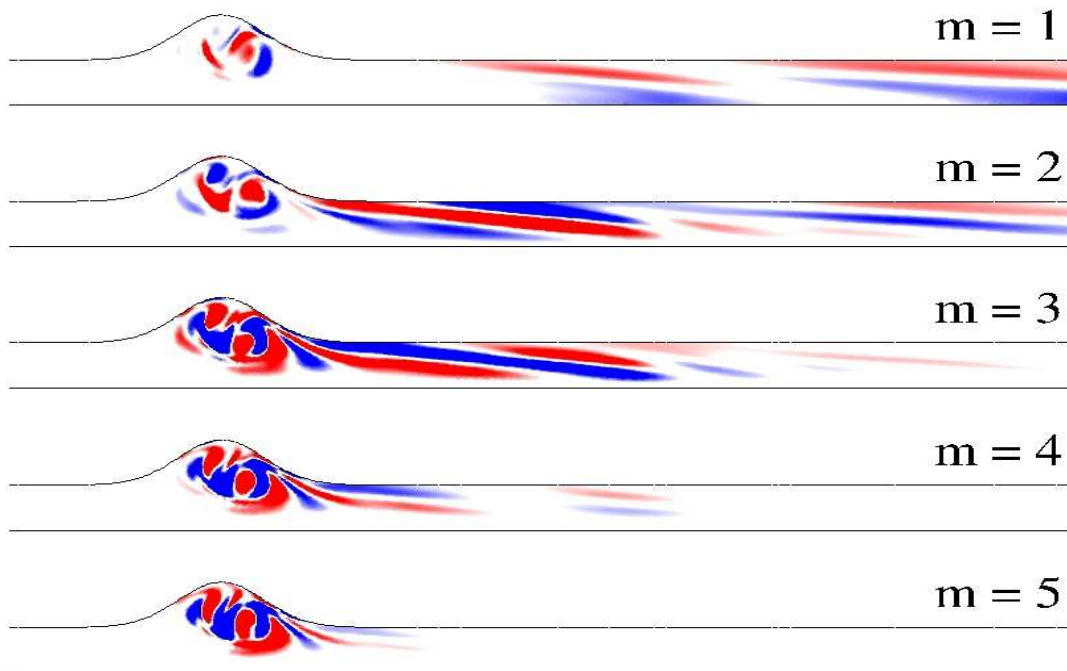
Figure 5.22: Azimuthal vorticity contours of the least stable eigenmode for various azimuthal mode numbers within an axial range $-2.5D \leq z \leq 10D$. Parameter settings: $Q2$, $H = 0.5$, $W = 0.5$, $Re = 500$, $Wo = 13.8$.

(a)   (b)
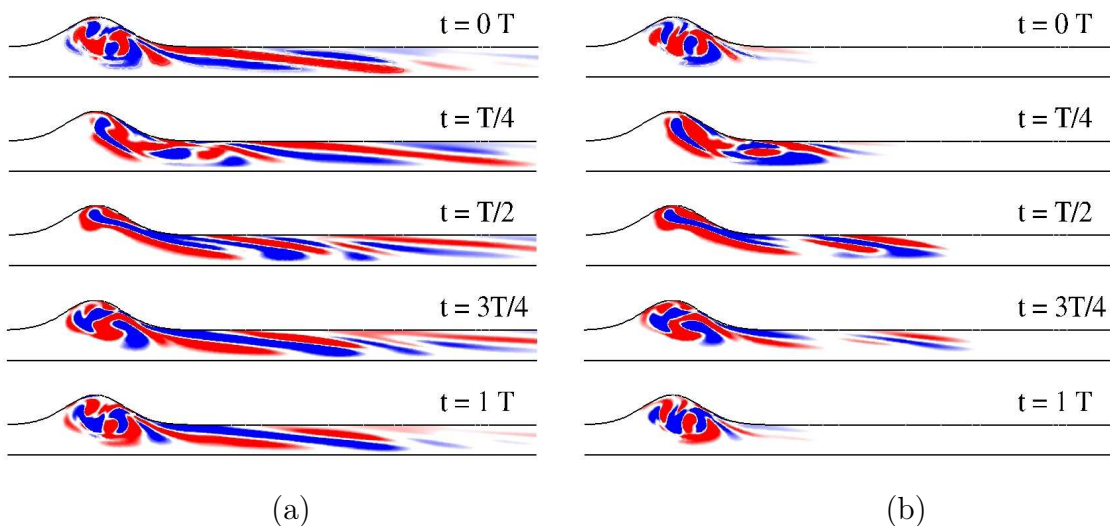
Figure 5.23: Azimuthal vorticity contours of the least stable eigenmode for (a) $m = 3$ (b) $m = 5$ within an axial range $-1.5D \leq z \leq 7.5D$ during a pulse cycle. Parameter settings: $Q2$, $H = 0.5$, $W = 0.5$, $Re = 500$, $Wo = 13.8$.
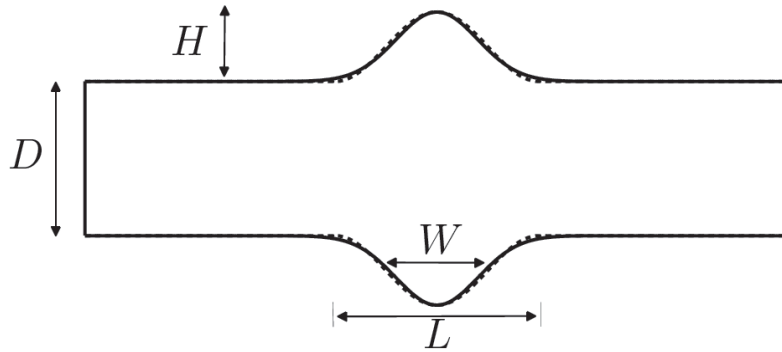
Figure 5.24: The geometry considered in the study by Sheard (2009) is shown using dotted lines, where the dilatation was modeled as a sinusoidal function. The corresponding gaussian equivalent geometry is shown using continuous lines. Parameter settings: $H = 0.45$, $L = 2.9$, $W = 0.58$.

5.7 Effect of wall modeling on flow dynamics

In the previous chapter (section 4.5), we had discussed the changes that arise due to a different choice of function used to model the AAA wall. Though the AAAs modeled using a sinusoidal and a gaussian function were very similar, the base flow characteristics, in particular the absolute values of the wall shear stresses (WSS) at the distal end, where the differences in the two geometries are more prominent, were significantly different. The two geometries are shown again in figure 5.24. More details regarding the geometries are given in chapter 2, section 2.4.2. We now discuss the differences in stability characteristics that arise in these geometries. As a study on flow characteristics in an AAA using a sinusoidal function was carried out recently by Sheard (2009), we consider the same geometrical and flow characteristics as in their study. The flow conditions correspond to the waveform $Q3$ (shown in figure 4.47, chapter 4) and the flow parameters are $Re = 330$ and $Wo = 10.7$. The same geometry and flow conditions were also employed in the study by Salsac *et al.* (2006).

The stability characteristics are summarized in figure 5.25. Figure 5.25(a) shows the evolution of $|\mu|$, obtained by modeling the AAA using a gaussian function. The absolute values of the Floquet multipliers are summarized in figure 5.25(b), where the dotted line corresponds to the values obtained using a sinusoidal function and the continuous line using a gaussian function. Firstly, it is seen that all the modes except $m = 1$ are unstable, for the case of a gaussian function. The least stable mode corresponds to $m = 3$. Secondly, for the case of a sinusoidal function, the absolute values of Floquet multipliers are higher, with even $m = 1$ being unstable, though the trends observed are quite similar. As discussed in the previous chapter (see section 4.5), the WSS values obtained using a sinusoidal function are found to be also higher, indicating slightly larger gradients near the wall, which is in congruence with higher Floquet multipliers. Thirdly, from the evolution of $|\mu|$, we can deduce that all the Floquet multipliers are complex. These observations agree with those made by Sheard & Ryan (2008).

The spatial distributions of the eigenmodes obtained using a sinusoidal and a gaussian function are shown in figure 5.26 (a) and (b) respectively. The distributions of the perturbations
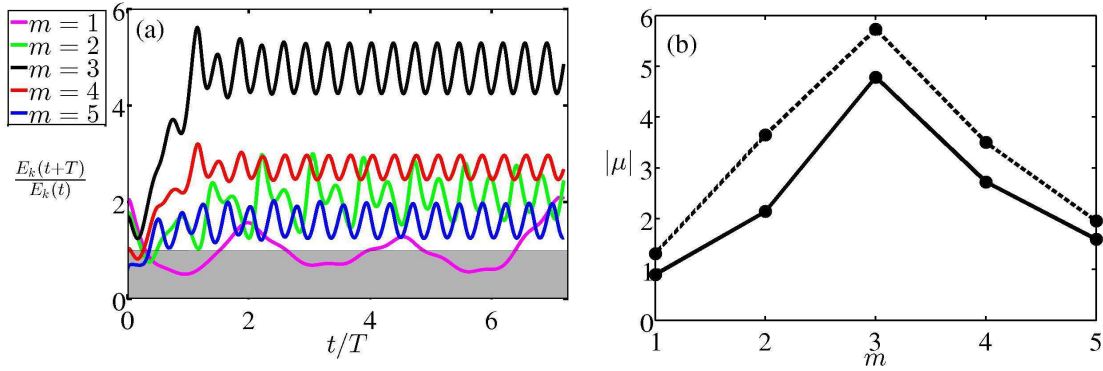
Figure 5.25: (a) Ratio of kinetic energies showing the evolution of the absolute value of Floquet multiplier obtained by modeling the aneurysm using a gaussian function. The shaded region indicates the stable region. (b) The absolute value of Floquet multipliers obtained by modeling the aneurysm using a sinusoidal (dotted line) and a gaussian (continuous line) function. Parameter settings: $Q3$, $H = 0.45$, $W = 0.58$, $Re = 330$, $Wo = 10.7$.
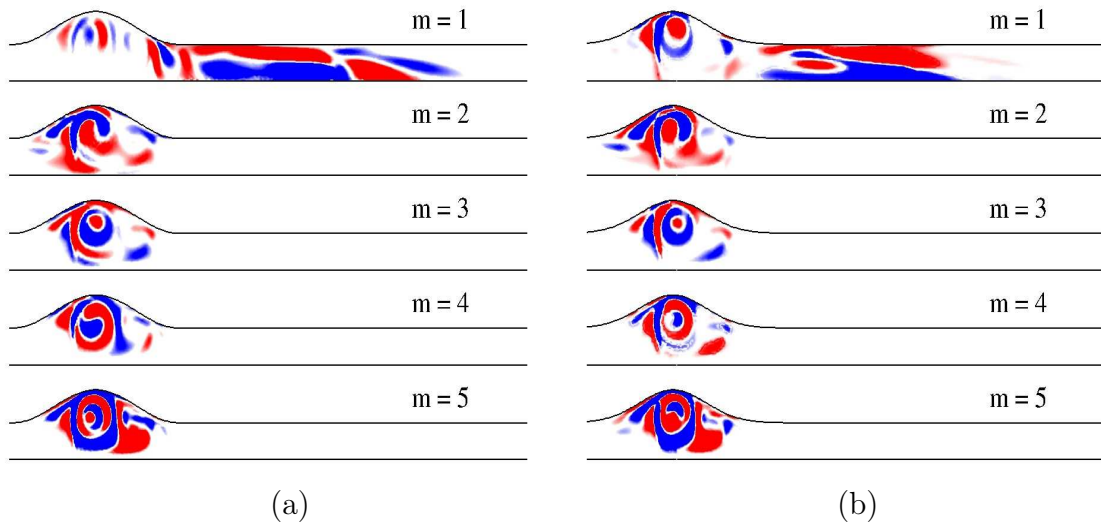
Figure 5.26: Azimuthal vorticity contours of the least stable eigenmode for different mode numbers m within an axial range $-2D \leq z \leq 10D$. (a) Sinusoidal AAA (b) Gaussian AAA. Parameter settings: $Q3$, $H = 0.45$, $W = 0.58$, $Re = 330$, $Wo = 10.7$.
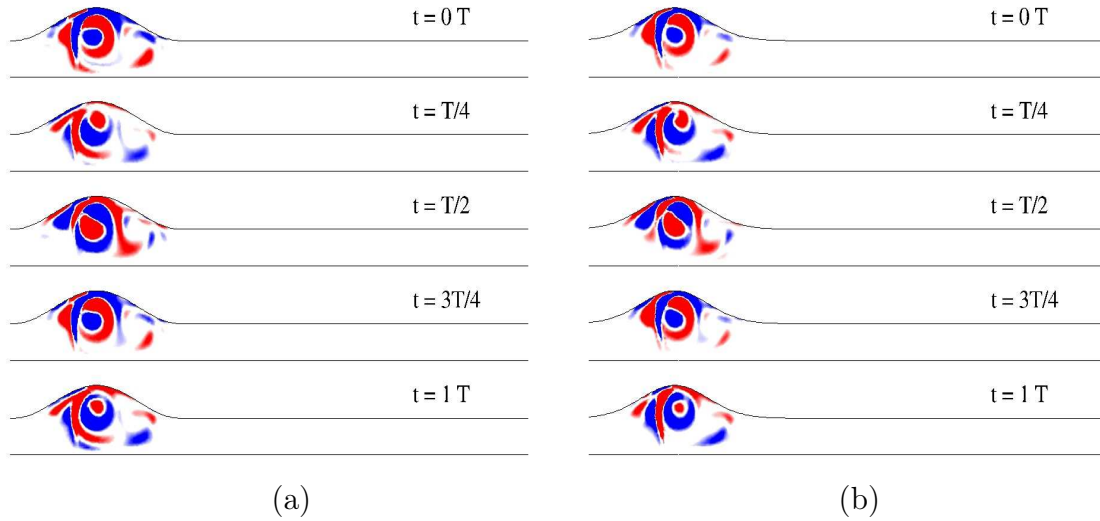
Figure 5.27: Azimuthal vorticity contours of the eigenmode corresponding to $m = 3$ at different phases. (a) Sinusoidal AAA (b) Gaussian AAA. Parameter settings: $Q3$, $H = 0.45$, $W = 0.58$, $Re = 330$, $Wo = 10.7$.

are found to be very similar but not indistinguishable for both the cases. The more unstable modes corresponding to $m = 2$, 3, 4, 5 are localized within the bulge region and do not extend downstream of the AAA dilatation. As a confirmation, we provide the snapshots of the eigenmodes corresponding to $m = 3$ obtained using an AAA modeled using both the functions at various time instants in a pulse cycle in figure 5.27. Once again, similar spatial distributions are observed for both the AAAs. Throughout the pulse cycle the perturbations are confined entirely to the AAA cavity. The eigenmode seems to rotate in an anti-clockwise direction as the cycle evolves. This comparison of stability characteristics between sinusoidal and gaussian shapes shows again that small but significant differences are due to minute changes in geometry.

5.8 Discussion

We have studied pulsatile flows in a smooth axiymmetric abdominal aortic aneurysm (AAA) using three-dimensional stability analysis. Our objective here has been to establish the stability characteristics and flow behaviour observed in an AAA under varying geometrical parameters and flow conditions.

Two types of physiological flow rate waveforms are considered, corresponding to rest ($Q1$) and exercise ($Q2$) conditions. The waveforms are obtained from the article by Suh *et al.* (2011) which were measured in patients having AAAs during resting and exercise conditions. Using the waveform $Q1$, the Womersley number Wo and the Reynolds number Re, are varied in the range 5–15 and 200–300 respectively. To the basic flow computed at different conditions, which are discussed in detail in the previous chapter 4, three-dimensional perturbations were superimposed and the temporal evolution of these perturbations was computed by time-marching the linearized Navier–Stokes equations. At a high Womersley number of 15, we have observed the flows to be stable

at Reynolds numbers 200 and 250. For small values of the azimuthal mode number m, the instability occurrs through a period-doubling bifurcation with a negative Floquet multiplier. Similar flow features were observed in stenotic flows (Sherwin & Blackburn, 2005, Blackburn & Sherwin, 2007, Griffith *et al.*, 2009, 2013). At a higher value of $Re = 300$, the most unstable mode corresponds to $m = 3$ with the eigenmode having a real positive Floquet multiplier, resulting in a harmonic bifurcation. An interesting feature observed in these analyses is that the perturbations are not entirely confined to the AAA cavity and extend well downstream, though the maximum values are observed near the distal end of the AAA. This implies that once an AAA is formed, the disturbed flow conditions may affect the undeformed arterial walls. These observations are in stark contrast with those made using steady base flows, as in the latter, the modes are entirely confined to the AAA. As a consequence the endothelial cells lining the arterial walls, even downstream of the AAA, experience disturbed flow conditions. These observations may be an important step in understanding the progression of this pathology as such disturbed flow conditions are known to promote atherosclerosis and thrombosis formation (Lasheras, 2007, Deplano & Siouffi, 1999, Barakat, 2013). These observations also indicate the need to consider the iliac bifurcation downstream of the AAA in future studies as they could play an important role in the spatial distribution of the perturbations.

The flows are found to be more unstable as the Womersley number is lowered to 10 and 12. The most unstable mode arises as a sub-harmonic bifurcation with an azimuthal mode number 2. As seen from the base flow characteristics, at a lower Womerlsey number, the flow separation at the proximal end of the AAA is found to occur earlier in the cycle resulting in stronger vortices within the aneurysm that persist for longer times. This explains why the Floquet multipliers observed at a lower Womersley number are higher. Also, for some parametric conditions, the Floquet multiplier is complex. The complex Floquet multiplier is identified using the temporal evolution of the absolute value of the Floquet multiplier. This shows the presence of different unstable modes and the true complexity of the flows in AAAs. As the Womersley number is reduced even further to a value of 5, as expected the flows are stable. The least stable modes are confined to the AAA dilatation. This is in congruence with the fact that by reducing the Womersley number, asymptotically one would get a steady flow regime, where the perturbations are confined entirely to the AAA cavity.

Using the waveform corresponding to rest conditions, $Q1$, the effect of the dilatation parameter and aspect ratio on stability characteristics has been investigated. The flow becomes unstable as the dilatation ratio is increased for a fixed value of bulge width W. Even at a small value of bulge height H, the spatial distributions of the perturbations are similar to those observed in a typical AAA, with eigenmodes extending downstream of the aneurysm to the healthy regions. These indicate the relevance of fluid mechanics even for an incipient aneurysm. Increasing the bulge width results in more stable flows. We have seen in the previous chapter that weaker disturbed flow conditions prevail in longer AAAs. This is further confirmed from the stability calculations as the perturbations are localized away from the arterial walls and the flows are globally stable.

Flows in AAAs during exercise conditions are investigated using the waveform $Q2$. They are characterised by a high peak velocity and large Reynolds numbers. We observed the flow to be unstable at $Re = 500$ and $Wo = 13.8$ to azimuthal mode numbers 2, 3, 4 and 5 through a period-doubling bifurcation. All the Floquet multipliers are real. The

spatial distributions reveal that the perturbations are strong within the AAA cavity, near the distal end and are prominent even downstream of the aneurysm. As remarked in the last chapter on the base flow characteristics, during exercise conditions the flow may be turbulent in AAAs. The presence of strong perturbations indicates that the mixing of blood flow is more prominent during exercise conditions. These flow patterns with increased flow magnitude and turbulence reduce regions of flow stasis that have been correlated with thrombus formation (Salsac *et al.*, 2004, Deplano & Siouffi, 1999, Reininger *et al.*, 1994). However, the final saturated states of these modes would be required to investigate this further.

Finally, the sensitivity of these results with respect to the details of the geometry has been investigated by considering two equivalent AAAs modeled, respectively, by a sinusoidal and a gaussian function. For this analysis, the flow conditions and geometrical parameters are chosen as in the studies by Salsac *et al.* (2006), Sheard (2009). The flow rate waveform $Q3$ corresponds to $Re = 330$ and $Wo = 10.7$. The stability characteristics observed in the sinusoidal and gaussian AAA are qualitatively similar. The Floquet multipliers are all complex with the dominant mode observed for the azimuthal mode number $m = 3$. The sinusoidal AAA has significantly higher growth rates than the gaussian AAA, whereas both geometries are difficult to distinguish visually and the discrepancy between the two models is negligible as compared to any real AAA. These results highlight the difficulty to establish general conclusions based on simplified and approximate models. The same difficulties are expected to prevail for patient-specific computations. The difference between a real AAA and a geometry reconstructed from CT-scans is at least of the same order than between our sinusoidal and gaussian shapes.

Conclusions and Perspectives

6.1   Conclusions

It has now been recognized that abdominal aortic aneurysms (AAA) result from a complex interplay between structural changes of the arterial wall and disturbed patterns of hemodynamic stresses acting on the vessel wall. Hemodynamic stresses (pressure and wall shear stresses) are thought to affect the mechanisms responsible for the formation, growth and rupture of AAAs via changes in the structure of the arterial wall resulting in wall degradation. Changes of the arterial wall in turn influence the flow through the arterial segment. Despite intensive investigation, a definitive correlation between arterial fluid mechanics and arterial wall dysfunction has remained elusive. Arterial wall dysfunction due to atherosclerotic lesions has been correlated with the formation and growth of an aneurysm. Recent studies have demonstrated that the endothelial cells that line the arterial vessel wall are receptive to spatial and temporal gradients and in particular, regions of low oscillatory wall shear stresses (WSS). The main objective of the dissertation has therefore been to characterize the changes in flow characteristics resulting from the enlargement of the abdominal aorta under physiologically varying flow conditions, in order to provide some insights on the role that the hemodynamic forces may play in the etiology and progression of the pathology. The WSS distributions and other base flow characteristics, and the linear stability of the flows were analysed numerically. The motivation behind linear stability analyses of the flows were to understand the mechanisms at the onset of instability that would help us in understanding the flow behaviour in more complex configurations. An axisymmetric AAA, modeled as an inflation of gaussian shape on a vessel of circular cross-section, is considered in the present study with the primary focus being on characterising the flow fields during the early stages of growth of an AAA. The model AAA is characterized by a maximum height H and width W, made dimensionless by the upstream vessel diameter. The use of a model AAA geometry, enabled us to systematically quantify the effects of various geometrical parameters on flow characteristics.

As a first step towards understanding the flow fields in AAAs, a steady flow was studied. Though steady flows may not be directly relevant to the understanding of hemodynamics within an AAA, as the flow in the aorta is pulsatile, it does provide us with information on the flow characteristics, without having the complexity brought in by the unsteadiness of the flow. The fluid is assumed to be Newtonian and the flow far upstream and downstream of the inflation is a Hagen–Poiseuille flow, characterized by its Reynolds number. The base flow through the model aneurysms is determined for non-dimensional heights and widths in the physiologically relevant ranges $0.1 \leq H \leq 1.0$ and $0.25 \leq W \leq 2.0$, and Reynolds numbers up to 7000, which corresponds to peak values recorded during pulsatile flows under physiological conditions. It is found that the base flow consists of a core of relatively fast moving fluid, surrounded by a slowly recirculating

fluid that fills the inflation; for the larger values of the ratio H/W a secondary recirculation region is observed. The wall shear stresses in the inflation are vanishingly small as compared to those in the straight vessels. The global linear stability of the base flows was analysed by determining the eigenfrequencies and eigenfunctions of small-amplitude perturbations. In order to understand the instability mechanisms, the energy transfer between the base flow and the perturbations was computed. As expected, the flows were observed to be stable for small values of H. The modes corresponding to different values of azimuthal mode numbers were observed to be dominant at various values of H and W. Relatively shallow aneurysms (of relatively large width) become unstable by the lift-up mechanism and have a perturbation flow which is characterized by stationary, growing modes. More localized aneurysms (with relatively small width) become unstable at larger Reynolds numbers, presumably by an elliptic instability mechanism; in this case the perturbation flow is characterized by oscillatory modes.

For the case of pulsatile flows, two types of physiological flow rate waveforms were considered in our study, corresponding to rest ($Q1$) and exercise ($Q2$) conditions. Using the waveform $Q1$, the flow parameters, the Womersley number Wo and the Reynolds number Re, were varied in the ranges 5–15 and 200–500, respectively. The flows are observed to remain attached to the walls during the systolic phase, with flow separation generally observed during the deceleration after the peak systole. During this phase, the vorticity is found to roll-up into a vortex at the proximal end. This vortex enlarges with time and impinges at the downstream end of the AAA, resulting in large spatial gradients of WSS along the wall. Our computations of flow fields for a range of AAA shapes have shown that the flow inside the aneurysm is characterized by the formation of regions of higher and lower values of WSS than in the healthy vessel. Regions with large spatial gradients in WSS distributions are observed, particularly at the distal end of the AAA, which are not found in the healthy case. For a typical AAA under rest conditions, at peak systole, the maximum WSS observed at the downstream end is about 1.7 times the value recorded in a healthy abdominal aorta. However, when considering the time-averaged WSS, a peak is found 2.8 times greater than the mean level in the healthy vessel, and an opposite-signed peak that is 4.8 times greater.

The flow conditions are observed to vary significantly with Womersley and Reynolds numbers. It is observed that the flow remains attached to the walls for longer times, as the Womersley number Wo increases. Due to this, the primary vortex formed during the deceleration phase is weaker and secondary vortices are not formed within the AAA cavity at higher Wo's. Inspection of axial velocity profiles, close to the wall also showed that the spatial variations along the wall, and local temporal fluctuations, are more marked at lower Womersley numbers. These observations are reflected in the WSS distributions which reveal that the peak maximum and minimum values increase with a decrease in Wo. The principal effect of increasing Re is that the primary vortex formed after peak systole is stronger, compounded by the fact that flow separation takes place earlier in the pulse cycle. As a result, peak WSS and spatial gradients of WSS along the arterial wall are found to increase.

Clinically relevant flow characteristics of aneurysmal flow, i.e. detachement of flow and impingement on the distal end, the presence of low oscillatory WSS within the AAA, were observed even for very shallow aneurysms. For deep aneurysms, multiple vortices are observed throughout the cycle within the AAA cavity. Moreover, it is seen that the peak WSS hardly changes with increase in bulge height and qualitativley similar WSS

distributions are observed. However, the minimum value of WSS, usually observed slightly upstream of the distal end is seen to increase sharply during the initial growth of an AAA. These studies indicate that the spatial distributions of WSS and their gradients, are more relevant for AAAs during the incipient stages, and may not be an important parameter in the expansion of AAAs during the latter stages. For longer aneurysms, weaker spatial and temporal variations along the wall have been observed, with a decrease in minimum and maximum values of WSS.

The analysis of pulsatile flows corresponding to exercise conditions revealed that the strength of vortices formed increases under exercise conditions, and the absence of reversed flow during the pulse cycle. The flow fields are more complex than under rest conditions. Such exercise-induced flow patterns with increased flow magnitude and moderate turbulence, reduce regions of flow stasis that have been correlated with thrombus formation. Analysing the velocity profiles close to the arterial wall reveals that the spatial and temporal gradients are significantly lower during exercise conditions, thereby reducing hemodynamic flow conditions known to promote arterial wall degradation. The WSS distributions observed are similar with a peak maximum value observed at the distal end and a minimum value observed slightly upstream. The effects of varying geometry on flow dynamics and consequently on the WSS distributions are smaller during exercise conditions than during resting conditions.

In order to investigate the stability of these pulsatile base flows at different conditions, the temporal dynamics of small-amplitude three-dimensional perturbations has been computed via the linearized Navier–Stokes equations. For a typical AAA under resting conditions, $m = 2$ is the leading azimuthal mode that is sub-harmonic with higher mode numbers being harmonic. The maximum values of the perturbations are observed near the distal end of the AAA. However, they are not entirely confined to the AAA cavity and extend downstream. This implies that once an AAA is formed, the disturbed flow conditions spread even to the undeformed arterial walls. These observations are in contrast with those made using a steady base flow, as in the latter, the modes are entirely confined to the AAA. As a consequence the endothelial cells lining the arterial walls, even downstream of the AAA, experience disturbed flow conditions. The waveform corresponding to rest conditions $Q1$ is used to investigate the effects of Womersley and Reynolds numbers on the stability characteristics. The flows are found to be unstable as the Womersely number is lowered from 15 to 10. At a relatively high Womersley number 15, the flow is observed to become unstable at $Re = 300$ through a harmonic bifurcation and $m = 3$ is the leading azimuthal mode. For lower values of Wo, the most unstable mode arises as a sub-harmonic bifurcation with an azimuthal mode number 2. When the Womersley number is reduced even further to a value of 5, as expected the flows were stable for the range of Re considered. The least stable modes are then confined to the AAA dilatation.

Similarly, the effect of the dilatation parameter and aspect ratio on stability characteristics has been investigated using the waveform $Q1$. The flow becomes unstable as the dilatation ratio is increased for a fixed value of bulge width W. Even at a small value of bulge height H, the spatial distributions of the perturbations are similar to those observed in a typical AAA, with eigenmodes extending downstream of the aneurysm to the healthy regions. This indicates the relevance of a stability analysis even for an incipient aneurysm. Increasing the bulge width results in more stable flows with weaker perturbations close to the arterial walls.

Flows in AAAs during exercise conditions, that are characterised by waveform $Q2$ with a high peak velocity and larger Reynolds numbers, were also studied. The flow then becomes unstable at $Re = 500$ and $Wo = 13.8$ to azimuthal mode numbers 3–8 through a period-doubling bifurcation. The dominant mode corresponds to $m = 5$. The spatial distributions reveal that the perturbations are strong within the AAA cavity, near the distal end and are significant even downstream of the aneurysm.

Finally, the sensitivity of these results with respect to the details of the geometry has been investigated by considering two equivalent AAAs modeled, respectively, by a sinusoidal and a gaussian function. Though both the AAA geometries almost superpose, small but significant differences in flow dynamics occur. Flow separation occurs earlier in the pulse cycle in a sinusoidal AAA, with the flow field obtained in a gaussian AAA slightly lagging in phase in comparison with a sinusoidal AAA. This is probably due to the fact that a gaussian function converges more smoothly at the proximal and distal ends of the AAA cavity. As a result, the WSS distributions are found to be slightly different, particularly at the upstream and downstream ends of the aneurysm. The stability analyses have shown that the Floquet multipliers are all complex with the dominant mode observed for the azimuthal mode number $m = 3$. The sinusoidal AAA has significantly higher growth rates than the gaussian AAA, whereas both geometries are difficult to distinguish visually and the discrepancy between the two models is negligible as compared to any real AAAs. These results highlight the difficulty to establish general conclusions based on patient-specific computations. Simplified models that would permit us to isolate the effect of a particular physical mechanism would probably be the best way forward to enhance our understanding of flows in abdominal aortic aneurysms.

6.2   Perspectives

The goal of fluid dynamicists is to enhance our understanding of flows in abdominal aortic aneurysms. As these flows are complex, it is important to analyse them using simplified models and hypotheses that would enable us to reach conclusions that reveal the underlying physics. Presented here are a number of possibilities for future work as a continuation of the present research.

(1) As a direct continuation of the present work, a fully nonlinear three-dimensional analysis could be implemented to investigate the saturated states that result from the instabilities identified in this thesis. A detailed investigation of the nonlinear dynamics would shed light on the disturbed flow conditions that prevail in these configurations.

(2) As seen in our present work, the data obtained using computations depend on the physiological flow rate waveforms that is used. Particularly, these waveforms vary from person to person, and also on the physiological activity that a person is engaged in. Hence it is important for fluid dynamicists working in this field to have an active co-operation with surgeons and doctors who have data on these waveforms observed *in vivo* AAAs. Ideally if one has a substantial data set of these waveforms, statistically speaking, is it possible to formulate a waveform that would encapsulate the characteristics present generally in AAA subjects? At the same time, as computations could be performed over a wide range of waveforms, is it possible to relate changes in flow characteristics to particular details of

these waveforms?

(3) Similarly, more data on AAA geometries would also be beneficial to scientists working in this field. As AAA geometries observed in reality are of complex shapes, information on geometrical parameters like the aspect ratio and dilatation ratio could help fluid dynamicists in choosing model AAAs, and what function one must use to model the AAA walls. However, it is important to understand the dependence of flow characteristics on geometrical parameters, and also on the function used to model the AAA walls, to use the physiological data in a better way.

(4) The effect of asymmetry on flow characteristics is another dimension that needs more investigation during the progressive enlargement of an AAA. As different sized AAAs rupture at different thresholds, this could be a significant parameter that would provide more information on the growth rate of AAAs, by taking into account the stresses acting on asymmetrical AAAs during its growth. Also, the presence of swirl in abdominal aorta has been observed; could it possibly influence the dynamics within an AAA?

(5) Most of the works in this field have not considered non-Newtonian effects on flow characteristics in AAAs, as they are deemed less significant in large arterial vessels. A study quantifying these effects, especially when the flow rates are small during the diastolic phase, could be necessary at some stage in providing a clearer picture on the flow dynamics.

(6) The influence of pulse pressure on cardiovascular prognosis is another point of view that needs more investigation. Since pulse pressure is partly determined by artery stiffness, the elasticity of arterial walls is considered to be a relevant parameter to assess cardiovascular risk. For instance, an AAA is located in the abdominal aorta, upstream of the iliac arteries, where the amplitude of the pressure pulse is considerably modified as a result of the reflection of the wave in the bifurcation. Such an increase in amplitude may initiate and accelerate the formation of the aneurysms in the elderly population. This could be investigated by a fluid-structure interaction problem considering elastic arterial walls.

(7) It has been observed that flows in AAAs are intermittently turbulent even during resting conditions. A transient growth analysis providing information on the amplification of energy and on the shapes of optimal perturbations would be useful in this regard. Also, if certain perturbation shapes that are most dangerous could be identified, along with the regions that are most sensitive, this could help identify "dangerous" features.

(8) The stability analysis carried out using pulsatile base flows revealed that the perturbations extended downstream of the AAA cavity. This brings up the question of the effect of the downstream iliac bifurcation on the flow dynamics observed in an AAA. Also, as an AAA is always observed upstream of this bifurcation, an analysis taking this into account could be appropriate.

(9) Finally, during the literature survey carried out during this work, it was seen that no systematic study of the stability of pulsatile pipe flows to non-axisymmetric disturbances is to be found, let alone for physiologically relevant pulsatile flows. Such a study would help us in identifying the characteristics of perturbations observed in a healthy abdominal aorta and how the perturbations triggered by the AAA bulge propagate in the upstream and downstream regions.

Bibliography

AIRD, W. C. 2007 Phenotypic heterogeneity of the endothelium: Part I Structure, function, and mechanisms. *Circ. Res.* **100**, 158–173. (Cited on pages 4 and 62.)

AMAR, J., RUIDAVETSB, J. B., CHAMONTINA, B., DROUETC, L. & FERRIÈRES, J. 2001 Arterial stiffness and cardiovascular risk factors in a population-based study. *J. Hypertens.* **19**, 381–387. (Cited on page 5.)

ARMON, M. P., WENHAM, P. W., WHITAKER, S. C., GREGSON, R. H. S. & HOPKINSON, B. R. 1998 Common iliac artery aneurysms in patients with abdominal aortic aneurysms. *Eur. J. Vasc. Endovasc. Surg.* **15**, 255–257. (Cited on page 1.)

ARZANI, A. & SHADDEN, S. C. 2012 Characterization of the transport topology in patient-specific abdominal aortic aneurysm models. *Phys. Fluids* **24**, 081901. (Cited on page 23.)

ASBURY, C. L., RUBERTI, J. W., BLUTH, E. I. & PEATTIE, R. A. 1995 Experimental investigation of steady flow in rigid models of abdominal aortic aneurysms. *Annals Bio. Med. Engg.* **23**, 29–39. (Cited on pages 20 and 57.)

BARAKAT, A. I. 2013 Blood flow and arterial endothelial dysfunction: Mechanisms and implications. *C. R. Physique* **14**, 479–496. (Cited on pages 84, 90, 126 and 146.)

BAYLY, B. J. 1988 Three-dimensional centrifugal-type instabilities in inviscid two-dimensional flows. *Phys. Fluids* **31**, 56–64. (Cited on page 76.)

BERGER, S. A. & JOU, L.-D. 2000 Flows in stenotic vessels. *Annu. Rev. Fluid Mech.* **32**, 347–382. (Cited on pages 8, 17 and 18.)

BLACKBURN, H. M. & SHERWIN, S. J. 2007 Instability modes and transition of pulsatile stenotic flow: pulse-period dependence. *J. Fluid Mech.* **573**, 57–88. (Cited on pages 17, 121, 124 and 146.)

BLACKBURN, H. M., SHERWIN, S. J. & BARKLEY, D. 2008 Convective instability and transient growth in steady and pulsatile stenotic flows. *J. Fluid Mech.* **607**, 267–277. (Cited on page 19.)

BLUESTEIN, D., NIU, L., SCHOEPHOERSTER, R. T. & DEWANJEE, M. K. 1996 Steady flow in an aneurysm model: correlation between fluid dynamics and blood platelet deposition. *Trans. ASME* **118**, 280–286. (Cited on pages 20, 57, 58 and 62.)

BROWN, P. M., PATTENDEN, R., VERNOOY, C., ZELT, D. T. & GUTELIUS, J. R. 1996 Selective management of abdominal aortic aneurysms in a prospective measurement program. *J. Vasc. Surg.* **23**, 213–220. (Cited on page 6.)

BUDWIG, R., ELGER, D., HOOPER, H. & SLIPPY, J. 1993 Steady flow in abdominal aortic aneurysm models. *Trans. ASME* **115**, 418–423. (Cited on pages 20, 57 and 62.)

CHIU, J. J. & CHIEN, S. 2011 Effects of disturbed flow on vascular endothelium: Pathophysiological basis and clinical perspectives. *Physiol. Rev.* **91**, 327–387. (Cited on pages 4 and 62.)

CHO, K. J., KIM, M. U. & SHIN, H. D. 1988 Linear stability of two-dimensional steady flow in wavy-walled channels. *Fluid Dyn. Research* **23**, 349–370. (Cited on pages 21 and 69.)

CHOKE, E., COCKERILL, G., WILSON, W. R. W, SAYED, S., DAWSON, J., LOFTUS, I. & THOMPSON, M. M. 2005 A review of biological factors implicated in abdominal aortic aneurysm rupture. *Eur. J. Vasc. Endovasc. Surg.* **30**, 227–244. (Cited on page 3.)

CONWAY, K. P., BYRNE, J., TOWNSEND, M. & LANE, I. F. 2001 Prognosis of patients turned down for conventional abdominal aortic aneurysm repair in the endovascular and sonographic era: Szilagyi revisited? *J. Vasc. Surg.* **33**, 752–757. (Cited on pages 6 and 7.)

COTRELL, D. L., MCFADDEN, G. B. & ALDER, B. J. 2008 Instability in pipe flow. *Proceedings of the National Academy of Sciences of the United States of America* **105**, 428–430. (Cited on page 21.)

DAVIS, S. H. 1976 The stability of time-periodic flows. *Annu. Rev. Fluid Mech.* **8**, 57–74. (Cited on page 16.)

DEPLANO, V., KNAPP, Y., BERTRAND, E. & GAILLARD, E. 2007 Flow behaviour in an asymmetric compliant experimental model for abdominal aortic aneurysm. *J. Biomech.* **40**, 2406–2413. (Cited on pages 22, 24, 79 and 80.)

DEPLANO, V., MEYERA, C., GUIVIER-CURIENA, C. & BERTRAND, E. 2013 New insights into the understanding of flow dynamics in an in vitro model for abdominal aortic aneurysms. *Med. Engg. Phys.* **35**, 800–809. (Cited on pages 23, 79, 80 and 130.)

DEPLANO, V. & SIOUFFI, M. 1999 Experimental and numerical study of pulsatile flows through stenosis: Wall shear stress analysis. *J. Biomech.* **32**, 1081–1090. (Cited on pages 19, 91, 94, 108, 121, 126, 146 and 147.)

DERHAM, G. 2011 Reduced-order models for linear dynamics and control in aerodynamics. PhD thesis, L'École Nationale Supérieure d'Arts et Métiers, France. (Cited on pages 27 and 29.)

DRAZIN, P. G. & REID, W. H. 1981 *Hydrodynamic stability*. Cambridge Univ. Press. (Cited on page 21.)

DUCLAUX, V., GALLAIRE, F. & CLANET, C. 2010 A fluid mechanical view on abdominal aortic aneurysms. *J. Fluid Mech.* **664**, 5–32. (Cited on pages 1, 22 and 79.)

EGELHOFF, C. J., BUDWIG, R. S., ELGER, D. F., KHRAISHI, T. A. & JOHANSEN, K. H. 1999 Model studies of the flow in abdominal aortic aneurysms during resting and exercise conditions. *Biorheology* **32**, 1319–1329. (Cited on pages 24 and 80.)

EHRENSTEIN, U. & GALLAIRE, F. 2005 On two-dimensional temporal modes in spatially evolving open flows: the flat-plate boundary layer. *J. Fluid Mech.* **536**, 221–233. (Cited on page 36.)

FEDELE, F., HITT, D. L. & PRABHU, R.D. 2005 Revisiting the stability of pulsatile pipe flow. *Eur. J. Mech. Fluids* **24**, 237–254. (Cited on pages 16 and 121.)

FILLINGER, M. F., MARRA, S. P., RAGHAVAN, M. L. & KENNEDY, F. E. 2003 Prediction of rupture risk in abdominal aortic aneurysm during observation: wall stress versus diameter. *J. Vasc. Surg.* **37**, 724–732. (Cited on page 7.)

FINOL, E. A. & AMON, C. H. 2002 Flow induced wall shear stress in abdominal aortic aneurysm: Part I – Steady flow haemodynamics. *Comput. Meth. Biomech. Biomed. Engng* **5**, 309–318. (Cited on page 20.)

FLORYAN, J. M. 2003 Vortex instability in a diverging–converging channel. *J. Fluid Mech.* **482**, 17–50. (Cited on page 21.)

FRY, D. L. 1968 Acute vascular endothelial changes associated with increased blood velocity gradients. *Circ. Res.* **22**, 165–197. (Cited on page 4.)

FRYDMAN, G., WALKER, P. J., SUMMERS, K., WEST, M., XU, D., LIGHTFOOT, T., CODD, C., DIQUE, T. & NATAATMADJA, M. 2003 The value of screening in siblings of patients with abdominal aortic aneurysm. *Eur. J. Endovasc. Surg.* **26**, 396–400. (Cited on page 3.)

FUKUSHIMA, T., MATSUZAWA, T. & HOMMA, T. 1989 Visualization and finite element analysis of pulsatile flow in models of the abdominal aortic aneurysm. *Biorheology* **26**, 109–130. (Cited on pages 21 and 22.)

FUNG, Y. C. 1993 *Biomechanics: Mechanical properties of living tissues*. New York: Springer-Verlag. (Cited on page 2.)

GAILLARD, E., BERGERON, P. & DEPLANO, V. 2007 Influence of wall compliance on hemodynamics in models of abdominal aortic aneurysm. *J. Endovasc. Ther.* **14**, 593–599. (Cited on page 22.)

GLAGOV, S., ZARINS, C., GIDDENS, D. P. & KU, D. N. 1988 Hemodynamics and atherosclerosis, insights and perspectives gained from studies of human arteries. *Arch. Pathol. Lab. Med.* **112**, 1018–31. (Cited on page 4.)

GRIFFITH, M. D. 2007 Stabilité et dynamique des écoulements en géométrie de sténose. PhD thesis, Université de Provence, Aix-Marseille and Monash University, Australia. (Cited on pages 17, 18, 38, 44 and 45.)

GRIFFITH, M. D., LEWEKE, T., THOMPSON, M. C. & HOURIGAN, K. 2008 Steady inlet flow in stenotic geometries: convective and absolute instabilities. *J. Fluid Mech.* **616**, 111–133. (Cited on pages 17, 38, 41, 42 and 43.)

GRIFFITH, M. D., LEWEKE, T., THOMPSON, M. C. & HOURIGAN, K. 2009 Pulsatile flow in stenotic geometries: flow behaviour and stability. *J. Fluid Mech.* **622**, 291–320. (Cited on pages 18, 19, 38, 45, 121, 124 and 146.)

GRIFFITH, M. D., LEWEKE, T., THOMPSON, M. C. & HOURIGAN, K. 2013 Effect of small asymmetries on axisymmetric stenotic flow. *J. Fluid Mech.* **721**, R1–1–R1–11. (Cited on pages 18, 121 and 146.)

GROSCH, C. E. & SALWEN, H. 1968 The stability of steady and time-dependent plane Poiseulle flow. *J. Fluid Mech.* **34**, 177–205. (Cited on pages 16 and 121.)

GROUP, MULTICENTRE ANEURYSM SCREENING STUDY 2002 Multicentre aneurysm screening study (MASS): cost-effectiveness analysis of screening for abdominal aortic aneurysms based on four year results from a randomised controlled trial. *BMJ* **325**, 1135–1138. (Cited on page 3.)

HE, C. M. & ROACH, M. R. 1994 The composition and mechanical properties of abdominal aortic aneurysms. *J. Vasc. Surg.* **20**, 6–13. (Cited on page 3.)

HOLZAPFEL, G. A. 2002 Biomechanics of soft tissues with application to arterial walls. *J.A.C. Martins and E.A.C. Borges Pires (eds.),"Mathematical and Computational Modeling of Biological Systems", Chapter 1, Centro Internacional de Matemática CIM: Coimbra, Portugal.* pp. 1–37. (Cited on pages 2 and 3.)

HOSHINA, K., SHO, E., SHO, M., NAKAHASHI, T. K. & DALMAN, R. L. 2003 Wall shear stress and strain modulate experimental aneurysm cellularity. *J. Vasc. Surg.* **37**, 1067–1074. (Cited on page 80.)

HUANG, Y., GLOVICZKI, P., DUNCAN, A. A., KALRA, M., HOSKIN, T. L., ODERICH, G. S., MCKUSICK, M. A. & BOWER, T. C. 2008 Common iliac artery aneurysm: Expansion rate and results of open surgical and endovascular repair. *J. Vasc. Surg.* **47**, 1210–1211. (Cited on page 1.)

HUMPHREY, J. D. & TAYLOR, C. A. 2008 Intracranial and abdominal aortic aneurysms: similarities, differences, and need for a new class of computational models. *Annu. Rev. Biomed. Engg.* **10**, 221–246. (Cited on pages 21 and 79.)

HYARIC, A. LE, HECHT, F., PIRONNEAU, O. & OHTSUKA, K. 2011 Freefem++ (version 3.16), Laboratoire Jacques-Louis Lions, Université Pierre et Marie Curie. (Cited on page 29.)

ISSELBACHER, E. M. 2005 Thoracic and abdominal aortic aneurysms. *Circulation* **111**, 816–828. (Cited on pages 4, 6 and 7.)

JILKOVA, Z. M., DEPLANO, V., VERDIER, C., TOUNGARA, M., GEINDREAU, C. & DUPERRAY, A. 2013 Wall shear stress and endothelial cells dysfunction in the context of abdominal aortic aneurysms. *Comp. Meth. Biomech. Biomed. Engg.* **16**, 27–29. (Cited on pages 4, 84 and 89.)

JOHNSTON, K. W., RUTHERFORD, R. B., TILSON, M. D., SHAH, D. M., HOLLIER, L. & STANLEY, J. C. 1991 Suggested standards for reporting on arterial aneurysms. Subcommittee on reporting standards for arterial aneurysms, ad hoc committee on reporting standards, society for vascular surgery and north american apter, international society for cardiovascular surgery. *J. Vasc. Surg.* **13**, 452–458. (Cited on page 1.)

JOSEPH, D. D. 1976 *Stability of Fluid Motions I, Springer Tracts in Natural Philosophy.* Springer. (Cited on page 37.)

KU, D. N. 1997 Blood flow in arteries. *Annu. Rev. Fluid Mech.* **29**, 399–434. (Cited on pages 4, 8, 9, 58, 62, 82 and 94.)

LANZERSTORFER, D. & KUHLMANN, H. C. 2012a Global stability of multiple solutions in plane sudden-expansion flow. *J. Fluid Mech.* **702**, 378–402. (Cited on pages 37, 73 and 75.)

LANZERSTORFER, D. & KUHLMANN, H. C. 2012*b* Global stability of the two-dimensional flow over a backward-facing step. *J. Fluid Mech.* **693**, 1–27. (Cited on pages 37 and 76.)

LASHERAS, J. C. 2007 The biomechanics of arterial aneurysms. *Annu. Rev. Fluid Mech.* **39**, 293–319. (Cited on pages 1, 2, 3, 21, 79, 84, 89, 90 and 146.)

LEDERLE, F. A., JOHNSON, G. R. & WILSON, S. E. 2001 Aneurysm Detection and Management Veterans Affairs Cooperative Study: abdominal aortic aneurysm in women. *J. Vasc. Surg.* **34**, 122–126. (Cited on page 3.)

LEDERLE, F. A., JOHNSON, G. R., WILSON, S. E., CHUTE, E. P., LITTOOY, F. N., BANDYK, D., KRUPSKI, W. C., BARONE, G. W., ACHER, C. W. & BALLARD, D. J. 1997 Prevalence and associations of abdominal aortic aneurysm detected through screening. Aneurysm Detection and Management (ADAM) Veterans Affairs Cooperative Study Group. *ANN. Intern. Med.* **126**, 441–449. (Cited on page 3.)

LEDERLE, F. A. & SIMEL, D. L. 1999 The rational clinical examination: does this patient have abdominal aortic aneurysm? *JAMA* **281**, 77–82. (Cited on page 5.)

LES, A. S., SHADDEN, S. C., FIGUEROA, C. A., PARK, J. M., TEDESCO, M. M., HERFKENS, R. J., DALMAN, R. L. & TAYLOR, C. A. 2010 Quantification of hemodynamics in abdominal aortic aneurysms during rest and exercise using magnetic resonance imaging and computational fluid dynamics. *Ann. Biomed. Eng.* **38**, 1288–1313. (Cited on pages 24, 79, 80, 108, 112 and 121.)

LIGHTHILL, M. J. 1972 Physiological fluid dynamics: a survey. *J. Fluid Mech.* **52**, 475–497. (Cited on page 19.)

LOH, S. A. & BLACKBURN, H. M. 2011 Stability of steady flow through an axially corrugated pipe. *Phys. Fluids* **23**. (Cited on page 21.)

MAIER, S. E., MEIER, D., BOESIGER, P., MOSER, U. T. & VIELI, A. 1989 Human abdominal aorta: comparative measurements of blood flow with MR imaging and multi-gated doppler US. *Radiology* **171**, 487–492. (Cited on page 15.)

MAO, X., SHERWIN, S. J. & BLACKBURN, H. M. 2011 Transient growth and bypass transition in stenotic flow with a physiological waveform. *Theor. Comput. Fluid Dyn.* **25**, 31–42. (Cited on pages 19 and 121.)

MARQUET, O. 2007 Stabilité globale et contrôle d'écoulements de recirculation. PhD thesis, Université de Poitiers, France. (Cited on page 27.)

MARQUET, O., LOMBARDI, M., CHOMAZ, J. M., SIPP, D. & JACQUIN, L. 2009 Direct and adjoint global modes of a recirculation bubble. *J. Fluid Mech.* **622**, 1–21. (Cited on pages 30, 31, 33 and 36.)

MARTINO, E. S. DI, GUADAGNI, G., FUMERO, A., BALLERINI, G., SPIRITO, R., BIGLIOLI, P. & REDAELLI, A. 2001 Fluid–structure interaction within realistic three-dimensional models of the aneurysmatic aorta as a guidance to assess the risk of rupture of the aneurysm. *Med. Eng. Phys.* **23**, 647–655. (Cited on page 23.)

MCDONALD, D. A. 1955 The relation of pulsatile pressure to flow in arteries. *J. Physiol.* **127**, 533–552. (Cited on page 8.)

NAYAR, N. & ORTEGA, J. M. 1993 Computation of selected eigenvalues of generalized eigenvalue problems. *J. Comp. Phys.* **108**, 8–14. (Cited on page 36.)

NEBAUER, J. R. A. & BLACKBURN, H. M. 2009 Stability of oscillatory and pulsatile pipe flow. *Seventh international conference on CFD in the minerals and process industries, Melbourne, Australia* . (Cited on page 16.)

NEREM, R. M., SEED, W. A. & WOOD, N. B. 1972 An experimental study of the velocity distribution and transition to turbulence in the aorta. *J. Fluid Mech.* **52**, 137–160. (Cited on pages 16 and 121.)

NICHOLS, W. W. & O'ROURKE, M. F. 1998 *McDonald's blood flow in arteries: theoretical, experimental and clinical principles (4th edn)*. London, Arnold. (Cited on pages 5 and 8.)

PEATTIE, R. A., ASBURY, C. L., BLUTH, E. I. & RUBERTI, J. W. 1996 Steady flow in models of abdominal aortic aneurysms. Part I: Investigation of the velocity patterns. *J. Ultrasound Med.* **15**, 679–688. (Cited on pages 20 and 57.)

PEATTIE, R. A., RIEHLE, T. J. & BLUTH, E. I. 2004 Pulsatile flow in fusiform models of abdominal aortic aneurysms: Flow fields, velocity patterns and flow-induced wall stresses. *J. Biomech. Eng.* **126**, 438–446. (Cited on page 22.)

PEATTIE, R. A., SCHRADER, T., BLUTH, E. I. & COMSTOCK, C. E. 1994 Development of turbulence in steady flow through models of abdominal aortic aneurysms. *J. Ultrasound Med.* **13**, 467–472. (Cited on pages 20 and 57.)

PEDLEY, T. J. 1979 *The Fluid Mechanics of Large Blood Vessels*. Cambridge Univ. Press. (Cited on pages 4, 8, 62 and 89.)

PEDLEY, T. J. 2003 Mathematical modelling of arterial fluid dynamics. *J. Engg. Math.* **47**, 419–444. (Cited on page 19.)

RAGHAVAN, M. L. & VORP, D. A. 2000 Toward a biomechanical tool to evaluate rupture potential of abdominal aortic aneurysm: identification of a finite strain constitutive model and evaluation of its applicability. *J. Biomech.* **33**, 475–482. (Cited on page 22.)

RAGHAVAN, M. L., VORP, D. A., FEDERLE, M. P., MAKAROUN, M. S. & WEBSTER, M. W. 2000 Wall stress distribution on three-dimensionally reconstructed models of human abdominal aortic aneurysm. *J. Vasc. Surg.* **31**, 760–769. (Cited on pages 22, 24 and 79.)

RAYLEIGH, LORD 1917 On the dynamics of revolving fluids. *Proc. R. Soc. Lond.* **A 93**, 148–154. (Cited on page 75.)

REDDY, J. N. 2006 *An introduction to the finite element method*. McGraw-Hill. (Cited on page 29.)

REININGER, A. J., HEINZMANN, U., REININGER, C. B., FRIEDRICH, P. & WURZINGER, L. J. 1994 Flow mediated fibrin thrombus formation in an endothelium-lined model of arterial branching. *Thrombosis Res.* **74(6)**, 629–641. (Cited on pages 80, 108, 121, 126 and 147.)

ROBICHAUX, J., BALACHANDAR, S. & VANKA, S. P. 1999 Three-dimensional Floquet instability of the wake of square cylinder. *Phys. Fluids* **11**, 560–578. (Cited on pages 37, 123 and 132.)

SALSAC, A. V. 2005 Évolution des contraintes hémodynamiques lors de la croissance des anévrismes aortiques abdominaux. PhD thesis, École Polytechnique. (Cited on pages 22, 79, 80, 91, 94 and 99.)

SALSAC, A. V., SPARKS, S. R., CHOMAZ, J. M. & LASHERAS, J. C. 2006 Evolution of the wall shear stresses during the progressive enlargement of symmetric abdominal aortic aneurysms. *J. Fluid Mech.* **560**, 19–51. (Cited on pages 11, 15, 22, 23, 40, 82, 83, 87, 115, 120, 143 and 147.)

SALSAC, A. V., SPARKS, S. R. & LASHERAS, J. C. 2004 Hemodynamic changes occurring during the progressive enlargement of abdominal aortic aneurysms. *Ann. Vasc. Surg.* **18**, 14–21. (Cited on pages 22, 79, 108, 121 and 147.)

SCHMID, P. J. & HENNINGSON, D. S. 2001 *Stability and transition in shear flows*. Springer. (Cited on pages 21 and 73.)

SCHRADER, T., PEATTIE, R. A., BLUTH, E. I. & COMSTOCK, C. E. 1992 A qualitative investigation of turbulence in flow through a model abdominal aortic aneurysm. *Invest. Radiol.* **27**, 515–519. (Cited on pages 20 and 57.)

SEXL, T. 1930 Über den von E. G. Richardson entdeckten 'Annulareffekt'. *Z. Phys.* **61**, 179–221. (Cited on page 8.)

SHAABAN, A. M. & DUERINCKX, A. J. 2000 Wall shear stress and early atherosclerosis: A review. *AJR* **174**, 1657–1665. (Cited on page 4.)

SHEARD, G. J. 2009 Flow dynamics and wall shear stress variation in a fusiform aneurysm. *J. Eng. Math.* **64**, 379–390. (Cited on pages 11, 15, 23, 40, 41, 79, 87, 113, 115, 120, 143 and 147.)

SHEARD, G. J. & BLACKBURN, H. M. 2010 Steady inflow through a model aneurysm: global and transient stability. *17th Australasian Fluid Mechanics Conference, Auckland, New Zealand* . (Cited on pages 20, 23 and 57.)

SHEARD, G. J. & RYAN, K. 2008 Wall shear stress and flow stability in a model fusifrom aneurysm. *ANZIAM J.* **50 (CTAC2008)**, C1–C15. (Cited on pages 23 and 143.)

SHEARD, G. J., THOMPSON, M. C. & HOURIGAN, K. 2005 Subharmonic mechanism of the mode C instability. *Phys. Fluids.* **17**, 111702. (Cited on pages 37, 123 and 132.)

SHEIDAEI, A., HUNLEY, S. C., ZEINALI-DAVARANI, S., RAGUIN, L. G. & BAEK, S. 2011 Simulation of abdominal aortic aneurysm growth with updating hemodynamic loads using a realistic geometry. *Med. Eng. Phys.* **33**, 80–88. (Cited on pages 23, 24 and 79.)

SHERWIN, S. J. & BLACKBURN, H. M. 2005 Three-dimensional instabilities and transition of steady and pulsatile axisymmetric stenotic flows. *J. Fluid Mech.* **533**, 297–327. (Cited on pages 17, 18, 19, 38, 39, 47, 121, 124 and 146.)

SORENSEN, D. C. 1992 Implicit application of polynomial filters in a k-step Arnoldi method. *SIAM J. Matrix Anal. Appl.* **13**, 357–385. (Cited on page 36.)

STAMATOPOULOS, C., MATHIOULAKIS, D. S., PAPAHARILAOU, Y. & KATSAMOURIS, A. 2011 Experimental unsteady flow study in a patient-specific abdominal aortic aneurysm model. *Exp. Fluids* **50**, 1695–1709. (Cited on pages 23, 24 and 79.)

STETTLER, J. C. & HUSSAIN, A. K. M. F. 1986 On transition of the pulsatile pipe flow. *J. Fluid Mech.* **170**, 169–197. (Cited on pages 16 and 121.)

SUH, G. Y., LES, A. S., TENFORDE, A. S., SHADDEN, S. C., SPILKER, R. L., YEUNG, J. J., CHENG, C. P., HERFKENS, R. J., DALMAN, R. L. & TAYLOR, C. A. 2011 Hemodynamic changes quantified in abdominal aortic aneurysms with increasing exercise intensity using MR exercise imaging and image-based computational fluid dynamics. *Ann. Biomed. Eng.* **39**, 2186–2202. (Cited on pages 11, 12, 13, 24, 79, 80, 81, 83, 108, 123, 140 and 145.)

SZYMANSKI, P. 1932 Quelques solutions exactes des équations de l'hydrodynamique du fluide visqueux dans le cas d'un tube cylindrique. *J. Math. Pure Appl.* **11**, 67–107. (Cited on page 8.)

TAYLOR, C. A., HUGHES, T. J. R. & ZARINS, C. K. 1999 Effect of exercise on hemodynamic conditions in the abdominal aorta. *J. Vasc. Surg.* **29**, 1077–1089. (Cited on pages 11, 24, 80 and 84.)

TAYLOR, C. A. & YAMAGUCHI, T. 1994 Three-dimensional simulation of blood flow in an abdominal aortic aneurysm–steady and unsteady flow cases. *J. Biomech. Engg.* **116**, 89–97. (Cited on pages 22, 79 and 80.)

THOMAS, C., BASSOM, A. P., BLENNERHASSETT, P. J. & DAVIES, C. 2011 The linear stability of oscillatory Poiseuille flow in channels and pipes. *Proc. R. Soc. Lond. A* **467**, 2643–2662. (Cited on pages 16 and 121.)

THOMPSON, M. M. 2003 Controlling the expansion of abdominal aortic aneurysms. *Br. J. Surg.* **90**, 897–898. (Cited on page 7.)

THUBRIKAR, M. J., ROBICSEK, F., LABROSSE, M., CHERVENKOFF, V. & FOWLER, B. L. 2003 Effect of thrombus on abdominal aortic aneurysm wall dilation and stress. *J. Cardiovasc. Surg.* **44**, 67–77. (Cited on page 4.)

TOZZI, J. T. & VON KERCZEK, C.H. 1986 The stability of oscillatory Hagen–Poiseuille flow. *J. Appl. Mech. ASME* **53**, 187–192. (Cited on pages 16 and 121.)

VARGHESE, S. S., FRANKEL, S. H. & FISCHER, P. F. 2007*a* Direct numerical simulation of stenotic flows. Part 1. Steady flow. *J. Fluid Mech.* **582**, 253–280. (Cited on page 17.)

VARGHESE, S. S., FRANKEL, S. H. & FISCHER, P. F. 2007*b* Direct numerical simulation of stenotic flows. Part 2. Pulsatile flow. *J. Fluid Mech.* **582**, 281–315. (Cited on page 18.)

VÉTEL, J., GARON, A., PELLETIER, D. & FARINAS, M. I. 2008 Asymmetry and transition to turbulence in a smooth axisymmetric constriction. *J. Fluid Mech.* **607**, 351–386. (Cited on page 18.)

VORP, D. A. 2007 Biomechanics of abdominal aortic aneurysm. *J. Biomech.* **40**, 1887–1902. (Cited on pages 22, 24, 79 and 80.)

VORP, D. A., LEE, P. C., WANG, D. H. J., MAKAROUN, M. S., NEMOTO, E. M., OGAWA, S. & WEBSTER, M. W. 2001 Association of intraluminal thrombus in abdominal aortic aneurysm with local hypoxia and wall weakening. *J. Vasc. Surg.* **34**, 291–299. (Cited on pages 5, 22, 80 and 91.)

VORP, D. A., RAGHAVAN, M. L. & WEBSTER, M. W. 1998 Mechanical wall stress in abdominal aortic aneurysm: Influence of diameter and asymmetry. *J. Vasc. Surg.* **27**, 632–639. (Cited on pages 20 and 57.)

WHITE, S. B. & STAVROPOULOS, S. W. 2009 Management of endoleaks following endovascular aneurysm repair. *Semin. Intervent. Radiol.* **26**, 33–38. (Cited on page 7.)

WOMERSLEY, J. R. 1955 Method for the calculation of velocity, rate of flow and viscous drag in arteries when their pressure gradient is known. *J. Physiol.* **127**, 553–563. (Cited on pages 8 and 9.)

YANG, W. H. & YIH, C. S. 1977 Stability of time-periodic flows in a circular pipe. *J. Fluid Mech.* **82**, 497–505. (Cited on pages 16 and 121.)

YU, S. C. M. 2000 Steady and pulsatile flow studies in abdominal aortic aneurysm models using particle image velocimetry. *Intl. J. Heat Fluid Flow* **21**, 74–83. (Cited on pages 20 and 57.)